Etudes d'un modèle temporel efficace pour la simulation d'objets communicants contenant des milieux complexes

Abdelrahman Ijjeh

▶ **To cite this version:**

Abdelrahman Ijjeh. Etudes d'un modèle temporel efficace pour la simulation d'objets communicants contenant des milieux complexes. Electromagnetism. Télécom Bretagne; Université de Bretagne Occidentale, 2014. English. NNT : . tel-01206239

HAL Id: tel-01206239
https://hal.science/tel-01206239

Submitted on 28 Sep 2015

HAL is a multi-disciplinary open access archive for the deposit and dissemination of scientific research documents, whether they are published or not. The documents may come from teaching and research institutions in France or abroad, or from public or private research centers.

L'archive ouverte pluridisciplinaire **HAL**, est destinée au dépôt et à la diffusion de documents scientifiques de niveau recherche, publiés ou non, émanant des établissements d'enseignement et de recherche français ou étrangers, des laboratoires publics ou privés.

THÈSE / Télécom Bretagne
sous le sceau de l'Université européenne de Bretagne

pour obtenir le grade de Docteur de Télécom Bretagne
En accréditation conjointe avec l'Ecole doctorale Sicma
Mention : Sciences et Technologies de l'Information et de la Communication

présentée par
Abdelrahman Ijjeh
préparée dans le département Micro-ondes
Laboratoire Labsticc

Etudes d'un modèle temporel efficace pour la simulation d'objets communicants contenant des milieux complexes

Thèse soutenue le 16 décembre 2014
Devant le jury composé de :

Raphaël GILLARD
Professeur, INSA-IETR - Rennes / rapporteur & président

Jean-Lou DUBARD
Professeur, Université de Nice Sophia Antipolis / rapporteur

Francesco ANDRIULLI
Professeur, Télécom Bretagne / examinateur

Michel NEY
Professeur, Télécom Bretagne / directeur de thèse

N° d'ordre 2014telb0334

Sous le sceau de l'Université européenne de Bretagne

Télécom Bretagne

En habilitation conjointe avec l'Université de Bretagne Occidentale

Ecole Doctorale – sicma

Etudes d'un modèle temporel efficace pour la simulation d'objets communicants contenant des milieux complexes

Thèse de Doctorat

Mention : Sciences et Technologies de l'Information et de la Communication (STIC)

Présentée par **Abdelrahman IJJEH**

Département : Micro-Ondes

Laboratoire : Lab-STICC Pôle : MOM

Directeur de thèse : Michel NEY

Soutenue le 16 Décembre 2014

Jury :

M. Raphaël GILLARD, Professeur à l'INSA, Rennes (Rapporteur)

M. Jean-Lou DUBARD, Professeur à Université de Nice Sophia Antipolis (Rapporteur)

M. Michel NEY, Professeur à TELECOM Bretagne (Directeur de thèse)

M. Francesco ANDRIULLI, Professeur à TELECOM Bretagne (Encadrant)

Acknowledgment

First of all, I would like to express my sincere gratitude and deepest appreciation to my advisor and teacher, Prof. Michel NEY, for his continued support during my research project. I am grateful for his patience, motivation, encouragement and immense knowledge and for always being present to answer all my questions, always providing clear explanations to teach me scientific research methods. His guidance and help have been invaluable in finishing this work.

I am very grateful to my teacher and co-advisor, Prof. Francesco ANDRIULLI, for all his time and patience, and for all his invaluable constructive criticism and sincere advice. I am thankful for his aspiring guidance and his support, which were crucial during my project.

Many thanks as well to Prof. Patrick QUÉFFÉLEC and his research group at the Université de Brest Occidental (UBO), especially to Dr. Grégory VERISSIMO and M. Armel LE GOUELLEC for their excellent collaboration and always being very helpful for the experimental part of the project.

Special thanks for the thesis reviewers, Prof. Jean-Lou DUBARD and Prof. Raphaël GILLARD for the effort they have done and all their valuable comments, questions and suggestions that added great value to this thesis.

My sincere thanks also go to Dr. Ibrahim MASSY, Dr. Fahad GOLRA and Dr. Yann BOUCHER for all the constructive discussions we have had together.

I would like to take this opportunity to thank Prof. André LE SAOUT and Prof. Aimee JOHANSEN from the language department at Telecom-Bretagne for their advice and support. Equally, I would like to thank my fellow lab mates and all the employees of Telecom Bretagne and LAB-STICC for their support.

Last but not least, I would like to thank my parents for all their support and encouragement and everything they gave to me.

Abdelrahman IJJEH

Table of Contents

Chapter III. Transmission Line Matrix Method (TLM) State of the Art

Chapter IV. Stability and Dispersion Analysis of a TLM Unified Approach for General Linear Media Transmission Line Matrix Method (TLM)

Appendix A

Table of Figures

List of acronyms

ABC:	Absorbing boundary condition
ADE:	Auxiliary differential equation
ADI:	Alternating direction implicit
CFL:	Courant-Friedrichs-Lewy
EFIE:	Electric field integral equation
EMC:	Electromagnetic compatibility
FD:	Frequency domain
FDFD:	Finite difference frequency-domain
FDTD:	Finite difference time-domain
FEM:	Finite element method
FIR:	Finite impulse response
FIT:	Finite integration technique
GD-TD:	Galerkin discontinues time-domain
GLL:	Gilbert- Landau- Lifshitz
GUI:	Graphical user interface
HSCN:	Hybrid symmetrical condensed node
IIR:	Infinite impulse response
LH:	Left hand
LOD:	Locally one-dimension
LTI:	Linear time invariant
MKL:	Math kernel library
MM:	Metamaterial
MoM:	Method of moment
MRTD:	Multi resolution time-domain
NAG:	Numerical algorithms group
PEC:	Perfect electric conductor
PLRC:	Piecewise-linear recursive convolution
PMC:	Perfect magnetic conductor

PML:	Perfectly matched layer
RCS:	Radar cross section
RH:	Right hand
RWG:	Rao-Wilton-Glisson
SCN:	Symmetric condensed node
SSCN:	Super symmetrical condensed node
SS-TLM:	Split step – TLM
TCL-TK:	Tool command language-toolkit
TD:	Time-domain
TE:	Transverse electric
TEM:	Transverse electric magnetic
TLM:	Transmission-line matrix
TM:	Transverse magnetic
TO:	Transformation optics

Chapter I
General Introduction

1.1 Introduction

Imagine a musical symphony composed out of one type of notes, an artistic painting with one color, or an architectural design with similar building blocks, it is boring, but also far from being optimal. In any creative or architectural design one needs a set of basic building components: different notes for musicians, different colors for painters are examples. And having these several basic building components gives the designer more freedom and more dimensionality to achieve very sophisticated designs.

In the area of engineering and applied sciences where the design process lies in the heart of these disciplines, we can see clearly how the invention of new materials (building components) has automatically led to a new revolution in the technology: semiconductors, graphene and modern nano-materials are simple examples.

Likewise in the area of electromagnetism and electromagnetic devices, the fact that there are media with different properties is a blessing, even though this may make the design and analysis process more difficult. It will allow us to design and build much advanced devices that outperforms the ones that use simple media only. A simple example which was one of the motivations behind writing this thesis is to study the effect and the potential usages of saturated [1.I] [2.I] and non-saturated ferrite material inside different devices [3.I], like waveguides or antennas…etc. Usually, this material is very complex since it is fully nonhomogeneous, frequency dependent, anisotropic, and all these properties depend on externally applied static magnetic-field. Even with these difficulties, the usage of this material in antennas (as a substrate) for instance has shown better performance, thanks to the tunability of antenna properties by means of an external applied magnetic field. Apart from the non-saturate ferrite, complex media in nature or those which are fabricated in laboratories are countless. Thus, we imagine the enormous number of applications that will benefit from using these media. Furthermore, we should not forget the electronic circuits that tend to increase their frequency of operation every

year and they will eventually require the use full-wave electromagnetic simulation. Also, as mentioned above, these circuits will benefit from the usage of complex media [4.I].

Besides the real life applications, dealing with complex media is a mathematical issue and hot topic of research. When dealing with fluid dynamics problems (Nervier-Stokes equations) [5.I], electromagnetism (Maxwell's equations) [3.I], thermodynamics (potentials equations) [5.I]…etc., whatever the domain of application considered, we always face the same problem of developing reliable computational schemes capable of handling these complex media. Last but not least, one has to elaborate reliable and relevant numerical experiments to test and validate these numerical schemes [6.I] [7.I].

In this introductory chapter of the thesis, we first define the computational electromagnetics and computational domain components. Then, we discuss three formulations to describe Maxwell's equations mathematically and how every formulation is more suitable in certain scenarios. It is followed by a comparison between different computational schemes. We explain further the problem statement, the objectives of this work and briefly what has been achieved. Finally, we will mention the computer resources that have been used to accomplish this work.

1.2 Computational Problem

A computational problem is defined as a mathematical object that contains a set of given data and a collection of questions and unknowns that computers possibly can solve [8.I] [9.I]; it could be a problem of factoring a number or a problem to solve a complex system of equations numerically or a problem of doing a full simulation of a very complex system...etc. In the field of numerical\computational electrodynamics, we usually face problems that involve a region of space-time filled by different media, in which some vector-quantities (electric and magnetic fields) are propagating and changing with time and space. Those fields are governed by a system of differential equations (Maxwell's equations), and the space-time region is surrounded by some boundary and initial conditions [10.I]. Figure.1.I shows different components of a computational problem which is detailed below:

- **The dynamical system of equations** (Maxwell's equations)

This system of equations which governs the evolution of fields in every localion (govern the local behaviour of the solution). In other words, at any given point in the computational domain, the system of differential equations provides us with full information about the way the fields are going to evolve, assuming we already know the present and the past values of the fields at that point and its neighborhood. However, if the system is time dependent (which means that it has some type of memory) then it will be necessary to know the previous values of the fields in that neighborhood in order to calculate the future values of the fields (like the case of dispersive media) [3.I] [11.I].

- **The boundary conditions**

Even though they may not appear explicitly in each point in the computational domain (usually they appear explicitly at the interface between two different media), they control the global behavior of the solution. The existence of specific modes of propagation inside a waveguide is an example. In computational electrodynamics, there are different types of boundary conditions, but it is more suitable to classify them into two categories:

  - **Natural boundary conditions**

At the interface of between different media, it is obligatory to respect some boundary conditions (the continuity of tangential electric and normal magnetic field induction components at the interface between different media) [12.I]. Furthermore, even inside homogenous media the boundary conditions should be respected at every point in the space, because they are direct implication of Maxwell's equations [11.I] [4.I]. A special case of natural boundary condition is the Perfect Electric Conductor (PEC) which ideally exists at the surface of media with infinte electric conductivity. The duality, that exists in electromagnetism allows the dual ideal (but ficticious) medium that has infinite magnetic conductivity. We thus refer to Perfect Magnetic Conductor (PMC) whose boundary conditions are the dual of the ones of the PEC.

- **Artificial boundary conditions**

For volumic numerical formulation, it is necessary for space unbounded problems to limit the computational domain by Artificial Boudaries Conditions (ABC) that emulate the truncated space outside. They can be classified into two categories:

- One-way equation techniques which evaluate field values at boundaries from nearby samples.
- Bérenger's type of ABC which extend the computational domain by a non-Maxwellian artificial medium that absorbs fields with negligible reflections back to the computational domain.

More about boundary conditions will be presented in chaper III [6.I] [13.I] [14.I].

- **Initial Conditions**

They are not relevant when steady-state solutions in linear time invarient (LTI) systems are desired. However, for time-domain solutions a full knowledge of them is required for evaluating the transient response. In time domain-methods, it is traditionally to assume that the fields are identically zeros at the beginning of the simulation (causality). Once the souce is applied, fields start to propagate [6.I] [10.I].

- **Sources**

In differential form of Maxwell's equations, we have to define current sources (or associated charge distributions) explicitly. This means that we need to know a priori the regions that contain them and the corresponding value of the source at each point in those regions. In 3D structures we have current and associated charge densities. If one is interested in illuminating a computational domain by a plane wave (or any type of waves), it is possible to use the technique of Huygens' surface. Equivalent surface current densities, both magnetic and electric are injected at the surface of the Huygens' surface that encloses the region to be illuminated with total field. These sources are related to incident fields by using equivalence principle [15.I] [16.I] [4.I].

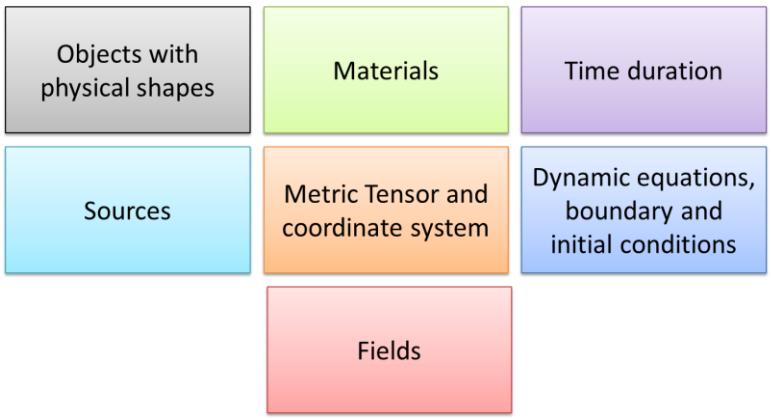

Figure 1.I, computational domain components

- **Materials**

Materials represent the environment in which fields evolve and propagate. As a material at the ultimate level may consist of charged elementary particles, these may interact with the electromagnetic fields. This interaction can take different forms, which are characterized by key parameters that are involved in fields' evolution. More about the physics of materials will be discussed in chapter II [3.I] [4.I].

- **Coordinate system**

The system of coordinates is a mathematical tool to describe the geometrical properties (shapes and positions) of different objects in the computational domain; it could be Cartesian, cylindrical, spherical, or any other appropriate coordinate system. There is another mathematical very important tool accompanied with any geometry, namely, the metric tensor [17.I] [18.I], which is usually ignored in most cases that deal with Euclidian and Minkowskian spaces. However, in a general geometry, one should state the metric tensor explicitly, because the coordinate system identifies every point in space with n-tuples that define that point uniquely. Also, the metric tensor gives full information about the distances between any two points [18.I]. The reason behind not mentioning the metric tensor in traditional Euclidean and Minkowskian spaces, is that the distance between any two points is by default governed by the Pythagorean Theorem. As we will see in the next section, to solve Maxwell's equations in presence of curved

space-time geometry like the one beside a black hole, one should use Maxwell's equations in tensor form and should work in the Riemannian geometry platform [17.I].

1.3 Maxwell's equations in different formulations

Maxwell's equations came into light after years of work by J. Clark Maxwell between 1861 and 1862. His formulation is based on many results obtained by several researchers who worked on the field before him like Michel Faraday, and Ampère…etc. Those equations came to govern all the aspects of wave-nature of electromagnetism. They also state the exact relations between electric and magnetic fields, and they show why they can't exist separately (except ate DC when dealing with static fields) [4.I].

Maxwell's equations have two main formulations, the microscopic version that works at the atomic and molecular level and macroscopic version that is valid for the case when media can be considered as continuous. In this case, any infinitesimal volume can be characterized by an average constitutive parameter value. By applying an appropriate statistical physic analysis, one can derive from the microscopic description the macroscopic model [3.I] [4.I].

Originally, Maxwell's equations were written in twenty scalar equations. It is later that Hertz and Heaviside wrote them in the modern vector form. Introducing the general Ohm's laws, they can be expressed in the general form (1.I). However, after the publication of the relativity theory, it became necessary to use suitable mathematical tools to describe electromagnetism in reference frames with high gravity fields, or with high speeds with respect to a frame of reference. In other words, when the metric tensor of the space-time is no longer Minkowskian [17.I], the reformulation of Maxwell's equations in tensor form (2.I) was a necessity to study the electromagnetic radiations in the presence of heavy objects such as stars and black holes in deep space [5.I] [19.I].

Table 1.I, Maxwell's equations in different mathematical forms [4.I] [20.I]

Vector Form	$\nabla \times \vec{E} = -\frac{\partial \vec{B}}{\partial t} - \bar{\bar{\sigma}}_m * \vec{H} - \vec{J}_m$ $\nabla \times \vec{H} = -\frac{\partial \vec{D}}{\partial t} - \bar{\bar{\sigma}}_e * \vec{E} - \vec{J}_e$ $\nabla . \vec{D} = \rho_v$ $\nabla . \vec{B} = 0$	(1.I)
Tensor Form	$\nabla_{[\alpha} F_{\beta\gamma]} = 0$ $\nabla_\alpha \left(\sqrt{-g} F^{\beta\alpha}\right) = \mu_o J^\beta$	(2.I)
Differential Form	$dF = 0$ $d * F = \mu_o J$	(3.I)

where $\vec{E}$ and $\vec{H}$ are the electric and magnetic fields intensities, respectively, $\vec{D}$ and $\vec{B}$ are the electric and magnetic field densities, respectively. $\bar{\bar{\sigma}}_e$ and $\bar{\bar{\sigma}}_m$ are the electric and magnetic conductivity tensors, respectively. $\vec{J}_e$ and $\vec{J}_m$ are the impressed magnetic and electric current sources, and ρ_v is the charge density.

While *tensor* formulation of Maxwell's equations is analogous to differential equation formulation in vector form, the *differential form* of Maxwell's equations (3.I) is analogous to integral equation formulation in vector form [20.I] [21.I]. If one is interested in solving Maxwell's equation in general (non-Minkowskian) space-time geometry, then the differential form provides a solid tool to perform the necessary integrations in this kind of complicated space-time geometry [18.I]. Even with normal Euclidian geometry one could apply numerical methods based on *differential form* of Maxwell's equations instead of tradition integral equation. This can help to overcome many numerical problems we encounter in vector calculus such as different types of singularities or dealing very fine details in multi-scale computational problems [16.I] [21.I]. Referring to table 1.I, fields in the tensor form are defined by [17.I] [5.I]:

$$F^{\alpha\beta} = \begin{bmatrix} 0 & -E^1 & -E^2 & -E^3 \\ E^1 & 0 & -cB^3 & cB^2 \\ E^2 & cB^3 & 0 & -cB^1 \\ E^3 & -cB^2 & cB^1 & 0 \end{bmatrix} \tag{4.I}$$

$$H^{\alpha\beta} = \begin{bmatrix} 0 & -D^1 & -D^2 & -D^3 \\ D^1 & 0 & -cH^3 & cH^2 \\ D^2 & cH^3 & 0 & -cH^1 \\ D^3 & -cH^2 & cH^1 & 0 \end{bmatrix} \tag{5.I}$$

The metric tensor $g_{\alpha\beta}$ is a square matrix, that uniquely defines distances between different points in space (this is the reason behind its name), and g is the determinant of the metric tensor. The latter is equal to unity in normal Minkowskian space-time. Thus it doesn't appear in traditional vector form of Maxwell's equations:

$$g = Det(g_{\alpha\beta}) \tag{6.I}$$

In general material, constitutive parameters are defined by the relation between the field tensors $F^{\alpha\beta}$ and $H^{\alpha\beta}$ which is given by some function f that is material dependent [17.I], such as:

$$H^{\alpha\beta} = f\left(F^{\alpha\beta}\right) \tag{7.I}$$

where f is some general tensorial function. For the special case of free space (7. I) becomes:

$$H_{\alpha\beta} = \varepsilon_0 F_{\alpha\beta} \tag{8.I}$$

In differential forms (3.I) the symbol $*$ is the Hodge-star operator, and fields are defined as [20.I]:

$$F = F_{\alpha\beta} dx^{\alpha} \wedge dx^{\beta} \tag{9.I}$$

where $\wedge$ is the exterior product operator, dx^{α} and dx^{β} are incremantal displacement 1-form quantities [18.I]. As shown in (6.I), fields are contained in the 2-form quantity F, and the objective of solving system (3.I) is to calculate the field 2-form F [20.I] [21.I].

1.4 Computational methods in electromagnetics

Analytical methods either in electrodynamics or any other discipline are practical only for simple problems; this includes simple geometry, simple boundary conditions and simple equation parameters (called constitutive equations in electromagnetics) [4.I]. This is because when facing a simple problem the amount of information one has to process is limited. For instance, the sphere is characterized by its radius and the position of its center. Hence, full analytical solutions can be obtained. In a general manner, one can state that an analytical solution is feasible if boundary conditions are invariant over fixed value of coordinate parameters. Thus, one necessary (but not sufficient) condition is that structure boundaries coincide with the coordinate system.

However, in real life, structures are complex in shape and material properties. Hence, some numerical techniques should be applied to obtain useful results. Thus, in the majority of practical problems, the use of numerical methods is indispensable. To name few: scattering of objects with arbitrary shape to calculate their radar cross section (RCS), to predict the performance of antenna systems or to simulate an electromagnetic compatibility test (EMC) for a new device [6.I] [13.I].

The above applications require a huge amount of variables to be processed. Hence, it is necessary to use a computer (or a super-computer) with efficient numerical techniques to obtain useful results within a realistic amount of time. In electrodynamics, as in many other fields in physics, there are plenty of numerical techniques that could be applied to solve the same problem. Obviously, any method should give the correct solution. However, all methods have their pros and cons and some are more suitable than others for certain types of problems as shown in table 2.I.

In computational electrodynamics there are two domains in which numerical schemes can be applied: time-domain (TD) or frequency-domain (FD). In addition, the initial problem can be formulated in different ways. For instance, curl's differential equations, Maxwell integral form, Helmholtz equation or variational form (see table 3.I). In the following pages we briefly discuss the most popular full-wave numerical schemes in EM for analyzing structures with general geometries, and categorize them in their typical domain of solution either in TD or FD [15.I].

1.4.1 Time-Domain methods

In some applications, the main interest is the transient response to an electromagnetic simulation. In others, we are rather interested in performing a very wideband characterization, for instance, a wideband antenna or filter. In some other applications, we may encounter material exhibiting nonlinear behavior. For all the above mentioned applications, using time-domain methods is the most suitable and natural choice for carrying out the necessary simulations. In addition, while frequency domain methods provide the steady state solution for exactly one frequency, time domain methods give us the complete spectrum of solutions (within the validity of the method and according to the frequency spectrum of the source signal), including the transient part [6.I] [7.I] [13.I].

- **Finite difference time domain (FDTD)**

FDTD method is the easiest and the most direct way to solve Maxwell's equations and, in general, any differential equation based system. The idea behind this method is to replace the derivatives with respect to time or space with discrete derivatives .i.e.

$$\frac{\partial F}{\partial \alpha} \approx \frac{F(\alpha+1,\bar{x})-F(\alpha,\bar{x})}{\Delta\alpha} \tag{10.I}$$

where $\bar{x}$ stands for the arguments that the function F may depend on. Similarly, one could derive expression for second or higher order derivatives by using Taylor's series approximation.

The next step is to construct a system of update equations, which depend on the previous time step (explicit form of solution) and the solution will evolve with time. Keep in mind that we should have the knowledge of both initial and boundary conditions. Note that because of the local nature of the formulation, the computational domain extends to the space where fields exist. One refers to volumic methods and in this case the computational domain should be limited by some known boundary conditions [22.I].

Even though finite difference techniques have been known for many decades, its usage for modeling electromagnetic problems became feasible just after the invention of computers, namely, in the sixties. In his very famous paper, K. Yee [10.I] presented an algorithm for FDTD to solve Maxwell's equations. He introduced two 3-D meshes for the same geometry, one for electric fields, and the other for magnetic fields. Meshes are staggered by half space and time steps.

- **Time-Domain Transmission-Line Matrix method (TD-TLM)**

Circuit theory approach for EM problems, is valid only when the wavelength is much larger than the circuit dimensions. In other words, we exclude the space from the problem and assume that quantities reach all points in the space domain simultaneously. The next improvement on the circuit theory model is to introduce transmission-lines between different connecting nodes separated by distances of the wavelength order. Hence, the model includes delay and reflection phenomena by using the transmission-line theory [14.I] [13.I]. The basic principle of the TLM is to replace the computational domain by a network of interconnected transmission-lines running along the Cartesian directions [23.I]. Field propagation is simulated by ordinary waves that travel along the interconnected transmission-line network. If the interconnecting lines are short compared to the wavelength signal, then the field propagation process is correctly simulated. Scattering processes take place at every node according to electromagnetic laws and produce local reflections. Fields are computed by linear combination of local waves. Details will be presented in chapter III and appendix A.

- **Finite Integration Technique (FIT)**

FIT is a computational method based on the Discretization of Maxwell's equations in their integral form. Unlike the FDTD (which is based on the discretization of the Maxwell's curl equations), the FIT inherently fulfils the divergence equations, hence, the conservation of charge and energy is guaranteed. As a result, FIT has a better behavior as FDTD in terms of stability. In addition, the compact matrix form is very elegant and mesh independent. Note that for Cartesian mesh both algorithms are identical [7.I].

- **Discontinuous Galerkin time-domain method**

Discontinuous Galerkin method is a computational technique developed in early 1970 to solve partial differential equations [24.I]. This technique combines different features from FEM (Finite-Element Method) and FIT methods. This makes it an efficient method to handle complex geometrical structures that that are discretized into conforming, non-conforming and locally

refined meshes [25.I]. The time-domain version of this method (DGTD) became an attractive numerical technique to solve time-domain Maxwell's equations especially when complex structures and fine-details are involved [25.I]. However, DGTD method is relatively new method, and presently, no well-known commercial solver uses it.

- **Multi-resolution time domain (MRTD)**

In essence the MRTD is an adaptive computational method based on FDTD technique, and the wavelet analysis. This method has very attractive features, such as the ability to work with larger spatial and time step sizes than normal FDTD, with high level of accuracy [26.I]. However, MRTD requires more operations per iteration and loses its advantages when refined mesh is required near singularities [27.I]. Therefore, it will not be discussed further.

1.4.2 Frequency-Domain methods

When the computational domain is linear (linear materials), and when the main interest is to calculate the response for single frequency, or few set of frequencies (for narrow band characterization), frequency-domain methods exceeds time-domain ones. Unlike time-domain schemes, they generate a matrix system to be solved for a given frequency. However, because of the huge advancement of the precondition and iterative linear solvers in the last few decades, solutions can be obtained in some reasonable time for thousands of degrees of freedom. In addition, interpolation techniques have been developed that necessitate solutions at few points within a given frequency range. However, accuracy is reached for rather smooth characteristics only.

Frequency-domain methods are also preferable when dealing with dispersive media, since in frequency-domain they are simply characterized by complex numbers well defined at the frequency of interest. In time domain the dispersive nature of any parameter translates in terms of convolution process. Therefore, unlike for FD methods, media are represented by filtering processes that should be performed every time step [13.I] [6.I].

Theoretically, every method has both its time and frequency-domain versions. This is due to the fact that any linear system that can be analyzed in time domain can also be analyzed in

frequency domain via Fourier-transformation. While in literature there are many frequency domain computational schemes, the following list contains the ones that are the most used by research labs in academic and industrial sectors in the domain of electromagnetism [13.I] [15.I] [28.I].

- **Finite Element method (FD-FEM)**

FEM is a numerical scheme used to solve for variational formulations. The original problem, which is the Helmholtz equation, is replaced by an associated functional to the Helmholtz operator with specified boundary conditions. This functional, which is a definite integral has a Kernel related to the unknown function to be determined. Using a numerical approach, it is made stationary (weak formulation) generating a linear system of equations whose unknowns are trial function coefficients. The FEM is specific to the choice of trial functions that approximate the solutions in a sub domain (element) by polynomials. Usually, elements that approximate the computational domain are tetrahedrons in 3D and triangles in 2D. In case of TD-FEM the procedure is done for every time step [29.I].

- **Method Of Moment (MoM)**

The MoM is a numerical method used to solve any linear equation that can be differential, integral, integro-differential. It is typically applied in electromagnetics to field or potential integral equation formulations [43.I]. Indeed, these quantities can be written in terms of integrals containing the unknown currents where the Kernel involves the problem Greens functions. To solve numerically, the unknown currents are expressed in terms of linear combination of weighted basis-functions defined in the computational domain. The objective is to find these weights by minimizing the residual error with respect to a set of testing functions. This procedure generates a linear system of equations from which the basis function weighing coefficients are determined to approximate the current distributions. Fields can then be computed from those distributions via Green's functions. The MOM is the most general numerical procedure and it can be shown that other methods can be expressed by a MOM

system if basis and test functions are chosen appropriately [30.I] [43.I]. In TD-MOM one perform this procedure every time step [31.I].

Table 2.I, typical solution domain of numerical methods [15.I]

Method	Formulation	Typical domain
FDTD	Differential equations	time-domain
TLM	Local wave decomposition	time-domain
MOM	Integral equations	frequency-domain
FEM	Variational	frequency-domain
FIT	Maxwell local integral form	time-domain
DGTD	Variational	time-domain

Table 2.I, comparison between different largely-used computational techniques, $***$ excellent, $**$ good, $*$ not optimal, No not appropriate [15.I]

Method	Non-homogeneous media	Curved Boundary Approximation	Dispersive media	Anisotropic media	Nonlinear and non-stationary media	Wide band characterization and transient
FDTD	**	*	**	**	**	**
TD-TLM	**	*	**	**	**	**
FIT	**	**	**	**	**	**
FD- (IE) MOM	**	**	***	*	No	*
FD-FEM	**	**	***	***	No	*

1.5 Categories of EM problem

As discussed earlier, the computational domain consists of several components shown in figure.1.I. In this section we will concentrate on two of them namely, the sources and the material:

- **Sources**

For deterministic problems, the structure has to be excited by sources which can be of various forms. The frequency content of the source is a crucial parameter in computational problems especially in time domain techniques as it is involved in the choice of time and spatial steps. For wide-band excitation, the highest frequency, which corresponds to the smallest wavelength, is to be considered to select the maximum cell size. This allows one to minimize the dispersion and fix the maximum time-step to insure stability. A point to mention here is that for solving eigenvalue problems in time-domain methods one should apply an excitation, which is not the case for frequency domain methods.

Generally a computational problem can be classified into three categories according to a source frequency component (or equivalently the wavelength) [6.I]:

- High frequency when $Object\ details\ are \gg wavelength$
- Low frequency when $Object\ details\ are \ll wavelength$
- Medium frequency when $Object\ details\ are \sim wavelength$

Usually the computational methods, also called "full-wave" methods, in their standard form are very effective in the range of medium frequencies up to few corresponding wavelengths. However, when using traditional numerical schemes, several problems appear for low and high frequencies. At high frequencies, the necessary discretization of the computational domain exhausts the computational resources. Thus, asymptotic methods [32.I] should be used instead.

At low frequencies, the problem is even worse for time-domain method. The reason is that for insuring stability, the time-step depends on the mesh size. Thus if small meshes (could be order of magnitudes smaller than the wavelength) are required for avoiding coarseness error in some locations, the time step is greatly reduced correspondingly. As a result, it is necessary to perform an excessive number of iterations to cover the whole time response (this issue will be

discussed later in more details). Ultimately, long term instabilities may occur. In frequency domain the corresponding system matrix becomes nearly singular with very high condition number. This makes the solution process very cumbersome or even impossible to solve accurately. Advanced preconditioning techniques and changing the mathematical formulation of the computational scheme such as in loop-star decomposition method for MOM at low frequencies must be applied [16.I] [33.I].

- **Media**

It is well known that media in nature (either natural or artificial) have different electromagnetic properties, as we will discuss in chapter II. From Maxwell's equation perspective, media properties can be categorized into several groups like linear, homogeneous, dispersive (frequency dependent properties), anisotropic, etc.

A full knowledge of which categories the material belongs to is crucial. For instance, a solver assuming linear material cannot be used for nonlinear ones. Also, a solver assuming isotropic media cannot handle structures including anisotropic material. However, writing a general solver that can solve any problem and deals with any material is a very difficult task. In addition, such a general solver would require a complex programming and the manipulation and storage of large constitutive parameter matrices, which is not necessary for simple media.

1.6 Research problem and hypotheses

In its original French description, the thesis is entitled « *Etudes d'un modèle temporal efficace pour la simulation d'objets communicants contenant des milieux complexes* ». Thus, the main objective of this thesis is to develop a simulator that can handle general geometrical structures, involving complex linear media, i.e. media that can be:

- Nonhomogeneous
- Dispersive
- Anisotropic
- Chiral

Once the simulator is implemented, tested, validated with several canonical examples and commercial EM solvers, it will be ready to be used to study different types of microwave and optical devices that use complex material substrates such as ferromagnetic media.

In a nutshell, the work that has been done during this thesis could be summarized in five points:

- Building a TLM based simulator for general linear media
- Implementing a graphical user interface (GUI) for the solver.
- Perform complete mathematical analysis for the dispersion and stability issues, for numerical scheme used in the solver.
- Presenting the potential usage of general coordinate transformation methods as a mapping technique to solve low-frequency problems using TLM or FDTD.
- Carrying out a performance comparison between the TLM method vs. FDTD at the interface between different media, and the impact of highly contrast material on the computation accuracy in both numerical techniques.

1.7 Justification for the research

It is necessary for general solver to simulate modern microwave/optical circuits or structures that include complex media, such as antennas with ferrite substrates, phase shifters, circulators, biological tissues, etc. Among the well-known commercial electromagnetic solvers like COMSOL Multiphysics [34.I]/CST Microwave Studio [35.I]/ FEKO [36.I]/ ANSYS HFSS [37.I], there are practical cases with general non homogeneous complex media which can be handled. However, there are special cases, for example anisotropic ferrite substrates with partial inhomogeneous magnetization, which cannot be handled by commercial software. The TLM solver developed in this work can tackle such special, yet practical, complex cases. Furthermore, the goal of an efficient solver is to have a permanent access to the code file for optimization and, least but not last, the possibility to introduce new models that suit the permanent need of the laboratory to tackle new challenging problems.

1.8 Methodology

Time-Domain TLM is a good candidate for electromagnetic simulations for several reasons: Compared to FDTD it is less dispersive. In other words, larger mesh can be used for equal accuracy. Then, it has been proved to give a better convergence when dealing with structures that have high-contrast constitutive parameters [38.I]. Unlike FDTD, the TLM always updates fields at the center of cells adjacent to interfaces without applying an averaging process and systematically enforcing field continuity conditions across interfaces. For the same reason, TLM is more accurate when irregular (structured) meshing is used with arbitrary mesh ratios. However, the price to pay is to manipulate more samples per cell than in FDTD. But the disadvantage is largely compensated when the degree of heterogeneity of the structure increases. To conclude, TD-TLM has some real potential to treat problems that involves complex media, with reasonable accuracy and efficiency. The different issues raised about salient features of the TLM and FDTD will be discussed in the final chapter where comparison between FDTD and TLM is presented.

1.9 Delimitations of scope and key assumptions

During our development of the TLM solver, we based our work on some key assumptions:

i. The media are linear
ii. Different kinds of boundary conditions are available including perfectly matched layer (PML), impedance boundary conditions, perfectly electric conductor (PEC) and perfectly magnetic conductor (PMC).
iii. The solver is implemented to solve Maxwell's equations in Cartesian coordinate system. This implies the use of parallelepipedic (hexahedral) cells, which implies stair-case approximation for curvilinear boundaries.
iv. The solver can handle irregular structured meshes with hexahedral cells.
v. Media properties and boundary conditions are stationary during the simulation time, LTI (linear time invariant computational domain). The media can be nonhomogeneous, anisotropic, dispersive, and chiral.

vi. Near to far-field transformation is implemented in the solver.

vii. Huygens' box to separate total from scattering field or to inject sources is available.

The two last items are needed for scattering and antenna problems.

1.10 Computer resources

For the development and implementation processes, we mainly used FORTRAN 90 programming language, with which we implemented the main TLM solver. The reason is that FORTRAN is still well suited for scientific computation. Also, it is associated with a complete set of subroutines and predefined functions, such as the scientific Numerical Algorithms Group (NAG) library or Math Kernel Library (MKL). The important part was to develop a graphical user interface, because the input data of complicated geometry carried out manually is very tedious with high probability of making mistakes. The GUI was accomplished using GiD mesher software [39.I], in which the user can design the required structure, assign the necessary materials, define the excitation and the necessary outputs. The GUI was implemented using TCL-TK script language, which produces a formatted file containing all the necessary information about the computational domain. Then, another interface between this formatted file and the TLM solver was implemented using again FORTRAN 90 [40.I] [41.I].

There are also dozens of other codes that were necessary to perform some post processing tasks, such as near to far-field transformation or s-parameters calculations. Some of them were developed using FORTRAN 90 while others were with MATLAB. Finally, for dispersion and stability analysis and the analytical transfer functions associated with different media, we used Mathematica9-Wolfram as symbolic algebra software [42.I].

1.11 Outline of the thesis

Following this first introductory chapter, the physics of complex media is presented in chapter II. It emphasizes that the main objective of this thesis is to develop a solver that can handle such media. The method that we have used to build the EM simulator namely, the transmission line matrix method (TLM), is presented in chapter III, with all necessary background material and state-of-the-art. In chapter IV, we discuss the TLM method, and reformulate it in matrix form. Then, we perform a complete stability and dispersion analysis for the general case in the presence of complex media.

Applications and results are presented in chapter V. In the first part we discuss the graphical user interface (GUI) that we developed for the solver with several canonical examples to validate both the solver and the GUI. In the second part of chapter V, we present the relevant results of this thesis, namely, simulations including several microwave devices containing complex media compared either with other theoretical results or measurements for validation purposes. In chapter VI, two issues are addressed: firstly the traditional and some alternate techniques to solve EM problems at very low frequencies using time-domain methods, including TD-TLM and FDTD. In the second part of the chapter, the inherent error problem in FDTD at the interface between different media is discussed and, how the improvement brought by the TLM technique can be achieved. Several examples comparing the performance of TLM vs. FDTD for high contrast structures are presented for illustration. Finally, chapter VII contains a general conclusion and future work.

References

[1.I] M. I. Yaich and M. Khalladi, "A SCN-TLM Model for the Analysis of Ferrite Media," *IEEE Microwave and Wireless Components Letters,* vol. 13, no. 6, pp. 217-219, 2003.

[2.I] M. I. Sobhy, M. W. R. Ng and R. J. Langley, "TLM Analysis fo Microstrip Patch Antenna on Ferrite Substrate," in *IEEE MTT-S Digest*, 1999.

[3.I] L. Landau and E. M. Lifshitz, Electrodynamcis of Continuous Media, Pergamon Press, 1984.

[4.I] J. D. Jackson, Classical Electrodynamics, JOHN WILEY & SONS, INC., 1999.

[5.I] L. D. Landau and E. M. Lifshitz, The Classical Theory of Fields, PERGAMON PRESS, 1962.

[6.I] A. Taflove and S. C. Hagness, Computational Electrodaynamics, The Finite-Difference Time-Domain Method, Norwood: Artch House, INC., 2005.

[7.I] M. Clemens and T. Weiland, "Discrete Electromagnetism with the Finite Integration Tequnique," *Progress In Electromagnetics Research,* no. PIER 32, pp. 65-87, 2001.

[8.I] A. N. Shiryayev and A. N. Kolmogorov, Selected Works of A. N. Kolmogorov: Volume III: Information Theory and the Theory of Algorithms (Mathematics and its Applications), Springer, 1993.

[9.I] D. E. Knuth, The Art of Computer Programming, Voulume 1: Fundamental Algorithms, Addison-Wesley, 1968.

[10.I] K. Yee, "Numerical solution of initial boundary value problems involving Maxwell's equation in isotropic media," *IEEE Transactions in Antennas and Propagations,* no. AP-14, pp. 302-307, May 1966.

[11.I] R. F. Harrington, Time-Harmonic Electromagnetic Fields, JHON WILEY & SONS. INC, 2001.

[12.I] J. Vanderlinde, Classical Electromagnetic Theory, KLUWER ACADEMIC PUBLISHERS, 2004.

[13.I] C. Christopoulos, The Transmission-Line Modeling (TLM) Method in Electromagnetics, Arizona: Morgan & Claypool, 2006.

[14.I] P. B.Johns, "A Symmetrical Condensed Node for the TLM Method," *IEEE Transactions on Microwave Theory and Techniques,* Vols. MTT-35, no. 4, pp. 370-377, 1987.

[15.I] D. B. Davidson, Computatioal Electromagnetics for RF and Microwave Engineering, CAMBRIDGE UNIVERSITU PRESS, 2005.

[16.I] W. C. Gibson, The Method Of Moments in Electromagnetics, Cahpman & Hall/CRC, 2008.

[17.I] S. Carroll, Spacetime and Geometry: An Introduction to General Relativity, 2003: Addison-Wesley.

[18.I] D. Lovelock and H. Rund, Tensors, Differential Forms, and Variational Principles, 1989: Dover Publications, INC., New York.

[19.I] L. Susskind, The Black Hole War, BACK BAY BOOKS, 2008.

[20.I] H. Flanders, Differential Forms with Applications to the Physical Sciences, Dover Publications, 1989.

[21.I] F. W. Hehl and Y. N. Obukhov, Foundations of Classical Electrodynamics Charge, Flux and Metric, Progress in Mathematical Physics Volume 33, 2003.

[22.I] J. B. Schneider, Understanding the Finite-Difference Time-Domain Method, 2012.

[23.I] P. Johns and R. Beurle, "Numerical solution of 2-dimensional scattering problems using a transmission line matrix," *Proceedings of the IEE,* vol. 188, pp. 1203-1208, 1971.

[24.I] W. H. Reed and T. R. Hill, "Triangular mesh methods for the neutron transport equation," Tech Report LA-UR-73-479, Los Alamos Scientific Labratory, 1973.

[25.I] G. Gohen, X. Ferrieres and S. Pernet, "A spatial high-order hexahedral discontinuous Galerkin method to solve Maxwell's equations in time domain," *Journal of Computational Physics*, vol. 217, pp. 340-363, 2006.

[26.I] N. A. Bushyager and M. M. Tentzeris, MRTD (Mutli Resolution Time Domain) Method in Electromagnetics, Morgan & Claypool, 2005.

[27.I] I. b. Massy, N. Pena and M. M. Ney, "Dispersion characteristic and stability analysis for an arbitrary MRTD scheme with variable mesh," *International Journal of Numerical Modelling: Electronic Networks, Devices and Fields,* vol. 23, no. 6, pp. 470-491, 2010.

[28.I] F. Olyslager and etal, "Recent Advances in Fast Multipole Methods to Simulate ever Larger and More Complex Structures," in *Proceedings of the Asia-Pacific Symposium on Electromagnetic Compatibility*, 2007.

[29.I] J.-F. Lee, R. Lee and A. Cangellaris, "Time-Domain Finite-Element Methods," *IEEE Transactions on Antennas and Propation,* vol. 45, no. 3, pp. 430-442, 1997.

[30.I] Z. D. Chen and M. M. Ney, "The Method of Weighted Residuals: A General Approach to Deriving Time-and Frequency-Domain Numerical Methods," *IEEE Antenna and Prop. Magazine,* vol. 51, no. 1, pp. 51-70, Feb. 2009.

[31.I] A. E. Yilmaz, J.-M. Jin and E. Michelssen, "A Parallel FFT Accelerated Transient Field-Circuit Simulator," *IEEE Transactions on Microwave Theory and Techniques*, vol. 53, no. 9, pp. 2851-2865, 2005.

[32.I] D. Bouché, F. Molinet and R. Mittra, Asymptotic Methods in Electromagnetics, Springer, 1997.

[33.I] F. P. Andriulli, "Loop-Star and Loop-Tree Decompositions: Analysis and Efficient Algorithms," *IEEE Transactions on Antennas and Propagation*, vol. 60, no. 5, pp. 2347-2356, 2012.

[34.I] http://www.comsol.com/.

[35.I] https://www.cst.com/.

[36.I] https://www.feko.info/.

[37.I] http://www.ansys.com/.

[38.I] A. L. J. Droute, "La Dosimétrie Numérique Sur La Bande 1-500 MHZ," in *17éme Colloque International et Exposition sur la Compatibilité ElectroMagnétique (CEM 2014)*, 2014.

[39.I] "GiD Reference Manual," CIMNE International Center for Numerical Methods in Engineering, 2013.

[40.I] J. C. Adams, W. S. Brainerd, J. T. Martin, B. T. Smith and J. L. Wagener, Fortran 90 Handbook, McGraw-Hill, 1992.

[41.I] S. J. Chapman, Fortran 90/95 for Scientists and Engineers, WCB/McGraw-Hill, 1998.

[42.I] G. Baumann, MATHEMATICA for Theoretical Physics; Electrodynamics, Quantum Mechanics, General Relativity and Fractals, Springer, 2005.

[43.I] R. Harrington, Field Computation Moment Methods, Wiley-IEEE press, 1993.

Chapter II
Physics of Complex Media

2.1 Introduction

A simple electrodynamic problem usually includes media that are defined by three electromagnetic parameters namely, permittivity, permeability and conductivity; all of them are positive scalar constant, when a simple medium is considered [1.II]. If any of these parameters violates the above assumption, the material is said to be complex. The complexity of the medium can manifest itself by possessing one or more of the following properties [2.II]:

- Inhomogeneity
- Dispersion
- Anisotropy
- Chirality
- Nonlinearity
- Time varying (non stationarity)

Apart from the mathematical and/or physical simplifications, all media in nature are complex, and sooner or later one should face this reality. In designing modern advanced electromagnetic devices, especially when working at higher frequencies, the complexity of the medium starts to clearly appear. Thus, for a correct design, it is necessary to know in details the complex behavior of the media. Furthermore, for specific applications we need to use media displaying certain characteristics (usually complex ones) to enhance the device performances. Another very important motivation behind the development of the use of complex media is the biomedical applications (since all tissues are complex media). For instance, in Magnetic Resonance Imaging (MRI) and Computerized Tomography (CT) scan the better we know the material behavior the more accurate the diagnosis.

In this chapter, we briefly discuss the physics of complex media for electrodynamic application perspective, and show different ways by which a material can display some complex behavior.

2.2 Maxwell's equations in general vector form

As discussed in the first chapter, one can formulate Maxwell's equations by using different mathematical tools i.e. tensor calculus, exterior calculus, or vector calculus. The latter, is the formulation that we are going to use throughout this chapter.

In a general media, the wave propagation is governed by the following four equations [2.II]:

$$\nabla \times \vec{E} = -\frac{\partial \vec{B}}{\partial t} - \bar{\bar{\sigma}}_m * \vec{H} - \vec{J}_{m,im} \tag{1.IIa}$$

$$\nabla \times \vec{H} = \frac{\partial \vec{D}}{\partial t} + \bar{\bar{\sigma}}_e * \vec{E} + \vec{J}_{e,im} \tag{1.IIb}$$

$$\nabla \cdot \vec{D} = \rho_v \tag{1.IIc}$$

$$\nabla \cdot \vec{B} = \rho_m \tag{1.IId}$$

where $\bar{\bar{\sigma}}_m$, $\bar{\bar{\sigma}}_e$ are the magnetic and electric conductivity matrices respectively, and $\vec{J}_{m,im}$, $\vec{J}_{e,im}$ are the impressed magnetic and electric currents respectively, ρ_v and ρ_m are the volume electric and magnetic charge distributions, respectively. The constitutive equations relate the electric and magnetic flux intensities $\vec{E}$, $\vec{H}$ with the electric and magnetic flux densities $\vec{D}, \vec{B}$, respectively. For a general media, the constitutive relations are given by [3.II]:

$$\vec{D}(\mathbf{r}, t) = \varepsilon_o \vec{E}(\mathbf{r}, t) + \vec{f}\left(\vec{E}, \vec{H}\right) \tag{2.IIa}$$

$$\vec{B}(\mathbf{r}, t) = \mu_o \vec{H}(\mathbf{r}, t) + \vec{g}\left(\vec{E}, \vec{H}\right) \tag{2.IIb}$$

where the vector functions $\vec{f}$ and $\vec{g}$ are general operators. They can take into account the various types of media, including nonlinear media.

If we include the possibility of electro-magnetic coupling, which occurs in chiral media or moving magnetized plasma, Maxwell's equations then write:

$$\nabla \times \vec{H} = \frac{\partial(\bar{\bar{\varepsilon}}\vec{E})}{\partial t} + \frac{\partial(\bar{\bar{\xi}}\vec{H})}{c_o \partial t} + \sigma_e * \vec{E} + \vec{J}_{e,im} \tag{3.IIa}$$

$$\nabla \times \vec{E} = -\frac{\partial(\bar{\bar{\mu}}\vec{H})}{\partial t} - \frac{\partial(\bar{\bar{\zeta}}\vec{E})}{c_o \partial t} - \sigma_m * \vec{H} - \vec{J}_{m,im} \tag{3.IIb}$$

which is equivalent to choose the vector functions $\vec{f}$ and $\vec{g}$ as:

$$\vec{f} = \bar{\bar{\varepsilon}}\vec{E} + \frac{\bar{\bar{\xi}}\vec{H}}{c_o} \tag{4.IIa}$$

$$\vec{g} = \frac{\bar{\bar{\zeta}}\vec{E}}{c_o} + \bar{\bar{\mu}}\vec{H} \tag{4.IIb}$$

The use of the above vector functions maintains Maxwell's equations in their simple form (1.II).

2.3 Solving an electrodynamic problem

In a general three dimensional electrodynamic problem, there are 20 unknowns to be calculated at any point in space inside the computational domain. Without loss of generality, we will assume that we are solving Maxwell's equations in Cartesian coordinates system. Thus, the unknowns are:

- Electric field intensity components E_x, E_y, E_z
- Electric field density (or displacement field) components D_x, D_y, D_z
- Magnetic field intensity components H_x, H_y, H_z
- Magnetic field density components B_x, B_y, B_z
- Electric current density components j_{ex}, j_{ey}, j_{ez}
- Magnetic current density components j_{mx}, j_{my}, j_{mz}
- Electric and magnetic charge densities ρ_{ev}, ρ_{mv}, respectively

To determine the above twenty scalar unknowns, one should have twenty independent equations:

1- The continuity equations for charges and currents [3.II] (two equations)

$$\nabla.\vec{J}_e = -\frac{\partial\, \rho_{ev}}{\partial t} \tag{5.IIa}$$

$$\nabla.\vec{J}_m = -\frac{\partial\, \rho_{mv}}{\partial t} \tag{5.IIb}$$

2- Constitutive relations (six equations)

$$\vec{D}(\mathbf{r},t) = \varepsilon_o \vec{E}(\mathbf{r},t) + \vec{f}\left(\vec{E},\vec{H}\right) \tag{5.IIc}$$

$$\vec{B}(\mathbf{r},t) = \mu_o \vec{H}(\mathbf{r},t) + \vec{g}\left(\vec{E},\vec{H}\right) \tag{5.IId}$$

3- Maxwell-Gauss' equations (two equations)

$$\nabla \cdot \vec{D} = \rho_{ev} \tag{5.IIe}$$

$$\nabla \cdot \vec{B} = \rho_{mv} \tag{5.IIf}$$

4- Electric and magnetic flux conservation (six equations)

$$\nabla \times \vec{E} = -\frac{\partial \vec{B}}{\partial t} - \vec{J}_m - \vec{J}_{m,im} \tag{5.IIg}$$

$$\nabla \times \vec{H} = \frac{\partial \vec{D}}{\partial t} + \vec{J}_e + \vec{J}_{e,im} \tag{5.IIh}$$

5- Ohms low (six equations)

$$\vec{J}_e = \bar{\bar{\sigma}}_e * \vec{E} \tag{5.IIi}$$

$$\vec{J}_m = \bar{\bar{\sigma}}_m * \vec{H} \tag{5.IIj}$$

Thus, we have 22-scalar equations from the above. However, taking the divergence of (5.IIg-5.IIh) and using (5.IIe-5.IIf), respectively, one retrieves the charge conservation laws (5.IIa-5.IIb). Thus, there are only 20 independent scalar equations that render Maxwell's equations consistent.

2.4 Dispersive media

In any type of media, Maxwell's equations using the four field quantities keep their form for any medium. Constitutive equations, that are medium dependent, allow the use of two field quantities only. For a general linear media the constitutive equations are defined by [4.II]:

$$\vec{f}(\vec{E},\vec{H}) = \varepsilon_o \int_{-\infty}^{+\infty}\int_{-\infty}^{+\infty} \overline{\overline{\psi}}_{11}(\mathbf{r},\acute{\mathbf{r}},t,\acute{t})\,\vec{E}(\mathbf{r},\acute{t})\,d\acute{r}d\acute{t} + \frac{\varepsilon_o}{c_o}\int_{-\infty}^{+\infty}\int_{-\infty}^{+\infty} \overline{\overline{\psi}}_{12}(\mathbf{r},\acute{\mathbf{r}},t,\acute{t})\,\vec{H}(\mathbf{r},\acute{t})\;d\acute{r}d\acute{t} \tag{6.IIa}$$

$$\vec{g}(\vec{E},\vec{H}) = \frac{\mu_o}{c_o}\int_{-\infty}^{+\infty}\int_{-\infty}^{+\infty} \overline{\overline{\psi}}_{21}(\mathbf{r},\acute{\mathbf{r}},t,\acute{t})\,\vec{E}(\mathbf{r},\acute{t})\,d\acute{r}d\acute{t} + \mu_o\int_{-\infty}^{+\infty}\int_{-\infty}^{+\infty} \overline{\overline{\psi}}_{22}(\mathbf{r},\acute{\mathbf{r}},t,\acute{t})\,\vec{H}(\mathbf{r},\acute{t})\;d\acute{r}d\acute{t} \tag{6.IIb}$$

In the above equations (6.IIa and 6.IIb), different phenomena are simultaneously included:

- The integration with respect to time stands for frequency dispersion. This means that the media operate as a frequency selective filter that translates to a convolution process in time domain.
- The integration with respect to space tells us that the spatial locality of the constitutive equations is not a necessary condition. Thus, the electromagnetic response at certain point may depend on its neighborhood. This phenomenon is well-known in statistical physics, especially at microscopic level.
- The fact that all $\overline{\overline{\psi}}_{11}, \overline{\overline{\psi}}_{12}, \overline{\overline{\psi}}_{21}, \overline{\overline{\psi}}_{22}$ are full matrices in general, stands for the anisotropy phenomena, in which the field intensity applied to one direction, induces flux density to other directions.
- The matrices $\overline{\overline{\psi}}_{11}, \overline{\overline{\psi}}_{12}, \overline{\overline{\psi}}_{21}, \overline{\overline{\psi}}_{22}$ stands for electric susceptibility, magneto-electric coupling, electro-magnetic coupling, and magnetic susceptibility, respectively.

If we assume the spatial locality of the constitutive relations (which is assumed to be true in this thesis unless stated otherwise) then, the above formulas become:

$$\vec{f}(\vec{E},\vec{H}) = \varepsilon_o \int_{-\infty}^{+\infty} \overline{\overline{\psi}}_{11}(\mathbf{r},t,\acute{t})\,\vec{E}(\mathbf{r},\acute{t})\,d\acute{t} + \frac{\varepsilon_o}{c_o}\int_{-\infty}^{+\infty} \overline{\overline{\psi}}_{12}(\mathbf{r},t,\acute{t})\,\vec{H}(\mathbf{r},\acute{t})\,d\acute{t} \tag{7.IIa}$$

$$\vec{g}(\vec{E},\vec{H}) = \frac{\mu_o}{c_o}\int_{-\infty}^{+\infty} \overline{\overline{\psi}}_{21}(\mathbf{r},t,\acute{t})\,\vec{E}(\mathbf{r},\acute{t})\,d\acute{t} + \mu_o\int_{-\infty}^{+\infty} \overline{\overline{\psi}}_{22}(\mathbf{r},t,\acute{t})\,\vec{H}(\mathbf{r},\acute{t})\;d\acute{t} \tag{7.IIb}$$

Equivalently in frequency domain we obtain:

$$\vec{F}(\vec{E},\vec{H}) = \varepsilon_o \overline{\overline{\psi}}_{11}(\mathbf{r},\omega)\vec{E}(\mathbf{r},\omega) + \frac{\varepsilon_o}{c_o}\overline{\overline{\psi}}_{12}(\mathbf{r},\omega)\vec{H}(\mathbf{r},\omega) \tag{8.IIa}$$

$$\vec{G}(\vec{E},\vec{H}) = \frac{\mu_o}{c_o}\overline{\overline{\psi}}_{21}(\mathbf{r},\omega)\vec{E}(\mathbf{r},\omega) + \mu_o\overline{\overline{\psi}}_{22}(\mathbf{r},\omega)\vec{H}(\mathbf{r},\omega) \quad (8.\text{IIb})$$

where $\vec{E}(\mathbf{r},\omega)$ and $\vec{E}(\mathbf{r},t)$ are connected via Fourier transform:

$$\vec{E}(\mathbf{r},\omega) = \int_{-\infty}^{+\infty}\vec{E}(\mathbf{r},t)e^{-j\omega t}dt \quad (9.\text{IIa})$$

$$\vec{E}(\mathbf{r},t) = \frac{1}{2\pi}\int_{-\infty}^{+\infty}\vec{E}(\mathbf{r},\omega)e^{+j\omega t}d\omega \quad (9.\text{IIb})$$

Similar expressions to (9.IIa) and (9.IIb) are valid for magnetic field and constitutive parameters $\overline{\overline{\psi}}_{11}$, $\overline{\overline{\psi}}_{12}$, $\overline{\overline{\psi}}_{21}$ $\overline{\overline{\psi}}_{22}$.

In most of the materials, the magneto-electric and the electro-magnetic coupling are negligible. Thus, if we apply the assumption that

$$\overline{\overline{\psi}}_{21}(\mathbf{r},\omega) = \overline{\overline{\psi}}_{12}(\mathbf{r},\omega) = 0 \quad (10.\text{II})$$

we obtain to the well-known polarization and magnetization vectors i.e.

$$\vec{P}(\mathbf{r},\omega) = \varepsilon_o\overline{\overline{\psi}}_{11}(\mathbf{r},\omega)\vec{E}(\mathbf{r},\omega) \quad (11.\text{IIa})$$

$$\vec{M}(\mathbf{r},\omega) = \mu_o\overline{\overline{\psi}}_{22}(\mathbf{r},\omega)\vec{H}(\mathbf{r},\omega) \quad (11.\text{IIb})$$

In general, a material is considered as frequency dispersive if its properties vary with angular frequency ω.

2.5 Anisotropic media

A material is said to be anisotropic if an electric field $\vec{E}$ applied to some direction produces in that material a flux density $\vec{D}$ pointing to another direction. The same definition holds for a magnetic field $\vec{H}$, and the induced magnetic flux density $\vec{B}$ in magnetic media. In these cases, constitutive relations write:

$$\vec{D}(\mathrm{r},\omega) = \bar{\bar{\varepsilon}}(\mathrm{r},\omega)\,\vec{E}(\mathrm{r},\omega) \quad (12.\text{IIa})$$

$$\vec{B}(\mathrm{r},\omega) = \bar{\bar{\mu}}(\mathrm{r},\omega)\,\vec{H}(\mathrm{r},\omega) \quad (12.\text{IIb})$$

in which constitutive parameters are tensors $\bar{\bar{\varepsilon}}$ or$\bar{\bar{\mu}}$, and are no longer identity matrices scaled by a real constant. As a result, the above tensors act as linear applications that modify the direction of the flux densities $\vec{D}, \vec{B}$ with respect to the applied fields $\vec{E}$ and $\vec{H}$, respectively.

According the previous formulation, the anisotropy occurs when the tensors $\overline{\overline{\psi}}_{11}(\mathrm{r},\omega)$ or $\overline{\overline{\psi}}_{22}(\mathrm{r},\omega)$ are general nonsingular 3×3 Hermitian matrices other that a scaled version of the identity matrix.

2.6 Transformation optics

In physics, usually basic laws like Maxwell's equations in electrodynamics, Hamilton and Lagrange equations in mechanics, etc., are usually expressed in tensorial form. That means they are coordinate system independent. In other words, if we use whatever coordinate system capable of describing the space-time geometry of the problem, results that describe the same physical phenomenon should be obtained [5.II] [6.II].

A tensor is a mathematical object $T^{\mu_1\cdots\mu_k}_{\nu_1\cdots\nu_l}$ of rank (k,l) which is a collection of numbers (vector for instance is a rank-one tensor) that operates a transformation between different coordinate systems according to the relation [5.II]:

$$T^{\mu'_1\cdots\mu'_k}_{\nu'_1\cdots\nu'_l} = \Lambda^{\mu'_1}_{\mu_1}\cdots\Lambda^{\mu'_k}_{\mu_k}\ \Lambda^{\nu'_1}_{\nu_1}\cdots\Lambda^{\nu'_l}_{\nu_l}\ \ T^{\mu_1\cdots\mu_k}_{\nu_1\cdots\nu_l} \tag{13.II}$$

where $\Lambda^{\mu'_1}_{\mu_1}$ is the Jacobian matrix (a differential-map between two coordinate systems) defined by [5.II]:

$$\Lambda^{\mu'_1}_{\mu_1} = \left(\frac{\partial x^{\mu'_1}}{\partial x^{\mu_1}}\right)_{\forall\ \mu_1,\mu'_1\in\{1,..,n\}} \tag{14.II}$$

A very interesting property of Maxwell's equations is that when a coordinate transformation is applied to them, all electromagnetic quantities follow the simple coordinate transformation rule (13.II). This fact could be used in different contexts, for instance:

- Using a coordinate transformation to simplify the geometry description of the underlying problem. In discrete world, we can use that transformation to reduce the effect of some approximation errors (like stair-case approximation of curved objects).
- In principle, one can use a Cartesian-coordinate-based solver to solve Maxwell's equations for any geometry described by any coordinate system. One should assume that the transformation between the new coordinate system and the Cartesian one is bijective (there is a one-to-one mapping between them).

- One can design structures that control the propagation of electromagnetic waves in a very flexible way, such as invisibility cloak, super lenses and many other applications.

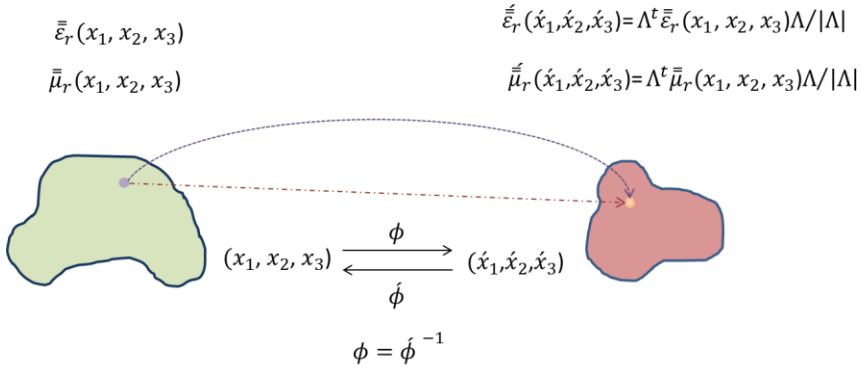

Figure 1.II, transformation optics (mapping of the computational domain between two coordinate systems)

In general, after applying the coordinate transformation ϕ, two things will happen to the computational domain

I. The geometry changes according to the map of coordinate transformation ϕ

II. The material property tensors are modified according to the Jacobian of the transformation Λ as presented in table 1.II, where:

$$\Lambda = \text{Jacobian}(\phi) \tag{15.II}$$

Table 1.II, Transformation optics formulas

Computational Domain Quantity	Original coordinate system (x_1, x_2, x_3)	Transnsformed coordinate system $(\acute{x}_1, \acute{x}_2, \acute{x}_3)$
Position of a point	(x_1, x_2, x_3)	$\phi(x_1, x_2, x_3) = (\acute{x}_1, \acute{x}_2, \acute{x}_3)$
Permittivity tensor	$\bar{\bar{\varepsilon}}_r$	$\acute{\bar{\bar{\varepsilon}}}_r = \Lambda^t\bar{\bar{\varepsilon}}_r\Lambda/\det(\Lambda)$
Permeability tensor	$\bar{\bar{\mu}}_r$	$\acute{\bar{\bar{\mu}}}_r = \Lambda^t\bar{\bar{\mu}}_r\Lambda/\det(\Lambda)$
Conductivity	$\bar{\bar{\sigma}}_r$	$\acute{\bar{\bar{\sigma}}}_r = \bar{\bar{\sigma}}_r\Lambda^t\bar{\bar{\varepsilon}}_r\Lambda/\det(\Lambda)$
Electric current density	$\vec{J}$	$\vec{J}' = \Lambda^t\vec{J}/\det(\Lambda)$
Electric charge density	ρ_{ev}	$\rho'_{ev} = \rho_{ev}/\det(\Lambda)$
Electric field	$\vec{E}$	$\vec{E}' = \Lambda^t\vec{E}$
Magnetic field	$\vec{H}$	$\vec{H}' = \Lambda^t\vec{H}$

2.7 Periodic structures

Periodic structure is a structure that is composed of identical or semi-identical substructures that repeat themselves in some region of space according to a specific pattern. They may exist naturally like different types of photonic crystals, or can be fabricated.

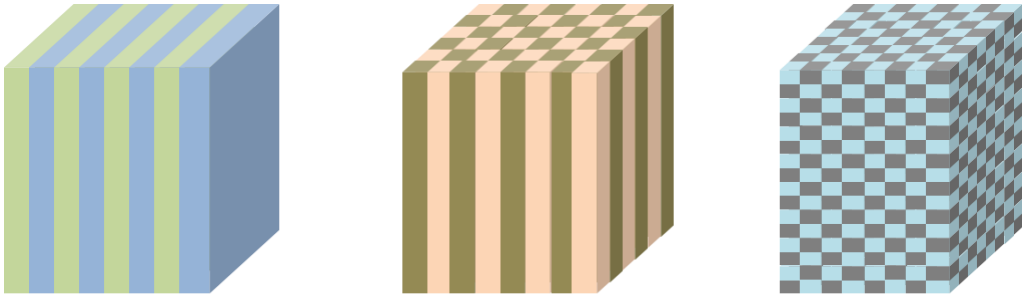

Figure 2.II, periodic structures of (a) one-dimension (b) two-dimension (c) three-dimension

Periodic structures have many applications such as filters or optical devices. In periodic structures, Bloch's theorem plays a central role for field computation in such media. This theorem is based on the idea of periodic potential function that respects the boundary conditions at the boundaries of every homogeneous region in the periodic structure [7.II].

2.8 Random media

Usually media in nature are inhomogeneous and contain many impurities; hence, it can't be described deterministically to infinite precision. To use these media in applications that require high accuracy, one should have a good stochastic model describing the media properties. By incorporating the mathematical tools of random processes with Maxwell's equations and using the model given for any random media one could extract some parameters like effective permittivity and permeability within a given frequency band. This allows the use of these materials in reliable and robust design procedures [8.II].

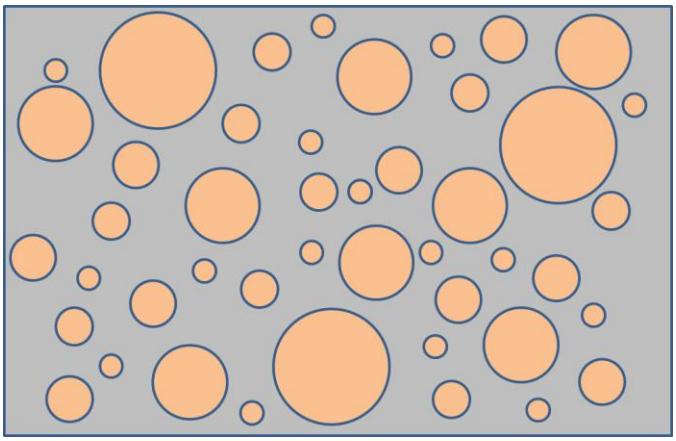

Figure 3.II, cross section of a random material

One can face the scenario of random media, when dealing with wave propagation in rainy condition for instance. Hence, it is necessary to use some stochastic model to describe the propagation channel physical characteristics. In geophysics, it is also of importance to have some stochastic model about the layers of the earth crust when searching for petroleum, water, or some other minerals, by using electromagnetic scattering based procedure.

Even though random media could be composed of simple inhomogeneous dielectrics, they are considered complex media because of the impossibility of taking all the random details into account.

2.9 Magneto-electric coupling

A Chiral medium is a medium in which the electric field may also couple with magnetization and magnetic field with electric polarization. In frequency domain the constitutive relationships are given by [2.II] [9.II]:

$$\bar{D}(\omega) = \varepsilon(\omega)\bar{E}(\omega) - \frac{j\kappa(\omega)}{c_o}\bar{H}(\omega) \tag{16.IIa}$$

$$\bar{B}(\omega) = \mu(\omega)\bar{H}(\omega) + \frac{j\kappa(\omega)}{c_o}\bar{E}(\omega) \tag{16.IIb}$$

or, following the termonology used in (8.IIa) and (8.IIb), we obtain:

$$\bar{\bar{\Psi}}_{11}(\mathbf{r},\omega) = \frac{\varepsilon(\omega)}{\varepsilon_o}\bar{\bar{I}}_3 \tag{17.IIa}$$

$$\bar{\bar{\Psi}}_{12}(\mathbf{r},\omega) = -\frac{j\kappa(\omega)}{\varepsilon_o}\bar{\bar{I}}_3 \tag{17.IIb}$$

$$\bar{\bar{\Psi}}_{21}(\mathbf{r},\omega) = \frac{j\kappa(\omega)}{\mu_o}\bar{\bar{I}}_3 \tag{17.IIc}$$

$$\bar{\bar{\Psi}}_{22}(\mathbf{r},\omega) = \frac{\mu(\omega)}{\mu_o}\bar{\bar{I}}_3 \tag{17.IId}$$

where ε, μ are the permittivity and the permeability, respectively, c_o is the speed of light in vacuum, κ is the chirality parameter, and $\mathbf{r}$ is the position vector. All parameters are frequency dependent according to the following relations [9.II]:

$$\kappa(\omega) = \frac{\tau\omega_o^2\omega}{\omega_o^2-\omega^2+j2\omega_o\xi\omega} \tag{18.IIa}$$

$$\varepsilon(\omega) = \varepsilon_o\varepsilon_\infty + \frac{(\varepsilon_s-\varepsilon_\infty)\varepsilon_o\omega_{oe}^2}{\omega_{oe}^2-\omega^2+j2\omega_{oe}^2\xi_e\omega} \tag{18.IIb}$$

$$\mu(\omega) = \mu_o\mu_\infty + \frac{(\mu_s-\mu_\infty)\mu_o\omega_{om}^2}{\omega_{om}^2-\omega^2+j2\omega_{om}^2\xi_m\omega} \tag{18.IIc}$$

where ω_o is the characteristic resonant frequency for the chiral material sample, ξ is the damping factor and τ is a time constant. Constants ω_{oe} and ω_{om} are resonant frequencies for the dielectric and magnetic models, respectively, and ξ_e, ξ_m are their damping factors, ε_s, μ_s are the static values of permittivity and permeability. Finally, $\varepsilon_\infty, \mu_\infty$ are permittivity and permeability values at a high frequencies, respectively [9.II].

2.10 Ferroelectric media

In some anisotropic crystals, the constitutive relation between electric field and flux density is given by [10.II]:

$$\vec{D} = \vec{D}_o + \bar{\bar{\varepsilon}}\vec{E} \tag{19.II}$$

This means that in these materials, there may exist a flux density $\vec{D}_o$ even when there is not external electric source. Such material is called pyroelectric. Pyroelectricity is an essential property for the crystal to acquire ferroelectric behavior [10.II].

Ferroelectric materials exhibit the property of spontaneous electric polarization that can be obtained by applying an external electric field. The various states of polarization follows the Hysteresis cycle illustrated in figure 4.IIa. Even after the applied external field vanishes, remanent polarization remains. Ferroelectricity has a phenomenon analogous to ferromagnetism in many aspects; for instance, both ferroelectric and ferromagnetic behaviors appear only below the phase transition temperature (Curie temperature, which is different for each ferroelectric or ferromagnetic material). Historically the ferroelectricity was first discovered by Valasek in Rochelle salt in 1920 [11.II].

Ferroelectric materials have several applications like the ferroelectric capacitors, which consists of two conductors with ferroelectric sample between them. These types of capacitors have very interesting property: their capacitance can be controlled by an external field (tunable capacitors). Also, the fact that the permittivity can go to high values near the resonant frequency of the material, they allow us to fabricate capacitors with very high capacitance and small physical size compared to dielectric capacitors (with similar capacitance value) [11.II].

The remanent polarization in the ferroelectric materials, which is shown in the hysteresis diagram of figure 4.IIa, can be used to save data such as in ferroelectric RAMs for computers [11.II].

2.11 Ferromagnetic media

As mentioned in the previous section, there is a close analogy between ferromagnetic and ferroelectric media. For instance, magnetic properties of a ferromagnetic material are dependent on the applied external static magnetic field and the permeability tensor is a function of the external applied field. Also remanent magnetization may exist as illustrated in the hysteresis cycle shown in figure 4.IIb. Note that the cycle shape depends on the maximum applied external field, before saturation value is attained.

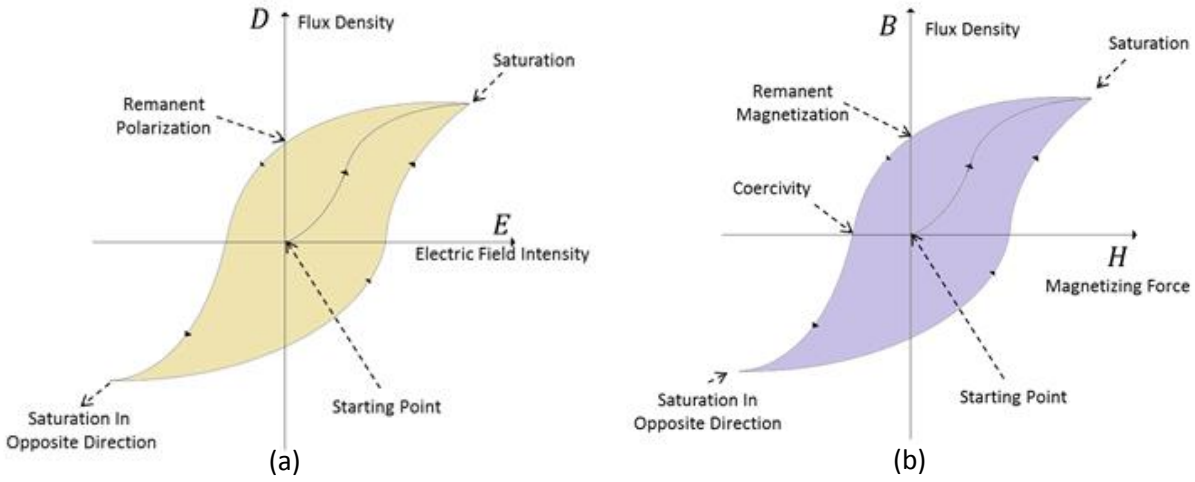

Figure 4.II, (a) hysteresis diagram for ferroelectric media, (b) hysteresis diagram of ferromagnetic media

Initially the magnetization state $\vec{M}$ in ferromagnetic media was modeled by the soviet physicists L. Landau and his student E. Lifshitz. They derived the equation from the Larmor's precession motion differential equation:

$$\frac{d\vec{M}}{dt} = -\gamma\vec{M} \times \vec{H}_{eff} + \lambda\vec{M} \times \left(\vec{M} \times \vec{H}_{eff}\right) \tag{20.II}$$

where γ the electron is gyromagnetic ratio, and λ is the phenomenological damping factor, which is often replaced by:

$$\lambda = -\alpha \frac{\gamma}{M_s} \tag{21.II}$$

where M_s is the magnetization at the saturation, and α is a dimensionless scalar called the damping factor. The effective magnetic field is defined as:

$$\vec{H}_{eff} = \vec{H}_i + \vec{h}_d \tag{22.II}$$

where $\vec{H}_i$ is the static biasing field, and $\vec{h}_d$ is the perturbating magnetic time-vayring field of small magnitude. This has some analogy with the transistors mode of operation, where $\vec{H}_i$ is analogous to the biasing current and $\vec{h}_d$ to the small sigal to be processed

Another modification Landau-Lifshitz equation came by E. Gilbert in which the magnetization vector $\vec{M}$ is governed by the equation (GLL):

$$\frac{d\vec{M}}{dt} = -\gamma\vec{M} \times \vec{H}_{eff} + \frac{a}{M_s}\vec{M} \times \frac{d\vec{M}}{dt} \tag{23.II}$$

When the applied field is above certain amplitude, the magnetic medium becomes saturated. As a result, the domains shown in figure 5.IIb disappear and the magnetization becomes uniform as shown in figure 5.II (a). For a small perturbating field one can characterize the saturated medium by the Polder tensor model [12.II] [13.II]:

$$\mu = \begin{pmatrix} \mu_{xx} & \mu_{xy} & 0 \\ \mu_{yx} & \mu_{yy} & 0 \\ 0 & 0 & \mu_{zz} \end{pmatrix} \tag{24.II}$$

On the other hand, if the applied magnetizing field does not enforce saturation, domains shown figure 5.II(b) exist and the magnetization is not uniform. In this case, one has to use more sophisticated models such as Gelin et al.'s that leads to a full tensor model [14.II] [15.II]:

$$\mu = \begin{pmatrix} \mu_{xx} & \mu_{xy} & \mu_{xz} \\ \mu_{yx} & \mu_{yy} & \mu_{yz} \\ \mu_{zx} & \mu_{zy} & \mu_{zz} \end{pmatrix} \tag{25.II}$$

(a) (b)

Figure 5.II, (a) saturated ferromagnetic material (b) non-saturated ferromagnetic material

To summarize, having the ferrite sample shown by figure 5.IIa and 5.IIb and depending on the strength of the applied DC magnetizing field, its permeability properties can be determined. When the DC magnetic field is very strong, the ferrite sample reaches the saturation state. In this case, the sample becomes homogenous and the permeability tensors follow Polder's model for saturated ferrite [12.II] shown in (24.II). However, if the DC magnetizing field is not strong enough, the different domains inside the sample acquire different magnetic properties. In such scenario, the permeability tensor usually follows the more general model (25.II) developed by Gelin and his colleagues [15.II]. The calculation of tensor components inside the non-saturate ferrite sample requires solving the GLL equation (23.II) [15.II] [14.II]. This equation is a nonlinear partial differential equation and usually very difficult to solve especially for non-canonical geometries. By solving (23.II), one can calculate the magnetization state inside each domain.

Usually, the process of calculating the permeability tensors, especially for non-saturated ferrite, is a multi-stage process and we can easily end up with non-accurate results. Initially, to analyze the ferrite sample it is necessary to have some experimental data about its properties (such as Curie temperature, its dimensions, its initial magnetization state…etc.). These data usually have some uncertainty due to experimental errors. This uncertainty may affect the solution of the GLL equations, hence, deviate the magnetization state in every domain from the real values.

2.12 Metamaterials

In theory of electrodynamics, metamaterials are media possessing unusual electromagnetic properties. For instance, the permeability or the permittivity or both of them can be negative, zero, or extremely high within some frequency bands [16.II] [17.II]. In practice, metamaterials are constructed artificially at the microscopic level and provides these unusual properties at the macroscopic scale. For one or two-dimensional propagation, they can be built by periodic structure of small metal motives printed on a dielectric substrate [18.II]. The metamaterial science opens a door for advancement in the theory of electromagnetics, assuming that we have full control of the material properties within a given frequency band [6.II].

Applications are numerous: highly efficient antennas, super lenses, invisibility clocks and microwave circuits, to name a few [19.II].

A special group of metamaterial is the left hand (LH) materials [3.II]. In such material, the phase velocity and the group velocity travels in opposite directions. LH metamaterials have attracted researchers because it adds new functionalities to media properties [20.II].

2.13 Kramers-Kronig's relation

For lossy media, it is possible to characterize losses in sinusoidal steady state by complex constitutive parameters. As the real part corresponds to energy storage, the imaginary part, which is negative for passive media, corresponds to lost energy. It can be shown that real and imaginary parts are not independent. In this section we discuss the relationship between the real and imaginary parts of permittivity. A similar discussion can be done for permeability.

For simplicity we consider an isotropic nonmagnetic linear dielectric dispersive homogeneous media. Hence, the constitutive relations become:

$$\vec{D}(\omega) = \varepsilon(\omega)\,\vec{E}(\omega) \tag{26.IIa}$$

$$\vec{B}(\omega) = \mu_o\,\vec{H}(\omega) \tag{26.IIb}$$

In time domain, (26.IIa) becomes [2.II]:

$$\vec{D}(\mathrm{t}) = \varepsilon_o\,\vec{E}(\mathrm{t}) + \varepsilon_o \int_0^\infty f(\tau)\vec{E}(\mathrm{t}-\tau)d\tau \tag{27.II}$$

where, $f(\tau)$ is a function of time that depends on the electric properties of the medium and relates to the well-known permittivity via Fourier transform [2.II] as:

$$\varepsilon(\omega) = \varepsilon_o\left(1 + \int_0^\infty f(\tau)e^{j\omega\tau}d\tau\right) \tag{28.II}$$

The frequency ω is defined as a complex variable:

$$\omega = \omega' + j\omega'' \tag{29.II}$$

Since the permittivity function defined in (28.II) is a complex in general, it is possible to rewrite it as [2.II]:

$$\varepsilon(\omega) = \varepsilon'(\omega) + j\varepsilon''(\omega) \tag{30.II}$$

However, from (28.II) we can see that:

$$\varepsilon\,(-\omega^{\dagger}) = \varepsilon^{\dagger}(\omega) \tag{31.II}$$

where † is the complex conjugate symbol. This yield:

$$\varepsilon'\,(-\omega) = \varepsilon'\,(\omega) \tag{32.IIa}$$

$$\varepsilon''\,(-\omega) = -\varepsilon''\,(\omega) \tag{32.IIb}$$

In other words, the real part of permittivity is an even frequency dependent function, while the imaginary part is and odd function. Now, if we assume that the function $\vec{E}(\mathrm{t})$ is given by the real mathematical expression, one obtains:

$$\vec{E}(\mathrm{t}) = \vec{E}_o e^{-j\omega t} + \vec{E}_o^{\dagger} e^{j\omega^{\dagger} t} \tag{33.IIa}$$

$$\vec{D}(\mathrm{t}) = \varepsilon\,(\omega)\,\vec{E}_o e^{-j\omega t} + \varepsilon\,(-\omega^{\dagger})\vec{E}_o^{\dagger} e^{j\omega^{\dagger} t} \tag{33.IIb}$$

After applying the appropriate mathematical analysis from complex theory, we reach to the well-known Kramers-Krong's relations:

$$\varepsilon'\,(\omega) - 1 = \frac{1}{2\pi} P\left\{\int_{-\infty}^{+\infty} \frac{\varepsilon''\,(\omega)}{x-\omega}\,dx\right\} \tag{34.IIa}$$

$$\varepsilon''\,(\omega) = -\frac{1}{2\pi} P\left\{\int_{-\infty}^{+\infty} \frac{\varepsilon'\,(\omega)-1}{x-\omega}\,dx\right\} \tag{34.IIb}$$

Since the integrals in (34.II) and (34.IIb) are improper integrals containing singularities, we are interested in calculating their principal value $P\{\cdot\}$.

A point to be mentioned here is that the above Kramers-Kronig's relations hold only for linear media. It has been proven that they are violated in nonlinear media [21.II], because calculating the principal value of integral requires certain symmetry which doesn't exist in these types of media. However, one can derive relations between imaginary and real parts of permittivity in nonlinear media; they will be problem dependent since they depend on the type of nonlinearity [22.II].

2.14 Conclusion

In this chapter we discussed some physical aspects of complex media from electrodynamic point of view at macroscopic scale. We presented different scenarios by which a material can acquire complex properties.

For instance, one can design fiber optic cable with some nonlinearity to mitigate dispersion, allowing higher data rates. The usage of ferroelectric and ferromagnetic media in microwave circuits allows some controllability by external electric or magnetic field. Another property of ferroelectric and ferromagnetic media is that they can induce very high permittivity and permeability values, respectively, which can contribute to circuit miniaturization.

The periodic structures are considered as complex media, even though they can consist of two types of simple dielectric arranged in certain way, the reason is that the periodic structures can possess very complex behavior that doesn't exist in simple media.

Transformation optics (TO) can be considered as a type of conformal mapping in which we transfer the whole computational domain into another simpler one. Then, obtaining the results in the transformed domain, we may come back to the original problem. This procedure is very similar to what we do in solving linear differential equations (ODE) using Laplace or Fourier transforms. On the other hand, TO can be used the other way around by which we search for certain behavior of the electromagnetic field propagation. The objective is to design a computational domain (material distribution) that can achieve various functions such as invisible clocks, super lenses and many others TO applications.

Finally, we discussed a very important relation between the real part and imaginary part of permittivity or permeability tensors in linear media namely, the Kramers-Kronig's relations. They mean that we cannot choose both of them arbitrarily (even from mathematical point of view perspective).

References

[1.II] D. K. Kalluri, Electromagnetics of Time Varying Complex Media, CRC Press, 2010.

[2.II] L. Landau and E. M. Lifshitz, Electrodynamcis of Continuous Media, Pergamon Press, 1984.

[3.II] J. D. Jackson, Classical Electrodynamics, JOHN WILEY & SONS, INC., 1999.

[4.II] C. Peucheret, "Elements of Electromagnetic Theory, Anisotropic Media, and Light Modulation by the Linear Electro-Optic Effect," DTU Fontonik, Department of Photonics Engineering, Technical University of Denmark, 2010.

[5.II] S. Carroll, Spacetime and Geometry: An Introduction to General Relativity, 2003: Addison-Wesley.

[6.II] A. J. Ward and J. B. Pendry, "Refraction and geometry in Maxwell's equaions," *Journal of Modern Optics,* vol. 43, no. 4, pp. 773-793, 1996.

[7.II] L. Brillouin, Wave Propagation in Periodic Structures, Dover Publications Inc., 1946.

[8.II] C. Moss, F. Teixeira, Y. E. Yang and J. A. Kong, "Finite-Difference Time-Domain Simulation of Scattering From Objects in Continuous Random Media," *IEEE Tansactions on Geoscience and Remote Sensing,* vol. VOL. 40, no. NO. 1, pp. 178-186, 2002.

[9.II] M. I. Yaich, M. Khalladi and M. Essaadi, "Efficient Modeling of Chiral Media Using SCN-TLM Method," *Serbian Journal of Electrical Engineering,* vol. 1, no. 2, pp. 249-254, 2004.

[10.II] A. S. Sidorkin, Domain Structure in Ferroelectrics and Related Materials, Cambridge University Press, 2006.

[11.II] K. M. Rabe, J.-M. Triscone and C. H. Ahn, Physics of Ferroelectrics: A modern perspective, Springer, 2007.

[12.II] D. Polder, "On the theory of ferromagnetic resonance," *philos. Mag,* vol. 40, p. 99, 1949.

[13.II] D. Polder and J. Smith, "Resonance phenomena in ferrites," *Rev. Mod. Phys,* vol. 25, no. 1, pp. 89-90, 1953.

[14.II] P. Gelin and P. Quéffélec, "Generalized Permeability Tensor Model: Application to Barium Hexaferrite in a Remanent State for Self-Biased Circulators," *IEEE Transactions on Magnetics,* vol. 44, no. 1, pp. 24-31, 2008.

[15.II] P. Gelin and K. Berthou, "New consistent model for ferrite permeability tensor with arbitrary magnetization state," *IEEE Transactions on Microwave Theory and Techniques,* vol. 45, no. 8, pp.

1185-1192, 1997.

[16.II] Z. Hao, "Finite-difference time-domain simulations of metamaterials," Thesis, Northeastern University, 2012.

[17.II] P. P. M. So and W. J. R. Hoefer, "Time Domain TLM Modeling of Metamaterials with Negative Refractive Index," in *IEEE MTT-S Digest*, 2004.

[18.II] P. So, *et al*, "Modeling of Metamaterials with Negative Refractive Index Using 2-D Shunt and 3-D SCN TLM Network," *IEEE Transactions on Microwave Theory and Techniques*, vol. 53, no. 4, pp. 1496-1505, 2005.

[19.II] N. B. Kundtz, D. R. Smith and J. B. Pendry, "Electromagnetic Design With Transformation Optics," *Proceedings Of The IEEE*, vol. 99, no. 10, pp. 1622-1633, October October2011.

[20.II] N. Doncov, *et al*, "TLM Modelling of Left-Handed Metamaterials by Using Digital Filering Techniques," *Microwave Review*, 2010.

[21.II] K. A. Shore and D. A. S. Chan, "Kramers-Kronig Relations for Nonlinear Optics," *Electronics Letters*, vol. 26, no. 15, pp. 1206-1207, 1990.

[22.II] K.E. Peiponen and J. J. Saarinen, "Generalized Kramers-Kronig relations in nonlinear optical- and THz-spectroscopy," *Rep. Prog. Phys*, vol. 72, 2009.

[23.II] G. P. Agrawal, Nonlinear Fiber Optics, Academic Press, 2006.

[24.II] V. Janyani, "The Development of TLM Model for Nonlinear Optics," *Microwave Review*, June, 2004.

[25.II] L. D. Landau and E. M. Lifshitz, The Classical Theory of Fields, PERGAMON PRESS, 1962.

[26.II] R. F. Harrington, Time-Harmonic Electromagnetic Fields, JHON WILEY & SONS. INC, 2001.

[27.II] J. Vanderlinde, Classical Electromagnetic Theory, KLUWER ACADEMIC PUBLISHERS, 2004.

[28.II] F. W. Hehl and Y. N. Obukhov, Foundations of Classical Electrodynamics Charge, Flux and Metric, Progress in Mathematical Physics Volume 33, 2003.

[29.II] A. Taflove and S. C. H. , Computational Electrodaynamics, The Finite-Difference Time-Domain Method, Norwood: Artch House, INC., 2005.

[30.II] N. Doncov, T. Asenov, Z. Stankovic and J. Paul, "Time-domain Modelling of Graded Refractive Index Metamaterials by using 3D TLM Z-Transform Method," in *TELSIKS*, Serbia, Nis, 2011.

[31.II] M. Zedler and G. V.Eleftheriades, "Anisotropic Tranmission-Line Metamaterials for 2-D

Transformation Optics Applications," *Proceedings of the IEEE,* vol. 99, no. 10, October 2011.

[32.II] C. Blanchard, *et al*, "Dispersion inherent to TLM nodes for modelling of metamaterials," *Electronics Letters*, vol. 46, no. 2, 2010.

[33.II] M. A. Eberspacher, T. F. Eibert and P. Russer, "An Analysis Procedure for 3D Metamaterial Unit Cell Based on the Rotated Transmission-Line Matrix Scheme," in *Loughborough Antennas & Propagation Conference*, Loughborough, 2010.

[34.II] M. G. Bray, "Finite-Difference Time-Domain Simulation of Electromagnetic Bandgap and Bi-Anisotropic Metamaterials," PhD Thesis, Pennsylvania State University, 2005.

Chapter III
Transmission Line Matrix Method (TLM) State of the Art

3.1 Introduction

In fundamental sciences, engineering and other disciplines, the common challenge is to solve problems with ever increasing complexity. As a result, several techniques have been developed, sometime simultaneously or separately, in various disciplines. For instance, the invention of genetic algorithms came from observing the evolution of living beings in biology from Darwinian perspective. Integral transformations (Fourier transform for instance), is analogue to currency change while trading between different markets. Linear systems either in mechanics or electric circuits end up with very similar equations that govern their behavior. Not very far from the theory of electromagnetics, the original form of Maxwell's equations was more similar to a system of fluid dynamic equations. The most important restriction in using this analogy is that a perfect or almost perfect mapping must exist between both problems. In other words, either zero or negligible amount of information is allowed to be lost in the mapping process.

Based on the same idea of analogy, Kron [1.III] proposed a new way to look at Maxwell's equations. He realized that in order to describe any linear circuit, we need sources and only three types of components: resistors, inductors and capacitors. Then, he proposed that it is possible to describe the medium in which the fields propagate using a network of interconnected components. To verify his idea, he studied a two-dimensional electrical-mesh of interconnected transmission lines (that can be represented by distributed capacitors and inductors). By exiting this network using a voltage source, the behavior of the node voltages and currents everywhere in the network is very similar to the solutions of Maxwell's equations in two-dimension for lossless dielectric medium. This experiment was sort of validation to his assumption that the mesh itself serves as a propagating medium. Later, the analogy between an electromagnetic

medium and the corresponding network of interconnected TL became more obvious. The different electrical components mimic what happens in Maxwell's equations locally i.e. resistors are analogous to losses, capacitors are analogous to electric energy storage and inductors are analogous to magnetic energy storage [2.III]. Transmission-lines provide the delay that mimics the field propagation phenomenon. It is from this experiment that later Johns proposed the TLM model of field propagation.

In this chapter we present the history of TLM algorithm and its development from one to three dimensions and the insertion of complex media into the TLM model [3.III] [4.III].

We mentioned in the first chapter, that the TLM method is most commonly used in time-domain. However, its frequency domain version also exists but will not be discussed here. For more information one can consult [5.III] [6.III] [7.III] [8.III]. The frequency domain TLM is potentially useful, only when we are dealing with linear media, single frequency or narrow band characterization.

Finally, one issue to be discussed in this chapter is the relation between FDTD and TLM. For many scientists working in computational electromagnetics, it is felt that TLM is just a slightly modified FDTD. In fact, we will show that the latter is as different from TLM as the MoM integral equation technique can be from the FEM. The subsequent developments of TLM have been made in a concomitant manner with the ones in FDTD [9.III] [10.III]. The reason of this erroneous perception of TLM comes from the fact that it was published almost 10 years after the FDTD and appeared to be more complicated as far its algorithm is concerned. Since FDTD Yee's algorithm looks simpler, practitioners found no advantage to move towards TLM simulation.

3.2 Diakoptic principle

This principle in electromagnetics allows one to solve rigorously a problem by first splitting it into several sub-problems. Then, solutions in one particular subdomain can be computed by discretizing one sub domain only and rigorously accounting for other sub domains via operations at its boundaries only. This principle has several versions in different contexts. For instance, in algorithm discipline it is called the divide and conquers technique, among which, we can find many algorithms such as FFT [11.III].

In computational electromagnetics, this principle provides us with a great idea that allows one to simplify the simulations: we discretize the computational domain into small cells, each considered as an isolated entity with input and output ports. Thus, field calculation is a local issue for each cell, and once they are calculated the interaction between neighboring cells happens through voltages exchange [1.III]. This philosophy allows us to include fine structures without affecting the computational procedure. For instance, we can do simulations of a structure that includes thin wires, thin panels, slots or any fine objects. Inside each cell, the small structure will interact with fields according to known laws. Hence, we can incorporate the small structure effect in the TLM algorithm locally. So, it is only required to modify the algorithm at cells which interact with the small structure [12.III]. Even though in principle this can be also done in FDTD and other volumic methods, the TLM method provides a very straightforward way to apply diakoptics. For instance, to include a thin wire model in FDTD we will face several issues like the half-step staggering between electric and magnetic fields. Also, the fact that in FDTD the update equations in one cell will depend on material contents in the neighboring cells will raise the issue of existence the thin wire for its neighbors. This issue doesn't exist in TLM since the fields calculation in every cell is independent form the material contents of other cells (considering the Symmetrical Condensed Node).

As we will see later in this chapter, by applying this methodology one can easily do simulations for media possessing complicated constitutive relations (dispersive or anisotropic media), just by adjusting field values at the cell center using some filtering process [13.III] [14.III].

3.3 TLM for simple media

In literature a lot of work has been done regarding TLM method for handling computational domains including simple media [15.III] [16.III] [17.III]. For interested readers, appendix A is dedicated for an extensive literature review for TLM basic algorithms for linear non-dispersive isotropic media.

3.4 TLM for Complex media

In the appendix A, we discuss the origins of the TLM techniques and some algorithms for simple media, i.e., linear, isotropic or with diagonal tensors only and non-dispersive (however allowing frequency independent conduction losses σ_e or σ_m). In literature, one can find many papers that have been published to address and handle non dispersive anisotropic media [18.III]. This is done by simply adjusting electric or magnetic field expressions at cell centers to include the (constant) coupling with field components from other directions. However, in the following section, we discuss how the TLM method can be extended to cover a wider range of EM phenomena, and how to handle more sophisticated types of materials that were discussed in chapter II in a unified systematic manner. This includes anisotropic media, material possessing magneto-electric coupling…etc.

3.4.1 TLM for Dispersive media

As presented in chapter II, dispersive media are those for which properties change according to the operating frequency. In other words, they behave like filters when an electromagnetic wave propagates through them (wave frequency selective media). It is obvious that in frequency domain, the frequency dependence of the material parameters don't affect the computational scheme except, perhaps, the need to change from real to complex arithmetic. In time domain, the problem is more involved and major modifications should take place in the core of the algorithm. In the literature, many papers have been published in FDTD or TD-TLM to address this problem for which parameter frequency variation must be translated in a time-domain filtering:

- Auxiliary differential equation technique (ADE) [19.III] [20.III] [21.III].
- Piece wise linear recursive convolution technique (PLRC) [22.III].
- z-transform based approach [23.III] [19.III] [21.III] [24.III] [25.III] [26.III] [27.III] [28.III].

Philosophically speaking, the three above techniques are very similar. They are just different algorithmic representations to compute the convolution process that should take place

between fields and the media impulse response in time domain. ADE and PLRC techniques are very efficient for isotropic media, because the convolutions process is well integrated inside the update equations. However, ADE and PLRC are problem dependent approaches (for instance the update equations for Debye medium are different than those of Lorentz medium). Furthermore, they are very difficult to derive for general anisotropic constitutive parameters. On the other hand, the last technique namely, the z-transform approach, is based on filtering processes and is very direct, systematic and generic. It is not problem dependent as we just need to know the corresponding digital filters that represent the constitutive parameters [29.III].

As mentioned earlier, the local field-matter interaction of the TLM method presents an elegant way to handle dispersive media. The same basic SCN algorithm presented by Johns [16.III] is used with some modifications. Instead of calculating fields by (40.III), we add a filtering process to account for the medium under study. Then, the algorithm continues as for usual non dispersive media.

3.4.2 TLM for metamaterial

The first attempts to simulate LH materials were through the change of the TLM network topology (one-dimension, two-dimension, or three-dimension model that is constructed by three shunt nodes connected to three series nodes) [30.III] [27.III]. In the proposed modified topologies, authors embedded shunt inductors, and series capacitors (as opposed to shunt capacitors and series inductors in normal RH media). But for rigorous numerical simulations, time-domain approaches were not appropriate. Hence, several algorithms have been developed to handle such materials in more sophisticated and systematic way. Frequency domain methods provide a possible choice, if one is interested in steady state and narrow band characterization. On the other hand, using full-wave time domain methods like FDTD or TLM opens the door for several observations about the way the media interact with fields in real time and how waves are created and modified at any point in the space. This is in addition to their wide bandwidth characterization capability.

In their paper [27.III], authors developed an algorithm based on z-transform and convolution for taking into account the frequency selective nature of the LH media [28.III]. In their approach, they assumed the material to be isotropic, which is not true for an arbitrary LH

material. On the other hand, the method discussed earlier in this chapter developed by Farhat et al [14.III] can handle such media in systematic way. In addition, their approach doesn't require paying special attention whether media are LH or RH isotropic or anisotropic. It just requires the full knowledge about the material properties in frequency domain. Hence, equivalent time domain filters can be designed and provide the required correction of fields at node centers.

An interesting point to be mentioned here is that LH materials are usually constructed out of arrays of identical metal and dielectric elements [31.III]. If the elements are small compared to wavelength, it can be simulated and its scattering matrix can be saved. This scattering matrix can be used in simulating the complete structure that contains this LH media instead of including these small elements in the overall computational process. This considerably decreases the computational effort.

3.4.3 TLM for general linear media

In [14.III] [23.III] [32.III] authors presented a TLM (symmetrical condensed node) formulation for general anisotropic media. In chapter IV this algorithm will be revised with all dispersion and stability analysis.

Maxwell's equations for general linear dispersive media can be written in time domain as [33.III]:

$$\begin{pmatrix} \nabla \times H \\ -\nabla \times E \end{pmatrix} - \begin{pmatrix} J_{ef} \\ J_{mf} \end{pmatrix} = \frac{\partial}{\partial t}\begin{pmatrix} \varepsilon_o E \\ \mu_o H \end{pmatrix} + \begin{pmatrix} \bar{\bar{\sigma}}_e * E \\ \bar{\bar{\sigma}}_m * H \end{pmatrix} + \frac{\partial}{\partial t}\begin{pmatrix} \varepsilon_o \bar{\bar{\chi}}_e & \frac{\bar{\bar{\xi}}}{c_o} \\ \frac{\bar{\bar{\zeta}}}{c_o} & \mu_o \bar{\bar{\chi}}_m \end{pmatrix} * \begin{pmatrix} E \\ H \end{pmatrix} \qquad (1.III)$$

where $\bar{\bar{\chi}}_e, \bar{\bar{\chi}}_m$ are the electric and magnetic susceptibility tensors respectively, $\bar{\bar{\sigma}}_e, \bar{\bar{\sigma}}_m$ the electric and magnetic conductivities tensors, and $\bar{\bar{\xi}}$, $\bar{\bar{\zeta}}$ the chirality (the electro-magneto coupling factors [34.III]) tensors respectively, and $*$ is the time domain convolution operator.

From the system (1.III) we can observe two main components:

- The spatial and temporal operators ($\nabla \times, \nabla ., \partial/\partial t$)
- The material properties tensors $\bar{\bar{\chi}}_e, \bar{\bar{\chi}}_m, \bar{\bar{\sigma}}_e, \bar{\bar{\sigma}}_m, \bar{\bar{\xi}}, \bar{\bar{\zeta}}$

Thus, it is legitimate to link the first components to a propagation phenomenon in vacuum and the second to a local interaction with the medium. .This observation is interestingly enough conform to the TLM process as shown later.

A proper TLM model of the above equations can be carried out by the general procedure described by Peña and Ney [15.III]. Now, we are going to describe the different steps in the TLM algorithm for general linear media, described by (1.III):

1- Field evaluation

The fields are calculated exactly as in free space with a SCN-TLM cell. Thus, there is no need to introduce reflection coefficients in the connecting arm across media interfaces. The field components at the cell center are updated as [14.III]:

$$\begin{pmatrix} \Delta x E_x \\ \Delta y E_y \\ \Delta z E_z \\ Z_o \Delta x H_x \\ Z_o \Delta y H_y \\ Z_o \Delta z H_z \end{pmatrix} = \begin{pmatrix} \gamma_{e,i}\left(V_{in,1} + V_{in,2} + V_{in,9} + V_{in,12} + \beta_{e,i} V_{in,13}\right) \\ \gamma_{e,i}\left(V_{in,3} + V_{in,4} + V_{in,8} + V_{in,11} + \beta_{e,i} V_{in,14}\right) \\ \gamma_{e,i}\left(V_{in,5} + V_{in,6} + V_{in,7} + V_{in,10} + \beta_{e,i} V_{in,15}\right) \\ \gamma_{m,i}\left(-V_{in,4} + V_{in,5} - V_{in,7} + V_{in,8} + \beta_{m,i} V_{in,16}\right) \\ \gamma_{m,i}\left(V_{in,2} - V_{in,6} - V_{in,9} + V_{in,10} + \beta_{m,i} V_{in,17}\right) \\ \gamma_{m,i}\left(-V_{in,1} + V_{in,3} - V_{in,11} + V_{in,12} + \beta_{m,i} V_{in,18}\right) \end{pmatrix} \quad (2.III)$$

where E, H are the electric and magnetic field components, respectively, at the cell center, Z_o is the wave impedance in free space. The other parameters are defined in table 1.III.

Table 1.III, update equation parameters in TLM algorithm of general linear media

$\Delta l = c_o \Delta t$	$\delta_1 = \frac{\Delta y \Delta z}{\Delta x}$
$\delta_2 = \frac{\Delta x \Delta z}{\Delta y}$	$\delta_3 = \frac{\Delta x \Delta y}{\Delta z}$
$\alpha_{m,i} = 1$	$\alpha_{e,i} = 1$
$\gamma_{m,i} = \frac{\Delta l}{\delta_i}$	$\gamma_{e,i} = \frac{\Delta l}{\delta_i}$
$\beta_{m,i} = 4\left(\frac{\delta_i}{2dl} - 1\right)$	$\beta_{e,i} = 4\left(\frac{\delta_i}{2dl} - 1\right)$

where $\Delta \boldsymbol{x}$, $\Delta \boldsymbol{y}$, $\Delta \boldsymbol{z}$ are the spatial-steps and Δt is the time step.

2- Field correction process

We first need to define the correction matrix, which is a 6×6 matrix of filters. Usually, these filters are first defined in Laplace s-transfom domain and they are obtained either from analytical expressions derived from physical models or using curve-fitting algorithms to obtain Pade-approximation of experimental data. The continuous media propertie tensors (3.II) that apear in the system (1.III) should be normalized according to the simulation parameters.Then, they can be used in building the correction matrix. The media tensors are expressed by:

$$\bar{\bar{\sigma}} = \begin{pmatrix} \sigma_e^{xx} & \sigma_e^{xy} & \sigma_e^{xz} & 0 & 0 & 0 \\ \sigma_e^{yx} & \sigma_e^{yy} & \sigma_e^{yz} & 0 & 0 & 0 \\ \sigma_e^{zx} & \sigma_e^{zy} & \sigma_e^{zz} & 0 & 0 & 0 \\ 0 & 0 & 0 & \sigma_m^{xx} & \sigma_m^{xy} & \sigma_m^{xz} \\ 0 & 0 & 0 & \sigma_m^{yx} & \sigma_m^{yy} & \sigma_m^{yz} \\ 0 & 0 & 0 & \sigma_m^{zx} & \sigma_m^{zy} & \sigma_m^{zz} \end{pmatrix} \tag{3.IIIa}$$

$$\bar{\bar{M}} = \begin{pmatrix} \chi_e^{xx} & \chi_e^{xy} & \chi_e^{xz} & \xi_r^{xx} & \xi_r^{xy} & \xi_r^{xz} \\ \chi_e^{yx} & \chi_e^{yy} & \chi_e^{yz} & \xi_r^{yx} & \xi_r^{yy} & \xi_r^{yz} \\ \chi_e^{zx} & \chi_e^{zy} & \chi_e^{zz} & \xi_r^{zx} & \xi_r^{zy} & \xi_r^{zz} \\ \zeta_r^{xx} & \zeta_r^{xy} & \zeta_r^{xz} & \chi_m^{xx} & \chi_m^{xy} & \chi_m^{xz} \\ \zeta_r^{yx} & \zeta_r^{yy} & \zeta_r^{yz} & \chi_m^{yx} & \chi_m^{yy} & \chi_m^{yz} \\ \zeta_r^{zx} & \zeta_r^{zy} & \zeta_r^{zz} & \chi_m^{zx} & \chi_m^{zy} & \chi_m^{zz} \end{pmatrix} \tag{3.IIIb}$$

Hence, tensors (3.IIIa) and (3.IIIb) must be modified accordring to table 2.III:

Table 2. III media normalization formulas

$\vartheta = 2c_o\Delta t$	$D_x = \frac{\vartheta\Delta x}{2\Delta y\Delta z}$
$D_y = \frac{\vartheta\Delta y}{2\Delta x\Delta z}$	$D_x = \frac{\vartheta\Delta z}{2\Delta x\Delta y}$
$\sigma_{e,n}^{ij} = Z_o\Delta k D_i\sigma_e^{ij}, \quad i \neq j$ $\sigma_{e,n}^{ii} = Z_o\frac{\Delta j\Delta k}{\Delta i}D_i\sigma_e^{ii}, \quad i = j$	$\sigma_{m,n}^{ij} = \frac{\Delta k D_i\sigma_e^{ij}}{Z_o}, \quad i \neq j$ $\sigma_{m,n}^{ii} = \frac{\Delta j\Delta k}{Z_o\Delta i}D_i\sigma_m^{ii}, \quad i = j$
$\xi_{r,n}^{ij} = \frac{\Delta t\Delta i}{2\Delta j}\xi_r^{ij}$	$\chi_{e,n}^{ij} = \frac{\Delta t\Delta i}{2\Delta j}\chi_e^{ij}$
$\zeta_{r,n}^{ij} = \frac{\Delta t\Delta i}{2\Delta j}\zeta_r^{ij}$	$\chi_{m,n}^{ij} = \frac{\Delta t\Delta i}{2\Delta j}\chi_m^{ij}$

where $i, j, k \in \{x, y, z\}$.

In the above table, $\sigma_{e,n}^{ij}$ and $\sigma_{m,n}^{ij}$ are the normalized electric and magnetic conductivities respectively, $\chi_{e,n}^{ij}$ and $\chi_{m,n}^{ij}$ the normalized electric and magnetic susceptibilities, respectively, and $\zeta_{r,n}^{ij}$ and $\chi_{m,n}^{ij}$ the normalized chiralities (electro-magnetic and magneto-electric coupling factors, respectively) of the element i, j. After performing the normalization process, we obtain the normalized version of (3.III a) and (3.IIIb) which we will refer to $\bar{\bar{\sigma}}_n$ and $\bar{\bar{M}}_n$, respectively.

Once the media tensors are normalized they are ready to be used to get the correction matrix in Laplace domain:

$$\bar{\bar{\Gamma}}(s) = \left(\bar{\bar{I}}_6 + \bar{\bar{\sigma}}_n + s\bar{\bar{M}}_n\right)^{-1} \tag{4.III}$$

where $\bar{\bar{I}}_6$ is the identiy matrix of rank 6. The correction matrix that results from (4.III) can be written as:

$$\bar{\bar{\Gamma}}(s) = \begin{pmatrix} \Gamma_{11}(s) & \cdots & \Gamma_{16}(s) \\ \vdots & \ddots & \vdots \\ \Gamma_{61}(s) & \cdots & \Gamma_{66}(s) \end{pmatrix} \tag{5.III}$$

The correction matrix $\bar{\bar{\Gamma}}(s)$ in (4.III) is dereived from discretized version of Maxwell's curl equation (1.III). For more details the reader can consult [33.III].

The next process is to prepare the correction matrix $\bar{\bar{\Gamma}}(s)$ to be used in TLM-time domain algorithm. This is done by using a bilinear transform to convert filter response into z-domain. The process of converting Laplace s-domain filter responses into z-domain is critical. It should be very accurate, otherwise we may end up with unstable or even unphysical system**.** Finally, we obtain the filter correction matrix $\bar{\bar{\Gamma}}(z)$ which is also a 6x6 matrix. Each element of this matrix is an infinite impulse response (IIR) filter that is defined by the general expression:

$$\Gamma_{ij}(z) = \frac{\sum_{k=0}^{M} b_{ijk} z^{-k}}{1+\sum_{k=1}^{M} a_{ijk} z^{-k}} = b'_o + \frac{\sum_{k=1}^{M} b'_{ijk}\, z^{-k}}{1+\sum_{k=1}^{M} a_{ijk} z^{-k}} \qquad (6.III)$$

Figure 1.III shows a realization of an arbitrary IIR filter in the correction matrix.

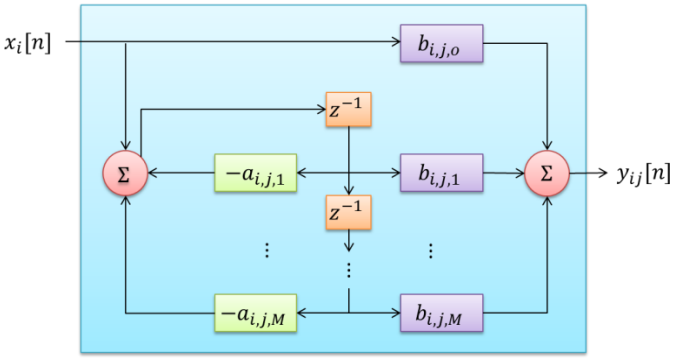

Figure 1.III the $\bar{\bar{\Gamma}}_{ij}(z)$ filter block diagram

Once all filters are obtaind in z-domain, we can incorporate them in (6.III) to perform the correction process [14.III]:

$$\begin{pmatrix} \Delta xE_x \\ \Delta yE_y \\ \Delta zE_z \\ Z_o\Delta xH_x \\ Z_o\Delta yH_y \\ Z_o\Delta zH_z \end{pmatrix}_{c,n} = \begin{pmatrix} \Gamma_{11} & \cdots & \Gamma_{16} \\ \vdots & \ddots & \vdots \\ \Gamma_{61} & \cdots & \Gamma_{66} \end{pmatrix} * \left[\begin{pmatrix} \Delta xE_x \\ \Delta yE_y \\ \Delta zE_z \\ Z_o\Delta xH_x \\ Z_o\Delta yH_y \\ Z_o\Delta zH_z \end{pmatrix}_{o,n} \middle| \begin{pmatrix} \Delta xE_x \\ \Delta yE_y \\ \Delta zE_z \\ Z_o\Delta xH_x \\ Z_o\Delta yH_y \\ Z_o\Delta zH_z \end{pmatrix}_{c,n-1} \middle| \cdots \middle| \begin{pmatrix} \Delta xE_x \\ \Delta yE_y \\ \Delta zE_z \\ Z_o\Delta xH_x \\ Z_o\Delta yH_y \\ Z_o\Delta zH_z \end{pmatrix}_{c,n-M} \right] \quad (7.III)$$

In (7.III) we can see that the correction process in general dispersive media requires the knowledge of the field values from previous time steps. This is expected because it is an IIR filtering process in essence, but for several field components. In figure 2.III we see the complete correction process for the electric field component in the x-direction.

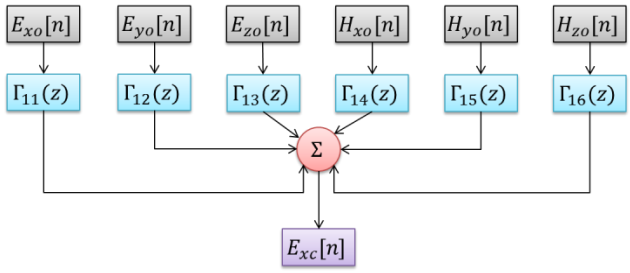

Figure 2.III, complete filtering process for electric field in x-direction

As we can see, the correction process takes into account the material presence. If the medium under consideration is just free space, the correction matrix becomes a diagonal matrix of delta functions. In fact, for a non-dispersive simple media with certain relative permittivity ε_r and relative permeability μ_r, the correction procedure becomes trivial and it will reproduce Johns' basic SCN formulation.

3- Scattering process

After fields at the center nodes are corrected by (6.III) , reflected voltages can be determined by the following vector expression:

$$\begin{pmatrix} V_{\mathrm{ref},1} \\ V_{\mathrm{ref},2} \\ V_{\mathrm{ref},3} \\ V_{\mathrm{ref},4} \\ V_{\mathrm{ref},5} \\ V_{\mathrm{ref},6} \\ V_{\mathrm{ref},7} \\ V_{\mathrm{ref},8} \\ V_{\mathrm{ref},9} \\ V_{\mathrm{ref},10} \\ V_{\mathrm{ref},11} \\ V_{\mathrm{ref},12} \\ V_{\mathrm{ref},13} \\ V_{\mathrm{ref},14} \\ V_{\mathrm{ref},15} \\ V_{\mathrm{ref},16} \\ V_{\mathrm{ref},17} \\ V_{\mathrm{ref},18} \end{pmatrix}_{n+1} = \begin{pmatrix} \Delta x E_x + Z_o \Delta z H_z - V_{in,12} \\ \Delta x E_x - Z_o \Delta y H_y - V_{in,9} \\ \Delta y E_y - Z_o \Delta z H_z - V_{in,11} \\ \Delta y E_y + Z_o \Delta x H_x - V_{in,8} \\ \Delta z E_z - Z_o \Delta x H_x - V_{in,7} \\ \Delta z E_z + Z_o \Delta y H_y - V_{in,10} \\ \Delta z E_z + Z_o \Delta x H_x - V_{in,5} \\ \Delta y E_y - Z_o \Delta x H_x - V_{in,4} \\ \Delta x E_x + Z_o \Delta y H_y - V_{in,2} \\ \Delta z E_z - Z_o \Delta y H_y - V_{in,6} \\ \Delta y E_y + Z_o \Delta z H_z - V_{in,3} \\ \Delta x E_x - Z_o \Delta z H_z - V_{in,1} \\ \Delta x E_x - V_{in,13} \\ \Delta y E_y - V_{in,14} \\ \Delta z E_z - V_{in,15} \\ \Delta x H_x - V_{in,16} \\ \Delta y H_y - V_{in,17} \\ \Delta z H_z - V_{in,18} \end{pmatrix}_{n} \quad (8.\mathrm{III})$$

Now, the reflected voltages can be connected to the neighboring nodes via the connection process for the next time iteration.

4- Connection process

The connection process can be written in following vector expression:

$$\begin{pmatrix} V_{in,1}(k,l,m) \\ V_{in,2}(k,l,m) \\ V_{in,3}(k,l,m) \\ V_{in,4}(k,l,m) \\ V_{in,5}(k,l,m) \\ V_{in,6}(k,l,m) \\ V_{in,7}(k,l,m) \\ V_{in,8}(k,l,m) \\ V_{in,9}(k,l,m) \\ V_{in,10}(k,l,m) \\ V_{in,11}(k,l,m) \\ V_{in,12}(k,l,m) \\ V_{in,13}(k,l,m) \\ V_{in,14}(k,l,m) \\ V_{in,15}(k,l,m) \\ V_{in,16}(k,l,m) \\ V_{in,17}(k,l,m) \\ V_{in,18}(k,l,m) \end{pmatrix}_{n+1} = \begin{pmatrix} V_{\mathrm{ref},12}(k,l-1,m) \\ V_{\mathrm{ref},9}(k,l,m-1) \\ V_{\mathrm{ref},11}(k-1,\mathrm{l},m) \\ V_{\mathrm{ref},8}(k,l,m-1) \\ V_{\mathrm{ref},7}(k,l-1,m) \\ V_{\mathrm{ref},10}(k-1,l,m) \\ V_{\mathrm{ref},5}(k,l+1,m) \\ V_{\mathrm{ref},4}(k,l,m+1) \\ V_{\mathrm{ref},2}(k,l,m+1) \\ V_{\mathrm{ref},6}(k+1,l,m) \\ V_{\mathrm{ref},3}(k+1,l,m) \\ V_{\mathrm{ref},1}(k,l+1,m) \\ V_{\mathrm{ref},13}(k,l,m) \\ V_{\mathrm{ref},14}(k,l,m) \\ V_{\mathrm{ref},15}(k,l,m) \\ V_{\mathrm{ref},16}(k,l,m) \\ V_{\mathrm{ref},17}(k,l,m) \\ V_{\mathrm{ref},18}(k,l,m) \end{pmatrix}_{n+1} \tag{9.III}$$

where (k,l,m) are the space cell indices. And, as usual, the complete process (field evaluation, field correction, scattering and connection processes) will repeat for the next time steps.

Some very interesting facts about this TLM scheme should be highlighted here:

- If we chose cubic cells, at maximum time step the parameters $\beta_{e,i} = 4\left(\frac{\delta_i}{2dl} - 1\right)$ and $\beta_{m,i} = 4\left(\frac{\delta_i}{2dl} - 1\right)$ will be identically zero. Hence, from update equations system (3.III) we no longer need the voltages $V_{in,13}$ to $V_{in,18}$ and $V_{\mathrm{ref},13}$ to $V_{\mathrm{ref},18}$. This is due to the fact that material presence is taken into account through a filtering process instead of stubs used in the original work by Johns [16.III].
- Even for simple media (isotropic and non-dispersive) other than free space, we need filters to represent these media. This is not the case in the original paper by Johns [16.III] since stub loading is used instead. However, with some mathematical analysis we can obtain the original Johns formulation exactly from the general media presented above.
- Free space is assumed to be the connection media. This means that wave propagation occurs only in free space (in the proposed SCN-TLM scheme). We may question what happens

when modeling other media, in which phase and group velocities are different from the ones of free space. The answer is twofold: first, the phase change that occurs in the filtering process corrects the phase velocity to the media one. Second, the maximum time step that comes from the stability criteria will provide the correct medium group velocity. For instance, in dielectrics in which the speed of light is less than the one in free space, the maximum time step is greater than the one in free space. Hence, the ratio between the cell dimensions over time step gives the correct phase velocity. This also applies to artificial media with permittivity less than the one of free space.

3.4.4 TLM for nonlinear media

In electrodynamics, the term nonlinearity refers to the wave propagation in media in which properties are field dependent. It has been shown experimentally that any material shows nonlinear behavior above certain range of frequencies or amplitudes [35.III]. Even though the nonlinearity in Maxwell's equations can occur if any of the material parameters behave as a function the field values (magnetic or electric fields), nonlinearities that involve the electric susceptibility are of special importance. This is due to the fact that most of the materials in nature possess electric susceptibility whilst very few materials possess magnetic susceptibility. In this section we will present the nonlinearity that occurs in the electric susceptibility only although, as a future work, one could study the effect of nonlinearity in magnetic susceptibility in a similar manner. However, non-linearity will not be investigated in details in the thesis

The nonlinear behavior of the media is due to the nonlinear dependence of polarization vector $\vec{P}$ (the electric susceptibility) with the field intensity $\overrightarrow{E}$. For instance [36.III]:

$$P = \varepsilon_o\left(\chi^{(1)}\,E + \chi^{(2)}\,E^2 + \chi^{(3)}\,E^3 + \cdots\right) = P^L + P^{NL} \tag{10.III}$$

where P^L and P^{NL} are the linear and nonlinear polarizations, respectively.

Generally for simulating a nonlinear media it is necessary to incorporate three scenarios [36.III]

- Linear dispersion.
- Instantaneous nonlinearity.
- The nonlinear dispersion.

In TD-TLM and FDTD there are two main methods to simulate the nonlinear media

I. **Nonlinear solver based on piecewise-linear recursive convolution method (PLRC)**

In this method, the update equations for E-field for next time-step construct a nonlinear algebraic system of equations; the objective is to find the roots of this system. Usually this is done by Newton' method and the root with lowest value is chosen as a physical solution [37.III] [19.III].

II. **Auxiliary Differential Equation Method (ADE)**

In this method, we introduce other differential equations (auxiliary) that relate the polarization and the electric flux density. These equations are time-stepped in synchronism with Maxwell's equations. This formulation eliminates the need to solve an algebraic polynomial equation at each time step like in the previous method [19.III] [20.III].

3.5 Implementation for fine details

TLM SCN-based algorithm has a very special feature, i.e., each cell can be treated as an isolated entity with input output ports. The mutual communication between the neighboring cells happens through simple rules of voltage exchange. Those rules are fixed and do not change at the interface between different media [38.III] [12.III] [39.III].

The above properties of TLM SCN-based nodes (which follows the diakoptic principle), allows us to incorporate fine structures (thin wires, thin panels) inside the TLM cell without the necessity to discretize those fine structures. Hence, it is sufficient to know the scattering properties (scattering matrix elements) of the TLM cell after including the fine structure inside it. Scattering properties can be calculated either analytically or numerically (at the cell level) [40.III]. In other words, if we are interested in simulating a structure containing fine details in some regions (for instance to include thin wires inside the TLM cell [41.III]), then to avoid the multi-scale problem, one first simulates these fine details alone. Then, one analyzes their

frequency dependent behavior to reconstruct a suitable correction matrix. The next step is to replace the fine details in the original computational domain by relatively big cells with the obtained correction matrices. These cells will produce the same effect of the original fine details. Consequently, we avoid using fine meshing for these fine structures in the computational process.

3.6 Modelling Time Dependent Computational Domain

Even though time varying media are usually more common in fluid dynamics or thermodynamics [42.III], the possibility of having a time varying computational domain in electrodynamics may occur. This can give us a deeper insight into some interesting electromagnetics phenomena, and how fields interact with time varying media or time varying boundary conditions [43.III]. As a matter of fact, to handle the time varying computational domain one should give special attention to the following points:

- If any parameter of the computational domain is changing with time (even the time step itself [44.III]), then we have a time dependent computational problem. This includes material properties, boundary conditions, discretization, location and orientation of components inside the computational domain (for instance, antennas in motion).

- One can argue for example that time varying media are special cases of dispersive media since both of them are frequency selective processes. If that is true, one should not ignore the fact that, in traditional dispersive media, the filter coefficients are constant with time. For time-varying scenarios, filters are time-varying coefficients. This has many implications on the implementation and validity [45.III].

- If the material properties (constitutive parameters) are varying extremely rapidly with time, the medium characteristics change dramatically. Many quantum related phenomena appear and should be included in any computational model [35.III].

- A modified version of Maxwell's equations should be used to include the relativistic effects. This model can be used in case of simulating objects that are moving at high relative velocity (such as elementary particles inside a cyclotron, or celestial objects in space) [43.III].

- Assuming that we want to simulate a material that is changing very rapidly with time. This may bring extra constrains on the choice of the time step of the simulation process. This fact is well known in adaptive filter theory for which the sampling time becomes very small when adaptive filter parameters change very rapidly [45.III].

Time-domain TLM method provides us with a powerful tool to tackle time-domain computational problems including complex media. Time varying media are a kind of complex media; but unfortunately, the derivations presented in this chapter is valid only for computational problems involving time invariant media. To include the time varying media a new derivation is required based on classical Maxwell's equations (1.III). However, the media properties will become functions of time. On the other hand, in case of computational problems involving relativistic effects, the necessary TLM derivation should be based on transformed Maxwell's equations via relativity theory [35.III] [43.III].

Finally, Porti et al [46.III] developed a TLM based algorithm that could handle time varying media such as moving plasma. They also studied the effect of time varying time step on the performance of the algorithm.

3.7 TD-TLM compared to FDTD

In his famous paper K. Yee [47.III] developed a systematic way to solve Maxwell's equation boundary value problems by constructing a new type of cells (known as Yee-cell in computational community). What he did was to discretize both curl equations in space and time directly. In each cell, there is room for the six field components, and the material properties at the location of the updated component. When field components are updated, they require samples from their own node and its neighbors. This means that when field samples are updated at interface, constitutive parameters from adjacent media are involved. It is easy to show that this

leads to averaging the values of the parameters. This may produce some substantial error, depending on the contrast and the number of interfaces (heterogeneity). This is where the TLM local property plays a significant role: fields are always updated in a homogeneous medium at both sides of the interface. In addition, field tangential components computed at the interface from either cell are always equal, insuring the field continuity conditions.

As seen previously in this chapter, TLM method became a general purpose rigorous method after the development of the SCN by Johns [16.III] Now, if we compare basic mechanisms of TLM and FDTD, we see that TLM algorithm is based on diakoptics principle that builds up solutions by superposition of local waves (proved to be totally compatible with Maxwell's theory). On the other hand, FDTD algorithm directly discretizes Maxwell's curl equations in space and time.

In terms of memory cost and calculation speed, the FDTD method needs to save six-field component values from the previous time step, and six in the current time step. On the other hand, TLM needs to keep track for 18-voltages at every cells (12-voltages if one use SSCN) and six-field components. However, TLM algorithm operates at the highest Courant condition limit without any instability problem. In FDTD one should always use a value less that the Courant condition to insure stability, thus increasing both the simulation time and the numerical dispersion.

For dispersive media the TLM method deals with dispersive media locally through the filtering and correction process. Furthermore, the TLM algorithm is standard and systematic for all types of linear media. The only requirement is to use time domain filters to represent dispersive media and no special issues appear at the interface between two dispersive media. However, in FDTD the update equations in PLRC and ADE approaches used to deal with dispersive media are problem dependent (the update equations for Lorentz media are different from those of the Debye media). This adds extra limitation on using FDTD, especially for anisotropic complex media such as non-saturated-ferrite. Furthermore, some issues should be raised at the interface between different dispersive media, since in FDTD the update equations depends on the field media properties on the neighboring cells. [14.III] [48.III].

To summarize, TLM and FDTD are two distinct numerical schemes to solve electromagnetic problems. They have very different dispersion properties, manipulate a different number of unknowns and update field components at different locations. They have their specific advantage and disadvantages. For the early computational electromagnetic practitioners, the simplicity of the FDTD algorithm was very attractive and the time-domain approach provided new possibilities. The TLM algorithm was published about 10 years later and many people did not fully understand the concept which was perceived as complicated. Despite some real advantages over the FDTD in certain practical cases, the TLM will never reach the notoriety of the FDTD. An explanation could be also the premature death of Peter B Johns with whom the TLM was starting to gain some interest in the scientific community.

3.8 N-port network characterization with TLM

The TLM method provides us with direct procedure to characterize a microwave device such as in calculating the s-parameters, propagation constant and input impedance, namely, S_{11}, β andZ_{in}, respectively. To perform this characterization for a microwave device, for any port we chose three points in a row (separated by some distance d) say $\{p_1, p_2, p_3\}$ as shown in figure 3.III. Then, we measure the voltages (or the currents) values at these three points.

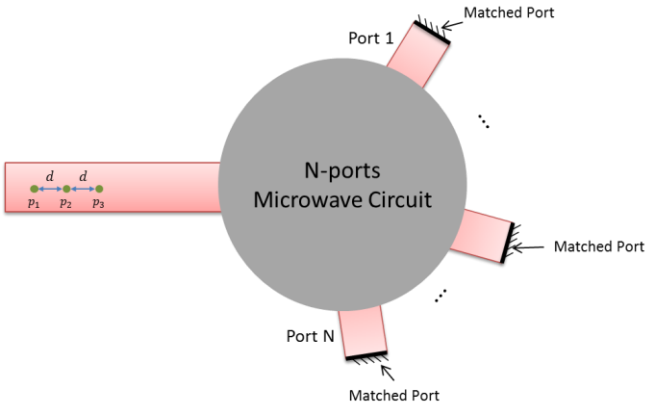

Figure 3.III, generic N-ports microwave network

From the basic knowledge of transmission line theory we can construct three equations based on those three voltages such as:

$$V(p_1) = V^+ e^{-jd\beta} + V^- e^{+jd\beta} \quad \text{(11.IIIa)}$$

$$V(p_2) = V^+ e^{-j2d\beta} + V^- e^{+j2d\beta} \quad \text{(11.IIIb)}$$

$$V(p_3) = V^+ e^{-j3d\beta} + V^- e^{+j3d\beta} \quad \text{(11.IIIc)}$$

Similarly for currents:

$$I(p_1) = I^+ e^{-jd\beta} + I^- e^{+jd\beta} \quad \text{(12.IIIa)}$$

$$I(p_2) = I^+ e^{-j2d\beta} + I^- e^{+j2d\beta} \quad \text{(12.IIIb)}$$

$$I(p_3) = I^+ e^{-j3d\beta} + I^- e^{+j3d\beta} \quad \text{(12.IIIc)}$$

By solving the previous systems (45.III) and (46.III) for $\{V^+, V^-, I^+, I^-, \beta\}$ we can find the reflection coefficients and the input impedance directly as:

$$S_{11}(\omega) = \frac{V^+(\omega)}{V^-(\omega)} = \frac{I^+(\omega)}{I^-(\omega)} \quad \text{(13.IIIa)}$$

$$Z_{in}(\omega) = \frac{V^t(\omega)}{I^t(\omega)} \quad \text{(13.IIIb)}$$

where V^t and I^t are the total voltages and currents at the input of the antenna (a linear combination of waves going both directions).

As we can see, this procedure is straight forward in TLM since voltages and currents are calculated by default in all points in the computational domain. However, in FDTD we need to calculate the voltage V and the current I by making integration of the E and H fields. A further remark is that in both techniques TLM or FDTD we should apply the previous procedure to calculate the microwave circuit parameters in frequency domain. This requires transferring the time domain-values of measured currents and voltages at the three points $\{p_1, p_2, p_3\}$ to the frequency domain as a first step. Finally to calculate the radiated far-field (which is at locations outside the computational domain) we use KISR (Kirchhoff's surface Integral representation) in both FDTD and TLM: all sources are enclosed by an arbitrary closed surface on which some field components are computed and stored. Far-field values are computed by integration of the stored components weighted by the free-space Green's function in time-domain [19.III].

3.9 Conclusion

One has to admit that there is no champion method that is optimal for all scenarios discussed in chapter I. For instance, MOM (applied to surface integral equation formulation) is an efficient technique for studying scattering problems from homogenous or conducting objects. On the other hand, FEM, FDTD or TLM are more natural choices when simulating nonhomogeneous structures [49.III].

In this chapter, a historical tracing of the development of TLM algorithm was presented, starting from the simple experimental observation of Kron [1.III] which showed the analogy between Maxwell's equations and Kirchhoff's circuit theory laws. Then, we described the evolution brought by P. Johns to build a numerical scheme based on this observation. Finally, we discussed how TLM was further extended to simulate complex media (anisotropic, dispersive, nonlinear …etc.

A comparison between time domain TLM and frequency domain TLM was discussed to show the common roots for both of them [9.III] and their specific advantages. Further, we briefly discussed topics relevant to TLM computation, such as the different types of meshing. Also, the possibility of including fine details (like thin wires or slots smaller than 0.1 λ) by modifying locally the algorithm was presented. It avoids mesh refinement that enforces a much smaller time-step and, thus, exhausts the simulation time. Further, the scenario of time varying computational problems and the way to handle them using TLM algorithm were briefly presented. Finally, a short discussion on FDTD and TD-TLM was presented to shed some light on the fundamental differences and try to stop the wrong perception by many time-domain practitioners that TLM is just a "disguised" FDTD.

References

[1.III] G. Kron, "Equivalent Circuit of the Field Equations of Maxwell-I*," *Proceedings of the I.R.E,* pp. 289-299, 1944.

[2.III] R. F. Harrington, Time-Harmonic Electromagnetic Fields, John Wiley & Sons, INC., 2001.

[3.III] P. Russer, M. Mongiardo and L. B. Felsen, "Electromagnetic field representation and computations in complex strucures III: network representaions of the connecgtion and subdomain circuits," *Int. J. Numer. Model,* vol. 15, pp. 127-145, 2002.

[4.III] L. B.Felsen, M. Mongiardo and P. Russer, "Electromagnetic field representation and computation in complex strucurtes I: complexity architecture and generalized network formulation," *Int. J. Numer. Model,* vol. 15, pp. 93-107, 2002.

[5.III] M. Attia, M. Ney and T. Aguili, "Comparitive Analysis between 3D-TLM Nodes in the Frequency Domain," in *URSI Interantional Symposium on Electrmagnetic Theory,* , 2010.

[6.III] H. Jin and R. Vahldiek, "Full-Wave Analysis of Coplanar Waveguide Discontinuities Using the Frequency Domain TLM Method," *IEEE Transactions on Microwave Theroy and Techniques,* vol. 41, no. 9, pp. 1538-1542, 1993.

[7.III] H. Jin and R. Vahldieek, "The Frequency-Domain Transmission Line Matrix Method- A New Concept," *IEEE Transactions on Microwave Theroy and Techniques,* vol. 40, no. 12, pp. 2207-2218, 1992.

[8.III] D. Johns and C. Christopoulos, "New frequency-domain TLM for numerical solution of steady-state electromagnetic problems," *IEE Proc. SCI, Meas. Technol.,* vol. 141, no. 4, pp. 310-316, 1994.

[9.III] P. B.Johns, "On the Relationship Between TLM and Finte-Difference Methods for Maxwell's Equations," *IEEE Transactions on Microwave Theory and Techniques,* Vols. MTT-35, no. 1, pp. 60-61, 1987.

[10.III] Z. Chen and J. Xu, "The Generalized TLM-Based FDTD- Summery of Recent Progress," *IEEE Microwave and Guided Wave Letters,* vol. 7, no. 1, pp. 12-14, 1997.

[11.III] S. S. Skiena and M. A. Revilla, Programming Challenges, Springer, 2002.

[12.III] P. Sewell, Y. K. Choong and C. Christopoulos, "An Accurate Thin-Wire Model for 3-D TLM Simulaitons," *IEEE Transactions on Electromagnetic Compatibility,* vol. 45, no. 2, pp. 207-217, 2003.

[13.III] J. Paul, C. Christopoulos and D. W. P. Thomas, "Generalized Material Models in TLM- Part 2: Materials with Anisotropic Properties," *IEEE Transactions on Antennas and Propagation,* vol. 47, no. 10, pp. 1535-1542, 1999.

[14.III] A. L. Farhat, S. L. Maguer, P. Quéffélec and M. Ney, "TLM Extension to Electromagnetic Field Analysis of Anisotropic and Dispersive Media: A Unified Field Equation," *IEEE Transactions on Microwave Theory and Techniques,* vol. 60, no. 8, pp. 2339-2351, 2012.

[15.III] N. Peña, M. M. Ney, "A General Formulation of a Three-dimensional TLM Condensed Node with the Modeling of Electric and Magnetic Losses and Current Sources," *12th Annual Review of Progress in APPlied Computational Electromagnetics,* pp. 262-269, 18-22 March 1996.

[16.III] P. B.Johns, "A Symmetrical Condensed Node for the TLM Method," *IEEE Transactions on Microwave Theory and Techniques,* Vols. MTT-35, no. 4, pp. 370-377, 1987.

[17.III] P. Johns and R. Beurle, "Numerical solution of 2-dimensional scattering problems using a transmission line matrix," *Proceedings of the IEE,* vol. 188, pp. 1203-1208, 1971.

[18.III] A. C. Cabeceira, A. Grande, I. Barba and J. Represa, "A Time-Domain Modeling for E: Wave Propagation in Bi-Isotropic Media Based on the TLM Method," *IEEE Transactions on Microwave Theory and Techniques,* vol. 54, no. 6, pp. 2780-2789, 2006.

[19.III] A. Taflove and S. C. H. , Computational Electrodaynamics, The Finite-Difference Time-Domain Method, Norwood: Artch House, INC., 2005.

[20.III] H. E. Fayali, M. I. Yaich and M. Khaladi, "Scattered-Field Modeling in Linear Dispersive Media Using ADE-TLM Algorithm," *IJETEE,* vol. 5, no. 1, July 2013.

[21.III] A. R. Luebbers and e. al, "A Frequency-Dependet Finite-Difference Time-Domain Formulation for Dispersive Materials," *IEEE Transactions on Electromagnetic Compatibility,* vol. 32, no. 3, pp. 222-227, 1990.

[22.III] D. F. Kelley and R. J. Luebbers, "Piecewise Linear Recursive Convolution for Dispersive Media Using FDTD," *IEEE Transactions on Microwave Theroy and Techniques,* vol. 44, no. 6, pp. 792-797, 1996.

[23.III] C. Christopoulos, The Transmission-Line Modeling (TLM) Method in Electromagnetics, Arizona: Morgan & Claypool, 2006.

[24.III] M. I. Yaich, M. Khalladi; I. Zekik;J. A. Morente, "Modeling of Frequency-Dependent Magnetized Plasma in Hybrid Symmetrical Condensed TLM Method," *IEEE Microwave and Wireless Components Letters,* vol. 12, no. 8, pp. 293-295, 2002.

[25.III] J. Paul, C. Christopoulos and D. W. P. Thomas, "Generalized Material Models in TLM- Part I: Materials with Frequency-Dependent Properties," *IEEE Transactions on Antennas and*

Propagation, vol. 47, no. 10, pp. 1528-1534, 1999.

[26.III] N. Doncov, T. Asenov, Z. Stankovic, J. Paul and B. Milovanovic, "TLM Z-Transform Method Modelling of Lossy Grin MTM with Different Refractive Index Profiles," *SER: Elec. Energ,* pp. 103-112, August 2012.

[27.III] N. Doncov and e. al, "TLM Modelling of Left-Handed Metamaterials by Using Digital Filering Techniques," *Microwave Review,* 2010.

[28.III] N. Doncov, T. Asenov, Z. Stankovic and J. Paul, "Time-domain Modelling of Graded Refractive Index Metamaterials by using 3D TLM Z-Transform Method," in *TELSIKS*, Serbia, Nis, 2011.

[29.III] V. Rawin, C. Christopoulos, D. Thomas and S. Greedy, "Application of Digital Filtering Techniques in Three-Dimensional Multi-Scale Problems," in *Loughborough Antennas & Propagation Conference*, Loughborough, 2010.

[30.III] M. A. Eberspacher, T. F. Eibert and P. Russer, "An Analysis Procedure for 3D Metamaterial Unit Cell Based on the Rotated Transmission-Line Matrix Scheme," in *Loughborough Antennas & Propagation Conference*, Loughborough, 2010.

[31.III] C. Blanchard and e. al, "Time domain simulation of electromagnetic cloaking strucures with TLM method," *Optical Society of America,* vol. 16, no. 9, 2008.

[32.III] J. Paul, "Modelling of General Electromagnetic Material Properties in TLM," PhD thesis, University of Nottingham, 1998.

[33.III] A. Farhat, P. Q. Ney and M. Ney, "Wideband TLM Modeling of Microwave Structures with Anisotropic and Dispersive Media," in *EuMa*, Paris, 2010.

[34.III] M. I. Yaich, M. Khalladi and M. Essaadi, "Efficient Modeling of Chiral Media Using SCN-TLM Method," *Serbian Journal of Electrical Engineering,* vol. 1, no. 2, pp. 249-254, 2004.

[35.III] J. D. Jackson, Classical Electrodynamics, JOHN WILEY & SONS, INC., 1999.

[36.III] G. P. Agrawal, Nonlinear Fiber Optics, Academic Press, 2006.

[37.III] J. Paul, C. Christopoulos and D. W. P. Thomas, "Generalized Material Models in TLM - Part 3: Materials With Nonlinear Properties," *IEEE Transactions on Antennas and Propagation,* vol. 50, no. 7, pp. 997-1004, 2002.

[38.III] J. Paul, V. Podlozny and C. Christopoulos, "The Use of Digital Filtering Techniques for the Simulation of Fine Features in EMC Problems Solved in the Time Domain," *IEEE Transactions on Electrmagnetic Compatability,* vol. 45, no. 2, pp. 238-244, 2003.

[39.III] Z. Li, "Contributions aux techniques de maillages irréguliers dans la méthode TLM:Applicqtions au calcul électromagnetique de structures à détails fins et interface non-cartésienns," These, L'Université de Bretagne Occidentale, 2005.

[40.III] J. Paul, C. Christopoulos, D. W. P. Thomas and X. Liu, "Time-Domain Modeling of Electromagnetic Wave Interaction With Thin-Wires Using TLM," *IEEE Transactions on Electromagnetic Compatibility,* vol. 47, no. 3, pp. 447-455, 2005.

[41.III] Ahmad, A.; Thomas, D.W.P.; Christopoulos, C., "Thin wire formulation for 3-D modeling of a ground wire," Transmission and Distribution Conference and Exposition, 2008. T&D. IEEE/PES , vol., no., pp.1,6, 21-24 April 2008.

[42.III] T. J. CHUNG, Computational Fluid Dynamics, Cambridge University Press, 2002.

[43.III] L. D. Landau and E. M. Lifshitz, The Classical Theory of Fields, PERGAMON PRESS, 1962.

[44.III] S.Y.R. Hui *et al*, "Variable time step techqniue for transmission line modelling," *IEE PROCEEDINGS,* vol. 140, no. 4, pp. 299-302, 1993.

[45.III] S. Hykin, Adaptive Filter Theory, Prentice Hall, 2001.

[46.III] J. A. Porti, J. A. Morente, A. Salinas, E. A. Navarro and M. Rodriguez-Sola, "A Generalized Dynamic Symmetrical Condensed TLM Node for the Modeling of Time-Varying Electromagnetic Media," *IEEE Transactions on Antennas and Propagation,* vol. 54, no. 1, pp. 2-11, 2006.

[47.III] K. Yee, "Numerical solution of initial boundary value problems involving Maxwell's equation in isotropic media," *IEEE trans. Antennas Propagat,* no. AP-14, pp. 302-307, May 1966.

[48.III] M. Zedler and G. V.Eleftheriades, "Anisotropic Tranmission-Line Metamaterials for 2-D Transformation Optics Applications," *Proceedings of the IEEE,* vol. 99, no. 10, October 2011.

[49.III] H. G. Dantanarayana, Application of TLM for Optical Microresonators, PhD Thesis, University of Nottingham, 2012.

Chapter IV
Stability and Dispersion Analysis of a TLM Unified Approach for General Linear Media

4.1 Introduction

In continuous media, the term dispersion refers to the change of phase velocity either due to the change in the operating frequency or due to the change in wave number in case of anisotropic media (which is responsible for velocity anisotropy in such media) [1.IV]. Since the phase velocity is a function of the wave-number, one can say that dispersion is a phenomenon that connects the frequency with the wave-vector. However, in discretized media, since it is impossible to have spherically symmetric cells in the entire computational domain, there must exist some kind of anisotropy in the wavenumber for different directions inside the computational domain, even for isotropic media. Hence, dispersion due to the discretization process is inevitable. This kind of dispersion is referred to as numerical dispersion, and it explains the difference between physical phase velocities in continuous media and the phase velocity calculated via numerical techniques [2.IV].

It is well-known that the limiting case of the discretized system of Maxwell's equations tends toward continuous form of Maxwell's equations as the mesh size and the time step go toward zeroes [2.IV]. Hence, one can intuitively predict that the numerical dispersion phenomenon will be negligible when dealing with very fine meshes. However, it will increase until it spoils the simulation results as we go toward coarser meshes or, equivalently, when the wavelength decreases as compared to the mesh size. In this context an important question arises: how to choose the mesh-size in an optimal way? In other words how to make the best tradeoff between mesh-size (computational requirements) and the tolerable level of numerical dispersion? One trivial answer is to do an initial simulation for a coarse-mesh, then to refine the mesh gradually until convergent results are obtained. However, when one deals with complicated

problems, especially those including complex media, then remeshing the computational domain and repeating the numerical experiment several times is not a tolerable option. Furthermore, for a given mesh-size it is important to have a systematic procedure to calculate the maximum time step to minimize the simulation time. These issues are going to be discussed in details in this chapter.

As far as time-domain models are concerned, their domain of validity in terms of dispersion and stability has not be thoughouly investigated in presence of complex media, in particular for the Transmission-Line Matrix (TLM) method. In this chapter, starting from a TLM algorithm for general linear media, procedures for dispersion and stablity analysis are given and special cases are presented.

Recall that the SCN proposed by Johns [3.IV] was selected for this work owing to its very good dispersion characteristics (no dispesion in the cartesian axis directions) and the fact that it can always operates at the maximum time-step [4.IV]. In [5.IV] [6.IV] authors presented a 3D formulation for anisotropic and dispersive media in TLM method, where the filtering process was done directly to TLM node voltages This requires a 18×18 matrix of filter transfer functions for the general case. The development of a unifying approach for a general linear media was done in [7.IV], where the filtering process was applied only on the 6 field components instead of voltages. As far as TLM dispersion is concerned, some analyses were reported for non-dispersive media [8.IV] [9.IV] [10.IV] [11.IV] [12.IV]. However, very little work has been reported for complex general media.

4.2 Dispersion analysis of continues linear media

As seen previously in chapter III, time-domain Maxwell's equations for general linear media is given by:

$$\begin{pmatrix} \nabla \times \vec{H} \\ -\nabla \times \vec{E} \end{pmatrix} = \frac{\partial}{\partial t}\begin{pmatrix} \varepsilon_o \vec{E} \\ \mu_o \vec{H} \end{pmatrix} + \bar{\bar{\sigma}} * \begin{pmatrix} \vec{E} \\ \vec{H} \end{pmatrix} + \frac{\partial}{\partial t}\left[\bar{\bar{M}} * \begin{pmatrix} \vec{E} \\ \vec{H} \end{pmatrix}\right] + \begin{pmatrix} \vec{J}_{im} \\ \vec{J}_{ie} \end{pmatrix} \tag{1.IV}$$

where $*$ denotes time convolution, $\bar{\bar{\sigma}}$ represents the conductivity tensor in continues medium:

$$\bar{\bar{\sigma}} = \begin{pmatrix} \sigma_e^{xx} & \sigma_e^{xy} & \sigma_e^{xz} & 0 & 0 & 0 \\ \sigma_e^{yx} & \sigma_e^{yy} & \sigma_e^{yz} & 0 & 0 & 0 \\ \sigma_e^{zx} & \sigma_e^{zy} & \sigma_e^{zz} & 0 & 0 & 0 \\ 0 & 0 & 0 & \sigma_m^{xx} & \sigma_m^{xy} & \sigma_m^{xz} \\ 0 & 0 & 0 & \sigma_m^{yx} & \sigma_m^{yy} & \sigma_m^{yz} \\ 0 & 0 & 0 & \sigma_m^{zx} & \sigma_m^{zy} & \sigma_m^{zz} \end{pmatrix} \tag{2.IV}$$

and the matrix $\bar{\bar{M}}$ is defined as:

$$\bar{\bar{M}} = \begin{pmatrix} \chi_e^{xx} & \chi_e^{xy} & \chi_e^{xz} & \xi_r^{xx} & \xi_r^{xy} & \xi_r^{xz} \\ \chi_e^{yx} & \chi_e^{yy} & \chi_e^{yz} & \xi_r^{yx} & \xi_r^{yy} & \xi_r^{yz} \\ \chi_e^{zx} & \chi_e^{zy} & \chi_e^{zz} & \xi_r^{zx} & \xi_r^{zy} & \xi_r^{zz} \\ \zeta_r^{xx} & \zeta_r^{xy} & \zeta_r^{xz} & \chi_m^{xx} & \chi_m^{xy} & \chi_m^{xz} \\ \zeta_r^{yx} & \zeta_r^{yy} & \zeta_r^{yz} & \chi_m^{yx} & \chi_m^{yy} & \chi_m^{yz} \\ \zeta_r^{zx} & \zeta_r^{zy} & \zeta_r^{zz} & \chi_m^{zx} & \chi_m^{zy} & \chi_m^{zz} \end{pmatrix} \tag{3.IV}$$

in which χ_e^{ij} and χ_m^{ij} are the electric and magnetic susceptibility, respectivily, ξ_r^{ij} and ζ_r^{ij}, electric-magnetic coupling factors related to varying media such as moving [7.IV]. Finally, $\vec{J}_{ie}$, $\vec{J}_{im}$ are the electric and magnetic impressed current sources, respectively. Note that $\bar{\bar{\sigma}}$ takes into account the possible presence of magnetic free charges. They can exist in fictitious media, or after doing some conformal tranformation to Maxwell's equations [7.IV] [13.IV].

To study the theoretical dispersion characteristics, we should find a relation between the frequency ω , and the wave vector $\vec{k}$ of a wave propagating in the medium, which is supposed to extend indefinitly. This will allow us to evaluate the wave velocity for a given frequency, as a function of its direction of propagation. It is a way to characterize the numerical model anisotropy. In the same time, the dispersion as a function of frequency for a given direction of propagation can be established. The first step is to write Maxwell's equations in spectral domain, assuming the medium understudy is source free. Hence, we obtain from (1.IV):

$$\left(\omega \bar{\bar{I}}_6 + \omega \bar{\bar{M}}(\omega) - j\bar{\bar{\sigma}}(\omega) + \bar{\bar{\Lambda}}\right)\begin{pmatrix} \vec{E} \\ \vec{H} \end{pmatrix} = 0 \tag{4.IV}$$

where $\bar{\bar{\Lambda}}$ represents the curl operator in spectral domain:

$$\bar{\bar{\Lambda}} = \begin{pmatrix} 0 & 0 & 0 & 0 & +k_z & -k_y \\ 0 & 0 & 0 & -k_z & 0 & +k_x \\ 0 & 0 & 0 & +k_y & -k_x & 0 \\ 0 & -k_z & +k_y & 0 & 0 & 0 \\ +k_z & 0 & -k_x & 0 & 0 & 0 \\ -k_y & +k_x & 0 & 0 & 0 & 0 \end{pmatrix} \tag{5.IV}$$

The necessary condition for (4.IV) to have a nontrivial solution is:

$$\det\left(\omega\bar{\bar{I}}_6 + \omega\bar{\bar{M}}(\omega) - j\bar{\bar{\sigma}}(\omega) + \bar{\bar{\Lambda}}\right) = 0 \tag{6.IV}$$

Equation (6.IV) provides us with a tool to test whether or not the material properties are physically feasible for a linear passive media. Given any direction of propagation $\vec{k} = k_x\hat{x} + k_y\hat{y} + k_z\hat{z}$, for all roots ω_k, the imaginary part should be greater than or equal to zero:

$$Im(\omega) \geq 0 | \left\{ \forall \vec{k} | \det\left(\omega\bar{\bar{I}}_6 + \omega\bar{\bar{M}}(\omega) - j\bar{\bar{\sigma}}(\omega) + \bar{\bar{\Lambda}}\right) = 0 \right\} \tag{7.IV}$$

where $\hat{x}$, $\hat{y}$ and $\hat{z}$ are the unite vectors in the directions of the axis x,y and z, repectively. If (7.IV) is not fulfilled, the waves propagating in such media, will be amplified, which violates the energy conservation principle.

4.3 Mathematical model of TLM

In this section we present a new formulation of the TLM algorithm for general media that presented in the previous chapter. The basic TLM algorithm presented in chapter III consists of four-steps, in the following formulation we will keep those steps but the quantities and the operations will be reformulated using Hilbert space representation [9.IV] [10.IV]. This will give us more concise version of the TLM algorithm than the one presented in chapter III. It will also ease the derivation of necessary eigenvalue equations to get the dispersion relation and the stability criteria.

4.3.1 Propagation process

Initially, fields at the center of each cell are calculated as a linear combination of the incident voltages from the adjacent cells:

$$\bar{F}_{o,n} = \bar{\bar{Q}}\bar{V}_{in,n} \tag{8.IV}$$

where $\bar{F}_{o,n}$, $\bar{V}_{in,n}$ are the fields and incident voltages vectors at n-*th* time step, respectivily, which write:

$$\bar{F}_{o,n} = \begin{pmatrix} \Delta x E_x \\ \Delta y E_y \\ \Delta z E_z \\ Z_o \Delta x H_x \\ Z_o \Delta y H_y \\ Z_o \Delta z H_z \end{pmatrix} \tag{9.IV}$$

$$\bar{V}_{in} = \begin{pmatrix} V_{in,1} \\ V_{in,2} \\ \vdots \\ V_{in,18} \end{pmatrix} \tag{10.IV}$$

and the transformation matrix between fields and incident voltages $\bar{\bar{Q}}$, is defined as

$$\bar{\bar{Q}} = \begin{pmatrix} \bar{\bar{\gamma}} & 0 \\ 0 & \bar{\bar{\gamma}} \end{pmatrix} \left[\bar{\bar{C}}_1 + \bar{\bar{C}}_2 + \begin{pmatrix} \bar{\bar{\beta}} & 0 \\ 0 & \bar{\bar{\beta}} \end{pmatrix} \bar{\bar{C}}_3 \right] \tag{11.IV}$$

In the above, several submatrices are used to represent the linear operator $\bar{\bar{Q}}$ in compact form as shown below:

$$\bar{\bar{\gamma}} = \begin{pmatrix} \gamma_1 & 0 & 0 \\ 0 & \gamma_2 & 0 \\ 0 & 0 & \gamma_3 \end{pmatrix} \tag{12.IV}$$

$$\bar{\bar{\beta}} = \begin{pmatrix} \beta_1 & 0 & 0 \\ 0 & \beta_2 & 0 \\ 0 & 0 & \beta_3 \end{pmatrix} \tag{13.IV}$$

where the elments of the matrices in (12.IV) and (13.IV) are defined in table 1.IV.

Table 1.IV, elements of $\bar{\bar{\gamma}}$ and $\bar{\bar{\beta}}$

$\gamma_1 = 4(\frac{\Delta y \Delta z}{2\Delta x \Delta t c_o} - 1)$	$\gamma_2 = 4(\frac{\Delta x \Delta z}{2\Delta y \Delta t c_o} - 1)$
$\gamma_3 = 4(\frac{\Delta x \Delta y}{2\Delta z \Delta t c_o} - 1)$	$\beta_1 = \frac{\Delta x \Delta t c_o}{\Delta y \Delta z}$
$\beta_2 = \frac{\Delta y \Delta t c_o}{\Delta x \Delta z}$	$\beta_3 = \frac{\Delta z \Delta t c_o}{\Delta x \Delta y}$

where $\Delta x, \Delta y, \Delta z, \Delta t$ are the spatial and temporal step sizes respectively, c_o is the speed of light in free space. Matrices $\bar{\bar{C}}_1$, $\bar{\bar{C}}_2$ and $\bar{\bar{C}}_3$ are defined as

$$\bar{\bar{C}}_1 = \bar{\bar{\Delta}}_{1,1} + \bar{\bar{\Delta}}_{1,2} + \bar{\bar{\Delta}}_{1,9} + \bar{\bar{\Delta}}_{1,12} + \bar{\bar{\Delta}}_{2,3} + \bar{\bar{\Delta}}_{2,4} + \bar{\bar{\Delta}}_{2,8} + \bar{\bar{\Delta}}_{2,11} + \bar{\bar{\Delta}}_{3,5} + \bar{\bar{\Delta}}_{3,6} + \bar{\bar{\Delta}}_{3,7} + \bar{\bar{\Delta}}_{3,10} \quad (14.IV)$$

$$\bar{\bar{C}}_2 = -\bar{\bar{\Delta}}_{4,4} + \bar{\bar{\Delta}}_{4,5} - \bar{\bar{\Delta}}_{4,7} + \bar{\bar{\Delta}}_{4,8} + \bar{\bar{\Delta}}_{5,2} - \bar{\bar{\Delta}}_{5,6} - \bar{\bar{\Delta}}_{5,9} + \bar{\bar{\Delta}}_{5,10} - \bar{\bar{\Delta}}_{6,1} + \bar{\bar{\Delta}}_{6,3} - \bar{\bar{\Delta}}_{6,11} + \bar{\bar{\Delta}}_{6,12} \quad (15.IV)$$

$$\bar{\bar{C}}_3 = \bar{\bar{\Delta}}_{1,13} + \bar{\bar{\Delta}}_{2,14} + \bar{\bar{\Delta}}_{3,15} + \bar{\bar{\Delta}}_{4,16} + \bar{\bar{\Delta}}_{5,17} + \bar{\bar{\Delta}}_{6,18} \quad (16.IV)$$

where $\bar{\bar{\Delta}}_{i,j}$ is a 6 by 18 matrix defined as:

$$\left[\bar{\bar{\Delta}}_{i,j}\right]_{pq} = \begin{cases} 1, & for\ the\ p = i, j = q \\ 0, & Otherwise \end{cases} \quad (17.IV)$$

The full derivation of the above expressions is obtained directly from discretized Maxwell's curl equations (1.IV), rearanging the update equations and applying the SCN-based TLM algorithm presented in [3.IV]. Full derivations and other details could be found in [14.IV], [7.IV] .

As previously shown, update equations are material independent. In other words, free-space is considered as the local voltage propagation medium. This highlights some interesting property of the TLM-SCN based algorithms: even when dealing with complex materials, there is no need for a special treatment at interfaces.

4.3.2 Correction process

After calculating fields at the center of each node as described by (8.IV), local material presence is accounted for by applying a convolution process with a 6×6 correction matrix, whose components are usually filter functions. From (2.IV) and (3.IV), the correction matrix in linear media is given by [7.IV]:

$$\bar{\bar{\Gamma}}(s) = \left(\bar{\bar{I}}_6 + \bar{\bar{\sigma}}_n + s\bar{\bar{M}}_n\right)^{-1} \tag{18.IV}$$

where the matrices $\bar{\bar{\sigma}}_n$ and $\bar{\bar{M}}_n$ are the normalized version of (2.IV) and (3.IV) as presented in chapter III.

The correction matrix $\bar{\bar{\Gamma}}(s)$ can be obtained in the Laplace s-domain, by two different ways: either from analytical expressions of constitutive parameters, or by applying some curve-fitting algorithms on media properties that are obtained experimentally. At the end of this step the correction matrix is known:

$$\bar{\bar{\Gamma}}(s) = \begin{pmatrix} \Gamma_{11}(s) & \dots & \Gamma_{16}(s) \\ \vdots & \ddots & \vdots \\ \Gamma_{61}(s) & \dots & \Gamma_{66}(s) \end{pmatrix} \tag{19.IV}$$

any element in (19), is a filter transfer function and is given by:

$$\Gamma_{ij}(s) = \frac{\sum_{k=0}^{N_P} a_k s^k}{1+\sum_{k=1}^{N_P} b_k s^k} \tag{20.IV}$$

where N_P is the number of poles of each filter. Once all filters are known in the correction matrix (19.IV), a transformation to z-domain is applied to obtain the expression of IIR filters:

$$\Gamma_{ij}(z) = \frac{\sum_{k=0}^{N_P} a'_k z^{-k}}{1+\sum_{k=1}^{N_P} \mathrm{b}'_k z^{-k}} \tag{21.IV}$$

As a result, filtering processes translate to convolution products in the time-domain. An important point to be mentioned is that the conversion process from s-domain to z-domain is a critical issue. It should be carried out very carefully with high precision, to avoid any potential source of instability.

After the fields are calculated by (8.IV), they should be modified through the convolution process with the correction matrix $\bar{\bar{\Gamma}}(z)$, such that:

$$\bar{F}'_{c,n} = \bar{\bar{\Gamma}}(z) * \bar{F}_{o,n} \tag{22.IV}$$

whrere $\bar{F}'_{c,n}$ is the corrected fields vector at the n-*th* time step, and defined as:

$$\bar{F}'_{c,n} = \begin{pmatrix} \Delta x E_x \\ \Delta y E_y \\ \Delta z E_z \\ Z_o \Delta x H_x \\ Z_o \Delta y H_y \\ Z_o \Delta z H_z \end{pmatrix}_{c,n} \tag{23.IV}$$

At this stage of the algorithm, if one is interested in calculating the actual fields, the denormalization operation below should be performed to the corrected fields vector $\bar{F}'_{c,n}$:

$$\bar{F}_{c,n} = \bar{\bar{N}} \bar{F}'_{c,n} \tag{24.IV}$$

where $\bar{F}_{c,n}$ is the vector of actual fields after the denormalization process:

$$\bar{F}'_{c,n} = [E_x \quad E_y \quad E_z \quad H_x \quad H_y \quad H_z]^T_n \tag{25.IV}$$

and, $\bar{\bar{N}}$ is the normalization matrix defined as:

$$\bar{\bar{N}} = \begin{pmatrix} \frac{1}{\Delta x} & 0 & 0 & 0 & 0 & 0 \\ 0 & \frac{1}{\Delta y} & 0 & 0 & 0 & 0 \\ 0 & 0 & \frac{1}{\Delta z} & 0 & 0 & 0 \\ 0 & 0 & 0 & \frac{1}{Z_o \, \Delta x} & 0 & 0 \\ 0 & 0 & 0 & 0 & \frac{1}{Z_o \, \Delta y} & 0 \\ 0 & 0 & 0 & 0 & 0 & \frac{1}{Z_o \, \Delta z} \end{pmatrix} \tag{26.IV}$$

where T is the matrix-transposition operator, and Z_o is the free-space wave impedance.

4.3.3 Scattering process

Once the correction process is completed, the reflected voltages form the 18 ports of each cell in the TLM computational domain are calculated. They will be used later to evaluate the incident voltages to the neighboring cells at the next time step. Defining the vector of reflected voltages at the n-*th* time step as:

$$\bar{V}_n = \begin{pmatrix} V_1 \\ \vdots \\ V_{18} \end{pmatrix}_n \tag{27.IV}$$

The reflected voltages can be expressed as a linear combination of the corrected fields at the center of the cell and the incident voltages at the same time step. This writes in matrix form:

$$\bar{V}_n = \bar{\bar{\Lambda}}\bar{F}'_{c,n} - \bar{\bar{\Phi}}\bar{V}_{in,n} \tag{28.IV}$$

where, the operators $\bar{\bar{\Lambda}}, \bar{\bar{\Phi}}$ are defiend as:

$$\begin{aligned}\bar{\bar{\Lambda}} = {} & \bar{\bar{\varphi}}_{1,1} + \bar{\bar{\varphi}}_{1,6} + \bar{\bar{\varphi}}_{2,1} - \bar{\bar{\varphi}}_{2,5} + \bar{\bar{\varphi}}_{3,2} - \bar{\bar{\varphi}}_{3,6} + \bar{\bar{\varphi}}_{4,2} + \bar{\bar{\varphi}}_{4,3} + \bar{\bar{\varphi}}_{5,3} - \bar{\bar{\varphi}}_{5,3} + \bar{\bar{\varphi}}_{6,3} + \\ & \bar{\bar{\varphi}}_{6,5} + \bar{\bar{\varphi}}_{7,3} + \bar{\bar{\varphi}}_{7,3} + \bar{\bar{\varphi}}_{8,2} - \bar{\bar{\varphi}}_{8,3} + \bar{\bar{\varphi}}_{9,1} + \bar{\bar{\varphi}}_{9,5} + \bar{\bar{\varphi}}_{10,3} - \bar{\bar{\varphi}}_{10,5} + \bar{\bar{\varphi}}_{11,2} + \bar{\bar{\varphi}}_{11,6} + \\ & \bar{\bar{\varphi}}_{12,1} - \bar{\bar{\varphi}}_{12,6} + \bar{\bar{\varphi}}_{13,1} + \bar{\bar{\varphi}}_{14,2} + \bar{\bar{\varphi}}_{15,3} + \bar{\bar{\varphi}}_{16,4} + \bar{\bar{\varphi}}_{17,5} + \bar{\bar{\varphi}}_{18,6}\end{aligned} \tag{29.IV}$$

$$\begin{aligned}\bar{\bar{\Phi}} = {} & \bar{\bar{\Theta}}_{1,12} + \bar{\bar{\Theta}}_{2,9} + \bar{\bar{\Theta}}_{3,11} + \bar{\bar{\Theta}}_{4,8} + \bar{\bar{\Theta}}_{5,7} + \bar{\bar{\Theta}}_{6,10} + \bar{\bar{\Theta}}_{7,5} + \bar{\bar{\Theta}}_{8,4} + \bar{\bar{\Theta}}_{9,2} + \bar{\bar{\Theta}}_{10,6} + \bar{\bar{\Theta}}_{11,3} + \\ & \bar{\bar{\Theta}}_{12,1} + \bar{\bar{\Theta}}_{13,13} + \bar{\bar{\Theta}}_{14,14} + \bar{\bar{\Theta}}_{15,15} + \bar{\bar{\Theta}}_{16,16} + \bar{\bar{\Theta}}_{17,17} + \bar{\bar{\Theta}}_{18,18}\end{aligned} \tag{30.IV}$$

where $\bar{\bar{\varphi}}_{i,j}$ is a 18 by 6 matrix defined as the transpose of the matrix $\bar{\bar{\Delta}}_{i,j}$ in (17.IV), and $\bar{\bar{\Theta}}_{i,j}$ is a 18 by 18 matrix defined as:

$$\left[\bar{\bar{\Theta}}_{i,j}\right]_{pq} = \begin{cases} 1, & if\ i = p\ and\ j = q \\ 0, & Otherwise \end{cases} \tag{31.IV}$$

where i, j, p, q are integers.

4.3.4 Connection process

After scattering processes took place at every TLM node, arm reflected voltages from one cell become incident voltages to its neighboring ones. This process, which can be seen as a discrete form of Huygens principles of wave propagation, is called the TLM connection process and it can be written as follows [14.IV]:

$$\begin{pmatrix} V_{in,1} \\ V_{in,2} \\ V_{in,3} \\ V_{in,4} \\ V_{in,5} \\ V_{in,6} \\ V_{in,7} \\ V_{in,8} \\ V_{in,9} \\ V_{in,10} \\ V_{in,11} \\ V_{in,12} \\ V_{in,13} \\ V_{in,14} \\ V_{in,15} \\ V_{in,16} \\ V_{in,17} \\ V_{in,18} \end{pmatrix}_{n+1} = \begin{pmatrix} V_{12}(k,l-1,m) \\ V_{9}(k,l,m-1) \\ V_{11}(k-1,l,m) \\ V_{8}(k,l,m-1) \\ V_{7}(k,l-1,m) \\ V_{10}(k-1,l,m) \\ V_{5}(k,l+1,m) \\ V_{4}(k,l,m+1) \\ V_{2}(k,l,m+1) \\ V_{6}(k+1,l,m) \\ V_{3}(k+1,l,m) \\ V_{1}(k,l+1,m) \\ V_{13}(k,l,m) \\ V_{14}(k,l,m) \\ V_{15}(k,l,m) \\ V_{16}(k,l,m) \\ V_{17}(k,l,m) \\ V_{18}(k,l,m) \end{pmatrix}_{n} \tag{32.IV}$$

where k, l, m are node spatial position indices of the node and n is the time index. Now, we can refer to the time shift property in discrete time fourier transform (DTFT):

$$DTFT\{\, g[n+1] \,\} = e^{j\Omega}\, G(\omega) \tag{33.IV}$$

where $G(\omega)$ is the DTFT of $g[n]$ and Ω is the normalized frequency defined as $\Omega = 2\pi\Delta t f$. In a similar manner, it turns out that the above connection process (32.IV) can be represented in Hilbert space using space and time shift operators [15.IV] [13.IV]:

$$\bar{V}_{in,n+1} = \bar{\bar{T}}\bar{V}_{in,n} \tag{34a.IV}$$

$$\bar{V}_{in,n+1} = \bar{\bar{\Psi}}\bar{V}_{n} \tag{34b.IV}$$

where $\bar{\bar{T}}$ is the time shift operator which increments the time index by one step value for each cells in the computational domain:

$$\bar{\bar{T}}\,|n;k,l,m\rangle = |n+1;k,l,m\rangle \tag{35.IV}$$

or in matrix form :

$$\bar{\bar{T}} = e^{j\Omega}\bar{\bar{I}}_{18} \tag{36.IV}$$

where $\bar{\bar{I}}_{18}$ is a unity matrix of size 18. Once the time shift operator is defined, the space shift operator can be defined in a similar way. It performs spatial shift in the right-hand side of (32.IV). It is written in matrix form as :

$$\bar{\bar{\Psi}} = \begin{pmatrix} 0 & \bar{\bar{\psi}}_1 & 0 \\ \bar{\bar{\psi}}_2 & 0 & 0 \\ 0 & 0 & \bar{\bar{I}}_6 \end{pmatrix} \tag{37.IV}$$

where $\bar{\bar{\psi}}_1$ and $\bar{\bar{\psi}}_2$ are

$$\bar{\bar{\psi}}_1 = \begin{pmatrix} 0 & 0 & 0 & 0 & 0 & Y^\dagger \\ 0 & 0 & Z^\dagger & 0 & 0 & 0 \\ 0 & 0 & 0 & 0 & X^\dagger & 0 \\ 0 & Z^\dagger & 0 & 0 & 0 & 0 \\ Y^\dagger & 0 & 0 & 0 & 0 & 0 \\ 0 & 0 & 0 & X^\dagger & 0 & 0 \end{pmatrix} \tag{38.IV}$$

$$\bar{\bar{\psi}}_2 = \begin{pmatrix} 0 & 0 & 0 & 0 & Y & 0 \\ 0 & 0 & 0 & Z & 0 & 0 \\ 0 & Z & 0 & 0 & 0 & 0 \\ 0 & 0 & 0 & 0 & 0 & X \\ 0 & 0 & X & 0 & 0 & 0 \\ Y & 0 & 0 & 0 & 0 & 0 \end{pmatrix} \tag{39.IV}$$

and the elements of the above matrices are defined in table 2.IV:

Table 2.IV, space-shift operators in spectral domain and Hilbert space

Spectral domain notation	Hilbert stapce notation
$X^\dagger = e^{-j\chi}$	$X^\dagger \lvert n;k,l,m\rangle = \lvert n;k-1,l,m\rangle$
$X = e^{j\chi}$	$X \lvert n;k,l,m\rangle = \lvert n;k+1,l,m\rangle$
$Y^\dagger = e^{-j\eta}$	$Y^\dagger \lvert n;k,l,m\rangle = \lvert n;k,l-1,m\rangle$
$Y = e^{j\eta}$	$Y \lvert n;k,l,m\rangle = \lvert n;k,l+1,m\rangle$
$Z^\dagger = e^{-j\xi}$	$Z^\dagger \lvert n;k,l,m\rangle = \lvert n;k,l,m-1\rangle$
$Z = e^{j\xi}$	$Z \lvert n;k,l,m\rangle = \lvert n;k,l,m+1\rangle$

where χ, η, ξ are the normalized spatial frequencies. In analogy with Ω in (33.IV),they are defined by:

- $\chi = 2\pi\Delta x k_x$
- $\eta = 2\pi\Delta y k_y$
- $\xi = 2\pi\Delta z k_z$

where the propagation frequency of the wave is replaced by the corresponding wave number component.

It is obvious from (38.IV) and (39.IV), that $\bar{\bar{\psi}}_1 = \bar{\bar{\psi}}_2{}^{\dagger}$, where † is the Hermetian operator. This implies that the space shift operator $\bar{\bar{\Psi}}$ is a Hermetian matrix. This leads us to an interesting geometrical interpretation: any cell works as an isotropic local radiator exactly like the secondary wavelets in Huygens' propagation model. Hence, operator that represents the radiation process should reflect the geometrical symmetry of the radiation propeties. Consequently, it should lead to a symmetrical operator, represented by a Hermitian complex matrix.

4.4 Dispersion Analysis

As shown earlier in section 4.2 for continuous media, the relationship between operating frequency and wave vector (6.IV), is the dispersion relation. For a discrete computational scheme, the procedure is similar. First, we express the update equations in spectral domain using Hilbert space representation. Then, by constucting a homogeneous linear system similar to (4.IV), the condition for nontrivial solutions yields eigen values and associated eigen functions. Now, starting from the simple observation of time shift operator (35.IV) , one can write the fields vector as:

$$\bar{F}_{o,n} = \bar{\bar{T}}\bar{F}_{o,n-1} \tag{40.IV}$$

and by combining (22.IV) , (28.IV) and (34.IV), we obtain:

$$\bar{V}_{in,n} = \bar{\bar{\Psi}}\left(\bar{\bar{\Lambda}}\,\bar{\bar{\Gamma}} * \bar{F}_{o,n-1} - \bar{\bar{\Phi}}\bar{V}_{in,n-1}\right) \tag{41.IV}$$

Using (8.IV) and the time shift operation (40.IV) in (41.IV) yields the eigenvalue equation:

$$\bar{\bar{T}}\bar{V}_{in,n-1} = \bar{\bar{\Psi}}\left(\bar{\bar{\Lambda}}\bar{\bar{\Gamma}}(z)\bar{\bar{Q}}\bar{V}_{in,n-1} - \bar{\bar{\Phi}}\bar{V}_{in,n-1}\right) \tag{42.IV}$$

or, equivalentely:

$$\left(\bar{\bar{T}} - \bar{\bar{\Psi}}\left(\bar{\bar{\Lambda}}\bar{\bar{\Gamma}}(z)\bar{\bar{Q}} - \bar{\bar{\Phi}}\right)\right)\bar{V}_{in,n-1} = 0 \tag{43.IV}$$

Equation (43.IV) is the discrete version of (4.IV) for continuous media. As in section 4.2, the sufficient condition for (43.IV) to have nontrivial solutions is:

$$\det\left(\bar{\bar{T}} - \bar{\bar{\Psi}}\left(\bar{\bar{\Lambda}}\bar{\bar{\Gamma}}(z)\bar{\bar{Q}} - \bar{\bar{\Phi}}\right)\right) = 0 \tag{44.IV}$$

After performing the determinant operation in (44.IV) for a specific medium with specific spatial and temporal discretizations $\{dx, dy, dz, dt\}$, we obtain the dispersion equation:

$$\Upsilon(\Gamma, \Delta x, \Delta y, \Delta z, \Delta t, k_x, k_y, k_z, \omega) = 0 \tag{45.IV}$$

The function Υ is equivalent to the determinant in (44.IV) that relates all the arguments in (45.IV) in a closed form relation. The above procedure is very general. However, evaluating (44.IV) to obtain Υ and doing the appropriate analysis to extract useful information about the dispersion level, is usually a difficult task. Generally, it cannot be done analytically for complex media and numerical procedures provided by dedicated mathematical software must be used.

It is of importance in any simulation process to determine the maximum allowed level of dispersion. This is equivalent to choose the maximum spatial discretizations to obtain negligible dispersion errors. In general, the effect of dispersion is a problem-dependant issue. For instance, resonant frequencies of a cavity are more sensitive to the dispersion than the radiation pattern of an antenna. But if one is interested in maintaining minimum level of dispersion, it is necessary to introduce some metrics to define the dispersion quantitatively. In the literature, there are two common ways to represent the level of dispersion, either by the relative error in phase (or group) velocity or the relative error in the magnitude of the wavevector $\vec{k}$, between discrete and continuous media.

For instance, assuming that the error in phase velocity is used as a reference quantity, then a problem may require a dispersion level that do not exceed a certain threshold $P_{max}\%$.

Consequently, one seeks for the maximum spatial discretizetion that fulfills:

$$\left\{\text{Max}\,\{\Delta x, \Delta y, \Delta z\}\middle|\left|\frac{V_{pd}-V_{pc}}{V_{pc}}\right| \leq P_{max}\%\right\} \tag{46.IV}$$

Note that if (46.IV) is fulfilled at the limit by a given cell dimension, selecting a smaller cell dimension is not optimal as that will increase the number of cells to fill the computational domain (spatial over-sampling) and, consequently, the computational cost. Thus, some good knowledge of the dispersion helps to obtain more efficient simulation.

In most publications, either for FDTD or TLM [14.IV] [2.IV], authors use the following inequality as a rule of thumb, to calculate the maximum cell size that maintains some acceptable level of dispersion:

$$\{\Delta x, \Delta y, \Delta z\} \leq Min\left[\frac{\lambda_o}{10\sqrt{\varepsilon_r \mu_r}}\right] \tag{47.IV}$$

where λ_o is the wavelength in free space, ε_r, μ_r are the permittivity and the permeability of the medium, respectively. Whenever, the computational domain consists of nonhomogeneous media (which is usually the case), one should use the minimum cell dimension, so that the overall dispersion will remain negligible everywhere, and this is the reason behind the Min operator in (47.IV). As a matter of fact, this relation (which agrees with the approach presented earlier) is trustful only for isotropic nondispersive lossless media. However, when complex media are involved and when it is necessary not to exceed a certain limit of dispersion, a mesh convergence test should be applied. This implies that successive simulations from a coarse to finer mesh should be performed, at least at some locations.

The alternative to a mesh convergence test is to know the level of dispersion a priori, by applying condition (46.IV). Therefore, one can use a maximum cell size in all regions which does not require fine spatial resolution.

4.5 Stability Analysis

As discussed earlier, the possibility to work with maximum spatial discretization, reduces the computational effort. In a simillar manner, the possibility to work on highest allowed time step, reduces the simulation time. However, the computational process is more sensitive to time under sampling, than to spatial discretization. Indeed, if in the later the dispersion level may

increase, instability will occur and no useful results at all can be obtained if the time step exceeds some limit. This limit is given by the well-known Courant-Friedrichs-Lewy condition (CFL) [14.IV] [2.IV].

In the literature, there are two general approaches to perform a stability analysis (to find the CFL limit). For an explicit computational scheme, one could apply Von-Neumann's approach in which the growth factor of any of field or voltage sample must not exeed unity at the maximum time step [2.IV]. An alternate approach is to use numerical dispersion relation (45.IV), by which it is possible to predict the instability. The idea is to find its roots $\omega_i$which must have either zero or positive imaginary part for a stable scenario. If the condition is not met, fields will grow exponentially with time and an instability will occur [14.IV] [10.IV] [2.IV].

4.5.1 Growth factor (Von-Neumann) method

From (42.IV), we obtain the matrix update equation:

$$\bar{V}_{in,n} = \bar{\bar{S}}\bar{V}_{in,n-1} \tag{48.IV}$$

where the system matrix $\bar{\bar{S}}$ is defined as:

$$\bar{\bar{S}} = \bar{\bar{\Psi}}\left(\bar{\bar{\Lambda}}\bar{\bar{\Gamma}}(z)\bar{\bar{Q}} - \bar{\bar{\Phi}}\right) \tag{49.IV}$$

The necessary condition for the system (48.IV) to be stable is that eigenvalues of the updating matrix $\bar{\bar{S}}$ lie inside the unit circle in the complex plan:

$$\|\lambda_i(\Delta t)\| \leq 1 \; \forall \; i \in \{1,18\} \tag{50.IV}$$

As shown in (49.IV), the matrix $\bar{\bar{S}}$ depends on local information of the the cell, including media properties and the spatial and temporal discretizations. If an analytic solution is feasible, one can seek the maximum common Δt that fullfils the condition (50.IV). In case of complex media, especially when $\bar{\bar{S}}$ contains complicated expressions (i.e. obtained by curvefitting), the process may be more time consuming. Indeed, one has to solve for eigenvalues of $\bar{\bar{S}}$ several times by incrementing Δt gradully until the condition limit (50.IV) is reached.

4.5.2 Complex frequency method

Assuming that the computational domain is excited by a sinusoidal signal of the form:

$$V_s = V_o e^{j\omega_o n\Delta t} \tag{51.IV}$$

where ω_o, is the signal frequency. The voltage $V_{k,l,m,n}$ at any space-time point in the TLM computational domain (k, l, m, n) writes [2.IV]:

$$V_{k,l,m,n} = \alpha_L V_o e^{j((\omega_{re}+j\omega_{im})n\Delta t + k_x k\Delta x + k_y l\Delta y + k_z m\Delta z)} \tag{52.IV}$$

where, α_L is some time-independent attenuation factor, V_o is the signal amplitude at the exitation region, $\{k_x, k_y, k_z\}$ are the wave vector components in x,y,z directions, respectively, ω_{re}, ω_{im} are the real and imaginary parts of the frequency ω, respectively. The dispersion relation, contains parameters such as operating frequency, time and spatial steps and the wave vector components. Consequently, for a given spatial discretization and wave vector, one could easily find a relationship between the operating frequency, and time step.

The necessary condition for a computational domain whose dispersion relation is described by (45.IV) to be stable is that ω_{im} be zero or a positive number, for each node:

$$Im\{\omega\} \geq 0, \forall\omega | \{\Upsilon(\Gamma, \Delta x, \Delta y, \Delta z, \Delta t, k_x, k_y, k_z, \omega) = 0 \quad , \forall\, k_x, k_y, k_z \in \mathbb{R}, \forall\, all\ cells\} \tag{53.IV}$$

Two points should be highlighted here. Firstly, since we are dealing with a linear time-invariant media, the real part of frequency ω_{re} in (52.IV) should be the same as the frequency of the source signal ω_o. Secondly, for a general computational domain, waves can propagate in any direction. Thus, in finding roots of (45.IV) as a function of the time step, the solutions should be valid for any direction of propagation. This is enforced by taking all possible combinations of directions in a parallelepipedic cell i.e. $\{\hat{x}, \hat{y}, \hat{z}, \hat{x}+\hat{y}, \hat{x}+\hat{z}, \hat{y}+\hat{z}, \hat{x}+\hat{y}+\hat{z}\}$ and finding the lowest limit among these directions. For isotropic media, and because of symmetry, it is sufficient to analyse only three directions $\{\hat{x}, \hat{x}+\hat{y}, \hat{x}+\hat{y}+\hat{z}\}$.

An important issue should be discussed here: as shown previously, the update equations are temporal step-size dependent. In addition, IIR filter coefficents require some a priori knowledge of the upper bound of the time step. Indeed, if it was unstable, the process of

recalculating the filter coefficients should take place again until an appropriate prediction is done. As discussed earlier, if one chooses a very small step compared to Δt_{Max}, the time response will be oversampled, and couputational resources will be exhausted.

The previously discussed approach to calculate Δt_{Max}, allows a systematic procedure, regardless the kind of the media. However, analytical expressions and empirical expressions exist in literature only for non-dispersive media [2.IV].

4.6 Results and discussions

In this section we present several numerical experiments to study the dispersion for different types of media. The first objective is to verify the validity of the procedure, and then, to show the impact of spatial and time step values on dispersion. Finally, both approaches for stability analysis are used to calculate $\Delta t_{Max}$for two different media. However, to simplify the calculations, without loss of generality, cubic cells of size Δl are used in all simulations.

4.6.1 Dispersion in free-space

In free space, the correction matrix is $\bar{\bar{\Gamma}} = \bar{\bar{I}}_6$. If we chose the maximum time step $\Delta t = \Delta l/(2c_o)$ and substitute it in (44.IV), we obtain the well-known dispersion equation for free space [12.IV]:

$$2\cos\left(\frac{2\pi\Delta l f}{c_o}\right) = \cos(\eta)(\cos(\xi) + \cos(\chi)) + \cos(\xi)\cos(\chi) - 1 \qquad (54.IV)$$

where f is the operating frequency. By choosing different time steps that respect the stability criteria, we end up with different dispersion relation. This shows that the numerical dispersion is also time-step value dependent. Several computational tests have shown that mimum dispersion occurs at the maximum allowed time step as already known. However, even for a very simple propagating medium like free space the optimum time-step is also direction dependent. For instance, let us analyze the dispersion in the directions (1,1,0), (1,0,1) or (0,1,1). These directions correspond to the modes propagation ($TE_{110}, TE_{101}, TE_{011}$) in a cubic cavity. As shown in figure.1.IV (V_{PN} is the numerical phase velocity, V_{PT} is the theoritical phase velocity calculated for the continuous medium model) the numerical dispersion is smaller when $\Delta t_{max}/2$ is chosen as compared to Δt_{max} along the diagonal face directions.

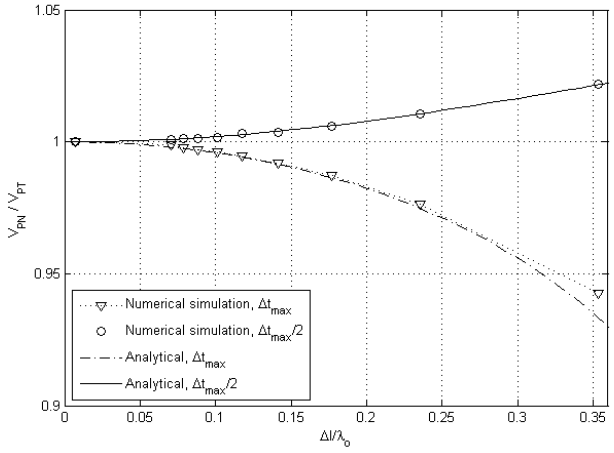

Figure 1.IV, dispersion in free space in face-diagonal directions (1,1,0), (1,0,1) , (0,1,1) with different Δt, analytical vs. numerical simulations

However, as expected, the dispersion is found minimal for maximum time step in the axis directions (1,0,0), (0,1,0) , (0,0,1), which is the case of minimum dispersion for the TLM cell.

4.6.2 Dispersion in anisotropic medium

In the second expriment, we chose a nonmagnetic, lossless anisotropic medium. The operating frequency $f = 500MHz$, and Δt_{max} was used.

As as shown in Figure.2.IV, different directions have different dispersion characteristics. For instance, in x-direction no dispersion appears, wheras, a maximum dispersion occurs along the main diagonal direction of the cube (1,1,1).

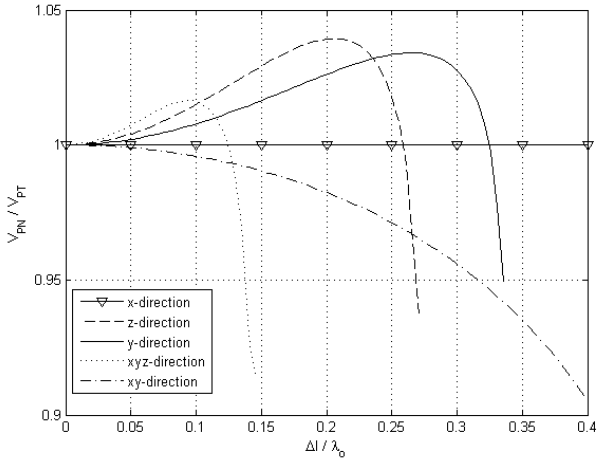

Figure 2.IV, dispersion curves in a nonmagnetic anisotropic medium at different directions of propagation, where $\bar{\bar{\varepsilon}}_r = diag\{1,2,3\}$

If one choses an empirical formula such as (47.IV), then the maximum spatial step will be $\lambda_o/10\sqrt{\varepsilon_{r,Max}} = 0.057\ \lambda_o$, for a negligible dispersion error, which matches results in figure 2.IV for around 1.0% error threshold.

4.6.3 Dispersion in Debye medium

The permetivity of a non magnetic Debye dispersive medium is given by [15.IV] [2.IV]:

$$\bar{\bar{\varepsilon}}_r = (\varepsilon_\infty + \frac{\varepsilon_s - \varepsilon_\infty}{1 + j\omega\tau_o})\,\bar{\bar{I}}_3 \qquad (55.IV)$$

where ε_∞ , ε_s is the permitivity at very high frequencies and at DC respectively, τ_o is the relaxation time of the medium. In Figure. 3.IV, different dispersion curves for different Debye materials in the axial-direction are illustrated at $f = 79.6\,MHz$. V_{PN} is the numerical phase velocity, V_{PT} is the theoritical phase velocity calculated for the continuous medium model [13.IV]. Each dispersion curve is normalized to its theortical phase velocity. In this numerical experiment the time step we used is slightly smaller than Δt_{max} (to decrease the number of decimal points in Δt to speed up the algabraic calculations done by Mathematica). As expected, the dispersion increases with ε_s.

If we chose the empirical formula (47.IV), then the maximum spatial step will be $\lambda_o/10\sqrt{\|\varepsilon_r(f)\|}$. Table 3.IV shows the difference between applying the proposed approach for 1.0% dispersion error margin in comparison with the simple formula (47.IV). The value of memory saving is calculated using

$$\text{Memory saving} = \left(\frac{\Delta l/\lambda_o \text{ 1.0\% Error}}{\Delta l/\lambda_o \text{ Rule (47.IV)}}\right)^3 \tag{56.IV}$$

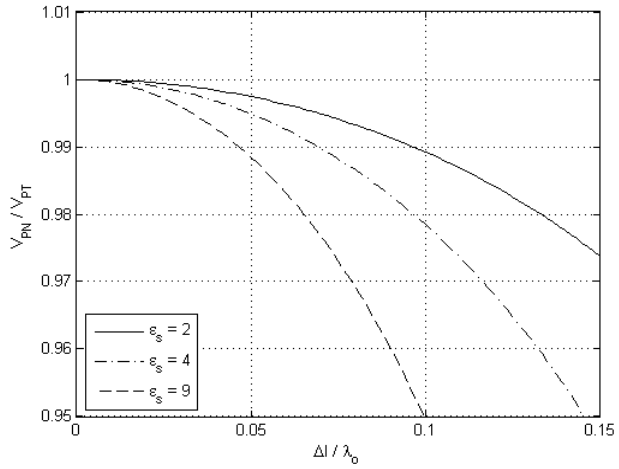

Figure 3. IV, dispersion curves in Debye medium along cell diagonal directions (1,1,1) with $\varepsilon_s = \{2,4,9\}$, $\varepsilon_\infty = 1$ and $\tau_o = 100ps$

Table 3.IV, comparison between the rigorous proposed approach and the rule (47.IV) for maximum cell size in terms of memory requirements for the Debye medium of the case of figure 3.IV

ε_s	$\Delta l/\lambda_o$ Rule (47.IV)	$\Delta l/\lambda_o$ 1.0% Error	Memory Saving %
2.0	0.071	0.095	239.5%
4.0	0.050	0.068	251.6 %
9.0	0.033	0.045	253.6 %

In the physical continuous dispersive medium, it is well known that the wave phase velocity is frequency dependent. Thus, the behaviour of a discrete model should converge to the one for continuous model as $\Delta l/\lambda_o \to 0$. Figure.4.IV shows dispersion curves of a Debye medium for propagation in the x-y plane for different values of Δl.By solving (6.IV) for the corresponding Debye continuous medium, the analytical solution is found to be:

$$k_x^2 + k_y^2 = k_o^2 \tag{57.IVa}$$

where k_o^2 is the magnitude squared of the wavenumber vector and given by:

$$k_o^2 = \left\| \frac{\omega_o^2}{c_o^2} \left(\frac{j\varepsilon_\infty - \tau_o \omega_o \varepsilon_s}{\tau_o \omega_o - j} \right) \right\| \tag{57.IVb}$$

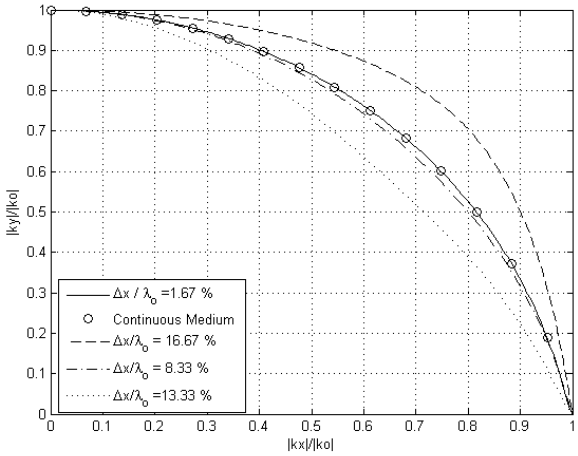

Figure 4. IV, $k_x - k_y$ for different values of Δx in a Debye medium, with $\varepsilon_\infty = 1, \varepsilon_s = 2, \tau_o = 1.667n,\ \omega_o = \pi 10^9 rad/sec$

One can observe in figure 4.IV the convergence of the discrete model to the analytical solution (57.IVb) as the spatial step-size is reduced relatively to the free-space wavelegnth.

4.6.4 Maximum step size in Debye medium

In this experiment, we study the impact of choosing different spatial discretization on the accuracy of the resonant frequencies of a cavity filled by a nonmagnetic Debye medium with permittivity relation (55.IV).

Theoretically, resonant frequencies are calculated by solving the following third-order equation:

$$\omega_r^3 - j\frac{\varepsilon_s}{\varepsilon_\infty \tau_o}\omega_r^2 - \frac{\rho}{\varepsilon_\infty}\omega_r + \frac{j\rho}{\varepsilon_\infty \tau_o} = 0 \tag{58.IV}$$

where ρ is defined as

$$\rho = \pi^2 \left[\left(\frac{m}{a}\right)^2 + \left(\frac{n}{b}\right)^2 + \left(\frac{p}{d}\right)^2 \right] c_o^2 \tag{59.IV}$$

The 3-tuple (m, n, p) represents the mode indices, ω_r is the resonant mode, and c_o is the speed of light in free space.

As expected, results in table 4.IV show that dispersion error is directly proportional to the cell size. However, the lack of an empirical formula for calculating the maximum allowed spatial step size with minimum dispersion shows a huge impact on the simulation process. For instance, the size of the computational domain when $\Delta l = 1.0\, mm$ is eight times larger than using $\Delta l = 2.0\, mm$. It is even more obvious for $\Delta l = 2.0\, mm$ compared to $\Delta l = 0.4\, mm$, for which the memory and simulation time requirements is increased by a factor 125.

Table 4.IV, dispersion error for different spatial discretization: Debye medium $\varepsilon_\infty = 2, \varepsilon_s = 10, \tau_o = 10$ ps

Resonant Mode	Resonant Frequency (GHz)	Relative Error %		
		$\Delta l = 2.0\, mm$	$\Delta l = 1.0\, mm$	$\Delta l = 0.4\, mm$
f_{110}	6.709	0.89	0.18	0.0
f_{111}	8.218	1.41	0.39	0.17
f_{120}	10.615	2.31	0.61	0.05
f_{121}	11.634	2.53	0.64	0.21

The procedure presented in this chapter allows one, to estimate the dispersion error as a function of the chosen Δl. Based on that knowledge, the appropriate spatial step size is chosen for minimum dispersion error. For instance $\Delta l = 1.2\, mm$ corresponds to a maximum dispersion error of 1.0%, for the maximum frequency of 12GHz in the cavity experiment of table 4.IV. If one uses the rule of thumb (47.IV), it is not clear which permittivity to be used $\{\varepsilon_s, \varepsilon_\infty, \varepsilon_r(\omega)\}$, because everyone will lead to different maximum step size $\Delta l = \{1.6\, mm, 1.0\, mm, 0.8\, mm\}$, respectively, which shows some ambiguity in applying (47.IV) for general dispersive media.

4.6.5 Dispersion in Lorentz medium

Now,we consider a nonmagnetic Lorentz medium, with permetivity defined as [2.IV] [16.IV]:

$$\bar{\bar{\varepsilon}}_r(\omega) = \left(\varepsilon_\infty + \frac{(\varepsilon_s - \varepsilon_\infty)\omega_o^2}{\omega_o^2 - \omega^2 + 2j\zeta_e\omega}\right)\bar{\bar{I}}_3 \tag{60.IV}$$

where ω_o is the characteristic resonant frequency of the Loretnz material sample, ζ_e the damping coefficient,ε_s the static value of permittivity and ε_∞ is the value at high frequencies.

In figure 5.IV, the dispersion curves for different values of operating frequency ω are presented where V_{PN} is the numerical phase velocity calculated by the discrete model (44.IV) and V_{PT} is the theoritical phase velocity calculated in continuous medium (6.IV). Each dispersion curve is normalized to its corresponding theortical phase velocity:

$$v_p = \frac{\omega}{\|\vec{k}\|} \tag{61.IV}$$

where the wave number vector $\vec{k}$ is calculated by solving (6.IV) for continuous medium, given by

$$\vec{k} = \frac{\omega}{c_o}\sqrt{\frac{\omega(\omega - 2j\zeta_e)\varepsilon_\infty - \omega_o^2\varepsilon_s}{2j\zeta_e\omega - \omega^2 + \omega_o^2}}\ \vec{a}_k \tag{62.IV}$$

where $\vec{a}_k$ is a unit vector in the direction of propagation. Along the horizontal axis $\Delta l/\lambda_o$, each curve is normalized to its own free space wavelength $\lambda_o = 2\pi\ c_o/\omega$.

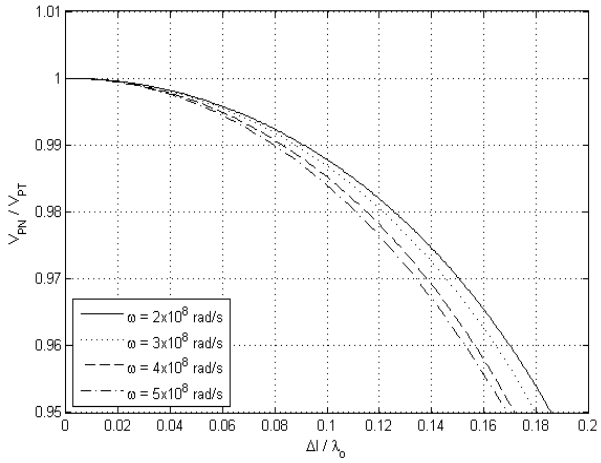

Figure 5. IV, numerical dispersion curves in Lorentz medium along the cell diagonal direction (1,1,1), with parameters, $\varepsilon_s = 2, \varepsilon_\infty = 1,\ \omega_o = 6 \times 10^{\,8}\ rad/s$ and $\zeta_e = 0.167\ \omega_o$

As observed in figure 5.IV, the dispersion characterestics change according the operating frequency ω due to the fact that the material properties are changing too. In this numerical experiment the time step we used is slightly smaller than Δt_{max} (to decrease the number of decimal digits in Δt to speed up the algabraic calculations done by Mathematica). Table 5.IV shows the difference between using (47.IV) as a rough estimation for the maximum spatial step, and using the proposed approach with 1.0 % error criteria.

Table 5.IV,comparison between the rigorous proposed approach and the rule (47.IV) for maximum cell size in terms of memory requirements for the Lorentz medium of the case of figure 5.IV

Frequency $(10^{\,8}\ rad/s)$	$\Delta l/\lambda_o$ Formula (47.IV)	$\Delta l/\lambda_o$ 1.0% Error	Memory saving %
2.0	0.0688	0.0914	234.46 %
3.0	0.0661	0.0871	228.80 %
4.0	0.0617	0.0828	241.68 %
5.0	0.0556	0.0791	287.94 %

It is obvious that using this approach, one can control the level of dispersion to the desired value but with some compromize with the computational requirements. For instance, fixing the maximum level of dispersion to 1.0%, leads to around half the computational effort compared to the rule (47.IV). Note that memory saving is calculated using (56.IV).

4.6.6 Stability in Anisotropic medium

In this example, we chose a rectangular cavity filled by the anisotropic material with diagonal permittivity and premeability tensors, and excited with a modulated-gaussian pulse($t_0 = 200\,\Delta t\,, \sigma = 50\,\Delta t, A = 1000, f_0 = 150\,GHz$). To obtain the maximum time step, we solved (45.IV).

As explainded before, the procedure to obtain Δt_{max}, is to plot the imaginary part of all the roots of (45.IV) vs. Δt for different directions of propagation (1,0,0), (0,1,0), (0,0,1). (1,1,0), (0,1,1), (1,0,1), (1,1,1). Then, among all obtained Δt we select the maximum value beyond which $Im(\omega)$ changes its sign.

Figure 6.IVa shows the simulation at the limit of the maximum time step for which stability can be observed. Any small increment of the time-step brings its value beyond the maximum limit for which instabilities can be observed in the short term as shown in Figure.6IVb

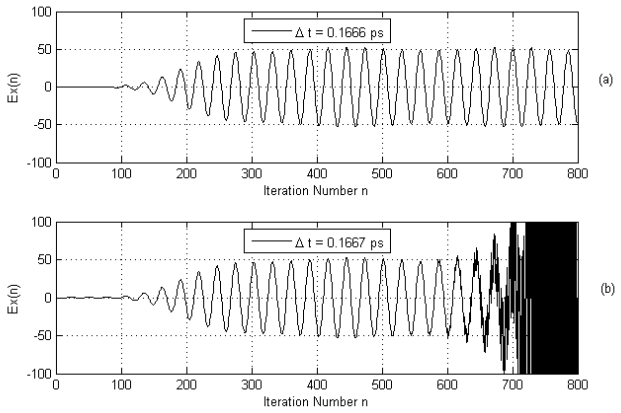

Figure 6.IV, E_x field vs. iteration number, with $\Delta l = 0.1mm$ and $\bar{\bar{\varepsilon}}_r = \bar{\bar{\mu}}_r = diag\{2.0,2.0,1.0\}$ a) at the stability limit. b), for a very small increment of the time step beyond the stability limit.

If one compares with the simple TLM CFL limit in an anisotropic lossless medium with diagonal permittivity and permeability tensors [17.IV]:

$$\Delta t_{Max} = \frac{\sqrt{\min(\varepsilon_i \mu_i)}}{c_o} \sqrt{\frac{4}{3}\left(\left(\frac{1}{\Delta x}\right)^2 + \left(\frac{1}{\Delta y}\right)^2 + \left(\frac{1}{\Delta z}\right)^2\right)} \tag{63.IV}$$

The results of applying (63.IV) perfectly agrees with stability limits calculated using the complex frequency approach presented in the previous section (as illustrated by figure 6.IVa). Note that the resonant mode triggered by the gaussian pulse reaching the steady state can be observed.

4.6.7 Stability in lossy dispersive medium

A similar experiment was carried out for a rectangular cavity filled by a lossy dielectric medium and excited with a modulated-gaussian pulse, where ($t_0 = 200\,\Delta t\,, \sigma = 50\,\Delta t, A = 1000, f_0 = 30\,GHz$).

As shwon in figure 7.IV a, the E_x field inside the cavity, is attenuated after a certain time, due to losses. A point to mention here is that the stabilty is not as sensitive as in the previous example. This is due to medium losses which compensate the growth that comes from the instability. If we exceed Δt_{Max}, for instance by 0.2% as shown in figure 7.IV b, the instability occurs after 500 iterations. However, if we chose a value 10.01 ps which is 0.1% above Δt_{Max}, the instability only appears after several thousands of iterations.

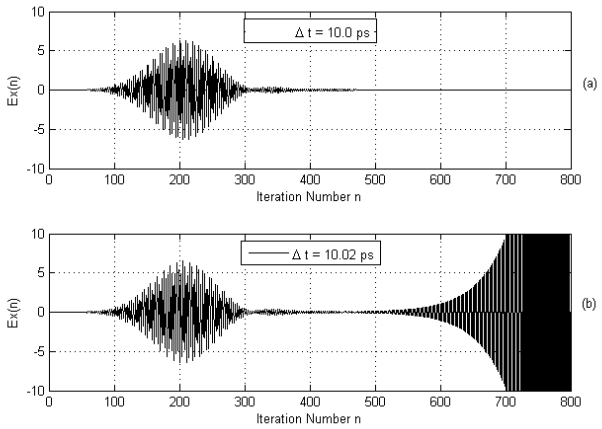

Figure 7. IV, E_x field vs. iteration number, where $\varepsilon_r = 2, \mu_r = 2$, and $\sigma_e = 1.5\ S/m$, for $\Delta l = 3.0mm$, a) At the limit of stability. b) With 0.2% time-step increase beyond the stability limit.

In this numerical experiment, Von-Neumann's approach was applied. We calculated the 18 eigenvalues as a function of Δt for the main directions of propagation (1,0,0), (1,1,0), (1,1,1). Note that since the material is isotropic, there is no need to consider other directions like in the previous example. Then, we found the point Δt_{Max} beyond which the the condition (50.IV) is violated.

4.7 Conclusion

In this chapter we presented a procedure to evaluate dispersion characteristics and stability condition of the TLM-SCN algorithm for general linear media. A similar approach can be applied for FDTD algorithm. It is only necessary to modify the corresponding update equations.

Several examples were presented to show the validity of the proposed procedure. Furthermore, for complex media no formulas are available for evaluating both maximum space and time steps. It is shown that the procedure allows one to select optimum values which leads to an efficient simulation, minimizing both the dispersion error and the computer expenditure. Finally, the procedure described here is valid for any linear, anisotropic, dispersive medium for field compution by the time-domain TLM model.

References

[1.IV] J. D. Jackson, Classical Electrodynamics, JOHN WILEY & SONS, INC., 1999.

[2.IV] A. Taflove and S. C. H. , Computational Electrodaynamics, The Finite-Difference Time-Domain Method, Norwood: Artch House, INC., 2005.

[3.IV] P. B.Johns, "A Symmetrical Condensed Node for the TLM Method," *IEEE Transactions on Microwave Theory and Techniques,* Vols. MTT-35, no. 4, pp. 370-377, 1987.

[4.IV] P. Saguet, Numerical Analysis in Electromagnetics: The TLM Method, Wiley-ISTE, 2012.

[5.IV] J. Paul, C. Christopoulos and D. W. P. Thomas, "Generalized Material Models in TLM- Part I: Materials with Frequency-Dependent Properties," *IEEE Transactions on Antennas and Propagation,* vol. 47, no. 10, pp. 1528-1534, 1999.

[6.IV] J. Paul, C. Christopoulos and D. W. P. Thomas, "Generalized Material Models in TLM- Part 2: Materials with Anisotropic Properties," *IEEE Transactions on Antennas and Propagation,* vol. 47, no. 10, pp. 1535-1542, 1999.

[7.IV] A. L. Farhat, S. L. Maguer, P. Quéffélec and M. Ney, "TLM Extension to Electromagnetic Field Analysis of Anisotropic and Dispersive Media: A Unified Field Equation," *IEEE Transactions on Microwave Theory and Techniques,* vol. 60, no. 8, pp. 2339-2351, 2012.

[8.IV] C. Huber, M. Krumpholz and P. Russer, "Dispersion in aniotropic media modeled by three-dimensional TLM," *IEEE Transactions on Microwave Theory and Techniques,* vol. 43, no. 8, pp. 1923-1934, 1995.

[9.IV] M. Krumpholz and P. Russer, "A field theoretical derivation of TLM," *IEEE Transactions on Microwave Theory and Techniques,* vol. 42, no. 9, pp. 1660-1668, 1994.

[10.IV] P. Russer and M. Krumpholz, "The Hilbert Space Fromulation of the TLM Method," *Interantional Journal of Numerical Modelling: Electronic Networks, Devices and Fields,* vol. 6, pp. 29-45, 1993.

[11.IV] M. Krumpholz and P. Russer, "A generalized method for the calculation of TLM dispersion relations," in *23rd European Microwave Conference,* 1993.

[12.IV] J. S. Nielsen and W. J. R. Hoefer, "Generalized dispersion analysis and spurious modes of 2-D and 3-D TLM formulations," *IEEE Transactions on Microwave Theory and Techniques* , vol. 41, no. 8, pp. 1375-1384, 1993.

[13.IV] L. Landau and E. M. Lifshitz, Electrodynamcis of Continuous Media, Pergamon Press, 1984.

[14.IV] C. Christopoulos, The Transmission-Line Modeling (TLM) Method in Electromagnetics, Arizona: Morgan & Claypool, 2006.

[15.IV] A. R. Luebbers, *et al*, "A Frequency-Dependet Finite-Difference Time-Domain Formulation for Dispersive Materials," *IEEE Transactions on Electromagnetic Compatibility,* vol. 32, no. 3, pp. 222-227, 1990.

[16.IV] Y. H. Ding and E. L. Tan, "Modeling Lorentz dispersive media in FDTD using the exponential time differencing method," in *APMC Asia-Pacific Microwave Conference*, 2008.

[17.IV] S. L. Maguer, "Développements de nouvelles procédures numériques pour la modélisation TLM: Application à la caractérisation de circuits plaqués de structures à symétrie de révolution en bande millimétrique," Thèse, L'Université de Bretagne Occidentale, 1998.

Chapter V
Results, Applications and Discussions

5.1 Introduction

In this chapter, we present and discuss the core results that have been obtained in this thesis. Initially, we started working with a TLM solver developed at the Laboratory Lab-STICC during the last two decades. This TLM solver was designed to handle general geometries, nondispersive media with diagonal tensors and different kinds of boundary conditions. However, that TLM solver was lacking two important features: first, it could not handle general dispersive linear media and, secondly, it lacked a Graphical User Interface (GUI) that renders the simulator impractical to create complex objects with non-Cartesian boundaries. One objective of this project was to add those two important features to the original TLM solver. At the beginning, we implemented the part that enables us to handle anisotropic dispersive media (media with general linear properties). Then, we implemented a GUI in connection with GiD mesher [1.V]. It allows us to construct complicated structures with a user-friendly approach. The contribution was necessary as no dedicated software that could be adapted to our needs, was available.

In the first part of this chapter, we briefly describe the TLM solver and some of its functionalities. Then, we present the GUI alongside with several numerical experiments intended to validate both the TLM-solver and the GUI. Finally, we present numerical experiments including complex media with the rigorous comparison either with analytical or experimental data.

5.2 TLM simulator

As presented in the previous chapters, the TLM algorithm is a time-domain full-wave computational method that is based on the analogy between Maxwell field equations and the circuit theory. So, we need to calculate all voltages and currents in each cell at each time step.

Then, we use correspondence relations to find all electric and magnetic field components. As seen before, this method has several features that we summarize below:

- Accuracy: depends on the spatial discretization.
- Speed: it operates at Δt_{max} and computes all field components at the same location and time. It also computes the tangential component on the cell faces which makes it easy to interface with other methods.
- As a result of the preceding feature, TLM provides better performance than FDTD when dealing with high contrast parameters. This will be detailed in the next chapter
- Memory requirement: it needs to save local physical characteristics of the media like any other method. However, it requires storing at most 18 voltages at each node when the SCN version is used.
- The TLM node is able to deal with anisotropic, dispersive and highly inhomogeneous structures.
- Simple basic algorithm with no complex pre-analytical procedure.

As discussed earlier in chapter III, TLM method is completely local which means that the update equations at any instant of time only depends on the local information inside the cell (besides incident voltages from neighboring cells), whereas in FDTD the update equations in any cell depend also on the media properties in the neighboring cells [2.V]. This implies some averaging that may introduces some error (as we will show in the next chapter). Furthermore, one can estimate the worst case scenario for such averaging for simple media in FDTD but this becomes much more difficult when including anisotropic dispersive media like non-saturated ferrite.

Features of the TLM solver

- It can simulate three-dimensional structures with general geometry (but presently only with staircase approximation of curved boundaries).
- The solver is written for Maxwell's equations in Cartesian coordinate system. However, it can handle general structured irregular Cartesian meshes.

- It can handle any linear media, which includes dispersive, nonhomogeneous, anisotropic, chiral media, and there is an access to every cell in the computational domain.
- The computational domain can be truncated using different kinds of boundary conditions such as perfectly matched layer (PML), perfectly electric (PEC) and magnetic (PMC) conductors, lossy boundary conditions and free space boundary conditions (radiation conditions).
- It is possible to use the PMC and PEC as symmetry or asymmetry planes, respectively, to reduce the computational effort.
- The solver is equipped with functions to show the field values, voltages and currents anywhere inside the computational domain both in time and frequency domain.
- The solver is based on symmetrical condensed node (SCN), which is an important and justifiable choice since both the Hybrid symmetrical condensed (HSCN) and the symmetrical super condensed (SSCN) nodes need voltage reflection coefficient between neighboring cells across interfaces between different media. As a result, when complex dispersive media are involved, elaborated interface processes (including filtering) must take place with HSCN and SSCN [3.V]. On the contrary, the SCN always assumes that the free space is the common medium and media presence is accounted for at the node center only.
- It allows far-field calculations using Kirchhoff's surface integral. This is useful in antenna and scattering problems and, for instance, to obtain the radiation pattern and the radar cross-section (RCS).
- Allows for several types of excitation, such as lumped port, mode template methods and Huygens surface.
- The solver is written using the FORTRAN90 language [4.V], in which we have imported several functions from the NAG computational library. The solver can work both under Windows and Linux operating systems.
- The code is serial; however, it can be parallelized to perform computations of large structures using parallel processor machine.

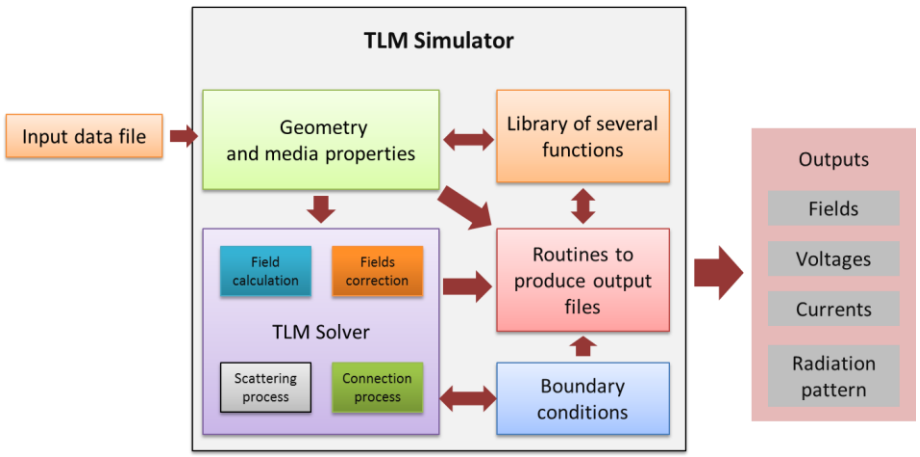

Figure 1.V, block diagram of the TLM simulator

Beside the simulator, we have several post-processing codes, such as S-parameter calculator, scattering field calculator, field distribution displayer…etc. In all post-processing routines, we use the output files from the TLM simulator. Figure 2.V, for instance shows the S-parameter calculator in access ports.

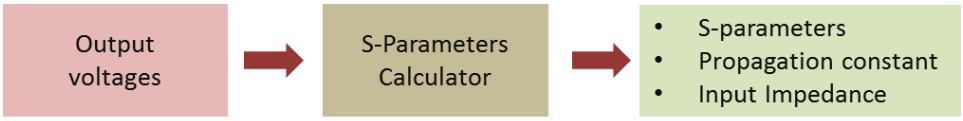

Figure 2.V, block diagram of s-parameters calculation post-process

As a final remark, writing a parallel version of the above program is a relatively easy task. The parallelization process should occur in two main places. First, we should parallelize the input procedure so each machine is responsible of a portion of the computational domain only. The role of this parallelization is to enhance the memory use. Secondly, it is necessary to parallelize the field calculation routines. Hence, each machine calculates fields inside some part of the computational domain, and sends values at the interface to the other machines. This parallelization is to enhance the speed performance [5.V].

5.3 Graphical user interface for the TLM solver (GUI)

We know that complex structures, especially curved ones, are very difficult to describe manually using an electromagnetic solver input file. Also, there is some high probability to make mistakes when defining the geometry in that manner. To overcome this difficulty, we implemented a graphical user interface for the TLM simulator via dedicated software which allows us to enter all input information in a user-friendly manner.

At the beginning we had to select a suitable mesher among different possible candidates, such as GMSH [6.V], Rhinoceros [7.V] and GiD [1.V]. After examining the previously mentioned software, we found that GiD is the most suitable for our objectives. It allows entering any geometry in a user-friendly manner. GiD is programmable, so we can create the output files in the format we like. We can also add several windows to control the configuration parameters of the TLM simulator, the material properties and the excitation. Finally, it was the only one that can produce structured Cartesian three-dimensional grids that is suitable to our solver. Figure 3.V shows two examples of structures that are created and meshed by using GiD.

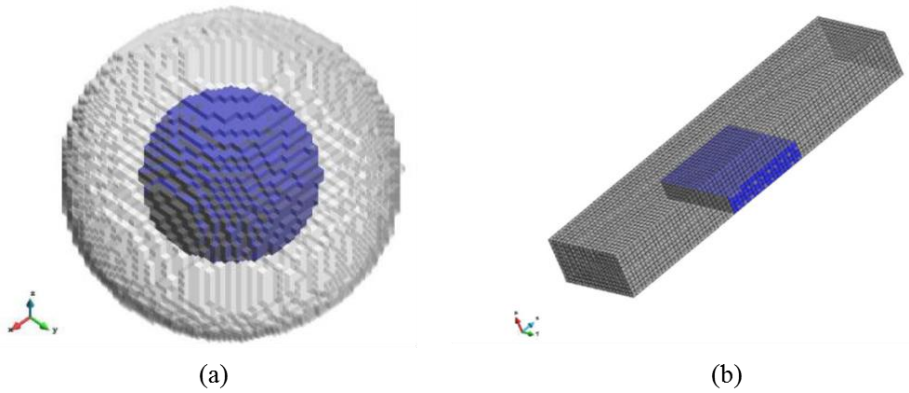

Figure 3.V, meshes creating using GiD, (a) double layered sphere (b) loaded rectangular waveguide

Figure 4.V shows the block diagram of the GiD GUI, in which we see abstractly how it can be used to control all the steps of the computational process, from designing the problem to analyzing the results.

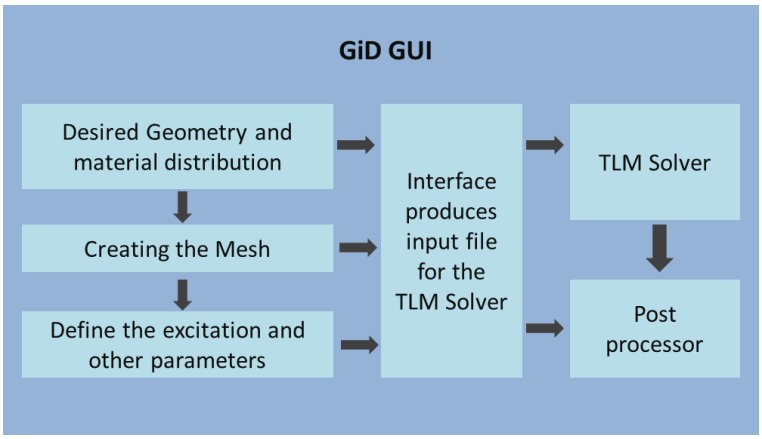

Figure 4.V, GiD graphical user interface structure (GUI)

In figure 5.V we see a flowchart diagram of how GiD operates in more details. The computational process is split into three main steps:

I. Pre-processing

In this step we define all the components of the computational domain which includes

- Drawing the geometry
- Assigning the material properties
- Defining the boundary conditions
- Define the general computational parameters like the time-step and the type of nodes.
- Define the sources, probe points for fields, voltages and currents
- Define the Kirchhoff' window to calculate the far field.

Once all the previous details are defined, we create a Cartesian mesh for the computational domain. Then, GiD (according to a script format, here we use TCL scripting language) produces different input files describing all the details of the computational domain. Finally, another interface code for formatting purposes is written in FORTRAN90. This code combines all these files to create one big file to be input to the TLM solver as shown in figure 1.V and 5.V.

II. Processing

After creating the input file from inside GiD, we can run the TLM solver to perform the simulation process.

III. Post-processing

Once the results are obtained, we can use GiD to visualize them with different appropriate displaying methods and different types of graphs. Note that for more elaborated analysis (for instance, to analyze the scattering parameters of a microwave circuit) additional codes in Matlab, FORTRAN 90 or C languages must be written by the user.

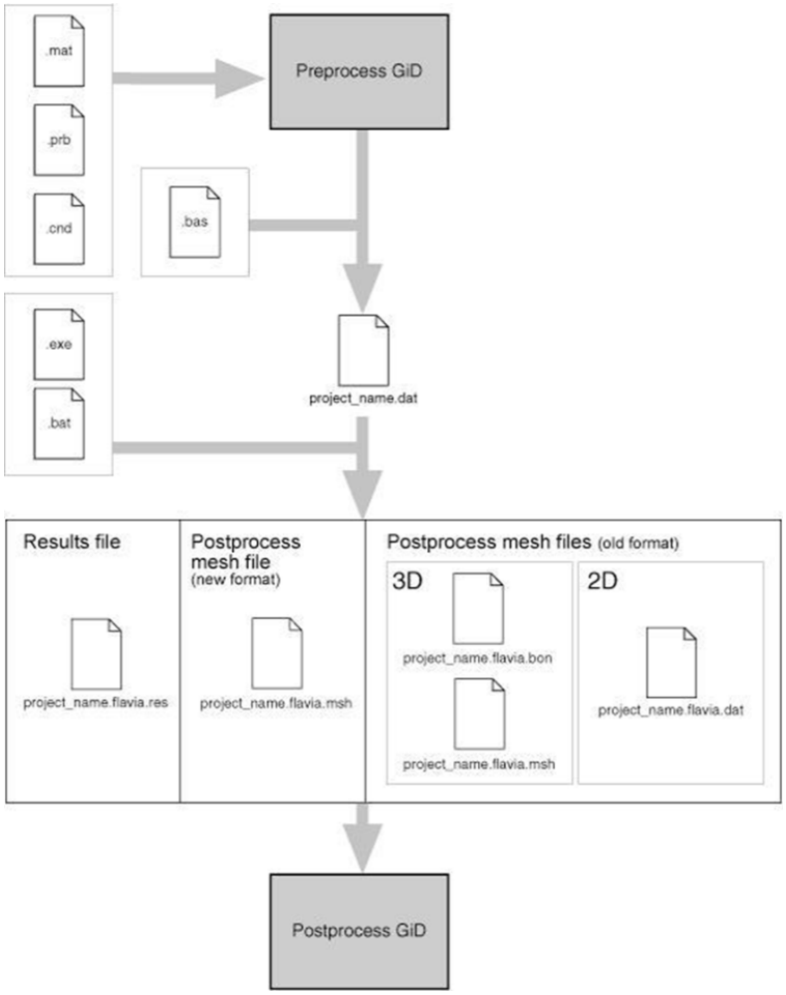

Figure 5.V, organization chart of the complete simulation process carried out by GiD [1.V]

5.4 Experiments including simple media

In this section, we present several numerical experiments. These experiments were created and meshed using the GiD interface. All the following experiments in this section will be used as a punch-mark to validate the TLM simulator as well as the GiD GUI, since all these experiments were created by GiD. The set of experiments includes:

- Scattering by a dielectric sphere, with which we experiment the solver performance in case of non-Cartesian boundaries and the effect of stair-case approximation. Moreover, to test the near-field far-field transformation using Kirchhoff's integral method.
- PML performance in an empty rectangular waveguide. In this experiment, the goal is to study the PML performance for all angles of incidence over a large spectrum of frequencies.
- Waveguide including discontinuities, which is dedicated to study the performance of structured irregular meshing.
- Microstrip patch antenna, were we compared with some measurements and other computational method due the lack of analytical solutions for such structure. This experiment is dedicated to test the solver's and the GUI's performance for some more complicated and non-canonical structure.

Unlike the experiments that will be presented in the next section, all the structures and computational problems presented in this section include only simple media, i.e., linear, nondispersive and isotropic.

5.4.1 Far-field plane wave scattering by dielectric sphere

In this experiment, we study the scattering of a plane wave impinging on a dielectric sphere, the computational domain was created via GiD GUI, and then a TLM simulation was carried out to calculate the scattered field. As shown in figure 6.V, scattered fields are calculated in the far field region at pointing angles $\theta \in [0^o, 180^o]$.

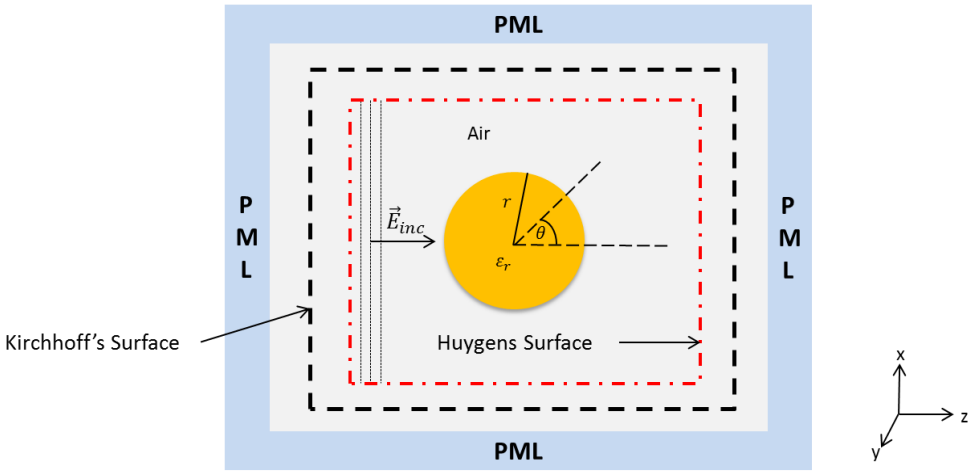

Figure 6.V, dielectric sphere illuminated by a plane wave

To create a plane wave inside the computational domain in TLM method we used Huygens surface excitation as a shown in figure 6.V. Using this kind of excitation has two benefits: firstly, it produces a perfect plane wave. Secondly, it allows us to calculate the scattered fields automatically; indeed, inside the red surface (Huygens surface) we have the total field, whereas outside there is only the field scattered by the sphere [8.V]. Then, to calculate the scattered fields in the far-field zone, we used Kirchhoff's surface integration technique to perform the near-field to far-field transformation. Finally, to absorb the scattered fields and to simulate the open boundaries, we used PML layer of 10-cells thickness for all six faces of the computational domain.

This simulation was repeated twice; in both of them we used cubic cells. In the first simulation we used mesh size of $\Delta l = 10.0$ mm, and for the second simulation we used $\Delta l = 5.0$ mm, that is equivalent to 35 cells/wavelength and 70 cells/wavelength, respectively. This choice of relatively small spatial step-size allows a good geometrical description of the sphere using stair-case approximation as shown in figure 7.V. Moreover, both mesh sizes ensure negligible level of numerical dispersion as expressed by (47.V). In both simulations, CFL maximum time-step was used, namely, 16.66 ps and 8.33 ps, respectively. The radius of the dielectric sphere is 10 cm. For time excitation, we used a modulated-Gaussian signal with parameters $\sigma = 100\Delta t$ and $t_o = 300\,\Delta t$. The simulation was performed for 2000 iterations until the incident and scattered fields practically vanished in the computational domain.

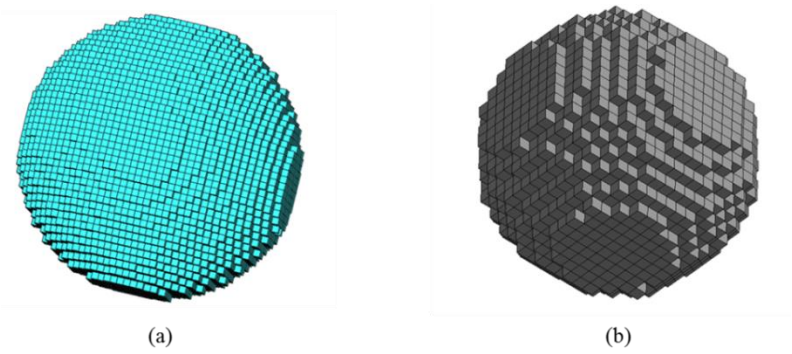

Figure 7.V, dielectric sphere discretized using GiD a) mesh size $\Delta l = 5.0$ mm, b) mesh size $\Delta l = 10.0$ mm

In figure 8.V we see the scattering profile as a function of the angle θ at a distance of R=100.0 meter from the center of the dielectric sphere. That distance is equivalent to 166.7 wavelengths at frequency of 500MHz.

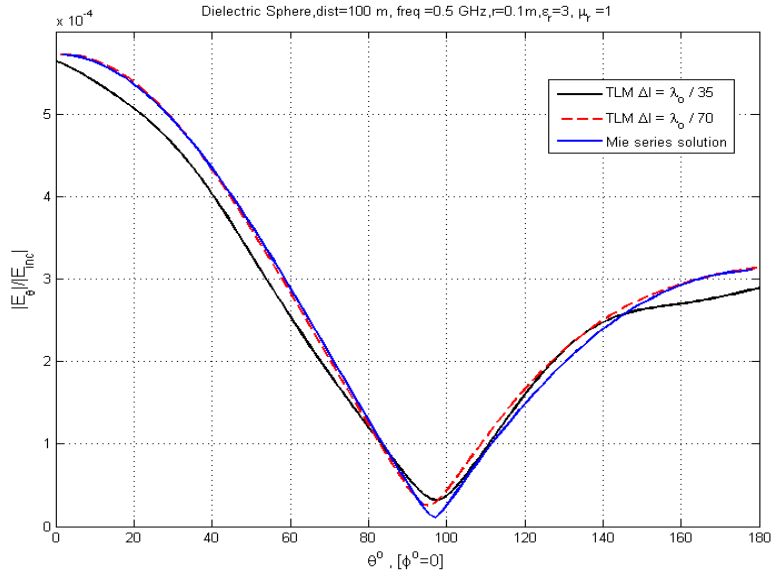

Figure 8.V, dielectric sphere normalized scattered electric field vs. angle θ in the far-field region

The results obtained using TLM are in good agreement with the analytical solution obtained by Mie series approximation [9.V] [10.V]. As expected, we obtain a closer solution to the analytical one as we decreased the mesh size. Hence, one can explain the discrepancy between the analytical solution and the simulation, due to the stair-case approximation effect.

5.4.2 Rectangular waveguide with discontinuity

In this experiment, we want to determine the mode cutoff frequencies of the ridged waveguide whose cross section is shown in figure 9.V. To find those frequencies, we considered a waveguide of one Δl length in the longitudinal direction terminated by PEC's. As a result, we obtain a resonator of length Δl and the first resonances will correspond to the mode cutoff frequencies that occur in the transverse plane only, with a good accuracy. This approximation no longer applies to very higher-order modes. The objectives of this experiment is to test the TLM solver for structured irregular meshes and to show the benefits of such meshing when fine details require mesh refinement in the computational domain.

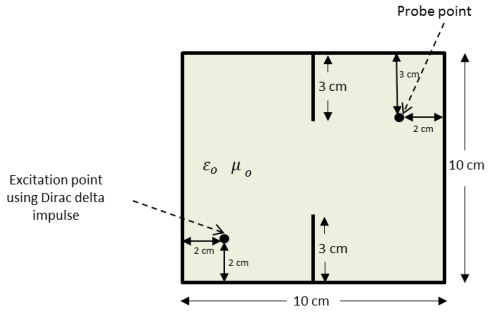

Figure 9.V, cross section of the ridged rectangular waveguide

In figure 10.V (a,b, and c) we can see the different meshes that we used to discretize the computational domain presented in figure 9.V. In figure 10.Va, a coarse mesh of around 14 cells per wavelength was used, while in figure 10.V c, a very fine mesh of around 42 cells per wavelength was used. In figure 10.Vb, we can see a structured irregular mesh, in which we used fine mesh only around the discontinuities.

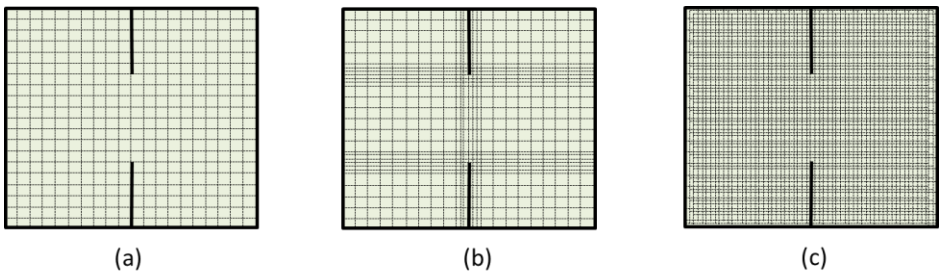

Figure 10.V, cross section of rectangular waveguide (a) uniform coarse mesh (b) nonuiform mesh (c) fine mesh

Table 1.V shows the different mesh parameters used in figure 10.V (a, b and c). In all three experiments we used delta function for excitation. And the simulations were performed for 30000 iterations.

Table 1.V, mesh and time step properties for the case of figure 10.V

	Mesh properties	Time step	Computational domain size
Mesh (a)	$\Delta x = \Delta y = 5\ mm = \frac{\lambda_o}{14}$	$\Delta t = 8.333\ ps$	400 cells
mesh (b)	$\Delta x = \Delta y = 5\ mm$ in the sparse region, and $\Delta x = \Delta y = 1.667\ mm$ in the dense region	$\Delta t = 1.389\ ps$	1008 cells
mesh (c)	$\Delta x = \Delta y = 1.667\ cm = \frac{\lambda_o}{42}$	$\Delta t = 2.77\ ps$	3600 cells

In table 2.V, we can see resonant frequencies obtained by using different meshes. Due to the lake of analytical solution, we used the results of mesh (c) as a reference since it is very fine (42 cells per wavelength).

Table 2.V, comparison of the performances of different meshes

Resonant Mode	Mesh (figure 10.Va)		Mesh (figure 10.Va b)		Mesh (figure 10.Va c) (Reference)
	Resonant frequency(GHz)	% Relative difference	Resonant frequency(GHz)	% Relative difference	Resonant frequency(GHz)
dominant mode	2.671	1.657%	2.725	0.331 %	2.716
second mode	3.419	1.605%	3.378	0.386 %	3.365
third mode	4.018	2.031 %	4.131	0.438 %	4.113
fourth mode	4.433	3.599 %	4.302	0.538 %	4.279

As we can observe, non-uniform meshing can dramatically reduce the computational cost and in the same time maintains an acceptable level of accuracy (less than 1%). One can notice in

table 1.V, that the memory gain when using the irregular meshing as in figure 10.Vb is around 357% compared to using the fine meshing of figure 10.Vc, and the time gain is around 178.6%. Note that the time gain is calculated using:

$$\text{time gain} = \frac{\Delta t\ non\ uniform\ meshing}{\Delta t\ uniform\ meshing}\left(\frac{number\ of\ cells\ in\ nonuniform\ meshing}{number\ of\ cells\ in\ fine\ uniform\ meshing}\right) \quad (1.V)$$

5.4.3 PML performance in an empty rectangular waveguide

In this experiment we calculate the back-to-back reflection coefficient of the PML layer in an empty wave guide as shown in figure 11.V. This experiment is the best suited for testing any ABC's as the TE_{10}-mode propagation can be seen as plane waves impinging with different incident angles on the PML interface when the frequency signal is changed.

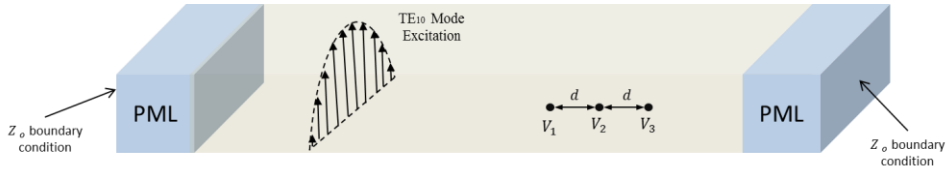

Figure 11.V, WR90 waveguide of dimensions 10.16 mm x 22.86 mm matched from both sides by a PML ABC

The computational domain was discretized using a uniform mesh of cubic cells of dimension $\Delta x = 1.27\ mm$, with a total size of 200 by 18 by 8 cells. The time step we used is $\Delta t = 2.11\ ps$. For time excitation, we applied a TE_{10} mode template at a distance 25.4 mm (20 cells), to ensure a single mode propagation inside the waveguide. The signal waveform we used was a modulated-Gaussian pulse with parameters $f_o = 10\ GHz, \sigma = 30\ \Delta t$ and $t_o = 300\Delta t$. Finally, the detection points are separated from the excitation plane by distances 16.51 cm, 171.45 cm and 17.78 cm, respectively.

The next step is to apply the post-processing technique presented in chapter III to calculate the reflection coefficient, in which we solve the transmission-line equations based on the knowledge of the voltages at three different points. Moreover, since there are two PML

layers at both ends of the waveguide, the actual value of the reflection coefficient will be half (-3dB) the one produced by the back-to-back configuration.

Figure 12.V shows the reflection coefficent for different PML layer widths. As we can see, a PML layer of 15 cells width gives better perfomance than a 10-cells width but at the cost of more computations in the PML layer. However after some simulated experiments, 15 cells only produces similar results than using a PML width of 20 cells. Results were obtain with 80000 iterations. Matched impedance boundary condition were used to terminate the PML layer to further decrease reflections due to PML layer truncation.

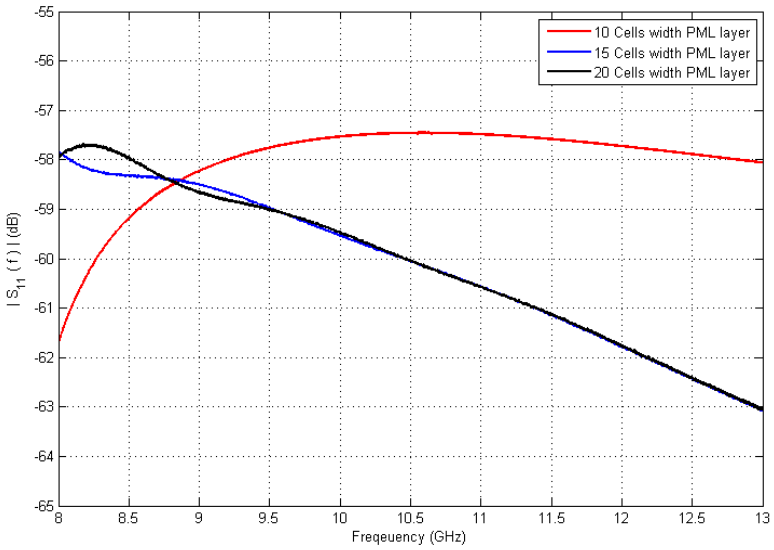

Figure 12.V, reflection coefficient vs. frequency for different PML layer of parabolic profile with $\sigma_{max} = 4.33\ S/M$, $\sigma_{max} = 2.885\ S/m$ and $\sigma_{max} = 2.164\ S/m$ for 10 cells, 15 cells, and 20 cells thickness PML layers, respectively.

We repeated this experiment again but, this time, we used simple PEC and PMC boundary conditions to terminate the PML layer. We observed some unstability after 30000 iterations. However, 30000 iterations were not sufficient to obtain smooth curves as in figure 12.V.

5.4.4 Microstrip-line fed rectangular patch antenna

The actual dimensions and other details of the microstrip antenna that we used in this experiment are shown in figure 13.V. The simulation of this antenna involves a direct use of the TLM algorithm with PML boundary conditions (10-cells width from all sides except the ground plane) to simulate the outer free space. To model the dimensions as accurately as possible we used $\Delta x = 0.40$ mm, $\Delta y = 0.389$ mm and $\Delta z = 0.296$ mm. Consequently, the maximum time step was 0.424 ps. The maximum spatial size is justified because it respects the negligible numerical dispersion criteria since the chosen value is $\Delta x \approx \lambda_g/25$ for the maximum frequency (20 GHz). This value is a good compromise between negligible numerical dispersion and accurate geometrical quantization to minimize the quantization error effects due to the use of parallelepipedic cells. The length of the microstrip-line used to feed the patch antenna is 50 Δx from the PML layer to the rectangular patch. The source was placed a 10 Δx from the side of the PML or 40 Δx from the patch. We used a modulated-Gaussian pulse of half-width of 15 ps, and time delay of 45 ps with a center frequency of 7.5 GHZ. Due to the resonant behavior of the structure the simulation was required 10000 iterations.

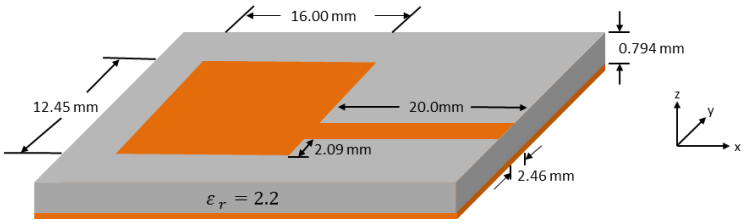

Figure 13.V, microstrip-line fed rectangular patch antenna detail [11.V]

The reflection coefficient S_{11} is shown in figure 14.V and some good agreement can be observed with both the FDTD simulation results and measured data [11.V]. The operating first resonance is 7.5 GHz which is almost exactly obtained by both numerical techniques and measurements. The other resonances are also in good match with both FDTD and measurements; however, there are small discrepancies which can be explained by the geometry quantization error (which occurs when using a coarse mesh that implies slightly different dimensions from the real structure). One should highlight here that we wanted to use the same meshing as in the reference paper [11.V] for comparison purposes and thus, kept the same quantization error.

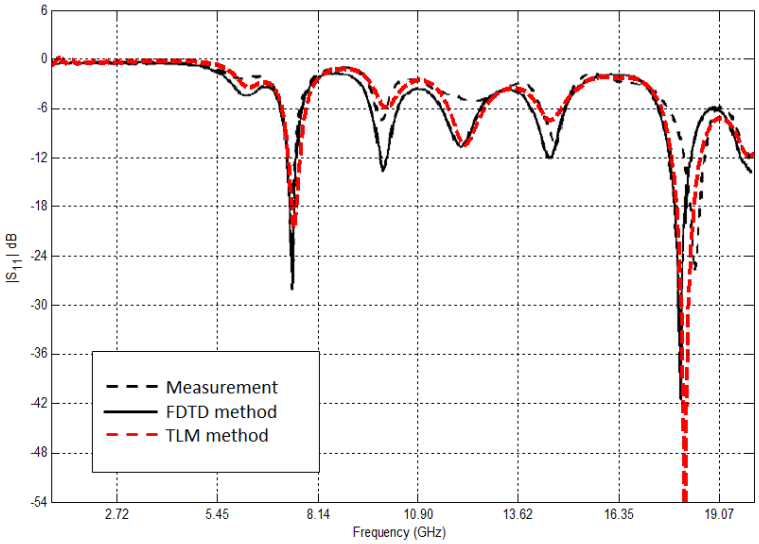

Figure 14.V, reflection coefficient of the rectangular patch antenna of figure 13.V

For calculating the reflection coefficient, we recorded the voltage values at three points on the microstrip-line at distances $25\Delta x$, $30\Delta x$, $35\Delta x$, where we located the source at a distance of 10 Δx from the PML layer. Then we applied the technique presented in chapter III, section 13.

5.5 Experiments involving complex media.

After testing and validating the TLM solver in previous section, we can make a step further to use it for structures including complex media. In this section, we present several experiments that validate the TLM solver for problems involving anisotropic and dispersive media.

First of all, we perform some comparisons with canonical examples. This includes, cavities filled by anisotropic or dispersive media, plane-wave scattering by a chiral sphere, and some experiments involving transformation optics (TO). After validating the solver for complex media, we present an example that involves a waveguide loaded by non-saturated ferrite material. The ferrite sample is fully nonhomogeneous, anisotropic and dispersive.

One point to mention here is that the objective of performing the following experiments is to show the correctness of the simulator. Hence, for all experiments we used fine meshes to

minimize the dispersion. However, to estimate the appropriate values of mesh size we used empirical formula such as (47.IV) presented in the previous chapter. Note that for computer cost optimization, dispersion studies described in chapter IV should rather be performed.

5.5.1 Rectangular resonators filled by anisotropic/dispersive media

I. Resonator filled by anisotropic media

In this experiment we compute resonant frequencies for a PEC rectangular resonator filled by an anisotropic material as shown in figure 15.V.

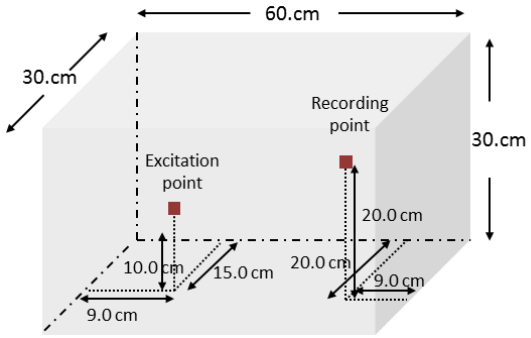

Figure 15.V, rectangular resonator filled by an anisotropic medium.

The anisotropic media constitutive parameters that we used in this numerical experiment are:

$$\varepsilon_r = \begin{pmatrix} 8 & 0 & 0 \\ 0 & 2 & 0 \\ 0 & 0 & 2 \end{pmatrix} \quad ; \quad \mu_r = \begin{pmatrix} 8 & 0 & 0 \\ 0 & 2 & 0 \\ 0 & 0 & 2 \end{pmatrix} \tag{2.V}$$

To obtain a negligible level of numerical dispersion, we used uniform mesh of cubic cells with size $\Delta l = 1\ cm$. This value ensures less than 1.0% error due to the numerical dispersion as discussed in chapter IV. Consequently, the corresponding time step is $\Delta t = 8.33\ ps$. For time excitation, we used a delta function to excite all modes. Note that, one could also use Gaussian pulse with appropriate bandwidth to cover the useful output spectrum.

Table 3.V, shows a comparison between analytical and simulated results for resonant frequency of a resonator filled with the anisotropic material described above.

Table 3.V, resonant frequencies of the rectangular cavity shown in figure 20.V

Modes	Simulation results	Analytical results	Relative error %
$\mathbf{f_{110}}$	176.8 MHz	176.78 MHz	0.011
$\mathbf{f_{111}}$	216.6 MHz	216.51 MHZ	0.041
$\mathbf{f_{102}}$	280.1 MHz	279.51 MHz	0.211
$\mathbf{f_{112}}$	306.7 MHz	306.19 MHz	0.166

As we can see, results generated by the TLM model are very accurate. This is due to the fact that we used small spatial step size (according to 47.IV). The choice of fine mesh size minimizes the effect of numerical dispersion, which is the main source of error in this experiment. Furthermore, we used the cell size to fit exactly the resonators dimensions to avoid geometry quantization errors.

II. Rectangular resonator filled by lossy/dispersive dielectric

In this experiment we calculate the quality factor of a rectangular resonator filled by lossy dispersive media. The quality factor in table 4.V is shown for different values of filling media conductivity σ. The process of computing the quality factor in numerical experiment includes two steps: firstly, to find the desired resonance frequency f_o and then, to measure the -3dB bandwidth Δf around f_o. Finally, the quality factor is defined as:

$$Q = f_o/\Delta f \tag{3.V}$$

In the simulation, we used regular mesh with cubic cells. For a negligible level of numerical dispersion we used the cell size to be $\Delta l = 10mm$, which is around to 25 cells per wavelength in the medium (according to 47.IV). The corresponding time step is $\Delta t = 8.33\, ps$ and 50000 iterations were performed. The time excitation was a delta (Dirac) function.

Table 4.V shows a good matching between analytical and simulation results. One can also observe that the quality factor of the cavity increases as the losses σ decreases.

Table 4.V, Quality factor of a cubic cavity of side length =30 cm, filled by dispersive media

ε_r=4.0, μ_r=1.0, $tan(\delta) = \sigma/(\omega_o \varepsilon_r \varepsilon_o)$, ω_o, for different σ.

Conductivity σ (S/m)	$Q = f_o/\Delta f$ (Simulation)	$Q = 1/\tan(\delta)$ (Analytical)	Relative Error in Quality factor calculation
0.004	18.6	19.1	2.62 %
0.003	25.97	25.42	2.16 %
0.002	38.52	38.12	1.05%
0.001	76.18	76.25	0.09%

One can also notice that, as the conductivity σ decreases the relative error between the analytical and simulation results decreases too. This can be explained by the fact that the increase of media conductivity for the same mesh size increases the numerical dispersion.

5.5.2 Near-field scattering by chiral sphere

In this experiment that exploits the TLM scheme presented in chapter III and chapter IV, we study the plane-wave scattering by a chiral sphere and make a comparison with Mie series analytical solution [9.V]. As we discussed in chapter II, chiral material is a medium in which the electric field may also couple with magnetization and magnetic field with electric polarization. In such media the constitutive parameters can be written in the frequency domain (chapter II) as [12.V]:

$$\kappa(\omega) = \frac{\tau\omega_o^2\omega}{\omega_o^2 - \omega^2 + j2\omega_o\xi\omega} \tag{18.IIa}$$

$$\varepsilon(\omega) = \varepsilon_o\varepsilon_\infty + \frac{(\varepsilon_s - \varepsilon_\infty)\varepsilon_o\omega_{oe}^2}{\omega_{oe}^2 - \omega^2 + j2\omega_{oe}^2\xi_e\omega} \tag{18.IIb}$$

$$\mu(\omega) = \mu_o\mu_\infty + \frac{(\mu_s - \mu_\infty)\mu_o\omega_{om}^2}{\omega_{om}^2 - \omega^2 + j2\omega_{om}^2\xi_m\omega} \tag{18.IIc}$$

We chose a chiral sphere of radius 10 cm and the chiral medium described by the dispersive equations (18.II) such that, at the frequency of 0.5 GHz, the values are $\varepsilon_r = 4.0, \mu_r =$

$2.0, \kappa = 0.0314$. Cubic cells, each with size of $1.0\ cm$ (since the chirality factor κ is relatively small), were used according to (47.IV) to obtain negligible numerical dispersion. The corresponding time step is $\Delta t = 16.60\ ps$ and 2000 total iterations were performed. Finally, for time excitation, we applied a modulated-Gaussian pulse signal with center frequency of 0.5 GHz and $\sigma = 100.0\Delta t$ and $t_o = 300.0\Delta t$. The scattered field values were recorded at a distance of 30.0 cm from the center of the sphere. Figure 16.V shows a comparison between TLM simulation and Mie series analytical solution [9. V]. As we can see, there is some good agreement between the analytical solution and TLM simulation curves.

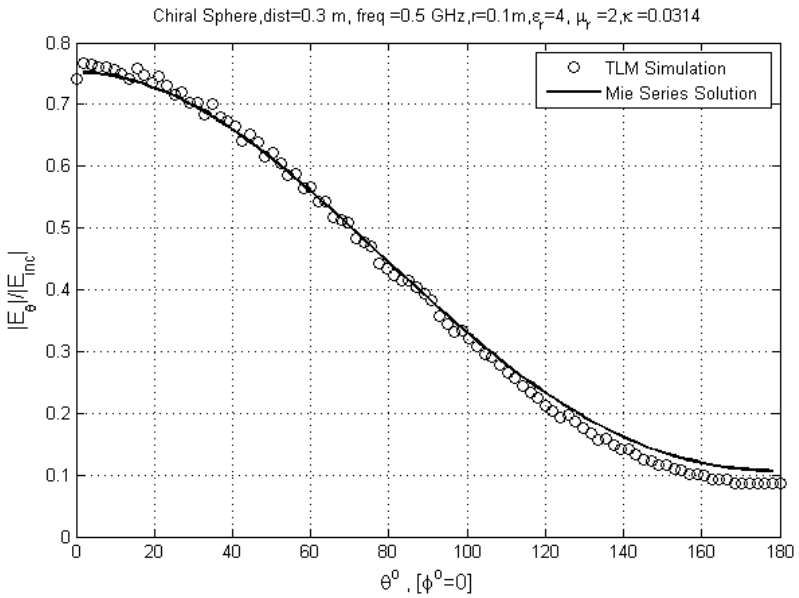

Figure 16.V, near-field scattering by chiral sphere of radius 10 cm, a comparison between simulated result and Mie series analytical solution.

As observed in figure 16.V, the small random ripples that appear in the TLM curve can be explained by the stair-case approximation of the computational domain position and the sphere (see figure 7.Vb). One can also notice that the relatively smooth curve of the simulated results can be explained by the fact that we chose a small sphere in comparison to the wavelength of the incident plane wave ($r = \lambda_o/6$).

5.5.3 Transformation optics (TO)

As presented in chapter III, transformation optics [13.V] [14.V] provides mathematical tools to study the same computational problem in different coordinate systems. As mentioned, any change in the coordinate system will directly reflect on the media properties inside the computational domain. In the next three experiments, we use the TO principle to transform simple media of the original computational domain into complex media in the transformed computational domain. This provides analytical solutions for some computational problems involving complex media (because we know the analytical solution for the simple media case); it is an interesting way to accurately evaluate the TLM solver (or any other method) for complex media.

I. Shrinking a dielectric slab in a parallel plate waveguide

In this first experiment shown in figure (17.Va) and (17.Vb), we compute the reflection and transmission coefficients from a lossless dielectric slab in a parallel-plate waveguide. In both cases, dielectric slab was excited by a TEM plane wave. To obtain a perfect plane wave, the computational domain was terminated by two parallel PEC walls at the top and bottom and two parallel PMC walls at both sides. This will ensure a TEM mode of propagation and generate a one-dimensional electromagnetic problem.

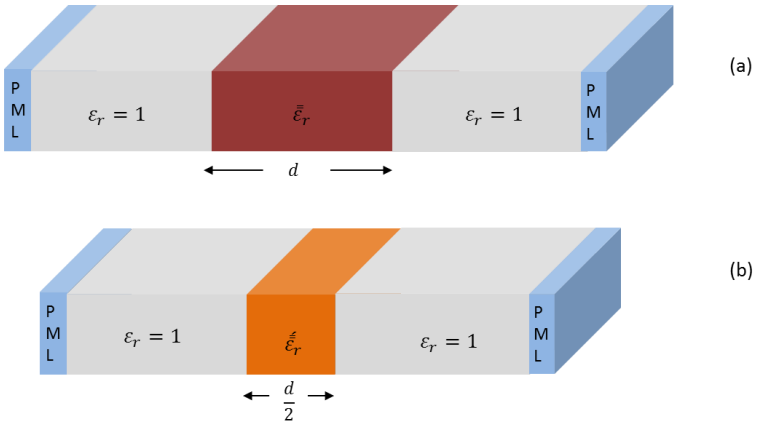

Figure 17.V, scattering problem in parallel plate waveguide, (a) original computational domain with simple media , (b) transformed computational domain with complex media

In the first scenario, we performed a numerical experiment with a simple nonmagnetic dielectric layer of permittivity $\bar{\bar{\varepsilon}}_r = 10.0\ \bar{\bar{I}}_3$ and thickness $d = 10.0\,cm$ (figure 17.Va). Then, we applied the TO coordinate transformation in which we shrink only the dielectric layer to $d/2 = 5.0$ cm (figure 16.Vb). This results in a new problem in which the dielectric layer has permittivity and permeability given by:

$$\bar{\bar{\varepsilon}}_r = \begin{pmatrix} 20 & 0 & 0 \\ 0 & 20 & 0 \\ 0 & 0 & 5 \end{pmatrix} \quad ; \quad \bar{\bar{\mu}}_r = \begin{pmatrix} 2 & 0 & 0 \\ 0 & 2 & 0 \\ 0 & 0 & 1/2 \end{pmatrix} \tag{4.V}$$

In this numerical experiment we used regular mesh of cubic cells. To maintain a negligible level of numerical dispersion, we used the cell size to be $\Delta l = 5\,mm$, which is equivalent to 27 cells per wavelength in the isotropic medium of the original domain before transformation. Consequently, the time step we used is $\Delta t = 4.0\,ps$. The time excitation was a modulated Gaussian pulse at center frequency $f_o = 0.5\,GHz$ and parameters $\sigma = 30\Delta t$ and $t_o = 300\Delta t$. The experiment was performed for 9000 iterations until all fields vanished in the computational domain.

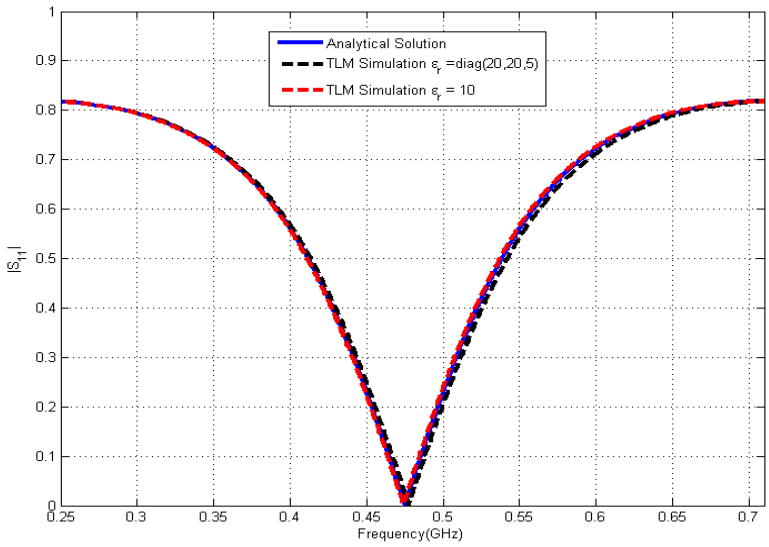

Figure 18.V, reflection coefficient: a comparison between analytical solution and TLM algorithm for both original computational domain and transformed domain

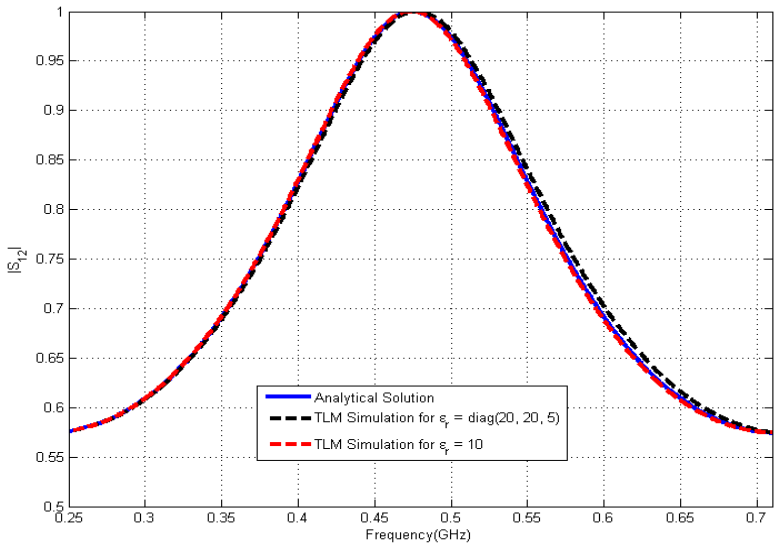

Figure 19.V, transmission coefficient: a comparison between analytical solution and TLM algorithm for both original domain and transformed computational domain

Figures 18.V and 19.V show the reflection and transmission coefficients, respectively over the frequency range from 250 to 700 MHz. As expected, we can see some good agreement between both TLM simulations (the original and transformed domain) and the analytical solution:

$$S_{11} = \frac{Z_{in} - Z_o}{Z_{in} + Z_o} \tag{5.Va}$$

$$Z_{in} = Z_o \sqrt{\frac{\mu_r}{\varepsilon_r}} \left(\frac{1 + \sqrt{\frac{\mu_r}{\varepsilon_r}} j tan(\beta d)}{\sqrt{\frac{\mu_r}{\varepsilon_r}} + j tan(\beta d)} \right) \tag{5.Vb}$$

where, Z_o is the free-space wave impedance and μ_r and ε_r are the relative permeability and permittivity of the dielectric slab in the original domain (figure 17.Va), respectively, β is the wave number inside the isotropic dielectric slab, and d is the thickness of the dielectric slab shown in figure 17.Va.

We can notice that the results obtained in the transformed domain have some higher (but still very small) discrepancy with the analytical solution than the results obtained in the original domain. This observation is expected since we used the same cell size for both original and transformed domains. In fact, the anisotropic media (as we discussed in chapter IV) generates higher dispersion characteristics than isotropic media. Finally, one can conclude that these results

validate the solver correctness and functionality for media having diagonal tensors constitutive parameters. They also validate the approach using TO.

II. Rotation of a PEC cylindrical cavity

In this example, we exploit the TO concept to create an example of a structure that uses anisotropic media with non-diagonal tensor. The analytical solution of this example is already known and will be used for comparisons with numerical results obtained by the TLM solver.

Consider a PEC cylindrical cavity of radius 18 mm and height of 6 mm filled by an anisotropic medium defined by the following constitutive parameters:

$$\bar{\bar{\varepsilon}}_r = \begin{pmatrix} \varepsilon_x & 0 & 0 \\ 0 & \varepsilon_y & 0 \\ 0 & 0 & \varepsilon_z \end{pmatrix} \quad ; \quad \bar{\bar{\mu}}_r = \begin{pmatrix} \mu_x & 0 & 0 \\ 0 & \mu_y & 0 \\ 0 & 0 & \mu_z \end{pmatrix} \tag{6.V}$$

Now, one applies the following coordinate transformation (rotation around the z-axis):

$$\begin{pmatrix} x' \\ y' \\ z' \end{pmatrix} = \begin{pmatrix} \cos(\phi) & -\sin(\phi) & 0 \\ \sin(\phi) & \cos(\phi) & 0 \\ 0 & 0 & 1 \end{pmatrix} \begin{pmatrix} x \\ y \\ z \end{pmatrix} \tag{7.V}$$

According to the rules of TO discussed in chapter II, we can obtain the permittivity and permeability expression in the new coordinate system:

$$\bar{\bar{\varepsilon}} = \begin{pmatrix} \cos^2(\phi)\varepsilon_x + \sin^2(\phi)\varepsilon_y & \sin(\phi)\cos(\phi)\varepsilon_y - \sin(\phi)\cos(\phi)\varepsilon_x & 0 \\ \sin(\phi)\cos(\phi)\varepsilon_y - \sin(\phi)\cos(\phi)\varepsilon_x & \sin^2(\phi)\varepsilon_x + \cos^2(\phi)\varepsilon_y & 0 \\ 0 & 0 & \varepsilon_z \end{pmatrix} \tag{8.Va}$$

$$\bar{\bar{\mu}} = \begin{pmatrix} \cos^2(\phi)\mu_x + \sin^2(\phi)\mu_y & \sin(\phi)\cos(\phi)\mu_y - \sin(\phi)\cos(\phi)\mu_x & 0 \\ \sin(\phi)\cos(\phi)\mu_y - \sin(\phi)\cos(\phi)\mu_x & \sin^2(\phi)\mu_x + \cos^2(\phi)\mu_y & 0 \\ 0 & 0 & \mu_z \end{pmatrix} \tag{8.Vb}$$

In reality, nothing has changed (just rotating the cylinder around its axis). However, if one looks from the new coordinate system perspective, it is possible to use the new material properties (8.Va) and (8.Vb) and maintain the same geometry (because of its invariance with the ϕ angle). The correction matrix $\bar{\bar{\Gamma}}(s)$ in s-domain that will be used in the TLM algorithm is:

$$\bar{\bar{\Gamma}}(s) = \begin{pmatrix} \bar{\bar{\Sigma}}_\varepsilon & \bar{\bar{0}} \\ \bar{\bar{0}} & \bar{\bar{\Sigma}}_\mu \end{pmatrix} \tag{9.Va}$$

where, $\bar{\bar{0}}$ is a 3x3 null matrix, and $\bar{\bar{\Sigma}}_\varepsilon$, $\bar{\bar{\Sigma}}_\mu$ are defined as follows:

$$\bar{\bar{\Sigma}}_\varepsilon = \begin{pmatrix} \frac{s\sin^2(\phi)\varepsilon_x + s\cos^2(\phi)\varepsilon_y - s + 1}{(s\varepsilon_x - s + 1)(s\varepsilon_y - s + 1)} & \frac{s\sin(\phi)\cos(\phi)(\varepsilon_x - \varepsilon_y)}{(s\varepsilon_x - s + 1)(s\varepsilon_y - s + 1)} & 0 \\ \frac{s\sin(\phi)\cos(\phi)(\varepsilon_x - \varepsilon_y)}{(s\varepsilon_x - s + 1)(s\varepsilon_y - s + 1)} & \frac{s\cos^2(\phi)\varepsilon_x + s\sin^2(\phi)\varepsilon_y - s + 1}{(s\varepsilon_x - s + 1)(s\varepsilon_y - s + 1)} & 0 \\ 0 & 0 & \frac{1}{s(\varepsilon_z - 1) + 1} \end{pmatrix} \tag{9.Vb}$$

$$\bar{\bar{\Sigma}}_\mu = \begin{pmatrix} \frac{s\sin^2(\phi)\mu_x + s\cos^2(\phi)\mu_y - s + 1}{(s\mu_x - s + 1)(s\mu_y - s + 1)} & \frac{s\sin(\phi)\cos(\phi)(\mu_x - \mu_y)}{(s\mu_x - s + 1)(s\mu_y - s + 1)} & 0 \\ \frac{s\sin(\phi)\cos(\phi)(\mu_x - \mu_y)}{(s\mu_x - s + 1)(s\mu_y - s + 1)} & \frac{s\cos^2(\phi)\mu_x + s\sin^2(\phi)\mu_y - s + 1}{(s\mu_x - s + 1)(s\mu_y - s + 1)} & 0 \\ 0 & 0 & \frac{1}{s(\mu_z - 1) + 1} \end{pmatrix} \tag{9.Vc}$$

The correction matrix (9.Va) will be used to construct the correction matrix in z-domain for any specific rotation angle ϕ. As an example, let us assume that the cylindrical cavity is filled by an anisotropic medium with the following properties:

$$\bar{\bar{\varepsilon}}_r = \begin{pmatrix} 3 & 0 & 0 \\ 0 & 1 & 0 \\ 0 & 0 & 2 \end{pmatrix} \quad ; \quad \bar{\bar{\mu}}_r = \begin{pmatrix} 3 & 0 & 0 \\ 0 & 1 & 0 \\ 0 & 0 & 2 \end{pmatrix} \tag{10.Va}$$

By applying the rotation transformation with $\phi = \frac{\pi}{4}$ the permeability and permittivity tensors become:

$$\bar{\bar{\varepsilon}}'_r = \begin{pmatrix} 2 & 1 & 0 \\ 1 & 2 & 0 \\ 0 & 0 & 2 \end{pmatrix} \quad ; \quad \bar{\bar{\mu}}'_r = \begin{pmatrix} 2 & 1 & 0 \\ 1 & 2 & 0 \\ 0 & 0 & 2 \end{pmatrix} \tag{10.Vb}$$

From (9.V), the corresponding correction matrix in z-domain is given by

$$\bar{\bar{\Gamma}}(z) = \begin{pmatrix} \frac{2z}{1+3z} & -\frac{1+z}{1+3z} & 0 & 0 & 0 & 0 \\ -\frac{1+z}{1+3z} & \frac{2z}{1+3z} & 0 & 0 & 0 & 0 \\ 0 & 0 & \frac{-1+z}{2z} & 0 & 0 & 0 \\ 0 & 0 & 0 & \frac{2z}{1+3z} & -\frac{1+z}{1+3z} & 0 \\ 0 & 0 & 0 & -\frac{1+z}{1+3z} & \frac{2z}{1+3z} & 0 \\ 0 & 0 & 0 & 0 & 0 & \frac{-1+z}{2z} \end{pmatrix} \tag{11.V}$$

In this experiment, we used a regular mesh with cubic cells. To maintain a negligible level of numerical dispersion, we used the cell size $\Delta l = 0.3\, mm$ which provides a sufficiently fine discretization to minimize the stair-case effect. It is also sufficient to maintain a negligible level of dispersion according to (47.IV). Consequently, the time step used was $\Delta t = 0.5\, ps$, and the cylinder was limited by PEC. For time excitation, one applied a delta function and we run the experiment for 20000 iterations until modes were established.

Table 5.V shows a comparison of the first few modes frequency resonances for different rotation angles as compared to the analytical solution.

Table 5.V, resonant frequencies for the first 4 modes with angles of rotation

Rotation angle	0°	30°	45°	60°	90°
Resonant mode	Relative Error%				
First mode	0.023%	0.093%	0.37%	0.265%	0.230%
Second mode	0.109%	0.563%	0.647%	0.395%	0.059%
Third mode	0.084%	0.240%	0.305%	0.305%	0.045%
Fourth mode	0.011%	0.094%	0.063%	0.063%	0.011%

As we can see, results produced by the TLM solver are very accurate. Furthermore, these results show us that the solver is working correctly in case of anisotropic media with full tensor. Moreover, we can see the robustness of the TLM approach and its coherence with the general theory of electrodynamics: two different materials (one is defined by simple diagonal set of digital filters while the other is defined by full matrix of digital filters) give identical solutions, which fulfills the TO theory.

III. Deformation of a PEC spherical resonator

In this numerical experiment we use TO to verify again the accuracy of our TLM solver for another complex media. Consider the conducting sphere of radius 15 cm, as shown in figure 20.Va, filled by a simple nonmagnetic dielectric with $\varepsilon_r = 2.0$.

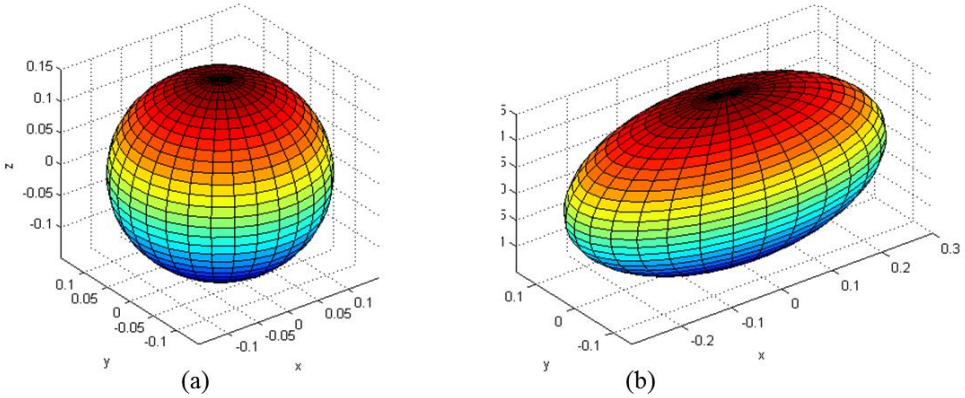

Figure 20.V, (a) spherical PEC resonator filled by an isotropic dielectric, (b) elliptical PEC resonator filled by an anisotropic dielectric medium

Now, we assume that the sphere is deformed to the ellipsoid shown in figure 19.Vb according to the following coordinate transformation:

$$\begin{pmatrix} \acute{x} \\ \acute{y} \\ \acute{z} \end{pmatrix} \rightarrow \begin{pmatrix} 2x \\ y \\ z \end{pmatrix} \tag{12.V}$$

This coordinate transformation modifies the material properties as presented in chapter II. Hence, the permittivity and permeability tensors become, respectively:

$$\bar{\bar{\varepsilon}}_r = \begin{pmatrix} 4 & 0 & 0 \\ 0 & 1 & 0 \\ 0 & 0 & 1 \end{pmatrix} \quad ; \quad \bar{\bar{\mu}}_r = \begin{pmatrix} 2 & 0 & 0 \\ 0 & 1/2 & 0 \\ 0 & 0 & 1/2 \end{pmatrix} \tag{13.V}$$

If we simulate an ellipsoid filled by this anisotropic (both dielectric and magnetic) material, we should get the same resonant frequencies as the original problem of the sphere before the deformation.

To perform the numerical experiments for both the elliptical and the spherical cavities described above, we used regular mesh of cubic cells. To maintain a negligible level of numerical dispersion, the cell size is $\Delta l = 3.3\, mm$ which is equivalent to 23 cells per wavelength with $\varepsilon_r = 2.0$ (relative error less than 1.0% according to (47.IV)). Moreover, this fine discretization was necessary to reduce the stair-case approximation for both structures. The corresponding time steps we used were 5.49 ps and 2.772 ps for the spherical and the elliptical cavities, respectively. The time excitation applied was a delta function and we run the experiment for 6000 iterations until modes were established. We used 753571 and 1507142 cells for the spherical and elliptical cavities, respectively.

Table 6.V shows a comparison between the numerical results of resonant frequencies calculated for the sphere filled by the isotropic media, the ellipsoid filled by the anisotropic media, and the analytical solution (of the spherical resonator) [15.V]. We can observe some very good matching between the three cases. This shows the validity of the TLM solver when dealing with anisotropic media.

Table 6.V, comparison between spherical and elliptical resonators with the analytical solution

Resonant Modes	Elliptical resonator (GHz)	Relative Error %	Spherical resonator (GHz)	Relative Error%	Analytical Solution (GHz)
First mode	1.329	0.241%	1.321	0.362%	1.3258
Second mode	1.866	0.209%	1.863	0.369%	1.8699
Third mode	2.184	0.603%	2.172	0.051%	2.1709
Fourth mode	2.399	0.162%	2.390	0.537%	2.4029
Fifth mode	2.810	0.912%	2.791	0.230%	2.7846

Finally, we highlight an interesting numerical phenomenon that appears in simulating the anisotropic media in (13.V): some of the diagonal values of the permeability are less that unity. In former TLM schemes, this led directly to instabilities. The reason is that stability condition when using stubs is that their characteristic impedance must be positive, which cannot be the case for relative permittivity less than unity. However, in the scheme presented in this thesis, only the digital filters that correspond to μ_y and μ_z are unstable (the poles are outside the unite circle in the complex plane in z-domain, or the poles are in the right hand side of the complex plane in s-domain). If will recall (38.III), one can easily derive:

$$\Gamma_{55}(s) = \Gamma_{66}(s) = \frac{1}{1-\frac{1}{2}s} \tag{14.Va}$$

or, in the z-domain:

$$\Gamma_{55}(z) = \Gamma_{66}(z) = \frac{\Delta t(1+z)}{z(\Delta t-1)+1+\Delta t} \tag{14.Vb}$$

Consequently:

$$\left\|z_{pole}\right\| = \left\|\frac{1+\Delta t}{1-\Delta t}\right\| \tag{14.Vc}$$

From (14.Vc), we can see that the poles of both filters are outside the unit circle for any positive value of Δt. However, the overall simulation process is stable. The explanation to this phenomenon is that negative impedances that appeared in the former TLM scheme rendered the simulation unstable. Remember that in the new scheme, all local waves propagate through the mesh in free space. The material presence is taken into account at the center of each node by filtering processes. As discussed in chapter IV, one can notice that the necessary condition for stability is that all the eigenvalues of the system matrix defined by (49.IV) lie inside the unit circle. However, there are no constraints on the filters of the correction matrix to reach stability. This is a crucial issue when dealing with complex media such as LH metamaterials. The reason is that permeability or permittivity tensors can have components less than unity or even less than zero for a given frequency range of interest. Hence, with this approach, one has to respect the stability conditions in (49.IV) only.

5.5.4 Waveguide Loaded by Ferrite Sample

In this numerical experiment, we determine the s-parameters for the ferrite-loaded waveguide shown in figure 21.V. The transverse and longitudinal cross sections dimensions are shown in figure 22.V. The ferrite sample is excited by an external DC magnetic field that adjusts its permeability tensor properties as discussed in chapter II. Generally, the calculation of the exact tensor components is a very difficult task, especially when the ferrite sample is not saturated [16.V]. When the DC magnetic field is very strong, the ferrite sample becomes completely saturated. Thus, it can be analytically described by the Polder tensor [17.V] and the ferrite sample becomes homogenous (magnetic domains disappeared). However, for the general case of magnetization one can obtain the permeability tensors by solving the GLL equation [18.V] presented in chapter II, for specific ferrite sample geometry and structure and specific applied DC magnetic field [18.V] [16.V].

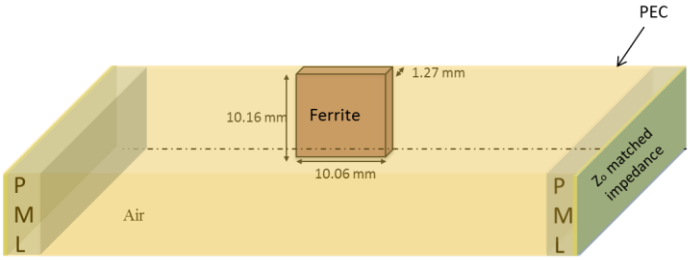

Figure 21.V, WR90 rectangular wave guide of dimensions 10.16 mm x 22.86 mm loaded by ferrite sample

As shown in figure 21.V, we used PML layer with 10-cells thickness as absorbing boundary conditions. The PML layer is terminated by free space Z_o impedance boundary condition to enhance the absorbing properties of the PML layer.

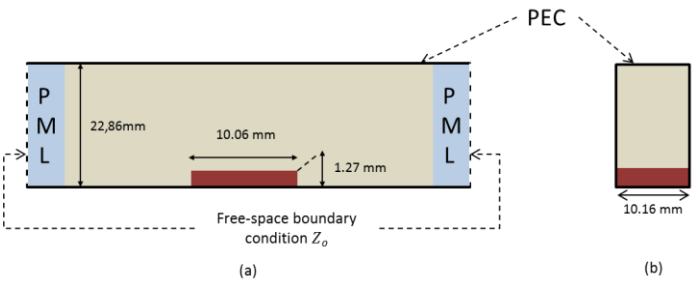

Figure 22.V, waveguide shown in figure 21.V a) top view b) front view.

The experiment was repeated three times. Initially, we assumed that the ferrite sample is homogeneously magnetized. Then, the ferrite sample was decomposed into nine homogeneous subdomains with different magnetic properties, to approximate the biasing DC field magnetization. Finally, we performed the experiment of a fully non-homogeneously magnetized ferrite sample, where the DC field magnetization approximation is made at the TLM cell level (this local DC-field mapping was computed by a magnetostatic simulator). The ferrite sample characteristics used in the following simulations are: $4\pi M_s = 0.28\,T$, $H_a = 318.3\,A/m$, $\Delta H = 3581\,A/m$, $\Delta H_{eff} = 318.3\,A/m$ and $\varepsilon_r = 16.6$ [19.V].

The permeability tensors and other sample parameters that we used in the experiments described above were provided by the material research group of the Lab-STICC at the University of Brest [19.V]. To obtain the correction matrix in every cell of the ferrite sample, we applied Prony's [20.V] [21.V] method for curve fitting. A second-order rational functions in Laplace s-domain were obtained. Then, we applied a bilinear transformation to obtain the time-domain filters [20.V].

In the simulations we used regular mesh of cubic cells. Due to the extremely complex properties of media tensors under study and to the lack of sufficient computer resources, we could not perform a complete dispersion analysis to calculate the optimal step size. However, because the smallest dimension in the geometry of figure 22.V is 1.27 mm, we decided to discretize it using 4 cells which mean $\Delta l = 0.3175\,mm$. Moreover, the same mesh size was used to discretize the ferrite sample in solving the GLL equation to obtain the permeability tensors. The corresponding time-step used is $\Delta t = 0.5\,ps$. The applied time excitation was a modulated-Gaussian pulse with parameters $f_o = 10.0\,GHz$, $\sigma = 100\Delta t$ and $t_o = 300\Delta t$. Finally, we ran the experiment for 100000 iterations until all fields practically vanished. The range of frequencies under consideration is from 8 to 12 GHz, for which only the TE_{10} mode propagates in the waveguide.

I. Homogeneous ferrite sample

Initially we assume that the sample is homogeneously magnetized as shown in figure 23.V. The permeability tensors were obtained by solving the GLL equation [18.V] [22.V] and assuming an average Gelin's model for permeability tensor in every cell.

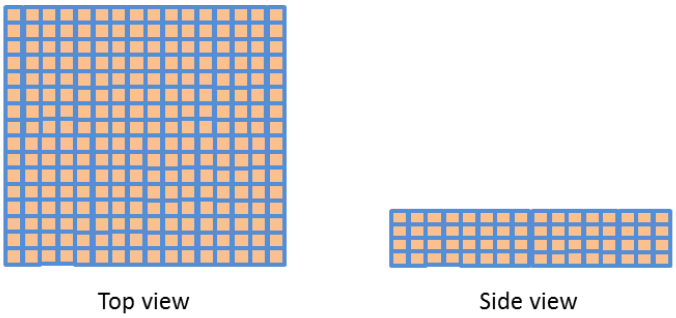

Figure 23.V, TLM discretized homogeneous ferrite sample. The permeability in each cell assumed to follow Gelin's model

In this experiment, the ferrite sample was discretized into 32 by 32 by 4 cells, whereas the complete computational domain was discretized into 401 by 72 by 32 cells. For matching purpose, we used PML layer at both ends of the waveguide each of 10-cells thickness.

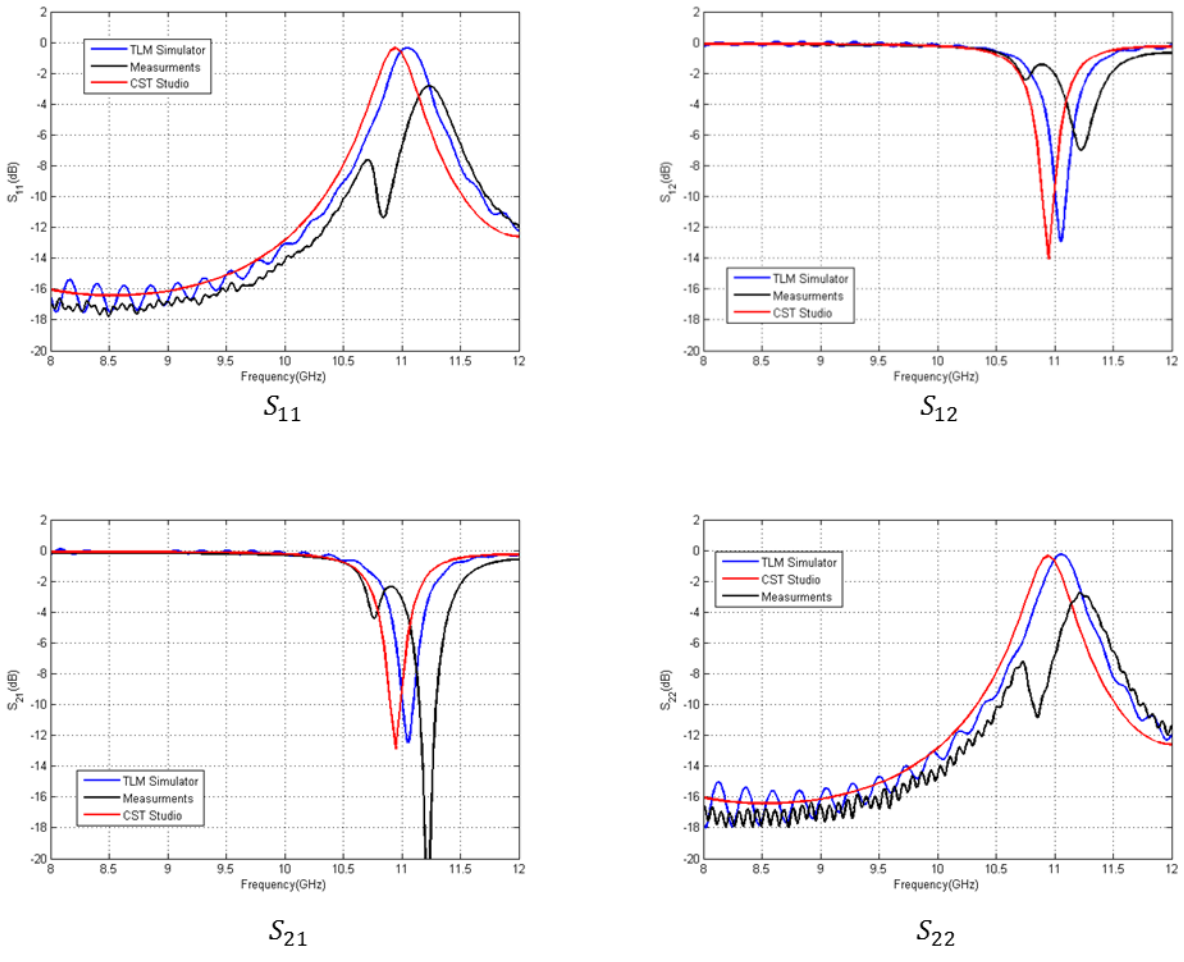

Figure 24.V, scattering parameters for the ferrite loaded waveguide of figure 21.V, with ferrite discretization of figure 23.V

As observed in figures 24.V, the time-domain TLM solver gives results slightly closer to the experiment than the frequency domain CST studio solver [23.V]. However, both solvers could not detect the secondary resonance at lower frequency, found by the measurement.

II. Approximation of the ferrite by nine-homogeneous subdomains

To enhance the model, we considered the more realistic case for which the sample in not uniformly magnetized by the DC external magnetic field. This is due to the demagnetizing field and the fact that the sample is unsaturated. Thus, we considered the ferrite sample as nine-blocs, each being homogeneous with a given magnetization state according to Gelin's model as shown in figure 25.V.

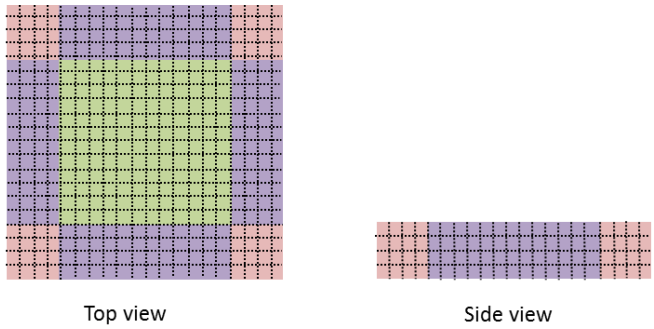

Figure 25.V, TLM discretization ferrite sample approximated by nine homogeneous blooks each of which follows Gelin's model

Figures 26.V shows a comparison between measurements (performed by the material research group of the Lab-STICC at the University of Brest [19.V]) and numerical solutions obtained by the TLM solver. This time, one can observe in all figures that results produced by the TLM solver are closer to the measurement than in the previous experiment. In particular, the secondary resonance appears around 10.6 GHz and reveals that it is not due to some parasitic coupling that occurred during the experiment.

The differences between the measurement and the numerical solutions can be explained as follow: First, nine-subdomain decomposition may not be a sufficient level of discretization to approximate the sample DC magnetization. Secondly, the physical model is not perfect. But, it

would be difficult to quantify the error. Finally, the physical experiment produces error also difficult to quantify.

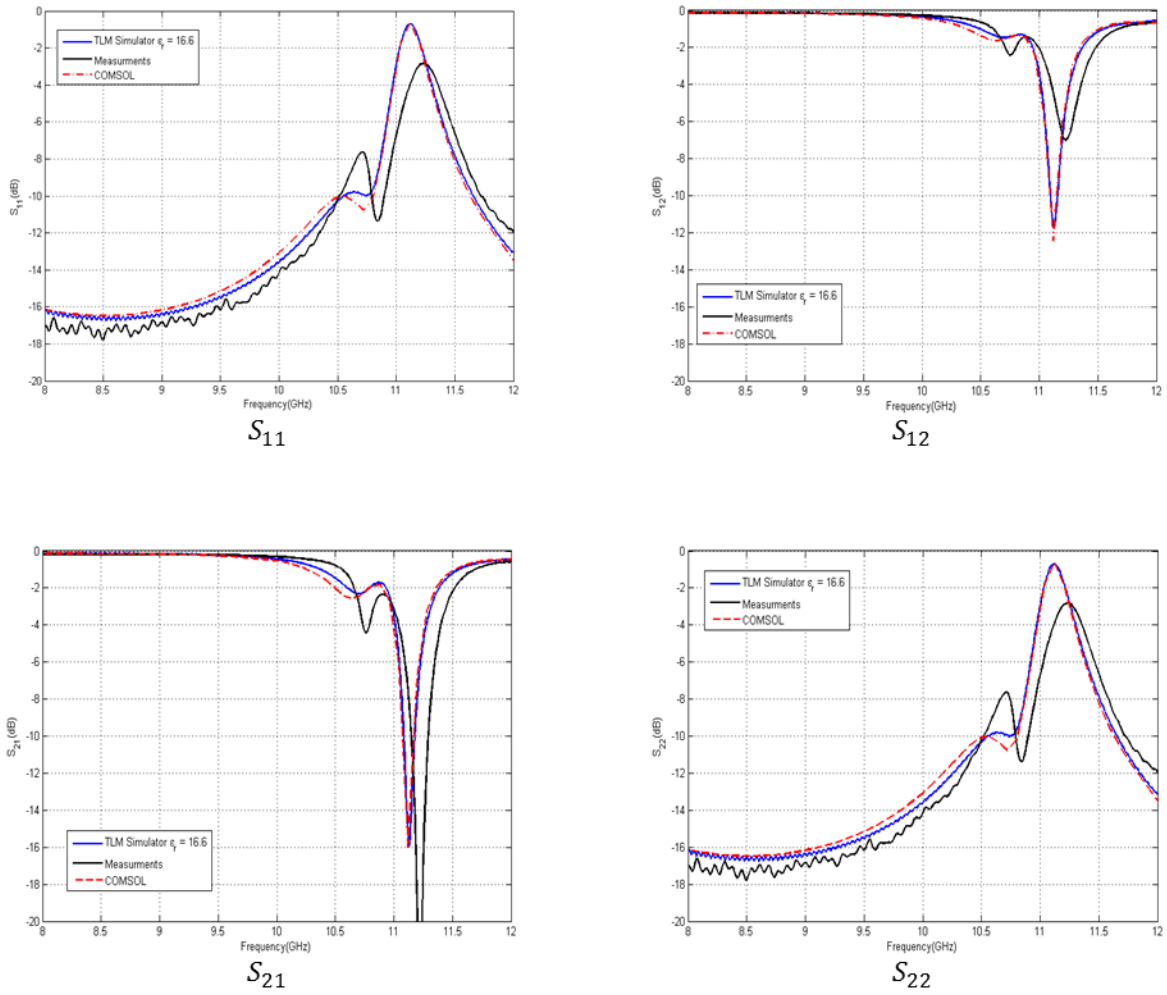

Figure 26.V, scattering parameters for the ferrite loaded waveguide of figure 21.V, with ferrite discretization of figure 25.V

One can also observe that the simulation results obtained by COMSOL [24.V] are very close to our TLM results, even though COMSOL is a frequency domain solver based on FEM that uses different discretization scheme. This can be an indication that the source of mismatch between numerical results and measurements may not be due to errors produces by numerical schemes only.

III. Full nonhomogeneous ferrite sample

To determine whether a finer discretization of the ferrite sample would give solution closer to the experiment, the GLL equation was solved for every cell. Therefore, each has its own local permeability tensor. The ferrite sample was discretized into $32 \times 32 \times 4$ parallelepipedic cells with dimensions $\Delta x = 0.3175\, mm$, $\Delta y = 0.3175\, mm$ and $\Delta z = 0.3175$ as shown in figure 27.V below.

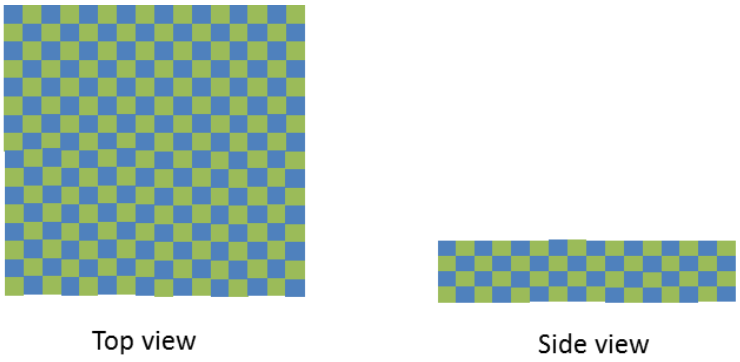

Figure 27.V, TLM discretized ferrite sample ($32 \times 32 \times 4$ *cells*) fully inhomogeneous with Gelin's model at the cell level.

Figures 28.V shows the comparison between measurements (performed by the same group at Brest University) and the numerical simulations using the TLM solver. The s-parameters of the waveguide loaded by the fully non-homogeneous ferrite sample shown in figure 27.V are represented. As we can see, using Gelin's model and the GLL equation to derive the local permeability tensor in each cell give a better representation of the ferrite sample. We can also observe that the second resonance obtained by both numerical simulations appears more clearly than in the previous experiment (see figure 26.V). However, some discrepancies concerning the resonance level can be observed.

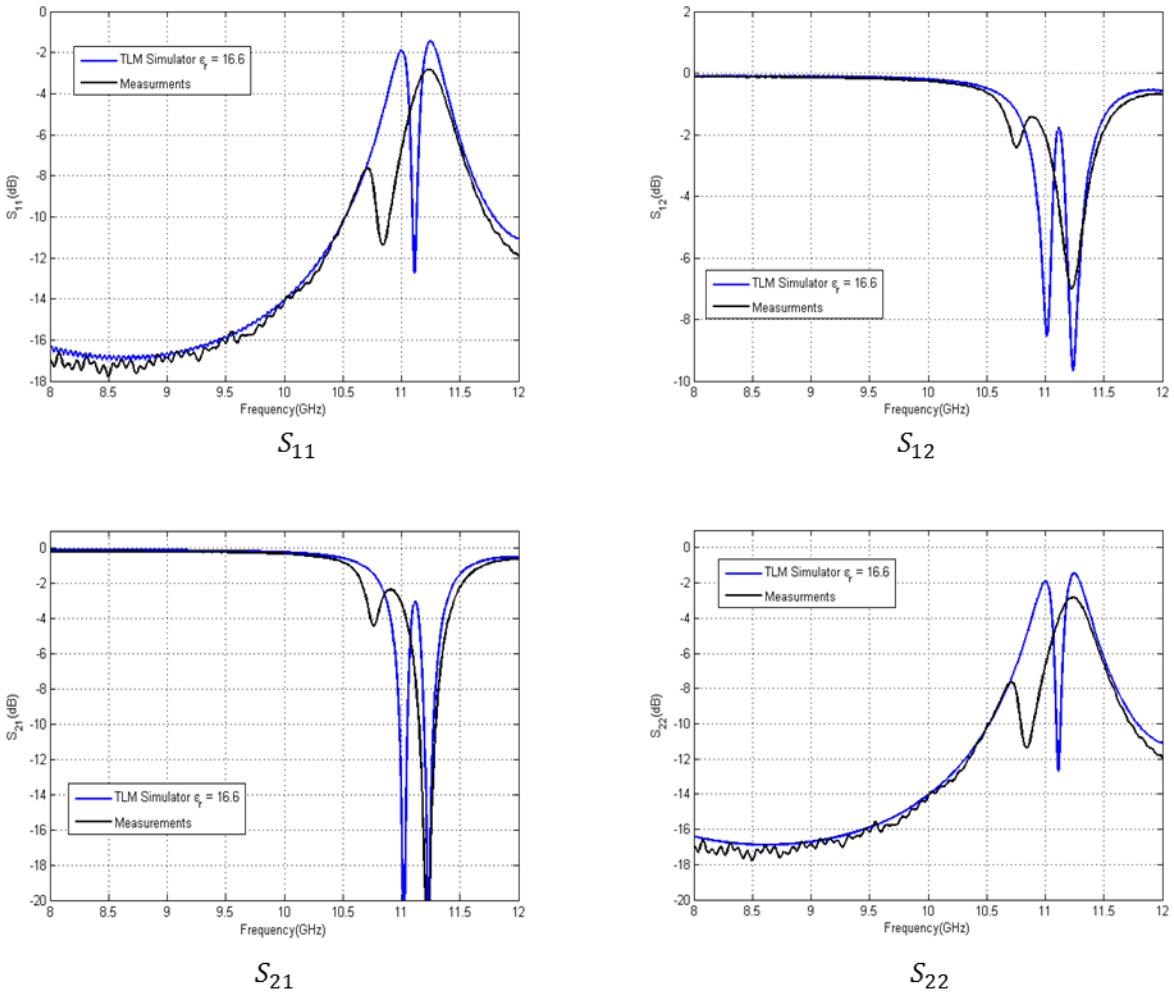

Figure 28.V, scattering parameters for the ferrite loaded waveguide of figure 21.V, with ferrite discretization of figure 27.V

The discrepancy between the numerical solutions and the measurement in figure 28.V can be explained by three following reasons: First, the process of solving the GLL equation is complicated and depends on different parameters that are also measured with some uncertainty; hence, the obtained permeability tensors has some corresponding inaccuracy. Secondly, the Gelin's model of ferromagnetic media has not been proven to be the ultimate model and may need some further improvement. Finally, repeated experimental measurements showed some small difference due to the sensitivity of the magnetization process and the sample position inside the waveguide.

It is worth to note that comparing these above simulations with commercial software such as COMSOL was almost impossible to implement due to the fact that the automati meshing

procedure wound up with a huge number of cells. Thus, as each of them requires its own tensor, the computing cost became exhaustive.

- **The effect of the uncertainty in ε_r**

Another explanation for the source of difference with the experiment may lie in the uncertainty of the permittivity value ($\varepsilon_r = 16.6$ was used previously) given by the manufacturer. Therefore, different values of ε_r were used to carry out retro-simulations whose results are shown in figure 34.V.

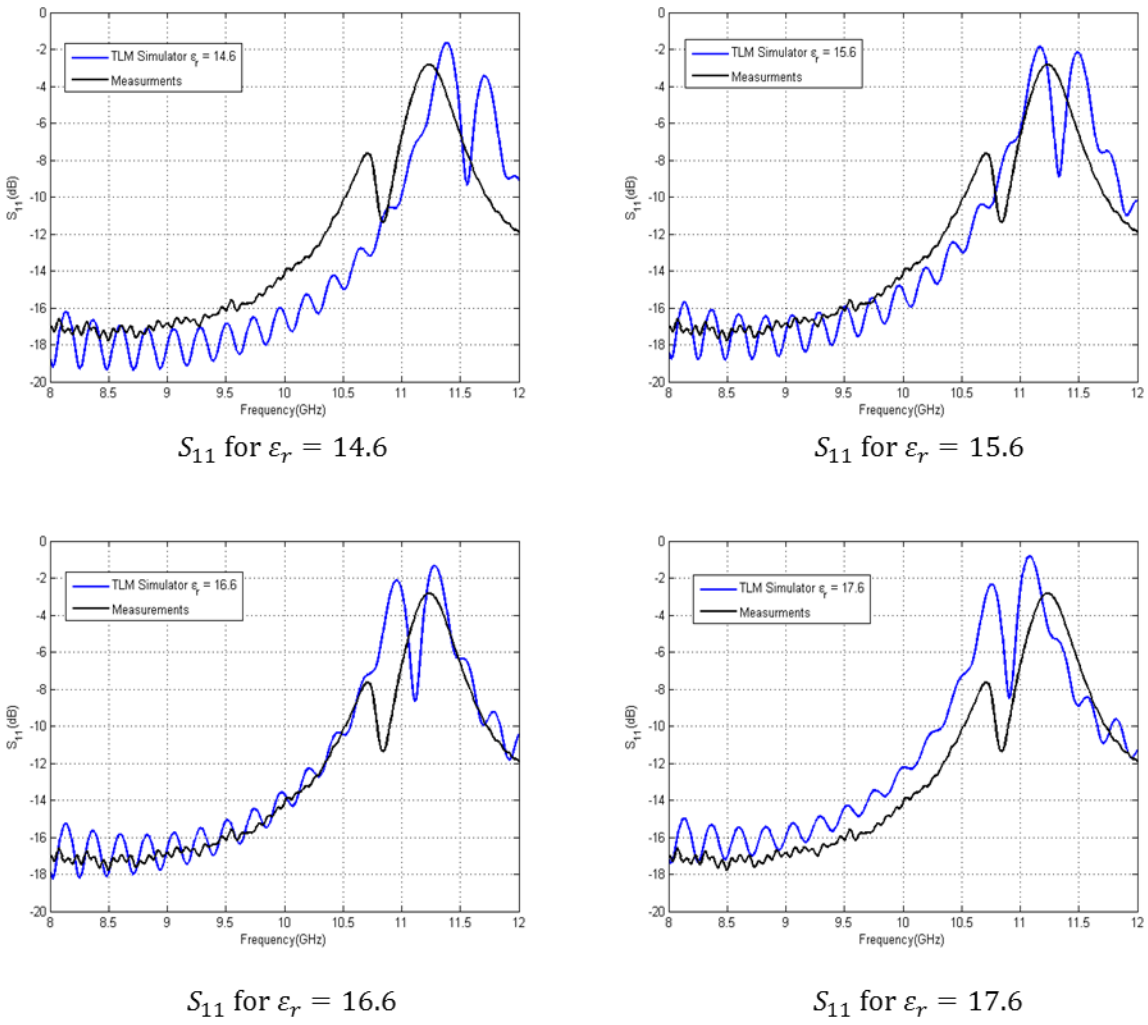

S_{11} for $\varepsilon_r = 14.6$ S_{11} for $\varepsilon_r = 15.6$

S_{11} for $\varepsilon_r = 16.6$ S_{11} for $\varepsilon_r = 17.6$

Figure 29.V, reflection coefficient for the ferrite loaded waveguide of figure 21.V, with ferrite discretization of figure 27.V for different value of $\boldsymbol{\varepsilon_r}$

In figure 29.V we see the reflection coefficient of the waveguide loaded by the ferrite sample for different ε_r = {14.6, 15.6, 16.6, and 17.6}. We observe that among the four curves, the case with ε_r = 17.6 produced resonances whose frequency better match those of the measurement. However, magnitudes are still different and this discrepancy may be explained by the reasons stated before.

- **Effect of the number of iterations**

In figure 30.V we present the curves of S_{11} and S_{12}, respectively, for different number of iteration. As we can observe, results seem to converge after 50000 iterations. An interesting fact is that the solver became unstable after 13000 iterations when we used PML of 10 cells thickness. It was also unstable even for PML of 20 cell thickness. However, when we changed the boundary condition at the end of the PML layer from PEC boundary condition to a free-space boundary condition Z_o, it was perfectly stable after 100000 iterations.

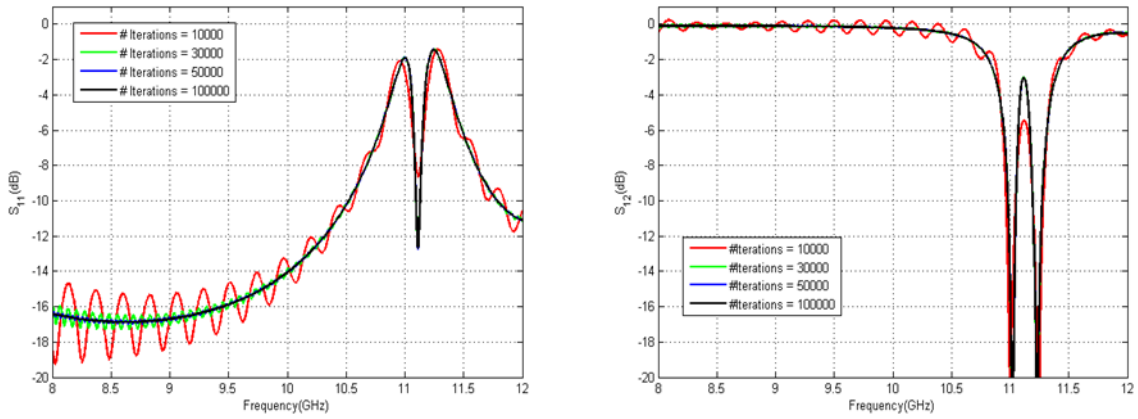

S_{11} S_{12}

Figure 30.V, $|S_{11}|$ and $|S_{12}|$ vs. frequency for different number of iterations for the case of figure 28.V

We can notice that it is necessary to run the simulation for a large number of iterations to eliminate the ripples at the lower frequency region of the diagram. One can also see that the values of $|S_{12}|$ can exceed the unity when a too small number of iterations is performed. In fact, the low frequency spectrum is generated by the long-term time response.

5.6 Conclusion

In this chapter we presented some practical contribution of this thesis. We started by briefly presenting the graphical user interface (GUI) that we implemented. It was necessary to replace the data interface of the former solver of the laboratory to allow a user-friendly procedure to enter and mesh arbitrary geometries. Then, we presented some canonical examples to validate the TLM solver for simple media and, in the same time, the interface GUI.

In the last part of this chapter, we presented three numerical experiments involving complex media with their analytical solution by which we could validate the TLM solver. In addition, the transformation optic (TO) procedure was opportunely used to generate analytical solutions useful for benchmarking. Finally, we presented an experiment involving realistic complex material namely, a non-uniformly magnetized ferrite sample inside a rectangular waveguide. Required tensors were generated by a physical model. Simulated results were compared with the experiment and some reasonable agreement was found. Retro simulations were performed to show effects produced by uncertainties related to the ferrite permittivity value. Finally, convergence test were also carried out concerning the number of iterations.

References

[1.V] http://www.gidhome.com/.

[2.V] A. Taflove and S. C. H. , Computational Electrodaynamics, The Finite-Difference Time-Domain Method, Norwood: Artch House, INC., 2005.

[3.V] M. I. Yaich, M. Khalladi; I. Zekik;J. A. Morente, "Modeling of Frequency-Dependent Magnetized Plasma in Hybrid Symmetrical Condensed TLM Method," *IEEE Microwave and Wireless Components Letters,* vol. 12, no. 8, pp. 293-295, 2002.

[4.V] S. J. Chapman, Fortran 90/95 for Scientists and Engineers, WCB/McGraw-Hill, 1998.

[5.V] M. Alexandru, "Efficient large electromagnetic simulation based on hybrid TLM and modal approach on grid computing and supercomputer", Thèse, L'Université De Toulouse, 2012.

[6.V] http://geuz.org/gmsh/.

[7.V] http://www.rhino3d.com/new/mesh.

[8.V] D. E. Merewether, R. Fisher and F. W. Smith, "On Implementing a Numeric Huygen's Source Scheme in a Finite Difference Program to Illuminate Scattering Bodies," *IEEE Transaction on Nuclear Science,* Vols. NS-27, no. 6, pp. 1829-1833, 1980.

[9.V] V. Demir, A. Elsherbeni, D. Worasawate and E. Arvas, "A Graphical User Interface (GUI) for Plane-Wave Scattering from a Conducting, Dielectric, or Chiral Sphere," *IEEE Antennas and Propagation Magazine,* vol. 46, no. 6, pp. 94-99, October 2004.

[10.V] S. J. Adams, ELECTROMAGNETIC THEORY, McGRAW-HILL BOOK COMPANY, INC., 1941.

[11.V] D. M. Sheen, S. M. Ali, M. D. Abdouzahra and J. A. Kong, "Application of the Three-Dimensional Finite-Difference Time-Domain Method to the Analysis of Planar Microwstrip Circuits," *IEEE Transactions on Microwave Theory and Techniques,* vol. 38, no. 7, pp. 849-857, 1990.

[12.V] M. I. Yaich, M. Khalladi and M. Essaadi, "Efficient Modeling of Chiral Media Using SCN-TLM Method," *Serbian Journal of Electrical Engineering,* vol. 1, no. 2, pp. 249-254, 2004.

[13.V] A. J. Ward and J. B. Pendry, "Refraction and geometry in Maxwell's equaions," *Journal of Modern Optics,* vol. 43, no. 4, pp. 773-793, 1996.

[14.V] N. B. Kundtz, D. R. Smith and J. B. Pendry, "Electromagnetic Design With Transformation Optics," *Proceedings of the IEEE,* vol. 99, no. 10, pp. 1622-1633, October October2011.

[15.V] J. D. Jackson, Classical Electrodynamics, JOHN WILEY & SONS, INC., 1999.

[16.V] P. Gelin and K. Berthou, "New consistent model for ferrite permeability tensor with arbitrary magnetization state," *IEEE Transactions on Microwave Theory and Techniques,* vol. 45, no. 8, pp. 1185-1192, 1997.

[17.V] D. Polder, "On the theory of ferromagnetic resonance," *philos. Mag,* vol. 40, p. 99, 1949.

[18.V] P. Gelin and P. Quéffélec, "Generalized Permeability Tensor Model: Application to Barium Hexaferrite in a Remanent State for Self-Biased Circulators," *IEEE Transactions on Magnetics,* vol. 44, no. 1, pp. 24-31, 2008.

[19.V] A. L. Goullec, *et al*, "Ferrite-based phase shifters design: the modeling problem of nonsaturated anisotropic ferrites" in *Microwave Symposium Digest (IMS), 2013 IEEE MTT-S International*, Seattle.

[20.V] L. L. Scharf, Statistical Signal Processing, Detection, Estimation, and Time Series Analysis, ADDISON-WESLEY PUPLISHING COMPANY, 1991.

[21.V] M. L. V. Blaricum and R. Mitra, "A Technique for Extracting the Poles and Residues of a System Directly from Its Transient Response," *IEEE Transactions on Antennas and Propagation,* Vols. AP-23, no. 6, pp. 777-781, 1975.

[22.V] L. Landau and E. M. Lifshitz, Electrodynamcis of Continuous Media, Pergamon Press, 1984.

[23.V] https://www.cst.com/.

[24.V] http://www.comsol.com/.

Chapter VI
Challenging Cases of Time-Domain Methods: Low frequency and high-contrasts constitutive parameters

6.1 Introduction

The chapter is dedicated to study some behaviors of time-domain methods such as TLM and FDTD for two special and challenging cases:

- **Low-frequency**

This issue appears when one is interested in solving the EM problems at low frequencies for which structure details imposes using a mesh size that is much smaller than the wavelength. As a result, the time step is correspondingly very small. This leads to an exhaustively large number of iterations to generate a complete time response with an increasing risk of late time instability. The above case belongs to the class of multi-scale problems.

In the first part of this chapter, we will present some of the solutions that have been applied in the literature to both the low-frequency and multi-scale problems. Then, we propose some approaches that may solve those problems. They involve mapping techniques such that the original domain is transformed to another one more adequate to perform full-wave simulations.

- **High contrasts**

It is well-know that the FDTD update equations involve some averaging of the media properties at the interface between different media. The impact on the accuracy becomes more obvious when the contrast is high between both media at both sides of an interface. For TLM, the local property of the algorithm modifies the impact of high contrast cases on the accuracy as no averaging is applied. After demonstrating the theoretical basis of this issue, we present several

numerical experiments that detect and magnify substantial differences between both methods when the computational domain involves highly contrasted media.

6.2 The stiffness problem of numerical techniques

Let us assume that we have the problem of solving the one-dimensional wave equation [1.VI]:

$$\frac{\partial^2 A}{\partial x^2} = \frac{1}{v^2}\frac{\partial^2 A}{\partial t^2} + \sin(2\pi f_o t) \tag{1.VI}$$

where $x \in [0, L]$ and $t \in \left[0, T_p\right]$ with boundary and initial conditions such as:

$$A(0, t) = g(t) \tag{2.VIa}$$

$$A(L, t) = h(t) \tag{2.VIb}$$

$$A(x, 0) = k(x) \tag{2.VIc}$$

where f_o is the frequency of the source, v is the wave velocity and $g(t)$, $h(t)$ and $k(x)$ are the initial and boundary values, respectively. We first assume that the medium is homogenous. As a result, the wave velocity v will remain constant in space and time.

If we use a FDTD discretization scheme to obtain the update equations corresponding to (1.VI), we obtain [2.VI]:

$$\frac{A(x+\Delta x,t)-2A(x,t)+A(x-\Delta x,t)}{(\Delta x)^2} = \frac{1}{v^2}\frac{A(x,t+\Delta t)-2A(x,t)+A(x,t-\Delta t)}{(\Delta t)^2} + \sin(2\pi f_o t) \tag{3.VI}$$

Some mathematical manipulations on (3.VI), yields:

$$A(x, t+\Delta t) = \frac{v^2(\Delta t)^2}{(\Delta x)^2}\left(A(x+\Delta x, t) - 2A(x, t) + A(x-\Delta x, t) - (\Delta x)^2 \sin(2\pi f_o t)\right) + 2A(x, t) - A(x, t-\Delta t) \tag{4.VI}$$

If we use a discrete notation, (4.VI) becomes:

$$A(m,n+1)=\frac{v^2(\Delta t)^2}{(\Delta x)^2}(A(m+1,n)-2A(m,n)+A(m-1,n)-(\Delta x)^2\sin(2\pi f_o n\Delta t)\,)+$$
$$2A(m,n)-A(m,n-1) \tag{5.VI}$$

where m and n are the space and time indices, respectively. The necessary condition for (5.VI) to have a solution and stable results is [2.VI]:

$$\frac{v^2(\Delta t)^2}{(\Delta x)^2}\leq 1 \tag{6.VI}$$

Recall the fact that in linear time invariant systems (LTI), the frequency of the response is identical to the one of the sources when the steady state is reached [3.VI]. In time domain simulations, we generally need to cover several time periods of the signal to insure that the steady-state is reached and to find the corresponding frequency spectrum of the output fields. This implies that the total simulation time T_p will be approximately:

$$T_p\sim\frac{1}{f_o} \tag{7.VI}$$

If the input signal contains multi-frequencies, then the denominator in (7.VI) should be the lowest spectrum frequency. As we can see with (7.VI), the total simulation time is independent on the numerical scheme used to solve the problem. It only depends on the frequency spectrum of the input signal. Thus, if we use a time-domain method to solve (1.VI) then, according to (7.VI), the total number of time iterations N_{iter} is:

$$N_{iter}=\frac{T_p}{\Delta t}\sim\frac{1}{f_o\Delta t} \tag{8.VI}$$

Now, if for any reason the spatial discretization must be very small at some location, the stability condition (6.VI) requires choosing a small time-step. This leads to:

$$\lim_{\Delta x\to 0}\Delta t=0 \tag{9.VIa}$$
$$\lim_{\Delta t\to 0}N_{iter}=\infty \tag{9.VIb}$$

The above relations illustrate the low-frequency issues in time-domain methods. As we can see, the total computational time depends only on the input signal frequency spectrum. This will result to a huge number of iterations when very small temporal discretization is used. This

relates to the definition of stiffness for the numerical scheme: Given a numerical scheme in finite region of absolute stability, it is applied to an initial and boundary value problem. If this numerical method is forced to use in a certain interval of integration over a step-length which is much smaller than the smoothness of the exact solution, then the system is said to be *stiff* in that interval [4.VI] [5.VI].

It is clear that the low-frequency problem in time domain numerical techniques means that the system becomes stiff as described above. In case we need small mesh size to accurately describe the geometry then, for stability issues, we need a small time step which is much smaller than the one obtained by applying the Nyquist criterion for signal time sampling. Finally, we should also keep in mind that this stiffness problem is an issue that is only related to the discrete numerical scheme and not to the analytical solution of the original continuous problem (because the analytical solutions are smooth at low frequency). This means that the impacts of the stiffness problem can be reduced by modifying the numerical schemes [5.VI].

6.3 Low-frequency problem in Maxwell's equations

In computational electromagnetics, to properly describe the geometrical shape of the physical objects, we need a certain level of spatial discretization; this level is mainly determined by:

- The physical shapes of the objects inside the computational domain such as corners, ridges, slots, etc., which require local higher spatial resolution to avoid coarseness error.
- Highly inhomogeneous structures with complex shape.

In the above cases, we reach to a scenario where $\{\Delta x, \Delta y, \Delta z\} \ll \lambda$, typically $< \lambda/100$, whereas in smooth quasi homogeneous (well-posed) problems one has $\max\{\Delta x, \Delta y, \Delta z\} \sim \lambda/20$. In summary, we can say that the low frequency problem can appear in the following practical scenarios:

- Highly heterogeneous computational domain of small electrical size, for instance the human body interaction with quasi-static frequencies. Indeed, to describe the human brain properly we need a spatial discretization at the centimeter or millimeter level. However, the brain signals are in the range of few Hz to few tenths of Hz [6.VI] [7.VI].

- Fine details inside the computational domain. For example a thin wire or any other fine objects, especially when they are radiation sources. In this scenario, a *multi-scale* issue appears. A typical application is the study of VLF antennas that operate at few kHz and have a wire structure of several hundreds of meters [8.VI].

Now, we should highlight the difference between wavelength of a wave and its time period which are defined by:

$$\lambda_o = \frac{c}{f} \tag{10.VIa}$$

$$T_o = \frac{1}{f} \tag{10.VIb}$$

As seen in chapter IV, the spatial discretization should be around 10 cells per minimum wavelength to obtain negligible numerical dispersion. In the case of low-frequency operation, cell dimensions are much smaller than one-tenth of the wavelength. However, we know that the time and space components are related by the speed of light in the medium according to (10.VIa) and (10.VIb). This implicitly means that the field time-responses are oversampled compared to Nyquist criterion and this phenomenon worsens as the operating frequency decreases.

In the example shown in figure 1.VI, we want to calculate the first few resonant frequencies of one-dimensional resonator loaded by a thin dielectric slab with permittivity ε_r. The simulation will be carried out using a time-domain method. To illustrate what happens at low-frequencies, we assume a uniform meshing.

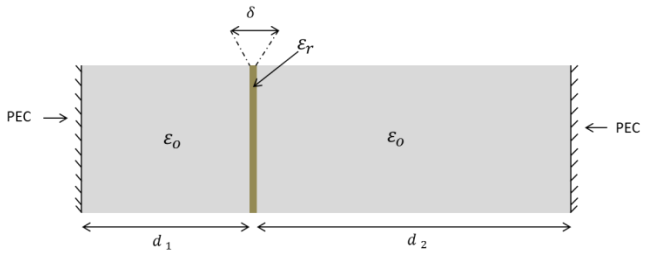

Figure 1.VI, one-dimensional resonator loaded by highly permitivity thin dielectric slab

A multi-scale problem appears due to the presence of fine details (the dielectric slab) inside the resonator. This multi-scale problem will lead to a low-frequency problem as discussed below.

Let us start our analysis from the analytical solution of the problem, to determine the required spatial discretization to obtain negligible dispersion. Hence, the n-*th* resonant frequency is given by [1.VI]:

$$f_n = \frac{c_o n}{2(d_1+d_2+\delta\sqrt{\varepsilon_r})} \tag{11.VI}$$

Next, assume that we are searching for the dominant mode. If the dielectric slab is absent, the appropriate cell size (for acceptable level of numerical dispersion) would be [9.VI]:

$$\Delta z \leq \frac{\lambda}{10} = \frac{c_o}{10 f_1} = \frac{d_1+d_2}{5} \tag{12.VIa}$$

The corresponding maximum time step is:

$$\Delta t = \frac{\Delta z}{c_o} = \frac{d_1+d_2}{5c_o} \tag{12.VIb}$$

In this case, the total number of cells with (12.VIa) is 5. Now, assuming that the dielectric slab is very thin for instance:

$$\delta = \frac{\lambda}{10000} = \frac{c_o}{10000 f_1} \tag{13.VI}$$

This means that to describe the computational domain accurately one should chose Δz to be less than the dielectric slab width, say, using 3 cells. Thus, with (13.VI) one obtains:

$$\Delta z \leq \frac{\delta}{3} = \frac{c_o}{30000 f_1} \tag{14.VIa}$$

and the new corresponding maximum time-step after including the slab in the computational domain and substituting in (12.VI) becomes:

$$\Delta t = \frac{\Delta z}{c_o} = \frac{d_1+d_2}{15000 c_o} \tag{14.VIb}$$

Finally, the total number of cells is

$$N_2 = \frac{d_1+d_2+\delta}{\Delta z} \cong 15000\ cells \qquad (14.\text{VIc})$$

This illustrates the low-frequency difficulty, even for a very simple scenario. The number of time iterations and number of necessary cells have been multiplied by 3000. This means that the space memory complexity became 3000 larger, while the time complexity became larger by 3000×3000 times. For more complicated computational problems one can imagine more severe impacts of the low-frequency problems (multi-scale problem). Note that if irregular meshing can solve the spatial problem by considerably reducing the number of cells, the time iteration issue will remain at the same level of complexity.

6.4 Time-domain vs. Frequency-domain methods for quasi-static problems

I. Time-domain methods

The FDTD and TLM methods have their explicit version [10.VI] [11.VI] and unconditionally stable version such as ADI-FDTD and SS-TLM [12.VI] [13.VI]. In explicit formulations CFL stability condition must be respected for stability considerations. However, in unconditionally stable formulations we cannot go far beyond the CFL limit (even though the algorithms are unconditionally stable). This is because of the numerical dispersion increases as we exceed the CFL limit [9.VI]. This means, that at low-frequency (in both conditionally and unconditionally stable techniques) a very high number of iterations is required to obtain a complete time response [14.VI]. In addition, late time instability may occur. Generally, it appears from the non-exact discretization of the curl operators [15.VI]. Also, instability can be generated by absorbing boundary conditions (PML for instance) [16.VI].

II. Frequency-domain methods

The low frequency problem is not only restricted to time-domain techniques, similar problems happen in frequency domain methods. These are referred to as low frequency break down [17.VI]. To investigate what happens in frequency domain methods, we start using potentials to represent the electric field [17.VI]:

$$\vec{E} = j\omega\vec{A} - \nabla\phi \tag{15.VI}$$

where $\vec{A}$ is the magnetic vector potential, and ϕ is the electric scalar potential. It is known that the contribution from the charge distribution ρ_v in Maxwell's equations is related to the scalar potential ϕ and the contribution from the current density $\vec{J}$ is related to the vector potential $\vec{A}$. The Helmholtz decomposition states that any vector quantity, say $\vec{J}$ can be decomposed into divergence-free (solenoidal) and curl-free (irrotational) components such that [17.VI]:

$$\vec{J} = \vec{J}_{sol} + \vec{J}_{irr} \tag{16.VI}$$

From Maxwell-Gauss and continuity equations we obtain at low frequencies:

$$\nabla \cdot \varepsilon\vec{E} = \rho = \lim_{\omega\to 0} \frac{\nabla.\vec{J}}{j\omega} = \lim_{\omega\to 0} \frac{\nabla.\vec{J}_{irr}}{j\omega} \tag{17.VI}$$

As we see, the solenoidal component of the current vector has no effect to the charge distribution. However, the irrotational component does. As a result, to have a finite charge as the frequency goes toward zero, $\vec{J}_{irr}$ should vanish linearly with the frequency as $\omega \to 0$. On the other hand, $\vec{J}_{sol}$ component doesn't require any scaling with frequency. We can also notice the decoupling between the electric field and magnetic field more clearly as the frequency goes down. At zero frequency, both fields are completely decoupled. Thus, the electrostatic field is produced by the irrotational component of the current source, while the magneto static field is produced by the solenoidal component.

Now, assume that we solve the electric field integral equation (EFIE) using MoM with Rao-Wilton-Glisson (RWG) basis functions [18.VI]. Once we build the impedance matrix to solve the MoM system, we will observe that the contribution from the vector potential is much smaller than the one that comes from the scalar potential. This is because of the lack of frequency scaling in the solenoidal part of the current source. This can be seen clearly from the EFIE equation [17.VI]:

$$\vec{E}(r) = j\omega\mu \iint_S g(r,\acute{r})\,\vec{J}(\acute{r})d\acute{r} - \frac{1}{j\omega\varepsilon}\nabla \iint_S g(r,\acute{r})\,\acute{\nabla}\cdot\vec{J}(\acute{r})d\acute{r} \tag{18.VI}$$

where S is the dielectric object surface, μ and ε are the permeability and permittivity of the medium, respectively. The first integral is the contribution of the vector potential field. Because of the finite computer precision, this term contribution vanishes during the numerical calculations as the frequency goes toward zero [17.VI]. However, the second term which is the scalar potential part has a null-space because of the divergence operator. Hence, the impedance matrix will become quasi singular. This makes it very difficult to solve, even with iterative solvers [17.VI].

Several approaches have been developed to tackle the low-frequency break down in frequency-domain methods such as loop-tree and loop-star decomposition for integral equation based methods [19.VI] [17.VI] and the tree-cotree splitting technique in FEM based methods [20.VI]. However, these approaches are valid only for simple structures and mostly for either homogeneous dielectrics or PEC structures; moreover, they suffer from rather complicated implementation [20.VI].

6.5 Low- frequency problem statement for time-domain methods

Consider a computational domain discretized into cells within which there is a medium defined by constitutive parameter values$\{\varepsilon, \mu, \sigma, \cdots \text{etc.}\}$. In this computational domain there exist sources (currents, voltages, incident fields …etc.). This domain is truncated by some boundary conditions, ABC, PEC, PMC …etc. Let us suppose that one deals with low-frequency conditions and, therefore, one uses a very small maximum time-step compared to the time period of the source signal. As discussed before, an exhaustive number of iterations is needed to cover the full response due to the source signal. The objective is to develop an alternate efficient method that achieves full-wave solutions under low-frequency conditions.

6.6 Classical time-domain methods for quasi-static Maxwell's equations

In this section we present the most intuitive techniques that already exist in the literature. They allow one to tackle the low-frequency problem in electromagnetics.

6.6.1 Curve-fitting incorporated with full-wave time domain solver

Let us assume that a transient response is negligible for $t > t_{tra}$. If the system is linear and if the source is assumed to contain a sequence of sinusoids at frequency $f = \{f_1, \cdots, f_N\}$, then the response should contain the same sequence of sinusoids $f = \{f_1, \cdots, f_N\}$. However, both amplitude and phase of these sinusoids are unknowns. Now, if we record the response for time samples after the transient period $t = \{t_1, \cdots, t_N\} > t_{tra}$, then, at any point $r = (x, y, z)$ in the computational domain, we can construct the following nonlinear system of equations [14.VI]:

$$F_j(r,t) = \sum_{i=1}^{M} A_i(r)\sin(\omega_i t_j + \varphi_i(r)) \tag{19.VI}$$

where $j \in \{1, \cdots, N\}$, and $M \geq 2N$.

Solving the system (19.VI), one obtains a sinusoidal approximation for E or H fields. The crucial condition here is that the transient time t_{tra} should not be too long; otherwise this method does not bring any advantage.

6.6.2 Changing the speed of light

In some scenarios when the media losses play an important role, the effect of changing the permittivity will not considerably affect the simulation results. However, as we studied in chapter IV, the CFL condition is mostly dependent on the permittivity value for lossy dielectrics such as sea water [21.VI]. In this approach (which is empirical and valid for highly lossy media), we increase the material permittivity such that the speed of light is reduced. This means that the wavelength is also reduced and, consequently, the Courant limit increase. As a result, we can use higher values for the time-step Δt. This approach is suitable for studying underwater communications. For instance, one can calculate the reflection and transmission coefficients for underwater antennas and optimize and manage the transmitter power. However, in more complex computational problems such as multi-scale microwave circuits this kind of assumptions (to increaseε_r) is not suitable [21.VI].

6.6.3 Unconditionally stable full-wave FDTD or TLM based approaches

Generally, update equations of time-domain Maxwell's at low frequencies produce a stiff system. However, for stiff equations, the traditional explicit *Runge-Kutta* method is not the optimal choice to solve such a system [5.VI]. Instead, implicit techniques can be applied. In these techniques, we divide each time step into substeps, and fields are updated within each substep. Hence, we can *control/optimize* those update equations subject to the stability condition [22.VI].

In time-domain computational methods, two implicit approaches were developed to solve Maxwell's equations:

- Alternating- Direction Implicit Method (ADI-FDTD) [22.VI], or Split-Step TLM [12.VI]
- Locally one-dimensional scheme (LOD-FDTD) [23.VI]

The above techniques are based on Crank-Nicolson scheme [22.VI] and are unconditionally stable everywhere, and, thus, don't require Courant condition fulfillment. However, beyond Courant limit, the numerical dispersion increases significantly [13.VI].

6.7 Proposed solutions

In this section we propose several ideas that may open a door for more efficient solutions to time-domain low-frequency problems.

6.7.1 Transfer function under sampling

As already mentioned, the time-domain field responses are highly oversampled at low-frequencies. Since fields are smoothly varying at low-frequency there is no physical or mathematical necessity for time oversampling, other than the stability condition. In this technique, we consider the whole 3D computational domain as a system composed of a large number of filters as illustrated by figure 2.VI. Let us assume that we have a low-frequency

source at discrete coordinate (i_1, j_1, k_1) and we want to calculate fields at any other point (i_2, j_2, k_2).

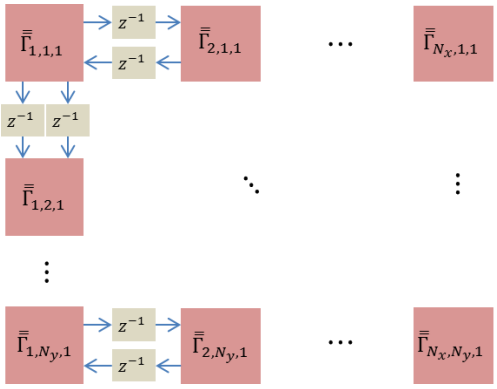

Figure 2.VI, block diagram of one layer of the computational domain seen as a large filter network

We represent the computational domain as in TD-TLM. Thus, as discussed in chapter III, each cell is fully defined by the material correction matrix $\bar{\bar{\Gamma}}$ that contains digital filters. At every time step, neighboring cells exchange 12 voltages. These voltage exchange process takes place every time step. The objective is to find the equivalent transfer function between the source point at (i_1, j_1, k_1) and the destination point (i_2, j_2, k_2). To accomplish this, we can apply several techniques from graph theory and control theory such as Mason's gain formula (MGF). Then, we can obtain the transfer function $H_{1,2}(z)$. The next step is to undersample this equivalent filter such that its sampling period becomes comparable to the one of the source signal [24.VI].

We can see the benefits of this approach by the fact that in the original computational problem, we were limited by CFL condition to maintain stability. However, after getting the equivalent transfer function and performing under sampling, we can increase the time step to much higher values than CFL (however, we are upper bounded by Nyquist time-sampling limit). Note that it is not necessary to worry about numerical dispersion if we respect it in the original problem. The reason lies in the fact that we didn't change the problem mesh size. However, this technique can be useful for small computational domain only. The reason is that the process of calculating the transfer function between the source and the destination point is quite cumbersome.

6.7.2 Applying the space-time coordinate transformation to map the computational domain

Here we are presenting a technique of transforming the original low-frequency computational problem, using a time-varying coordinate transformation. This kind of 4D space-time transformation modifies the metric tensor and changes the behavior of the computational problem [25.VI] [26.VI]. The objective is to search for a transformation that will transfer the computational problem to higher frequencies. Then, using standard full-wave solvers, we can obtain the results at high frequencies with reasonable time-step values. Finally, we apply the inverse time-space coordinate transformation to obtain solutions to the original low-frequency problem.

For simplicity, we will show the procedure to perform such a transformation for one-dimensional wave equation in homogenous medium, which is solution of [1.VI]:

$$\frac{\partial^2 A}{\partial z^2} = \frac{1}{v^2}\frac{\partial^2 A}{\partial t^2} + s(t,z) \tag{20.VI}$$

Then, we apply the coordinate transformation

$$\begin{pmatrix} \acute{z} \\ \acute{t} \end{pmatrix} = \begin{pmatrix} az + bt \\ cz + dt \end{pmatrix} = \begin{pmatrix} a & b \\ c & d \end{pmatrix}\begin{pmatrix} z \\ t \end{pmatrix} \tag{21.VI}$$

for which its inverse transform is:

$$\begin{pmatrix} z \\ t \end{pmatrix} = \frac{1}{ab-cd}\begin{pmatrix} d & -b \\ -c & a \end{pmatrix}\begin{pmatrix} \acute{z} \\ \acute{t} \end{pmatrix} \tag{22.VI}$$

Using the chain rule for the second derivative [27.VI]:

$$\frac{\partial^2 A}{\partial x_i \partial x_j} = \sum_{k=1}^{M}\frac{\partial A}{\partial u_k}\frac{\partial^2 u_k}{\partial x_i \partial x_j} + \sum_{k=1}^{M}\sum_{l=1}^{M}\frac{\partial^2 A}{\partial x_i \partial x_j}\frac{\partial u_k}{\partial x_i}\frac{\partial u_l}{\partial x_j} \tag{23.VI}$$

where x_i is the original coordinate system, u_k is the new coordinate system after transformation and M is the dimensionality of the space. Applying (23.VI) with $M = 2$ and the transformation (22.VI) to the original wave equation (20.VI) yields:

$$\frac{\partial^2 A}{\partial z^2} = a^2\frac{\partial^2 A}{\partial \acute{t}^2} + c^2\frac{\partial^2 A}{\partial \acute{z}^2} + 2ac\frac{\partial^2 A}{\partial \acute{z}\partial \acute{t}} \tag{24.VIa}$$

$$\frac{\partial^2 A}{\partial t^2} = b^2 \frac{\partial^2 A}{\partial \acute{t}^2} + d^2 \frac{\partial^2 A}{\partial \acute{z}^2} + 2bd \frac{\partial^2 A}{\partial \acute{z} \partial \acute{t}} \tag{25.VIb}$$

Then, by combining the above equations and substituting them in (20.VI) we obtain:

$$\frac{\partial^2 A}{\partial \acute{z}^2} = \left(\frac{b^2/v^2 - a^2}{c^2 - d^2/v^2}\right) \frac{\partial^2 A}{\partial \acute{t}^2} + 2\left(\frac{bd/v^2 - ac}{c^2 - d^2/v^2}\right) \frac{\partial^2 A}{\partial \acute{z} \partial \acute{t}} + \frac{s(\acute{t}, \acute{z})}{c^2 - d^2/v^2} \tag{26.VI}$$

From above, we see that we have a new wave equation:

$$\frac{\partial^2 A}{\partial \acute{z}^2} = \frac{1}{\acute{v}^2} \frac{\partial^2 A}{\partial \acute{t}^2} + \gamma \frac{\partial^2 A}{\partial \acute{z} \partial \acute{t}} + \acute{s}(\acute{t}, \acute{z}) \tag{27.VI}$$

where the equation parameters are defined as:

$$\acute{v} = 1 \Big/ \sqrt{\left(\frac{b^2/v^2 - a^2}{c^2 - d^2/v^2}\right)} \tag{28.VIa}$$

$$\gamma = 2\left(\frac{bd/v^2 - ac}{c^2 - d^2/v^2}\right) \tag{28.VIb}$$

$$\acute{s}(\acute{t}, \acute{z}) = \frac{s(\acute{t}, \acute{z})}{c^2 - d^2/v^2} \tag{28.VIc}$$

As an example, if we chose a space-time transformation in which the factor γ is to be identically zero, one has the condition:

$$bd/v^2 - ac = 0 \tag{29.VI}$$

Now we have a mapped computational problem governed by (20.VI) by a new problem which is governed by (27.VI) that has the same mathematical form. However, we changed the frequency and the CFL limit such as:

$$\Delta \acute{t}_{CFL} = \frac{\Delta \acute{z}}{\acute{v}} \tag{30.VIa}$$

Instead of

$$\Delta t_{CFL} = \frac{\Delta z}{v} \tag{30.VIb}$$

The main objective of this approach is to search for the space-time transformation that will change the CFL limit to finally decrease the huge number of iterations at low frequencies.

Further research should be done to know the limitations of this proposed approach and its potential advantages and to develop systematic techniques to find the useful transformation.

6.7.3 Applying local transformation optics

Another approach to solve for the low-frequency case is to use the techniques of transformation optics (TO) [28.VI] that was presented in chapter II. It consists to apply some coordinate transformations to regions with fine details to magnify them. Hence, fine details and their related issues will disappear in the new transformed domain.

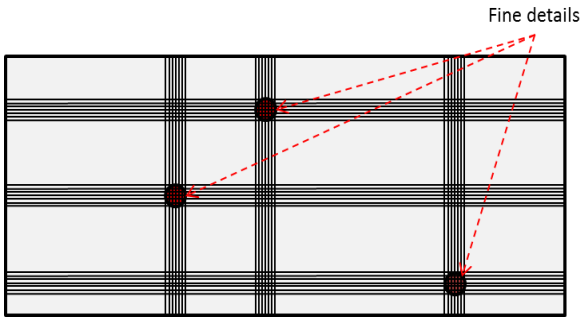

Figure 3.VI, original multi-scale computational domain

As we can see in figure 3.VI, after the appropriate coordinate transformation one obtains a computational domain with no fine-details as shown in figure 4.VI.

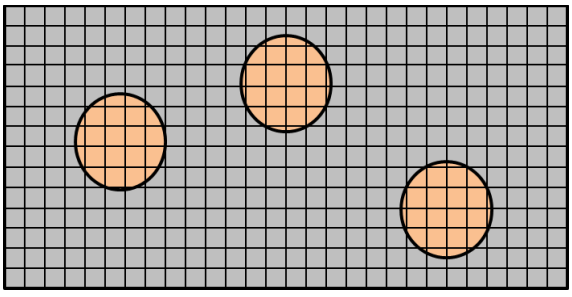

Figure 4.VI, transformed computational domain

Example with thin wire

Consider a computational domain that includes a thin wire (as a fine object). Instead of doing simulation of the structure that includes those thin wires directly, we will apply TO to avoid the usage of very small cells. To show its effectiveness, we solve the above problem in two dimensions by considering the 2D scattering of a very thing wire by cylindrical electromagnetic waves as shown in figure 5.VIa.

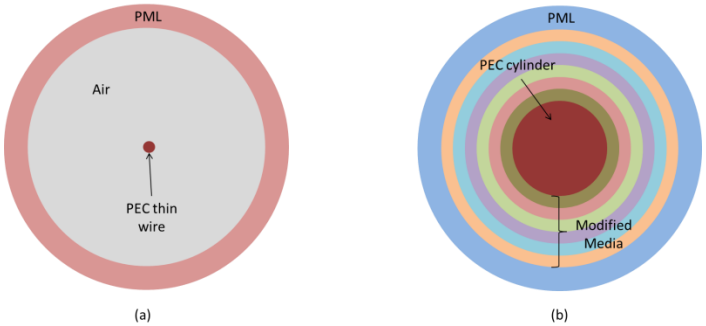

Figure 5.VI, cross sections of a cable with a thin wire, (a) original domain, (b) tranformed domain

To show the effectiveness of TO, we solve the above problem in two dimensions in transforming the original problem to the geometry shown in figure 5.VIb. If we apply TO directly in Cartesian coordinates, we wind up with a two-dimensional transformation. However, if we use cylindrical coordinate system, the transformation takes place only along the radial direction, because of the symmetry. Starting from the relation between cylindrical and Cartesian coordinate systems [28.VI]:

$$\rho = \sqrt{x^2 + y^2} \tag{31.VIa}$$

$$\phi = \tan^{-1}\left(\frac{y}{x}\right) \tag{31.VIb}$$

$$z = z \tag{31.VIc}$$

we obtain the Jacobian matrix of the transformation:

$$\Lambda_1 = \begin{pmatrix} \cos(\phi) & -\rho\sin(\phi) & 0 \\ \sin(\phi) & \rho\cos(\phi) & 0 \\ 0 & 0 & 1 \end{pmatrix} \tag{32.VI}$$

An interesting fact is that, in such coordinate system, the free-space permittivity and permeability tensors become diagonal [28.VI]:

$$\bar{\bar{\varepsilon}}_r = \bar{\bar{\mu}}_r = \frac{\Lambda_1 {\Lambda_1}^t}{\det(\Lambda_1)} = \begin{pmatrix} \rho & 0 & 0 \\ 0 & 1/\rho & 0 \\ 0 & 0 & \rho \end{pmatrix} \tag{33.VI}$$

Now, we apply the radial geometry transformation to enlarge the size of the thin wire to become a cylinder of large diameter, as shown in figure 6.VI.

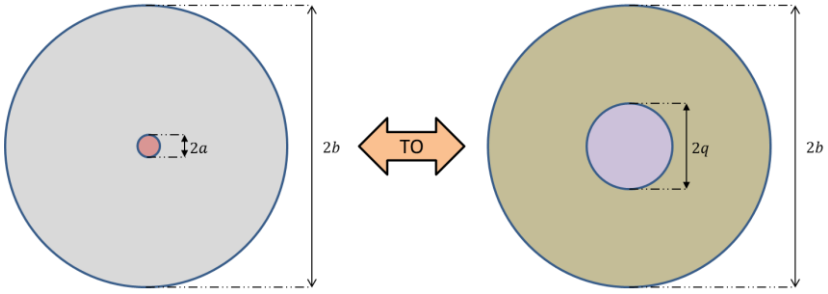

Figure 6.VI, original thin wire or radius ***a*** transforms to a big cylinder of radius *q*

Thus, one has the transformation:

$$\acute{\rho} = \begin{cases} \frac{q}{a}\rho, \ 0 \le \rho \le a \\ q + (b-q)\frac{(\rho-a)}{b-a}, \ a \le \rho \le b \end{cases} \tag{34.VIa}$$

$$\acute{\phi} = \phi \tag{34.VIb}$$

$$\acute{z} = z \tag{34.VIc}$$

The Jacobian of the above coordinate transformation (34.VI) is:

$$\Lambda_2 = \begin{cases} \begin{pmatrix} \frac{q}{a} & 0 & 0 \\ 0 & 1 & 0 \\ 0 & 0 & 1 \end{pmatrix} & , \ 0 \le \rho \le a \\ \begin{pmatrix} \frac{b-q}{b-a} & 0 & 0 \\ 0 & 1 & 0 \\ 0 & 0 & 1 \end{pmatrix} , & a \le \rho \le b \end{cases} \tag{35.VI}$$

We see that this Jacobian matrix is not continuous across the domain. However, the geometric transformation (34.VIa) is continuous, which is of crucial importance. If it is not the case, either there will be holes of undefined regions in the computational domain, or some regions will overlap. In both cases, the resulting complexity makes the new problem more difficult to solve.

Since the thin wire is assumed to be a PEC, no fields propagate inside it. Thus, the computational region is outside this thin wire, or outside the cylinder in the transformed domain. After this transformation, the material properties in cylindrical coordinates can be found by using table1.II (see chapter II):

$$\bar{\bar{\varepsilon}}_r = \bar{\bar{\mu}}_r = \frac{\Lambda_2 \left(\frac{\Lambda_1 \Lambda_1{}^t}{\det(\Lambda_1)} \right) \Lambda_2}{\det(\Lambda_2)} = \frac{b-a}{b-q} \begin{pmatrix} w_1 & 0 & 0 \\ 0 & w_2 & 0 \\ 0 & 0 & w_3 \end{pmatrix} \tag{36.VI}$$

where, w_1, w_2, w_3 are defined by:

$$w_1 = \left(\frac{b-q}{b-a} \right)^2 \left((\acute{\rho} - q) \frac{b-a}{b-q} + a \right) \tag{37.VIa}$$

$$w_2 = \left((\acute{\rho} - q) \frac{b-a}{b-q} + a \right)^{-1} \tag{37.VIb}$$

$$w_3 = \left((\acute{\rho} - q) \frac{b-a}{b-q} + a \right) \tag{37.VIc}$$

The final step in this procedure is to come back to the Cartesian coordinate system by using:

$$x = \acute{\rho} \cos(\acute{\phi}) \tag{38.VIa}$$

$$y = \acute{\rho} \sin(\acute{\phi}) \tag{38.VIb}$$

$$z = \acute{z} \tag{38.VIc}$$

The previous coordinate transformations have been performed to transform the thin wire in (x, y, z) original Cartesian coordinate system, into a cylinder with a relatively large radius in the same Cartesian coordinate system. Finally, the overall effect of these transformations on the media constitutive parameters outside the PEC cylinder is given by [28.VI]:

$$\bar{\bar{\varepsilon}}_r = \bar{\bar{\mu}}_r = \begin{pmatrix} \frac{\partial \acute{\rho}}{\partial \rho}\frac{\rho x^2}{\acute{\rho}^3} + \frac{\partial \rho}{\partial \acute{\rho}}\frac{y^2}{\acute{\rho}\rho} & \frac{\partial \acute{\rho}}{\partial \rho}\frac{xy}{\acute{\rho}^2} - \frac{\partial \rho}{\partial \acute{\rho}}\frac{xy}{\acute{\rho}\rho} & 0 \\ \frac{\partial \acute{\rho}}{\partial \rho}\frac{\rho xy}{\acute{\rho}^2} - \frac{\partial \rho}{\partial \acute{\rho}}\frac{xy}{\acute{\rho}\rho} & \frac{\partial \acute{\rho}}{\partial \rho}\frac{\rho y^2}{\acute{\rho}^3} + \frac{\partial \rho}{\partial \acute{\rho}}\frac{x^2}{\acute{\rho}\rho} & 0 \\ 0 & 0 & \frac{\partial \rho}{\partial \acute{\rho}}\frac{\rho}{\acute{\rho}} \end{pmatrix} \tag{39.VI}$$

Now, it is possible to perform the simulations for the transformed domain with a solver that can handle such complex media and determine all the necessary fields. Once calculated, we apply the inverse coordinate transformation as described in chapter II.

This approach may be also very useful for frequency domain techniques, for instance in FEM method, even though time-step in frequency-domain methods is not relevant. The mesh can be non-hexahedral and irregular. However, to have an accurate solution, certain growth factor in the irregular meshing should be limited to low values. For instance, one may need to mesh very finely a region with small details while the adjacent region (for example air-filled) can be meshed with much larger cells. Therefore, to avoid the problem mentioned above, the cell size must gradually increase towards the region where much larger meshes are used. This is illustrated by figure 7.VI and figure 8.VI.

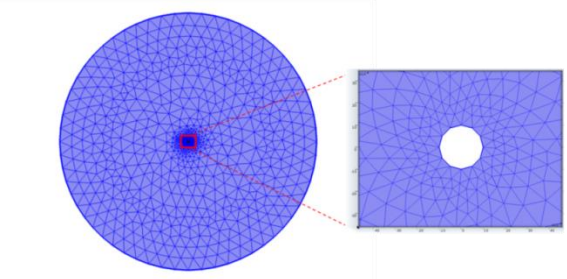

Figure 7.VI, original domain discretized (thin PEC wire of radius 1mm). The number of cells is 1732. Mesh created using COMSOL.

In both experiments we excited the structure by a current flowing in the wire in the z-direction (where the axe z is parallel to the cylinder axis), at the frequency of 1 GHz. This produces cylindrical waves with E_z polarization. These waves will exhibit the same polarization in both scenarios (because the axis-symmetry is conserved after transformation in this case).

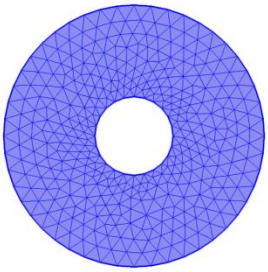

Figure 8.VI, transformed domain discretized (PEC cylinder of radius 30 cm). The number of cells is 672. Mesh created using COMSOL.

In figure9.VI we see the scattered E_z field of the original problem of the thin-wire. In figure 10.VI we see the scattered E_z field in the transformed domain.

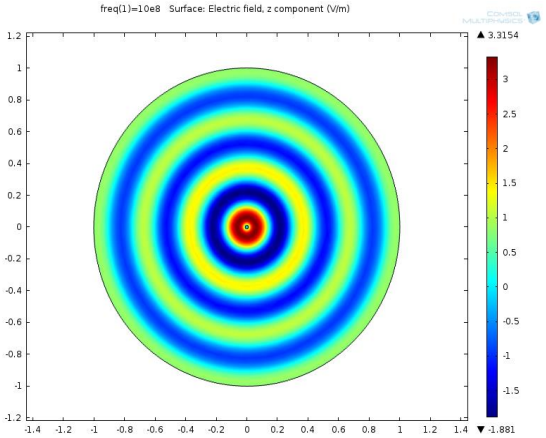

Figure 9.VI, cylindrical wave E_z-component generated by the z-oriented current in the thin wire located at the center of the 2D computational original domain. Simulation by using COMSOL

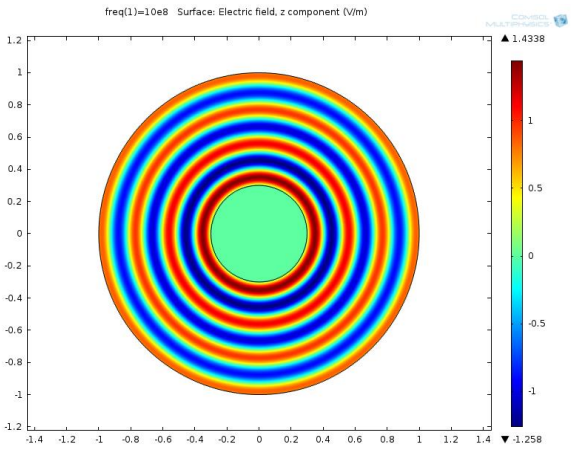

Figure 10.VI, cylindrical wave E_z- component generated by the z-oriented current in the thin wire located at the center of the 2D computational transformed domain. Simulation by using COMSOL

As shown in figure 11.VI, we compared the E_z results of the original problem through the radial direction ρ with the results of the transformed domain after performing the inverse coordinate transformations (see chapter II, section 2.6) of figure 10.VI. In figure 11.VI we can see some very good agreement between both numerical approaches namely, the direct solution and the TO approach by COMSOL, with the analytical solution [1.VI].

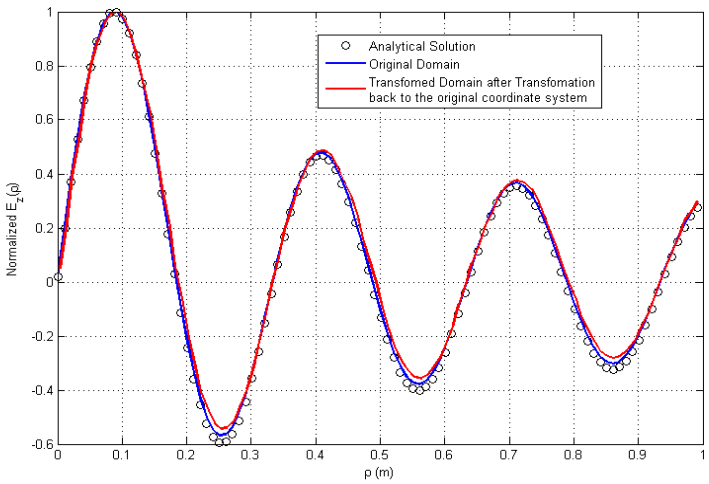

Figure 11.VI, normalized electric field $E_z(\rho)$ component along the radial direction, comparison between analytical and numerical solutions generated by COMSOL

The original problem with the thin-wire illustrated in figure 7.VI was solved with COMSOL using 1732 elements, while for the transformed domain (figure 8.V) the system matrix

was reduced to 672 elements. This is a considerable difference, either in terms of memory or in computational time. However, there is a price to pay. If we refer to (47.VI), it is obvious that the transformed domain contains complex media (fully anisotropic tensors) which is usually more difficult to simulate than isotropic media.

The previous experiment was carried out by a frequency domain commercial solver for simplicity. However, the time domain techniques can benefit from this mapping technique as well. Hence, after the appropriate coordinate transformations these fine details become of normal size compared to the other objects in the computational domain and eventually decrease the memory requirement. Furthermore, there is no longer need for using a very small time step; hence, the low-frequency problem can be solved more efficiently. However, there is also a price to pay for time-domain methods: after the transformation, we have to simulate anisotropic media (note that the TLM solver described in chapter V can do it). In addition, for open problems a full implementation of PML that can truncate any full tensor linear media (which has not been implemented yet to our TLM solver) is necessary.

The mapping approach presented here for the moment is limited for only PEC fine details, because the PEC properties don't change with transformation. Further studies should be done for applying this approach to other kind of media. Moreover, a complete theory must be developed to systematically find the suitable coordinate transformation that can magnify the fine details smoothly, yet without producing new-fine details in other regions in the new computational domain.

6.8 Volumic time-domain methods in presence of highly contrasted media and irregular structured meshes with high transition ratios.

Time-domain techniques in electrodynamics are mainly concerned in solving both Maxwell's curl equations [9.VI]. To solve those curl equations using direct discretization of Maxwell's equations, one can apply either the FDTD scheme for the curl equations in differential form or the FIT scheme for the same equations in integral form. Both the FDTD and FIT requires an important assumption due to the discretization scheme: electric and magnetic

fields are defined within two different meshes in space. When using hexahedral meshes either in FDTD or in FIT, both meshes are staggered by a half-step size from each other.

This half-step staggering between electric and magnetic field meshes allows a minimum number of field samples to be manipulated and stored. But there is a price to pay: the loss of the locality concept in the constitutive parameters, hence, the interaction between the media and the electric or magnetic fields does not happen at the same location and time. While in a homogeneous medium this issue is negligible, it becomes clear when handling nonhomogeneous media especially when the contrast is high between both sides of the interface.

Figure 12.VI and Figure 13.VI show the fields updating process at the interface between two different media for both the magnetic H_z, and the electric E_y, respectively. The dielectric interface must run as shown to enforce the tangential electric field continuity. All field update equations can be found in [9.VI].

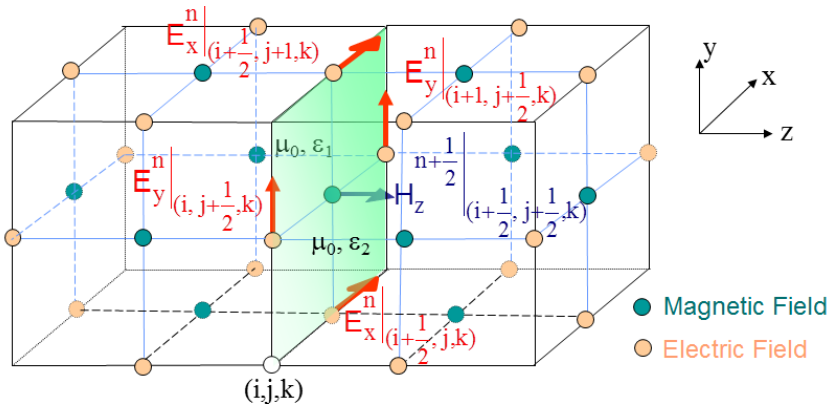

Figure 12.VI, magnetic field updating in Yee scheme

For instance, the update equation for the magnetic field component H_z, relevant to figure 12.VI is given by Faraday's law in finite difference form:

$$H_z\big|_{i+\frac{1}{2},j+\frac{1}{2},k}^{n+\frac{1}{2}} = H_z\big|_{i+\frac{1}{2},j+\frac{1}{2},k}^{n-\frac{1}{2}} + \frac{\Delta t}{\mu_{i+\frac{1}{2},j+\frac{1}{2},k}}\left(\frac{E_x\big|_{i+\frac{1}{2},j+1,k}^{n} - E_x\big|_{i+\frac{1}{2},j,k}^{n}}{\Delta y} - \frac{E_y\big|_{i+1,j+\frac{1}{2},k}^{n} - E_y\big|_{i+1,j+\frac{1}{2},k}^{n}}{\Delta x} + J_z\big|_{i+\frac{1}{2},j+\frac{1}{2},k}^{n+\frac{1}{2}}\right) \tag{40.VIa}$$

As both media across the interface are assumed to have the same permeability, there is no ambiguity to apply the above update across the interface separating both dielectric media.

Now, consider the update equation for the electric field component E_y relevant to figure 13.VI. From Ampère's law, the finite-difference form yields:

$$E_y|_{i,j+\frac{1}{2},k}^{n+1} = E_y|_{i,j+\frac{1}{2},k}^{n} + \frac{\Delta t}{\varepsilon_{i,j+\frac{1}{2},k}} \left(\frac{H_x|_{i,j+\frac{1}{2},k+\frac{1}{2}}^{n+\frac{1}{2}} - H_x|_{i,j+\frac{1}{2},k-\frac{1}{2}}^{n+\frac{1}{2}}}{\Delta z} - \frac{H_z|_{i+\frac{1}{2},j+\frac{1}{2},k}^{n+\frac{1}{2}} - H_z|_{i-\frac{1}{2},j+\frac{1}{2},k}^{n+\frac{1}{2}}}{\Delta x} \right) \qquad \text{(40.VIb)}$$

Here, there is some ambiguity as both media across the interface are assumed to have different permittivity and a single value is needed by (40.VIb) exactly on the interface. One way to overcome the problem is to average the loop integrals around partial path on each side of the interface. It is easy to show that this results exactly in considering the average permittivity around the entire loop across the interface.

A dual reasoning can be easily made for an interface between two magnetic media. It can be felt that the evaluation of the update equations will be even more critical if the interface separates two complex media, for instance being both dielectric and magnetic.

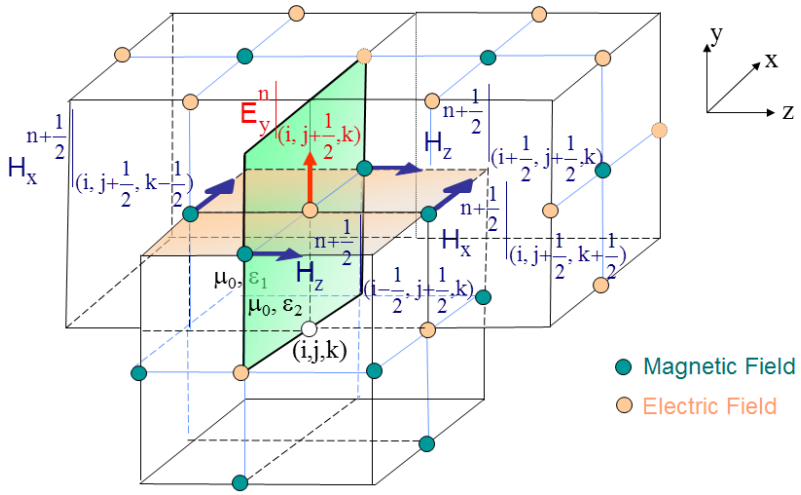

Figure 13.VI, electric field updating in Yee scheme

In literature, various types of averaging were reported [29.VI]. In table 1.VI, we can see three ways to perform the approximation namely, using arithmetic mean, harmonic mean or geometric mean. Whatever the kind of averaging we use, some error occurs at the interface. Note that the error obviously decreases as the mesh size is reduced. Finally, the staggering between

electric and magnetic field meshes also exists in FIT and some averaging must also be applied as in FDTD [30.VI]. However, in this chapter we only address this issue for FDTD method, which, in case of hexahedral cells, have the same operator.

One important point to highlight here is that this averaging issue is completely different from numerical dispersion phenomenon. While the latter is due to the discretization of continuous system as discussed in chapter IV (usually the equations of dispersion are derived for homogenous medium only), the former comes from the presence of interface between different media and hence appears in nonhomogeneous media.

Table 1.VI, different kinds of media properties averaging at the interface [29.VI]

Averaged Constitutive parameter	Arithmetic mean	Harmonic mean	Geometric mean
$\mu_{i,j+\frac{1}{2},k+\frac{1}{2}}$	$\frac{\mu_{i,j,k}+\mu_{i+1,j,k}}{2}$	$\frac{2\mu_{i,j,k}\mu_{i+1,j,k}}{\mu_{i,j,k}+\mu_{i+1,j,k}}$	$\sqrt{\mu_{i,j,k}\mu_{i+1,j,k}}$
$\mu_{i+\frac{1}{2},j,k+\frac{1}{2}}$	$\frac{\mu_{i,j,k}+\mu_{i,j+1,k}}{2}$	$\frac{2\mu_{i,j,k}\mu_{i,j+1,k}}{\mu_{i,j,k}+\mu_{i,j+1,k}}$	$\sqrt{\mu_{i,j,k}\mu_{i,j+1,k}}$
$\mu_{i+\frac{1}{2},j+\frac{1}{2},k}$	$\frac{\mu_{i,j,k}+\mu_{i,j,k+1}}{2}$	$\frac{2\mu_{i,j,k}\mu_{i,j,k+1}}{\mu_{i,j,k}+\mu_{i,j,k+1}}$	$\sqrt{\mu_{i,j,k}\mu_{i,j,k+1}}$
$\varepsilon_{i+\frac{1}{2},j,k}$	$\frac{\varepsilon_{i,j,k}+\varepsilon_{i+1,j,k}}{2}$	$\frac{2\varepsilon_{i,j,k}\varepsilon_{i+1,j,k}}{\varepsilon_{i,j,k}+\varepsilon_{i+1,j,k}}$	$\sqrt{\varepsilon_{i,j,k}\varepsilon_{i+1,j,k}}$
$\varepsilon_{i,j+\frac{1}{2},k}$	$\frac{\varepsilon_{i,j,k}+\varepsilon_{i,j+1,k}}{2}$	$\frac{2\varepsilon_{i,j,k}\varepsilon_{i,j+1,k}}{\varepsilon_{i,j,k}+\varepsilon_{i,j+1,k}}$	$\sqrt{\varepsilon_{i,j,k}\varepsilon_{i,j+1,k}}$
$\varepsilon_{i,j,k+\frac{1}{2}}$	$\frac{\varepsilon_{i,j,k}+\varepsilon_{i,j,k+1}}{2}$	$\frac{2\varepsilon_{i,j,k}\varepsilon_{i,j,k+1}}{\varepsilon_{i,j,k}+\varepsilon_{i,j,k+1}}$	$\sqrt{\varepsilon_{i,j,k}\varepsilon_{i,j,k+1}}$

It is worth to mention that in the TLM approach presented in chapter III, the treatment of interface between different media doesn't appear explicitly. This is because in TLM-SCN based algorithm all voltages interactions happen in free-space. The material presence is taken into account using the correction process at the center of the cell. This means that the cell with its

specific constitutive parameters is a single entity. Furthermore, the field update equations imply only the cell media properties which are always homogeneous. Indeed, TLM cell boundaries are always located on media interfaces (if they exist) whether dielectric, magnetic or both. Finally, note that, tangential field components continuity is enforced at all-time steps by the voltage exchange process.

In the following section we present several numerical experiments to show how TLM and FDTD behave as the contrast between two media increases. As it is well-known that TLM is less dispersive than FDTD, one has to make sure that any result that would favor TLM is not due to the higher dispersion of the FDTD. Consequently, one chose spatial step values largely below the ones used normally for simulations.

6.8.1 Modes cutoff frequencies in a rectangular waveguide partially filled by dielectric

In this experiment, we compute the dominant mode cutoff frequency in the rectangular waveguide whose cross-section is with dimensions $a = b = 10\ cm$ and half-filled by a dielectric slab of permittivity ε_r as illustrated in figure 14.VI.

The objective of this experiment is to study the effect of the interface between the two dielectrics (the air and the dielectric slab) using both TLM and FDTD methods. Analytical solution is taken as a reference for comparison [31.VI] [32.VI].

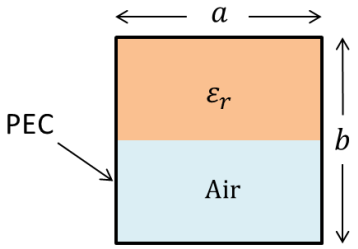

Figure 14.VI, cross section of a waveguide partially filled with dielectric

Note that in this experiment,, the dominant mode cutoff frequency f is not constant inside the waveguide, since it is material depended. However, for standardizing the comparison criteria and because all dominant modes cutoff frequencies for the different values of permittivity were

less than 1.3 GHz, we chose that upper frequency limit as the maximum frequency range in the simulation. The value $\varepsilon_r = 40.0$ was taken as a reference in calculating λ_d defined as:

$$\lambda_d = \frac{c_o}{f\sqrt{\varepsilon_r}} \tag{41.VI}$$

because it defines the shortest wavelength. One has to remember that using 10-cells/wavelength or more allows one to neglect numerical dispersion effects. Finally, we used cubic cells, and we performed the FDTD and the TLM for 100000 iterations, with maximum time step used for TLM and half the Von-Neumann limit for the FDTD, to ensure stability.

In figure 15.VI, we study the relative error in calculating the dominant mode in the waveguide as compared to the analytical solution for various values of permittivity and various spatial discretization. As observed, the TLM algorithm over performs the FDTD for the same spatial step-size. Furthermore, we can observe the effect of increasing the permittivity on the relative error in FDTD: it increases monotonically as the contrast increases whereas it remains quite stable for TLM. We can also note that the TLM algorithm with 10 cells per wavelength, yields an accuracy similar to FDTD with 40 cells per wavelength for high contrast. On the other hand, when the contrast is low all curves tend to give similar results.

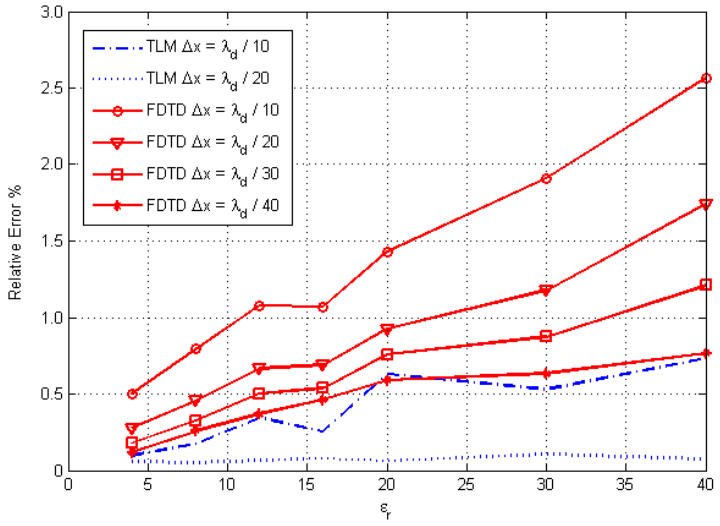

Figure 15.VI, Numerical scheme relative error, with respect to the analytical solution, of the dominant mode cutoff frequency of the dielectric loaded waveguide of figure 14.VI as a function of relative permittivity

6.8.2 Scattering parameters from periodic slabs in a parallel-plate waveguide

In this experiment, we study the reflection coefficient of TEM wave in a parallel-plate waveguide produced by a one-dimensional structure composed of several dielectric layers. This structure consists of consecutive interleaved dielectric layers with free-space gaps as shown in figures 16.VI and 17.VI.

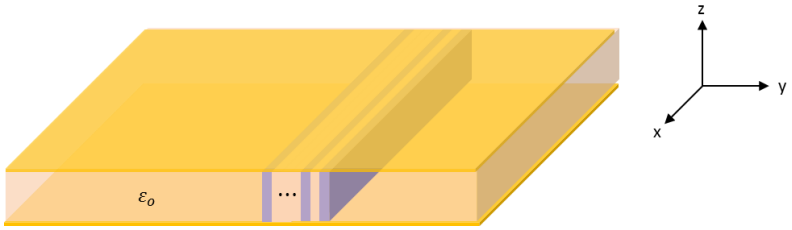

Figure 16.VI, parallel plate waveguide loaded by 8 dielectric slabs each of width 4 mm and separated by 4 mm

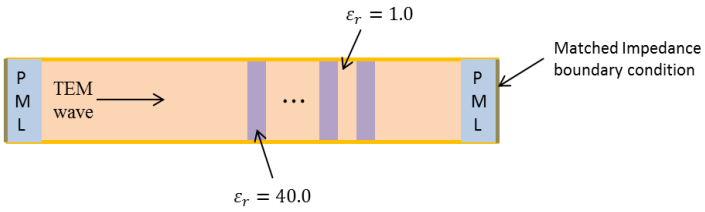

Figure 17.VI, side cross-section of figure 16.VI

To respect the numerical dispersion criteria for both TLM and FDTD methods, we consider the wavelength in the dielectric material:

$$\lambda_d = \frac{c_o}{max(\sqrt{\varepsilon_r}) f_{max}} = 15.811\ mm \tag{42.VIa}$$

and select the spatial mesh size:

$$\Delta x \leq \frac{\lambda_d}{10} \cong 1.58\ \ mm \tag{42.VIb}$$

In figure 18.VI we show a comparison between FDTD and TLM methods, taking the analytical solution as a reference. As observed, the FDTD curves approach the analytical solution as the mesh size decreases. However, it is clear that the TLM outperforms the FDTD even when TLM uses a mesh size which is 3 times larger than the one used for FDTD.

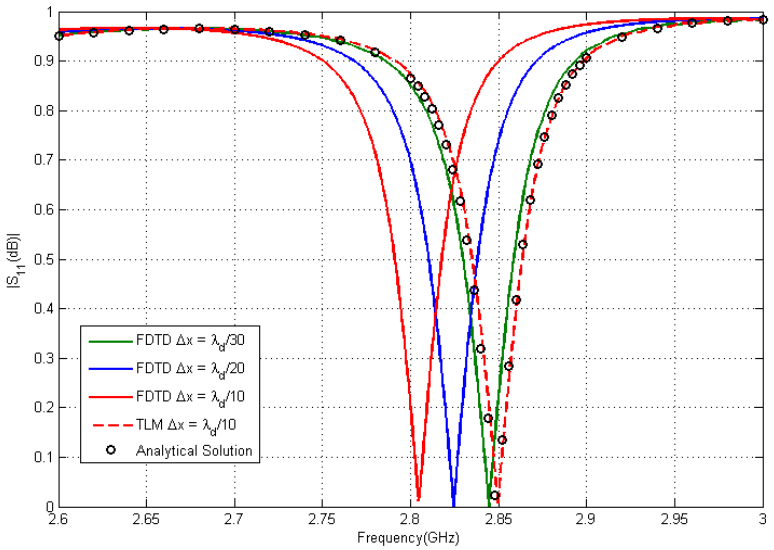

Figure 18.VI, case of figure 17.VI: reflection coefficient as a function of frequency, comparison between FDTD, TLM and the analytical solution for different spatial-step values

The numerical dispersion of FDTD and TLM cells is negligible when using a mesh size of 10 cells / wavelength or more. This means that the source of error in FDTD simulations is not mainly due to the numerical dispersion but to the high contrast between the periodic slabs. One should mention that in [33.VI] authors reached a similar conclusion that TLM shows better performance that FIT in highly contrasted media, for the same spatial level of discretization. The structure under test was highly heterogeneous and with significant differences between media (computational dosimetry). It is mentioned that the ambiguity at interfaces may be the source of the slow convergence of the FIT as compared to TLM computations.

6.8.3 The effect of irregular structured meshing

Extending the same reasoning of the previous section, we can expect that at the interface between two regions of different mesh size, we will face a similar issue. Consider a computational domain with irregular meshing which is filled by a homogenous medium. Let us

analyze field update equations at the interface between two regions with different mesh sizes as shown in figure19.VI.

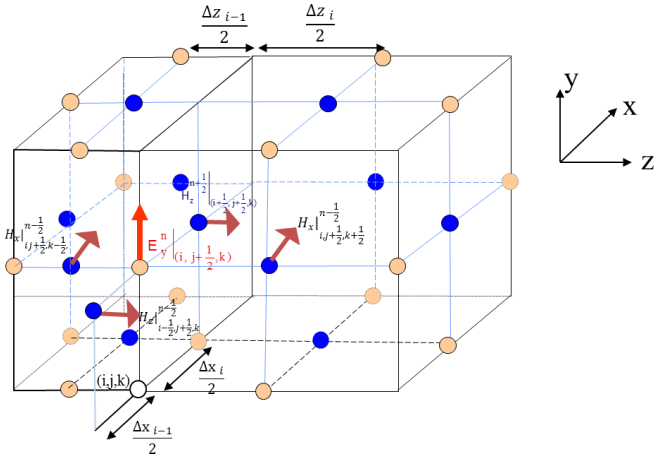

Figure 19.VI, electric field z- component at the interface bwteen two differnt mesh size.

For instance, magnetic and electric field component in the y-direction are expressed by finite-difference equations [9.VI]:

$$E_y|_{i,j+\frac{1}{2},k}^{n+1} = E_y|_{i,j+\frac{1}{2},k}^{n} + \frac{\Delta t}{\varepsilon_{i,j+\frac{1}{2},k}}\left(\frac{H_x|_{i,j+\frac{1}{2},k+\frac{1}{2}}^{n+\frac{1}{2}} - H_x|_{i,j+\frac{1}{2},k-\frac{1}{2}}^{n+\frac{1}{2}}}{\Delta h_{z_i}} - \frac{H_z|_{i+\frac{1}{2},j+\frac{1}{2},k}^{n+\frac{1}{2}} - H_z|_{i-\frac{1}{2},j+\frac{1}{2},k}^{n+\frac{1}{2}}}{\Delta h_{x_i}}\right) \quad (43.\text{VIa})$$

$$H_y|_{i+\frac{1}{2},j,k+\frac{1}{2}}^{n+\frac{1}{2}} = H_y|_{i+\frac{1}{2},j,k+\frac{1}{2}}^{n-\frac{1}{2}} + \frac{\Delta t}{\mu_{i+\frac{1}{2},j,k+\frac{1}{2}}}\left(\frac{E_z|_{i+1,j,k+\frac{1}{2}}^{n} - E_z|_{i,j,k+\frac{1}{2}}^{n}}{\Delta x_i} - \frac{E_x|_{i+\frac{1}{2},j,k+1}^{n} - E_x|_{i+\frac{1}{2},j,k+1}^{n}}{\Delta z_i} + J_y|_{i+\frac{1}{2},j,k+\frac{1}{2}}^{n+\frac{1}{2}}\right) \quad (43.\text{VIb})$$

where the averaged spatial steps Δh_{x_i} and Δh_{z_i} are defined as:

$$\Delta h_{x_i} = \frac{\Delta x_i + \Delta x_{i-1}}{2} \quad (44.\text{VIa})$$

$$\Delta h_{z_i} = \frac{\Delta z_i + \Delta z_{i-1}}{2} \quad (44.\text{VIb})$$

As we can notice, that at the interface between two different mesh sizes, the FDTD scheme is no longer a central difference. As a result, the error is no longer of order $O((\Delta x)^2)$ but higher, depending on the ratio between cell sizes on sides of the interface.

In the following experiments, we will compare both the FDTD and TLM methods in presence of irregular (but structured) meshing in terms of cell ratios. Figure 20.VI shows a top view of an irregularly meshed parallel-plate waveguide. For this structure, we calculate the level of parasitic reflections that occur from the interface between differently meshed zones. The computational domain is terminated at both sides by PML absorbing boundary conditions. Moreover, to ensure exact plane wave excitation (TEM mode) we used PEC at the top and bottom of the waveguide, and PMC at both sides. For wideband excitation, we applied a modulated-Gaussian pulse with parameters $f_o = 10.0\ GHz, \sigma = 30\Delta t$ and $t_o = 300\Delta t$ and we run the experiment for 40000 iterations until all fields practically vanished. Then, we calculated the reflection coefficient over the range of frequencies from 8 to 13 GHz.

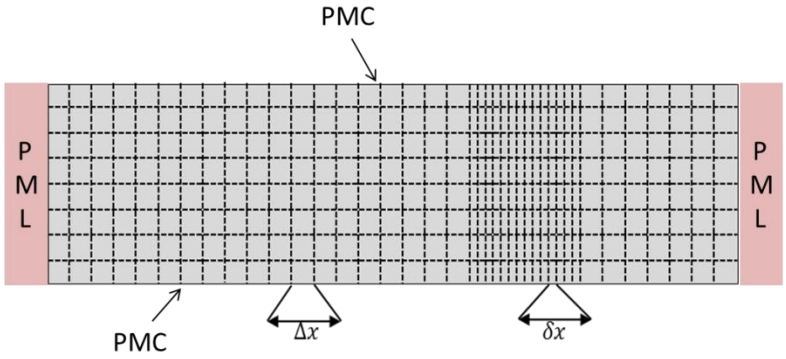

Figure 20.VI, top view of the parallel plate waveguide showing the structured irregular mesh

One can expect that the error produced by the irregular meshing will depend on the ratio between mesh sizes $\Delta x/\delta x$ (see figure 20.VI). It can be reasonably expected that the level of parasitic reflections will increase with that ratio. In figure 21.VI, we show the reflection coefficient from the irregularly meshed slab. To ensure a negligible numerical dispersion we used very small mesh size (75 cells / wavelength). We can observe that the reflection coefficient increases with the ratio $\Delta x/\delta x$. The reflection coefficient in case of regular meshing was around -100 dB; hence, the reflection levels observed are indeed due to irregular meshing.

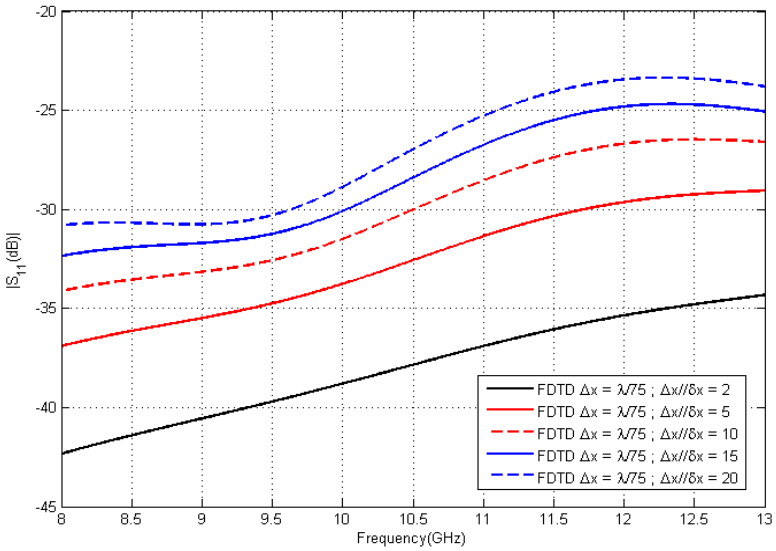

Figure 21.VI, reflection coefficient from irregularly meshed regions for different mesh ratios using FDTD method.

Case of figure 20.VI.

In figure 22.VI we show the effect of reducing the mesh size Δx while keeping the ratio $\frac{\Delta x}{\delta x} = 10$ at the interface. As expected, the finer the mesh size, the lower the error due to the irregular meshing. In this experiment, we used very fine meshes to ensure a negligible level of numerical dispersion. One can notice that the TLM method shows better performance at 40 cells / wavelength compared to FDTD, even with 115 cells/wavelength. This can be explained by the fact there is no averaging in TLM-SCN method at the interface between different mesh sizes (in structured meshes).

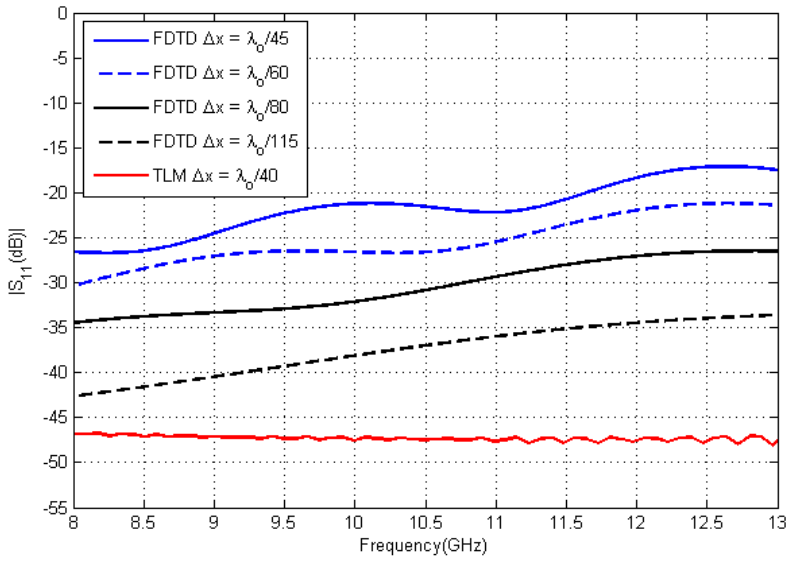

Figure 22.VI, reflection coefficient from irregularly meshed slab (of ratio$\frac{\Delta x}{\delta x} = 10$) for different values of Δx, comparison between FDTD and TLM methods. Case of figure 20.VI.

In figure 23.VI, results for the same experiment are shown for different mesh ratios but, this time, compared with the TLM over the same frequency band. We can observe two phenomena: first, the TLM at 20 cells / wavelength outperforms the FDTD at 100 cells / wavelength for different mesh size ratios. Secondly, in both FDTD and TLM the error increases with the mesh ratio. The inherent error in FDTD explained above is confirmed by these results as the dashed curves move up with the ratio $\frac{\Delta x}{\delta x}$. If this phenomenon is less apparent for the TLM method, as the numerical dispersion increases with the cell aspect ratio, one also observes an increase yet much less rapidly for TLM. It can be explained as follows: the numerical dispersion increases in the cells with higher aspect ratios. That means that the numerical phase velocity is different in the two regions of figure 20.VI; equivalently, the numerical wave impedance in the discretized media is different for different mesh discretization ratios $\frac{\Delta x}{\delta x}$ in the TLM mesh. Thus, parasitic reflections are generated at interfaces as that ratio increases. Note that this source of numerical dispersion error is not restricted to TLM only but also exists in FDTD and hexahedral FIT.

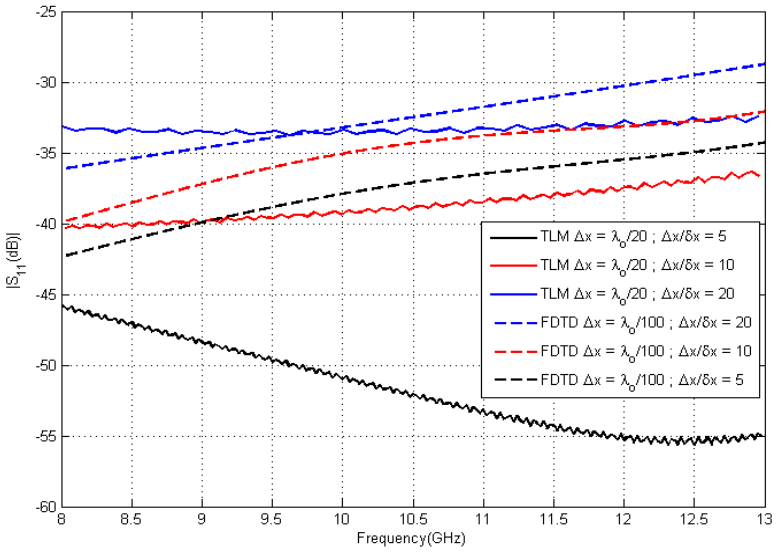

Figure 23.VI, reflection coefficient from irregularly meshed slab for different change ration, comparison between FDTD method and TLM method. Case figure 20.VI

Finally, we performed a simulated experiment regarding an air-filled rectangular waveguide WR90. In this experiment, we calculated the parasitic reflection coefficient in an irregularly meshed TLM computational domain (a transversal slab of 5 δx width in the middle of the waveguide, elsewhere we used cubic cells of dimension Δx). As a TE_{10} wideband excitation, we applied a modulated-Gaussian pulse with parameters $f_o = 10.0\,GHz, \sigma = 30\Delta t$ and $t_o = 300\Delta t$ and we run the experiment for 80000 iterations until all fields practically vanished. Then, we calculated the reflection coefficient over the range of frequencies from 8 to 13GHz. As absorbing boundary condition we used 10-cells PML layer at both ends of the waveguide, and to enhance the absorption characteristics we terminated the PML layer with a Z_o free-space impedance boundary condition. Finally, we used $\Delta x = 1.27\,mm$ and, consequently, the time steps we used were 0.211 ps, 0.14 ps and 0.105 ps for the mesh ratios $\frac{\Delta x}{\delta x} = 10$, $\frac{\Delta x}{\delta x} = 15$ and $\frac{\Delta x}{\delta x} = 20$, respectively.

In figure 24.VI we can see the effects of using different mesh size ratios.

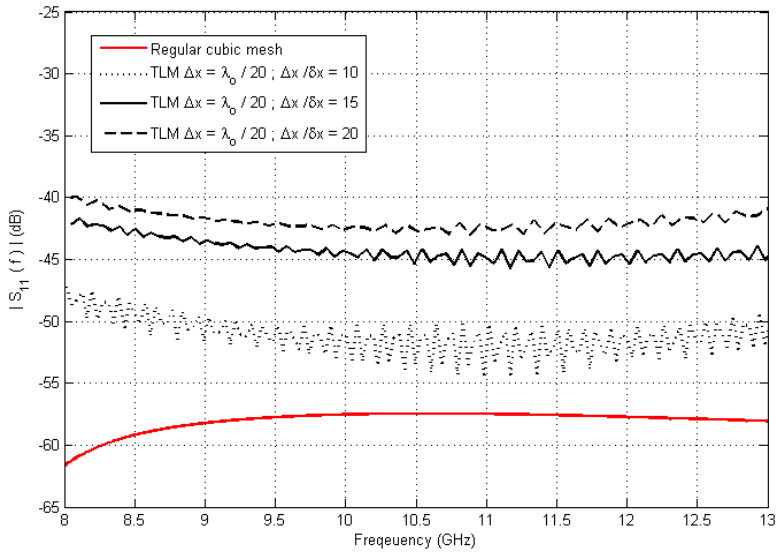

Figure 24.VI, reflection coefficient in an empty WR90 waveguide with irregularly meshed slab

As expected the reflection coefficient increases with the ratio $\frac{\Delta x}{\delta x}$. This can be explained by the effective wave-impedance discretized medium, as mentioned in the previous experiment. Finally, we should mention that the WR90-experiment is very different form the parallel-plate one. Indeed, unlike the TEM mode, the TE_{10} mode impinges at angles which are not normal to the mesh interface and varies with the frequency signal.

6.9 Conclusion

In this chapter, two main issues were discussed. In the beginning, we presented the multi-scale and low-frequency problems in time domain techniques and their associated difficulties. Then, we proposed some novel solutions by applying mapping techniques. They are based on modifying the metric tensor of both space and time domains and transforming the original problem into a well-posed one and easier to solve. However, further research should be done to know the full potentials of these mapping approaches.

In the second part of this chapter, we addressed other challenging cases for time-domain methods namely, their performance in presence of high contrast heterogeneous and high cell ratios in irregular structure mesh. More particularly, comparison between FDTD and TD-TLM methods were carried out. Dedicated numerical experiments were carried out to emphasize the error produced at the interface between two different materials or different meshed regions in homogenous medium. Simulated results clearly confirm that TD-TLM outperforms FDTD method for the same spatial discretization level (especially for highly contrasted media). That means the TD-TLM method needs fewer number of mesh cells than the FDTD to give the same level of accuracy.

References

[1.VI] R. F. Harrington, Time-Harmonic Electromagnetic Fields, John Wiley & Sons, INC., 2001.

[2.VI] M. N. Sadiku, Numerical Techniques in Electromagnetics, CRC Press, July, 2000.

[3.VI] T. Kailath, Linear Systems, Prentice-Hall, 1980.

[4.VI] W. L. Miranker, Numerical Methods for Stiff Equations and Singular Perturbation Problems, D. REIDEL PUBLISHING COMPANY, 1981.

[5.VI] E. Hairer and G. Wanner, Soving Ordinary Differential Equations II Stiff and Differential-Algebraic Problems, Springer, 2010.

[6.VI] A. Miaskowski, *et al*, "Low Frequency FDTD Algorithm and its Application to Inductive Hyperthermia," in *PREZEGLAD ELECTROTECHNICZNY*, 2012.

[7.VI] A. Trakic, *et al*, "Cylindrical 3D FDTD algorithm for the computation of low frequency transient eddy currents in MRI," in *IEEE*, 2006.

[8.VI] B. LABRI, "Modélisation de structures antennaires VLF/LF," PhD thesis; Universite de Nice-Sopia Antipolis, Nice, 2006.

[9.VI] A. Taflove and S. C. Hagness. , Computational Electrodaynamics, The Finite-Difference Time-Domain Method, Norwood: Artch House, INC., 2005.

[10.VI] K. Yee, "Numerical solution of initial boundary value problems involving Maxwell's equation in isotropic media," *IEEE Transactions in Antennas and Propagation*, no. AP-14, pp. 302-307, May 1966.

[11.VI] P. B.Johns, "A Symmetrical Condensed Node for the TLM Method," *IEEE Transactions on Microwave Theory and Techniques*, Vols. MTT-35, no. 4, pp. 370-377, 1987.

[12.VI] S. Le Maguer, *et al*, "Split-Step TLM (SS TLM) - A New Scheme for Accelerating Electromagnetic-Field Simulaion," *IEEE Transactions on Microwave Theory and Techniques*, vol. 52, no. 4, pp. 1182-1190, 2004.

[13.VI] A. P. Zhao, "Analysis of the Numerical Dispersion of the 2-D Alternating-Direction Implicit FDTD Method," *IEEE Transactions on Microwave Theory and Techniques*, vol. 50, no. 4, pp. 1156-1164, 2002.

[14.VI] H. Zhao, *et al*, "A new approach to the solution of Maxwell's equations for low frequency and high-resolution biomedical problems," in *Austral. Mathematical Soc*, 2003.

[15.VI] B.n. Jiang, J. Wu and L. A. Povinelli, "The Orign of Spurious Solutions in Computational Electromagnetics," NASA Techniqal Memorandum 106921 ICOMP-95-8, 1995.

[16.VI] S. Le Maguer and M. M. Ney, "Extended PML-TLM node: an efficient approach for full-wave analysis of open structures," *Intnational Journal of Numerical Modelling* , vol. 14, pp. 129-144, 2001.

[17.VI] J.S. Zhao and W. C. Chew, "Integral Equation Solution of Maxwell's Equations from Zero Frequency to Microwave Frequencies," *IEEE Transactions on Antennas and Propagation,* vol. 48, no. 10, pp. 1635-1645, 2000.

[18.VI] S. M. Rao, D. R. Wilton and A. W. Glisson, "Electromagnetic Scattering by Surfaces of Arbitrary Shape," *IEEE Transactions on Antennas and Propagation,* Vols. AP-30, no. 3, pp. 409-418, 1982.

[19.VI] F. P. Andriulli, "Loop-Star and Loop-Tree Decompositions: Analysis and Efficient Algorithms," *IEEE Transactions on Antennas and Propagation,* vol. 60, no. 5, pp. 2347-2356, 2012.

[20.VI] S. Lee and J. Jin, "Application of the tree-cotree splitting for improving matrix conditioning in the full-wave finite-element analysis of high-speed circuits," *Microwave and Optical Technology Letters,* vol. 50, no. 6, pp. 1476-1481, 2008.

[21.VI] D. M. Yang Xia, "Underwater FDTD Simulation at Extremely Low Frequencies," *IEEE Antennas and Wireless Propagation Letters,* vol. 7, 2008.

[22.VI] T. Namiki, "3-D ADI-FDTD Method – Unconditionally Stable Time-Domain Algorithm for Solving Full Vector Maxwell's Equations," *IEEE Transactions on Microwave Theory and Techniques,* vol. 48, no. 10, 200.

[23.VI] E. L. Tan, "Unconditionally Stable LOD-FDTD Method for 3-D Maxwell's Equations," *IEEE Microwave and Wireless Components Letters,* vol. 17, no. 2, 2007.

[24.VI] A. V. Oppenheim and R. W. Schafer, Discrete-Time Signal Processing, Prentice Hall; 3 edition, 2009.

[25.VI] S. Carroll, Spacetime and Geometry: An Introduction to General Relativity, 2003: Addison-Wesley.

[26.VI] J. D. Jackson, Classical Electrodynamics, JOHN WILEY & SONS, INC., 1999.

[27.VI] D. Lovelock and H. Rund, Tensors, Differential Forms, and Variational Principles, 1989: Dover Publications, INC., New York.

[28.VI] N. B. Kundtz, D. R. Smith and J. B. Pendry, "Electromagnetic Design With Transformation Optics," *Proceedings of the IEEE,* vol. 99, no. 10, pp. 1622-1633, October October2011.

[29.VI] K.P. Hwang and A. C. Cangellaris, "Effective Permittivities for Second-Order Accurate FDTD Equations at Dielectric Interfaces," *IEEE Microwave and Wireless Components Letters,* vol. 11, no. 4, pp. 158-160, 2001.

[30.VI] M. Clemens and T. Weiland, "Discrete Electromagnetism with the Finite Integration Technique," *Progress In Electromagnetics Research,* vol. 32, pp. 65-87, 2001.

[31.VI] M. P. Mladenovic, A. S. Marinic and B. D. Milovanovic, "Calculation Of Resonances Of Microwave Resonator Loaded With Inhomogeneous Dielectric Layer," *Electronics Letters,* vol. 27, no. 24, 1991.

[32.VI] T. G. Mihran, "Microwave Oven Mode Tuning by Slab Dielectric Loads," *IEEE Transactions on Microwave Theory and Techniques,* Vols. MTT-26, no. 6, pp. 381-387, 1978.

[33.VI] A. L. J. Droute, "La Dosimétrie Numérique Sur La Bande 1-500 MHZ," in *17éme Colloque International et Exposition sur la Compatibilité ElectroMagnétique (CEM 2014)*, 2014.

Chapter VII
Conclusion and Future Work

7. 1 General conclusion

In this PhD project, we mainly focused on time-domain numerical techniques in electrodynamics for structures including complex media. In particular, we investigated on the transmission line matrix (TLM) method as a computational method to implement in an electromagnetic simulator that can handle general three-dimensional geometries and media possessing general linear constitutive parameters. In chapter II, we presented different kinds of complex linear media and how their behaviour can be expressed mathematically and how electromagnetic fields interact with them. In chapter III, we briefly revised the theory of TLM from its beginnings to wind up with a more advanced algorithm that can deal with complex media that were used later in this research. As the TLM simulator formerly used in the laboratory completely lacked the interface with the TLM engine to enter complex structures, a new graphic interface (GUI) to render it user-friendly was then developed. Also, the former TLM engine was completed with additional features, including a unified environment that can simulate nontraditional materials such as chiral media, metamaterials, and experiments involving transformation optics...etc. Finally, we performed many experiments to validate both the TLM simulator and the module GUI by several comparisons with analytical solutions, other commercial simulators and measurements.

All other available time-domain commercial EM solvers that we tested are limited in comparison to our TLM simulator in terms of the material they can handle. First, when it comes to dispersive media they use frequency-domain methods only (to avoid dealing with time-domain filters). Secondly, they are limited when dealing with highly non homogeneous complex media. In the case of non-saturated ferrites, for example, validated results are obtained only when each cell are described with a local tensor, which can be handle by our TLM simulator.

In the next chapter, we developed a complete theoretical analysis for numerical dispersion phenomena and stability conditions for the TLM model when dealing with complex

media. This was necessary as a simple rule of the thumb, which is generally used in the literature, has not been proved valid. It was shown that in certain cases, the maximum mesh size was underestimated, thus increasing uselessly the computer expenditure. As a result, it is recommended that in the presence of complex (dispersive, anisotropic), a dispersion and stability evaluation be carried out. The general procedure and examples are presented in these cases. It was also shown that an a priori knowledge of both the maximum allowed mesh size and time-step allow the user to optimize the computer resources, given a required level of accuracy.

In chapter VI, some challenging cases that have several impacts on time-domain methods were investigated and solutions proposed. First of all, the low-frequency problem which usually leads to multi-scale difficulty was considered. To avoid coarseness error (spatial resolution), it is shown that the time step becomes very small to insure stability. As a result, the simulation time explodes because the response signal is oversampled way beyond the Nyquist's criterion. For this classical problem, we proposed a new solution based on space or time-space mapping techniques. In this kind of mapping, the objective is to transfer the original computational domain into a new one in which the low frequency problem disappears. Simple examples were shown with promising results.

In the second part of the chapter, the presence of high contrast of constitutive parameters was investigated. Although it may also be relevant for typical frequency domain methods, only time domain methods such as FDTD and TD-TLM were considered. First of all, the main difference between both algorithms concerning field update equations at cells on an interface separating two different media was explained. Numerical experiments show clearly that both algorithms do not behave the same way and produce different accuracy in a substantial manner. This trend is enhanced when the electromagnetic property contrast increases. In this case, results show a better behaviour for the TLM algorithm. This was explained by the inherent local feature of its algorithm, which does not require some averaging process at the interface. Some care was taken to clearly identify the interface problem error from the dispersion difference between both algorithms.

Finally, to pursue with the interface problem between media, we investigated the case of parasitic reflections produced at the interface between regions with different mesh size. The behaviour of both TLM and FDTD were investigated when the mesh ratio between both meshes was modified. Simulation experiments show clearly the better performance of the TLM which

cannot be explained by its better dispersion behaviour. It is concluded that, again, the local character of the TLM algorithm explains its better behaviour in terms of parasitic reflection, as compared to the FDTD.

7. 2 **Future work**

The solver developed in this project is serial; hence, one can significantly enhance its performance by parallelizing the algorithm to benefit from the computational power of several processing units. In the frame of a coming national research project, it will constitute the core of a dedicated TLM solver for highly inhomogeneous structures with application to dosimetry, i.e., the field deposition and induces current density inside biological tissues, when irradiated by high-amplitude fields. Several enhancements should be considered: first, the use of non-orthogonal cells developed by Li *et al* [1.VII] should be implemented. It was shown to have excellent performances for curved geometry, to be local (unlike conformal cells) and to yield minimum dispersion with a slight decrease of the time step as compared to the one of cubic cells. Also, if irregular (structured) meshing is now available in the simulator, block meshing technique is still to be investigated [1.VII]. Indeed, the circuit concept used in TLM provides an exact connection between blocks with arbitrary mesh ratios by the use of ideal transformers. This is valid when the global time-step limit is used. To substantially reduce the computation cost, time-step inherent to each block size should rather be used. However, for time-domain methods in general, middle to long term instabilities arise if the local time-step is used.

Secondly, coupling with other physical phenomena, more particularly the heat conduction should be considered. This coupling will be implemented in the future TLM solver that will be developed in the coming national research project on dosimetry. It will allow one to account for the change of the constitutive parameters with the temperature when fields contribute to heat the media. Other coupling may be investigated such as with acoustic propagation for which there is on-going research in RFID applications [2.VII]. Previous work has shown that TLM model can be integrally applied to other physical phenomena [3.VII] which make it totally compatible with other physical coupling.

Finally, as far as multi-scale or low-frequency problems are concerned. If some ideas were proposed in the thesis, the full potential of the approaches discussed should be investigated

in the case of more complex 3D structures. At the other side of the spectrum, some more research should be carried out on the coupling with asymptotic methods such as GTD or UTD. To that respect, some pioneer work was done for the optimization of antenna positioning in tunnels [4.VII]. TLM was used for mode decomposition approximation for propagation in the tunnels. However, the coupling between the antenna TLM computational domain and the tunnel propagation model based either on mode decomposition or GTD remain to be carried out.

References

[1.VII] L. P. Zaiqing, "Contributions aux techniques de maillages irréguliers dans la méthode TLM : applications au calcul électromagnétique de structures à détails fins et interfaces non-cartésiennes," PhD thesis, Institut Mines-Télécom-Télécom Bretagne-UEB, Brest, 2005.

[2.VII] O. Nova, N. Pena and M. Ney, "FDTD simulation of SAW RFID tags," in *IEEE International Conference on RFID-Technologies and Applications (RFID-TA)*, Nice, 2012.

[3.VII] W. J. R. Hoefer, "The Transmission-Line Matrix Method-Theory and Applications," *IEEE Transactions on Microwave Theory and Techniques*, Vols. MTT-33, no. 10, pp. 882-893, 1985.

[4.VII] J. A. Castiblanco, D. Seetharamdoo, M. Berbineau, M. Ney and F. Gallée, "Electromagnetic Wave Propagation Modeling for Finding Antenna Specifications and Positions in Tunnels of Arbitrary Cross-Section," *Intelligent Transport Systems and Telecommunications*, pp. 678-683, 2011.

Appendix A
Introduction to Transmission Line Matrix Method (TLM)

A.1 Introduction

In this appendix, we present the necessary background regarding the basic TLM algorithm in one, two and three dimensions for simple media. Then, several kinds of boundary conditions such as perfectly matched layer PML are presented.

A.2 One-dimensional TLM

In this section, we will show that the current and voltage distributions in a one-dimensional transmission line and field distributions in a one-dimensional space are governed by the same equations if one uses the appropriate normalization. Figure 1.A shows the infinitesimal equivalent transmission-line circuit. We will show later that TLM mimics wave propagation by channeling local waves in a mesh of interconnected transmission-lines [1.A].

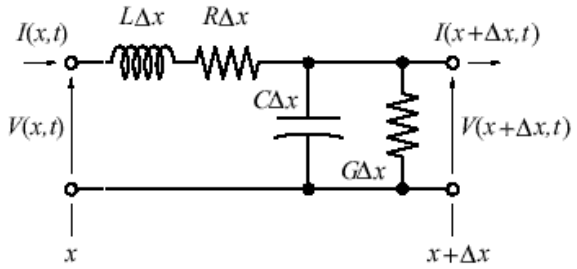

Figure 1.A, TLM one-dimensional cell [1.A]

Governing equations of circuit quantities in figure 1.A are found by applying Kirchhoff's voltage and current laws (KVL) and (KCL), respectively:

$$\frac{V(x+\Delta x,t)-V(x,t)}{\Delta x}\Delta x = -L\frac{I(x,t+\Delta t)-I(x,t)}{\Delta t} - R\, I(x,t) \qquad (1.A)$$

$$\frac{I(x+\Delta x,t)-I(x,t)}{\Delta x}\Delta x = -C\frac{V(x,t+\Delta t)-V(x,t)}{\Delta t} - G\,V(x,t) \tag{2.A}$$

From the above equations, if we take the limit $\Delta x \to 0$, we obtain the well-known telegraphists' equations. By eliminating for instance the current, we obtain with (1.A) and (2.A):

$$\frac{\partial^2 V(x,t)}{\partial x^2} = \frac{LC}{(\Delta x)^2}\frac{\partial^2 V(x,t)}{\partial t^2} + \frac{LG+RC}{(\Delta x)^2}\frac{\partial V(x,t)}{\partial t} + \frac{RG}{(\Delta x)^2}V(x,t) \tag{3.A}$$

Similarly, by eliminating the voltage, one obtains:

$$\frac{\partial^2 I(x,t)}{\partial x^2} = \frac{LC}{(\Delta x)^2}\frac{\partial^2 I(x,t)}{\partial t^2} + \frac{LG+RC}{(\Delta x)^2}\frac{\partial I(x,t)}{\partial t} + \frac{RG}{(\Delta x)^2}I(x,t) \tag{4.A}$$

where R and G mimic losses. Now, if we take a one-dimensional Maxwell's equations scenario, for instance, assuming $\vec{E} = (0, E_y, 0)$ and $\overrightarrow{H} = (0,0, H_z)$, both curl equations become:

$$\frac{\partial E_y(x,t)}{\partial x} = -\mu\frac{\partial H_z(x,t)}{\partial t} - \sigma_m H_z(x,t) \tag{5.A}$$

$$\frac{\partial H_z(x,t)}{\partial x} = -\varepsilon\frac{\partial E_y(x,t)}{\partial t} - \sigma_e E_y(x,t) \tag{6.A}$$

By combining (5.A), and (6.A), we obtain:

$$\frac{\partial^2 E_y(x,t)}{\partial x^2} = \varepsilon\mu\frac{\partial^2 E_y(x,t)}{\partial x^2} + (\mu\sigma_e + \varepsilon\sigma_m)\frac{\partial E_y(x,t)}{\partial t} + \sigma_e\sigma_m E_y(x,t) \tag{7.A}$$

for the electric field. Similarly, for magnetic field we obtain:

$$\frac{\partial^2 H_z(x,t)}{\partial x^2} = \varepsilon\mu\frac{\partial^2 H_z(x,t)}{\partial x^2} + (\mu\sigma_e + \varepsilon\sigma_m)\frac{\partial H_z(x,t)}{\partial t} + \sigma_e\sigma_m H_z(x,t) \tag{8.A}$$

As we can notice, the electric and magnetic field equations (7.A) and (8.A) are identical to (5.A) and (6.A), respectively, provided that the coefficients are adjusted according to table 1.A. One can follow the procedure presented in [1.A] to derive a discrete update scheme to numerically solve the above equations.

Table 1.A, analogy between circuit and field quantities for a one dimensional propagation problem [2.A]

$V - I$	$E_y - H_z$
$R/\Delta x$	σ_m
$G/\Delta x$	σ_e
$L/\Delta x$	μ
$C/\Delta x$	ε
$I(x,t)/\Delta x$	$H_z(x,t)$
$V(x,t)/\Delta x$	$E_y(x,t)$

At any instant of time, the resulting voltage at any arm (port) of the n-*th* node at k-*th* time step, as shown in figure 2.A, is given by:

$$ {}_kV_n = {}_kV_n^i + {}_kV_n^r \tag{9.A}$$

Whereas, the voltage value at the center of the node is the summation of either incident or reflected voltages at any instant of time:

$$ {}_kV_n{}^c = {}_kV_n^{i,1} + {}_kV_n^{i,2} = {}_kV_n^{r,1} + {}_kV_n^{r,2} \tag{10.A}$$

The above voltage values can be used with table 1.A, to determine the correspondent equivalent fields with some normalization factor (the cell dimension).

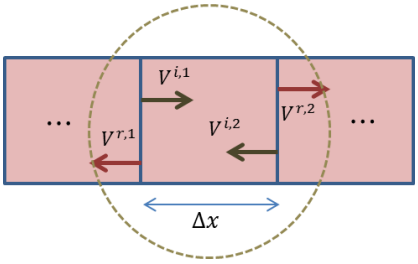

Figure 2.A, one-dimensional TLM mesh

Generally, update equations in the basic TLM algorithm are split into two main steps:

1- Connection process

It is the process in which reflected voltages from one side of the port become the incident ones to the other side of the same port for the next time-step, as shown in figure 2.A. This process writes:

$$\begin{pmatrix} {}_kV_n^{i,1} \\ {}_kV_n^{i,2} \end{pmatrix} = \begin{pmatrix} {}_kV_{n-1}^{r,1} \\ {}_kV_{n+1}^{r,2} \end{pmatrix} \tag{11.A}$$

This process is equivalent to a propagation mechanism in the mesh, through which the voltages exchanges take place and the waves propagate.

2- Scattering process

This process is local and takes into account the material existence; hence, the material field interactions happen at this stage of the TLM algorithm. The incident fields, decomposed in local waves under the form of incident voltages, enter the TLM cell and interact with matter. Then, fields scatter from the node under the form of reflected voltages. This process writes:

$$\begin{pmatrix} {}_{k+1}V_n^{r,1} \\ {}_{k+1}V_n^{r,2} \end{pmatrix} = \begin{pmatrix} S_{11} & S_{12} \\ S_{21} & S_{22} \end{pmatrix} \begin{pmatrix} {}_kV_n^{i,1} \\ {}_kV_n^{i,2} \end{pmatrix} \tag{12.A}$$

Two points need to be mentioned here: first, the components of the scattering matrix are problem dependent. At maximum time-step operation, they depend on the cell size and material only. For more details, please refer to [1.A]. The second point is that a similar analysis can be done for currents. Once the voltages and currents are known in each cell and at each time step, we can calculate all field components by using table 1.A.

A.3 Two-dimensional TLM method

Solving Maxwell's equations in one-dimension always produces transverse Electro-Magnetic (TEM) solutions. The model extension to two-dimensions can produce two additional types of solutions namely, Transverse Electric (TE) or Transverse Magnetic (TM) configurations, which have each three field components and can propagate in two dimensions [3.A]. To achieve such a model using TLM, one needs interconnected transmission-lines to

mimic propagation in the 2D plane [4.A]. Each type of solution is modeled with one specific type of connection, as detailed below:

I- Shunt node

This type of node (figure 3.A) generates TM solutions: The only E component is perpendicular to the computational plane (E_y) and the two only magnetic field components are in that plane (H_x, H_z).

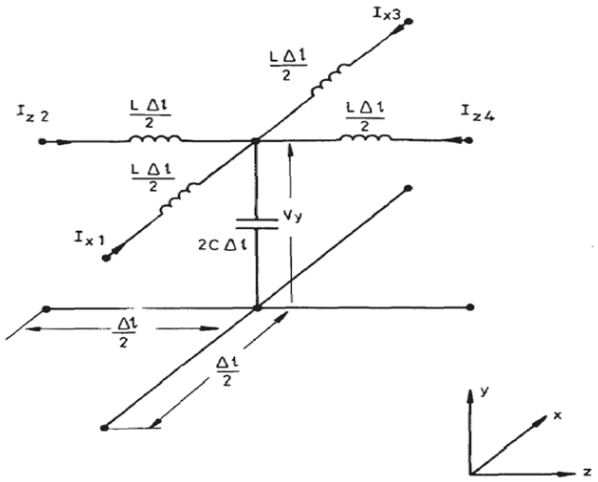

Figure 3.A, 2D TLM Shunt Node [4.A]

By applying Kirchhoff's laws to the node in figure 3.A, we obtain at the infinitesimal limit:

$$-\frac{\partial}{\partial x}(I_{x1} - I_{x3}) - \frac{\partial}{\partial z}(I_{x2} - I_{x4}) = 2C\frac{\partial V_y}{\partial t} \tag{13.Aa}$$

$$-\frac{\partial V_y}{\partial x} = L\frac{\partial}{\partial t}(I_{x1} - I_{x3}) \tag{13.Ab}$$

$$-\frac{\partial V_y}{\partial z} = L\frac{\partial}{\partial t}(I_{x2} - I_{x4}) \tag{13.Ac}$$

Combining (13.A a, b, c) yields:

$$\frac{\partial^2 V_y}{\partial x^2} + \frac{\partial^2 V_y}{\partial x^2} = 2LC\frac{\partial^2 V_y}{\partial t^2} \tag{14.A}$$

If we now consider curl Maxwell's equations for TM solution, i.e., the field components H_x, H_z, E_y and $\frac{\partial}{\partial y} \equiv 0$, one obtains:

$$\frac{\partial H_x}{\partial z} - \frac{\partial H_z}{\partial x} = \varepsilon \frac{\partial E_y}{\partial t} \tag{15.Aa}$$

$$\frac{\partial E_y}{\partial x} = -\mu \frac{\partial H_z}{\partial t} \tag{15.Ab}$$

$$\frac{\partial E_y}{\partial z} = \mu \frac{\partial H_x}{\partial t} \tag{15.Ac}$$

Combining (15.A a, b, c) yields for the electric field components:

$$\frac{\partial^2 E_y}{\partial x^2} + \frac{\partial^2 E_y}{\partial x^2} = \mu\varepsilon \frac{\partial^2 E_y}{\partial t^2} \tag{16.A}$$

Comparing (14.A) and (16.A) yields the correspondence between circuit and field quantities shown in table 2.A.

Table 2.A, analogy between circuit and field quantities for shunt node [5.A]

$V - I$	$E_y - H_z$
V_y	E_y
$(I_{x1} - I_{x3})$	H_z
$(I_{x4} - I_{x1})$	H_x
L	μ
$2C$	ε

II- Series node

This type of node is capable of generating both configurations but with dual circuit quantities [6.A]. For instance in TE configuration, the magnetic field only component is perpendicular to the computation plane and corresponds to a loop current (figure 4.A) and the two only electric field components in the computational plane are represented by voltages. The TM configuration is also possible by proper correspondences which can be similarly determined by comparison between Kirchhoff's laws and curl Maxwell' equations.

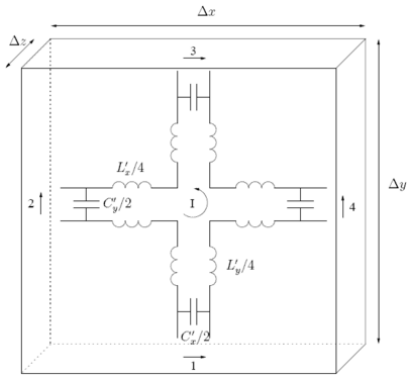

Figure 4.A, TLM Series Node [5.A]

For shunt or series node, the process of wave propagation and material field interaction is the same as for one-dimensional case: there are two steps that should be followed, namely, the connection and scattering processes, as detailed further:

1- Connection process

Similar to the one-dimensional case, the connection process is responsible for voltages exchange, as presented in figure 5.A and expressed by:

$$\begin{pmatrix} {}_kV_{n,m}^{i,1} \\ {}_kV_{n,m}^{i,2} \\ {}_kV_{n,m}^{i,3} \\ {}_kV_{n,m}^{i,4} \\ {}_kV_{n,m}^{i,5} \end{pmatrix} = \begin{pmatrix} {}_kV_{n-1,m}^{r,1} \\ {}_kV_{n,m-1}^{r,2} \\ {}_kV_{n+1,m}^{r,3} \\ {}_kV_{n,m+1}^{r,4} \\ {}_kV_{n,m}^{r,5} \end{pmatrix} \tag{17.A}$$

where n, m are the indices in x, y directions, respectively. As in the one-dimensional case, this process of voltage exchange is responsible for wave propagation inside the mesh. This can be thought conceptually as an equivalence to Huygens principle: once the waves reach any cell, this cell becomes a secondary radiator. Finally, the fifth voltage is reserved for a stub inside each node to take into account the material presence [7.A].

The voltage at the center of the node (referred as node voltage) is proportional to the field component as shown in Table 2.A. It is given by a linear combination of all voltages either incident or reflected at any time step:

$${}_kV_n{}^c = \sum_{p=1}^{4} {}_kV_n^{i,p} = \sum_{p=1}^{4} {}_kV_n^{r,p} \tag{18.A}$$

Note that similar voltage combination can be expressed for the node current of the series node.

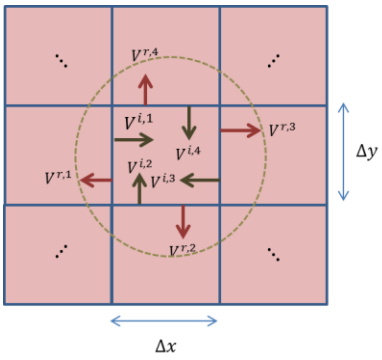

Figure 5.A, two-dimensional TLM mesh

2- Scattering process

This process is local and takes into account the material presence; hence, the material field interactions occur at this stage of the TLM algorithm. In this process, incident voltages enter the TLM cell, impinge to the TLM cell node center, and then scatter at all accesses as reflected voltages. They are ready for the connection stage that prepares the next time iteration step. This process is generally represented by the scattering matrix (3.19) since the TLM node can be seen as a 5-port device. Note that this explains the name of the method (should not to be called transmission-line method, which is another approach). Hence, the computational domain is filled with a network of interconnected nodes, each characterized with its scattering matrix [7.A]:

$$\begin{pmatrix} {}_kV_{n,m}^{r,1} \\ {}_kV_{n,m}^{r,2} \\ {}_kV_{n,m}^{r,3} \\ {}_kV_{n,m}^{r,4} \\ {}_kV_{n,m}^{r,5} \end{pmatrix} = \begin{pmatrix} s_{11} & s_{12} & s_{13} & s_{14} & s_{15} \\ s_{21} & s_{22} & s_{23} & s_{24} & s_{25} \\ s_{31} & s_{32} & s_{33} & s_{34} & s_{35} \\ s_{41} & s_{42} & s_{43} & s_{44} & s_{45} \\ s_{51} & s_{52} & s_{53} & s_{54} & s_{55} \end{pmatrix} \begin{pmatrix} {}_kV_{n,m}^{i,1} \\ {}_kV_{n,m}^{i,2} \\ {}_kV_{n,m}^{i,3} \\ {}_kV_{n,m}^{i,4} \\ {}_kV_{n,m}^{i,5} \end{pmatrix} \tag{19.A}$$

As in one-dimensional case, the components of the scattering matrix are problem dependent since they depend on the cell size, local material and time step (only if not operating

at maximum time step). For all nodes, fields at the node center can be retrieved by linear combination of the incident voltages or currents (which can be expressed in terms of voltages via transmission-line theory), using the correspondences of Table III. It is worth to mention that unlike FDTD, the 2D-TLM always operates at maximum time-step, is inherently stable and compute fields at the same location and time.

For the expression of the scattering matrix components of (19.A), one can refer to [7.A]. Note that to the fifth port, one connects an open circuited stub (shunt node) whose characteristic admittance value depends on local medium constitutive parameters. Note that a sixth port connected to an infinitely long (or matched) line could be used to account for local losses. Since the voltage never returns to the node, the port is not used and matrix components only are modified when losses are present. Finally, stub loading must also be used when the cell has an aspect ratio different than unity.

All the above applies to the 2D shunt node in a dual manner. Note that TE or TM configuration whether or not for magnetic or dielectric media can be modeled by either the shunt or series node with appropriate correspondences [8.A]. However, it is customary to use the shunt node with the node voltage as the electric field component only (stub loading for dielectric medium) and series node with the node current as the magnetic field component only and stub loading for magnetic media.

A.4 Three-dimensional TLM method

For general structures, the decomposition of independent solutions in TE and TM configurations is no longer possible. Thus, one needs all 6 components of the electromagnetic field [5.A] [9.A]. Therefore, it is necessary to create a three dimensional type of nodes that incorporate both series and shunt nodes to compute all 6 components as illustrated in figure 6.A [5.A] [6.A] [9.A].

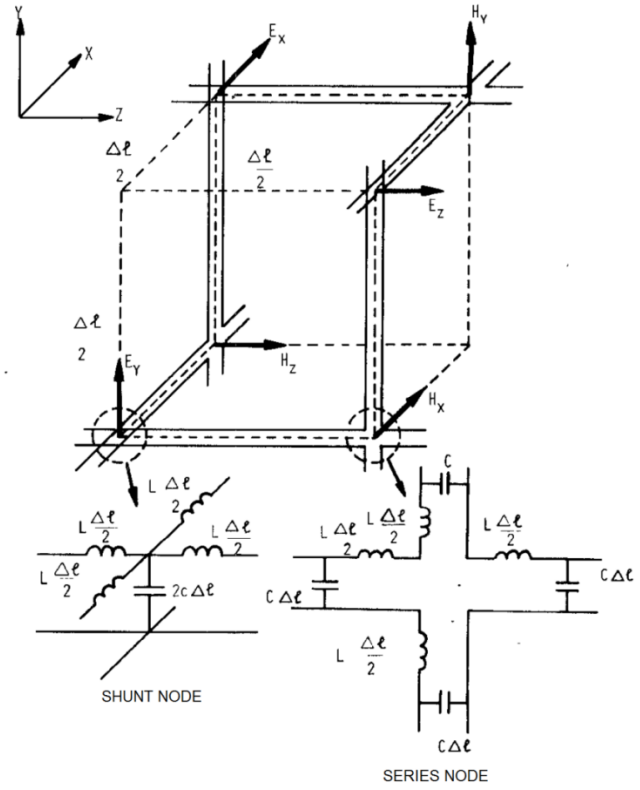

Figure 6.A, three-Dimensional TLM distributed node [5.A]

Combining series and shunt nodes in an appropriate way, one obtains the basic distributed 3D TLM cell that describes the complete set of 3D Maxwell's equations in Cartesian coordinates. As shown in figure 6.A, at three vertices of the cell, there are shunt nodes whose node voltages relate to $E_x, E_{y,} E_z$ and at the remaining vertices, there are series nodes whose node currents relate to $H_x, H_{y,} H_z$.

As one can observe, electromagnetic field components are not defined at the same time and position by this TLM cell. On refers to the distributed TLM cell, which turns out to be the same as Yee's FDTD cell and same dispersion properties at maximum time-step. However, the TLM needs more operations and, therefore, does not bring any advantage over Yee's cell. Subsequent work was carried out to develop a condensed version of the 3D TLM node. First, Saguet and Pic [10.A] proposed a condensed TLM node by eliminating the interconnections between nodes illustrated in figure 6.A. However, the node presents some asymmetry which provokes errors in the solution, depending on the type of boundaries applied. This is only 5 years

later that John's published the 3D-Symmetrical Condensed Node (SCN) which is now widely used.

A.5 Symmetric Condensed Node

Peter Johns, professor at the University of Nottingham carried out investigation to come up with an optimized cell that would present the following features:

- It can carry all $\vec{H}$ and $\vec{E}$ field components.
- It can account for all material properties μ, ε, σ.
- It should be symmetric to provide the same characteristics for all Cartesian directions (for cubic cells).
- It should fulfill the charge and energy conservation principles.
- It should fulfill Maxwell's curl's equations.
- It should have minimum, even zero, dispersion along the Cartesian directions.

From the above conditions, the device that represents the TLM node, should have symmetry (scattering matrix property of symmetry) and capable of modeling in a unique manner the 6-fields components $\{E_x, E_y, E_z, H_x, H_y, H_z\}$ or their 6-curls components, and 6-flux quantities $\{D_x, D_y, D_z, B_x, B_y, B_z\}$ that account for the presence of matter. If one considers the TLM usual principle, one should have at most 18 voltages to have a consistent system to build the 18 electromagnetic quantities mentioned above. As there are 6 ports to feed the node (incidence-reflection along each Cartesian coordinates), each should contain two orthogonal voltages. This accounts for both polarizations of the traveling waves in the port line-access. It will be shown that line-voltage combination corresponds to tangential field components at the cell faces.

In his paper [23.A], Johns, describes the construction of such a node that he called "Symmetrical Condensed Node". Although, a pure circuit description is possible (published afterwards), he gave up the circuit description concept and simply applied the multi-port theory to come out with a general 12-port device, with 6 arms, each having two orthogonal voltages as illustrated in figure 7.A. The TLM cell refers to "unloaded SCN" as no stub connections appear.

To account for the presence of matter, fields at the node center must be modified. This is done by adding inductances or/and capacitances at the node center. To keep with the TLM concept, these immittances are modeled by stubs connected to the center: 3 stubs for the inductive loading (magnetic material) and 3 stub for the capacitive loading (dielectric material). Thus, the completely loaded TLM node includes at most 18 voltages. As a result, the fully loaded TLM cell can be characterized by an 18x18 scattering matrix.

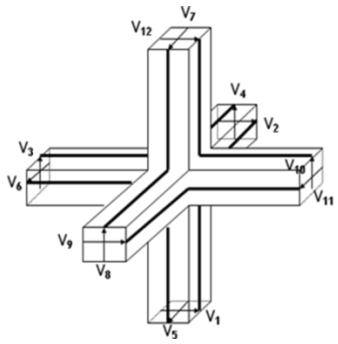

Figure 7.A, unloaded Symmetrical Condensed Node (SCN) [2.A]

A complete description and derivation of the SCN scattering matrix, based on Maxwell's equations under integral form was published by Peña and Ney [43.A]. This procedure allows the systematic development of any new TLM cell, starting from the definition of arm node voltages as a function of field components at cell faces:

In this section we will present a version of SCN-based TLM algorithm that can deal with nondispersive media with diagonal tensors for permittivity, permeability, electric and magnetic conductivities [11.A] [12.A], as shown in table 3.A. To minimize the number of operations and storage, we will not make use of the scattering matrix published by Johns, but rather express the field components at the cell center as a function of the incident arm voltages and then, compute reflected voltages from these quantities [13.A].

Table 3.A, media property tensors for SCN-TLM algorithm

$\bar{\bar{\varepsilon}}_r = \begin{pmatrix} \varepsilon_{rxx} & 0 & 0 \\ 0 & \varepsilon_{ryy} & 0 \\ 0 & 0 & \varepsilon_{rzz} \end{pmatrix}$	$\mu_r = \begin{pmatrix} \mu_{rxx} & 0 & 0 \\ 0 & \mu_{ryy} & 0 \\ 0 & 0 & \mu_{rzz} \end{pmatrix}$
$\bar{\bar{\sigma}}_e = \begin{pmatrix} \sigma_{exx} & 0 & 0 \\ 0 & \sigma_{eyy} & 0 \\ 0 & 0 & \sigma_{ezz} \end{pmatrix}$	$\bar{\bar{\sigma}}_m = \begin{pmatrix} \sigma_{mxx} & 0 & 0 \\ 0 & \sigma_{myy} & 0 \\ 0 & 0 & \sigma_{mzz} \end{pmatrix}$

The computational domain is replaced by interconnected SCN-TLM nodes as shown in figure 8.A. Voltage exchanges happen at the interconnection planes, half way between neighboring cells. Given the parameter medium and cells, constants used in the update equations can be computed and are shown in table 4.A.

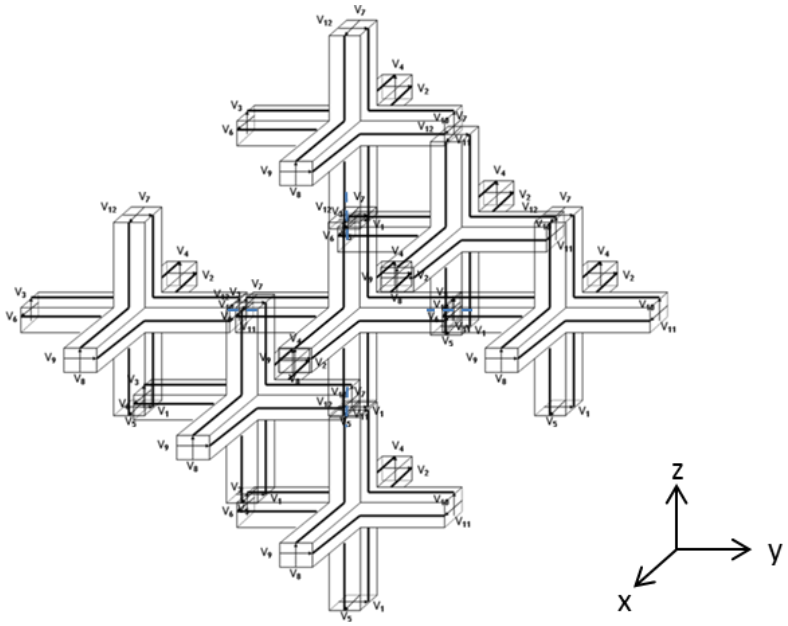

Figure 8.A, three-dimensional TLM mesh based on SCN nodes

Table 4.A, constant terms used in TLM update equations

$\delta_1 = \frac{\Delta y \Delta z}{\Delta x}$	$\delta_2 = \frac{\Delta x \Delta z}{\Delta y}$	$\delta_3 = \frac{\Delta x \Delta y}{\Delta z}$
$dl = c_o dt$		$s = 2dl$
$\alpha_{e,i} = \frac{4}{4 + Z_o \sigma_{e,i} s / \varepsilon_{r,i}}$		$\alpha_{m,i} = \frac{4}{4 + \sigma_{m,i} s / (Z_o \mu_{r,i})}$
$\beta_{e,i} = 4\left(\frac{\varepsilon_{r,i}\delta_i}{2dl} - 1\right)$		$\beta_{m,i} = 4\left(\frac{\mu_{r,i}\delta_i}{2dl} - 1\right)$
$\gamma_{e,i} = \frac{dl}{\varepsilon_{r,i}\delta_i}$		$\gamma_{m,i} = \frac{dl}{\mu_{r,i}\delta_i}$

Update equations for normal SCN-base node at every time step is given by [11.A]:

$$\begin{pmatrix} \Delta x E_x \\ \Delta y E_y \\ \Delta z E_z \\ Z_o \Delta x H_x \\ Z_o \Delta y H_y \\ Z_o \Delta z H_z \end{pmatrix}_n = \begin{pmatrix} \alpha_{e,i}\left(\gamma_{e,i}\left(V_{in,1} + V_{in,2} + V_{in,9} + V_{in,12} + \beta_{e,i} V_{in,13}\right)\right) \\ \alpha_{e,i}\left(\gamma_{e,i}\left(V_{in,3} + V_{in,4} + V_{in,8} + V_{in,11} + \beta_{e,i} V_{in,14}\right)\right) \\ \alpha_{e,i}\left(\gamma_{e,i}\left(V_{in,5} + V_{in,6} + V_{in,7} + V_{in,10} + \beta_{e,i} V_{in,15}\right)\right) \\ \alpha_{m,i}\left(\gamma_{m,i}\left(-V_{in,4} + V_{in,5} - V_{in,7} + V_{in,8} + \beta_{m,i} V_{in,16}\right)\right) \\ \alpha_{m,i}\left(\gamma_{m,i}\left(V_{in,2} - V_{in,6} - V_{in,9} + V_{in,10} + \beta_{m,i} V_{in,17}\right)\right) \\ \alpha_{m,i}\left(\gamma_{m,i}\left(-V_{in,1} + V_{in,3} - V_{in,11} + V_{in,12} + \beta_{m,i} V_{in,18}\right)\right) \end{pmatrix}_n \quad (20.A)$$

where Z_o is the free space wave impedance and $V_{in,1}$ to $V_{in,18}$ are the incident voltages to the TLM node. Thus, electric and magnetic fields are computed first at the TLM cell center using (20.A). Then, reflected voltages can be computed by:

$$\begin{pmatrix} V_{\mathrm{ref},1} \\ V_{\mathrm{ref},2} \\ V_{\mathrm{ref},3} \\ V_{\mathrm{ref},4} \\ V_{\mathrm{ref},5} \\ V_{\mathrm{ref},6} \\ V_{\mathrm{ref},7} \\ V_{\mathrm{ref},8} \\ V_{\mathrm{ref},9} \\ V_{\mathrm{ref},10} \\ V_{\mathrm{ref},11} \\ V_{\mathrm{ref},12} \\ V_{\mathrm{ref},13} \\ V_{\mathrm{ref},14} \\ V_{\mathrm{ref},15} \\ V_{\mathrm{ref},16} \\ V_{\mathrm{ref},17} \\ V_{\mathrm{ref},18} \end{pmatrix}_{n+1} = \begin{pmatrix} \Delta x E_x + Z_o \Delta z H_z - V_{in,12} \\ \Delta x E_x - Z_o \Delta y H_y - V_{in,9} \\ \Delta y E_y - Z_o \Delta z H_z - V_{in,11} \\ \Delta y E_y + Z_o \Delta x H_x - V_{in,8} \\ \Delta z E_z - Z_o \Delta x H_x - V_{in,7} \\ \Delta z E_z + Z_o \Delta y H_y - V_{in,10} \\ \Delta z E_z + Z_o \Delta x H_x - V_{in,5} \\ \Delta y E_y - Z_o \Delta x H_x - V_{in,4} \\ \Delta x E_x + Z_o \Delta y H_y - V_{in,2} \\ \Delta z E_z - Z_o \Delta y H_y - V_{in,6} \\ \Delta y E_y + Z_o \Delta z H_z - V_{in,3} \\ \Delta x E_x - Z_o \Delta z H_z - V_{in,1} \\ \Delta x E_x - V_{in,13} \\ \Delta y E_y - V_{in,14} \\ \Delta z E_z - V_{in,15} \\ \Delta x H_x - V_{in,16} \\ \Delta y H_y - V_{in,17} \\ \Delta z H_z - V_{in,18} \end{pmatrix}_{n} \tag{21.A}$$

Reflected voltages will be the incident ones to the adjacent cells at the next time step through the connection process descibed further. If one is interested in calculating the actual fields, the denormalization process should be performed through the multiplication with the denormalization matrix:

$$\begin{pmatrix} E_x \\ E_y \\ E_z \\ H_x \\ H_y \\ H_z \end{pmatrix}_n = \begin{pmatrix} 1/\Delta x & 0 & 0 & 0 & 0 & 0 \\ 0 & 1/\Delta y & 0 & 0 & 0 & 0 \\ 0 & 0 & 1/\Delta z & 0 & 0 & 0 \\ 0 & 0 & 0 & \frac{1}{Z_o \Delta x} & 0 & 0 \\ 0 & 0 & 0 & 0 & \frac{1}{Z_o \Delta y} & 0 \\ 0 & 0 & 0 & 0 & 0 & \frac{1}{Z_o \Delta z} \end{pmatrix} \begin{pmatrix} \Delta x E_x \\ \Delta y E_y \\ \Delta z E_z \\ Z_o \Delta x H_x \\ Z_o \Delta y H_y \\ Z_o \Delta z H_z \end{pmatrix}_n \tag{22.A}$$

After the scattering process descibed above, the connection process takes place, where reflected voltages are exchanged with the adjacent nodes for the next iteration:

$$\begin{pmatrix} V_{in,1}(k,l,m) \\ V_{in,2}(k,l,m) \\ V_{in,3}(k,l,m) \\ V_{in,4}(k,l,m) \\ V_{in,5}(k,l,m) \\ V_{in,6}(k,l,m) \\ V_{in,7}(k,l,m) \\ V_{in,8}(k,l,m) \\ V_{in,9}(k,l,m) \\ V_{in,10}(k,l,m) \\ V_{in,11}(k,l,m) \\ V_{in,12}(k,l,m) \\ V_{in,13}(k,l,m) \\ V_{in,14}(k,l,m) \\ V_{in,15}(k,l,m) \\ V_{in,16}(k,l,m) \\ V_{in,17}(k,l,m) \\ V_{in,18}(k,l,m) \end{pmatrix}_{n+1} = \begin{pmatrix} V_{\mathrm{ref},12}(k,l-1,m) \\ V_{\mathrm{ref},9}(k,l,m-1) \\ V_{\mathrm{ref},11}(k-1,\mathrm{l},m) \\ V_{\mathrm{ref},8}(k,l,m-1) \\ V_{\mathrm{ref},7}(k,l-1,m) \\ V_{\mathrm{ref},10}(k-1,l,m) \\ V_{\mathrm{ref},5}(k,l+1,m) \\ V_{\mathrm{ref},4}(k,l,m+1) \\ V_{\mathrm{ref},2}(k,l,m+1) \\ V_{\mathrm{ref},6}(k+1,l,m) \\ V_{\mathrm{ref},3}(k+1,l,m) \\ V_{\mathrm{ref},1}(k,l+1,m) \\ V_{\mathrm{ref},13}(k,l,m) \\ V_{\mathrm{ref},14}(k,l,m) \\ V_{\mathrm{ref},15}(k,l,m) \\ V_{\mathrm{ref},16}(k,l,m) \\ V_{\mathrm{ref},17}(k,l,m) \\ V_{\mathrm{ref},18}(k,l,m) \end{pmatrix}_{n+1} \tag{23.A}$$

Finally, the simulation cannot take place if one does not include sources and boundary conditions that are required to limit the TLM computational domain. The way those are implemented in the TLM node will be described later.

In general, one has many parameters linked to the TLM cell that can be utilized and modified in various manners to compute fields in a given medium. One can mention the six stub characteristic immittances and the 18 access-line impedances. In the literature, different types of cartesian cells have been presented beside the SCN node. The hybrid symmetical condensed node (HSCN) and the super symmetrical condensed node (SSCN) are the most well known [1.A]. The main idea for these two nodes was to reduce the number of voltages to manipulate, i.e., the number of stubs. For instance, the SSCN does not use stubs at all but rather includes in the 12 line characteristic impedance values, the presence of material. However, a scattering process should take place in the connecting lines accross interfaces [14.A]. The HSCN compromizes between SCN and SSCN as it uses only three stubs and characteristic impedances

values of lines runing along the three space directions. In table 5.A we presents a comparison between the three types of common TLM nodes.

Table 5.A, comparison between different TLM condensed cells

	SCN	**HSCN**	**SSCN**
Number of voltage lines in parallelepipedic cell	18	15	12
The necessity for explicitly define boundary conditions at the interface between two different media	No	Yes	Yes
Characteristic impedance	Z_o	Material dependent	Material dependent

As one can see, SCN node doesn't need any knowledge such as material properties and shape of its neighboring cells. However HSCN and SSCN nodes do, as access lines with different impedances are directly connected across media interface. Thus, a scattering process takes place and reflection and transmission coefficients must be computed. When the media are simple (isotropic and non-dispersive) calculating the reflection coefficient is not a great deal. However, it should be mentioned that the cost in additional operation increases with the number of cells at interfaces, in other words, for increasing heterogeneity. When dealing with complex media, dispersive media for instance, the scattering process is much more involved. Intuitively, we know that those coefficients between two dispersive media are frequency dependent quantities. This means that some filtering process is necessary at the interface between different media. In this case, HSCN and SSCN rapidly become less attractive than SCN. However, further studies are necessary on that subject.

A.6 Boundary Conditions

In system theory, the differential equation that models a system defines the rules of evolution of that system and how variables are connected together. The relation between the system and the outer space is done by using boundary conditions, which usually come from physical observations of how the system reacts with its exterior [15.A]. In fact, the way of truncating a computational domain depends mathematically on the problem formulation:

I. Integral equation formulation

In field integral equation formulation, the use of Greens function allows one to avoid any truncation process for open problems. Indeed, sources are variables only and bounded in space. The boundary conditions are already included in the Green's function and fields can be computed everywhere. One sometime refers them as exact boundary conditions [15.A] [16.A].

II. Differential equation formulation

In this type of formulation, it is necessary to carry out a space truncation as fields are the unknowns to be determined and theoretically extend to infinity for open problems. Thus, some truncation methodology should be developed that minimizes parasitic reflections back to the limited computational domain [17.A] [18.A] [19.A] [20.A].

Recalling that TLM algorithm belongs to volumic approaches, there are several ways to truncate the computational domain, depending on the purpose of this truncation and the subtleties of the problem under study. The most common types of boundary conditions encountered in TLM (like in other volumic approaches) are discussed below [2.A] [21.A] [22.A] [23.A] [24.A] [25.A].

1- Perfect Electric Conductor (PEC)

They have to be enforced where the computational domain is limited by a perfect conductor. PEC's are also useful in exploiting the symmetry in the computational domain, for instance when we can define a plane where the electric field is purely normal and the magnetic field purely tangential. This allows a reduction of the computational domain [26.A] [11.A]. In TLM, PEC is simply implemented by short circuiting the related ports in the TLM node lines adjacent to the PEC boundary [2.A] (see figure 9.A).

2- Perfect magnetic conductors (PMC)

PMC are the dual of PEC and do not represent real medium boundary. However, they are also very useful for taking advantage of symmetries to reduce a problem size. Such a plane exists if everywhere on that plane the magnetic field is purely normal and the electric field purely

tangential [15.A] [5.A]. In TLM, PMC are implemented by simply open circuiting the related ports in the TLM node lines adjacent to the PMC boundary [2.A] (see fig. 10.A).

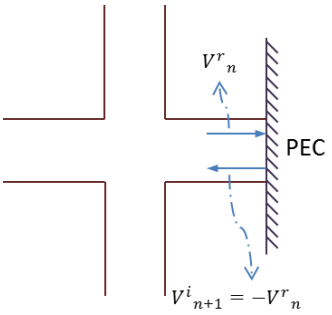

Figure 9.A, PEC boundary condition

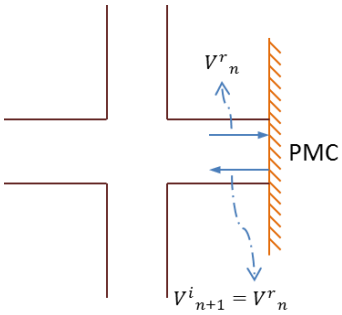

Figure 10.A, PMC boundary condition

3- Lossy boundary conditions

These boundary conditions occur for various cases. For instance, suppose that the computational domain is limited at some location by a good but not perfect conductor. The impinging signal is mainly reflected and partially penetrates the conductor by several skin depths before it vanishes. One intuitive approach to handle such BC's is to assume that they are composed of several layers of TLM cells (to cover several skin depths), and each of which has the conductivity (or the imaginary parts of permeability or permittivity) of the medium. But one of the major drawbacks of this approach is that the skin depth is very small, which means that the cell size used to discretize it will be very small too. Knowing that the time step will be correspondingly very small to insure stability, the total simulation time will explode. This was one of the reasons that drove J. Pendry to write his famous paper [27.A] to overcome this problem by modifying the coordinate system and the material properties.

An alternate way to solve the problem is ti consider the boundary condition at the interface with lossy media is given by:

$$E_s(\omega) = Z_s(\omega) H_s(\omega) \tag{24.A}$$

where $E_s(\omega)$, $H_s(\omega)$ are the tangential components of the electric field and the magnetic field, respectively, at angular frequency ω, $Z_s(\omega)$ is the surface impedance at the good conductor interface which is defined by:

$$Z_s(\omega) = \sqrt{\frac{j\omega\mu}{\sigma}} \tag{25.A}$$

In their paper J. Paul *et al* [28.A], have presented a digital filtering based approach to model the process of interaction of electromagnetic field with the lossy medium, by finding the equivalent time domain filter of $Z_s(\omega)$, and applying a convolution process in time-domain. However, using this approach has some drawback when higher-order filters are used to enhance the simulation accuracy. The computational complexity increases and instabilities can occur.

To overcome this problem a full-time domain representation of the phenomena was proposed, using the concept of fractional derivative [29.A]. This allows a very accurate representation of the BC without the need of direct filtering process with their inherent complexities [29.A] [30.A]. In their approach, the authors modified the update equations of fields adjacent to the lossy boundaries, to take the condition (24.A) into account. For more details, one can refer to [29.A].

4- Absorbing boundary conditions (ABC's)

These conditions are enforced at the computational domain boundaries in two distinct cases:

- To mimic the open free space scenario outside the computational domain without reflections. They are typically used when simulating antennas or free-space scattering problems.
- To simulate wideband matching load terminating the computational domain, typically for waveguide discontinuity characterization.

In literature there are two types of wideband ABC's for time-domain simulations:

- One-way equation techniques (such as Mur, Higdon, Enquist, Majda, Taylor, etc...). In this category of ABS' the fields are evaluated at boundaries from nearby samples inside the computatioal domain using extrapolation techniques [31.A] [32.A] [26.A] [7.A].
- Stretched coordinate or split-field techniques or sometimes called Bérenger's type of ABC [19.A]. In this category, we extend the computational domain by a non-Maxwellian artificial medium that absorbs fields with negligible reflections back to the computational domain. [20.A] [23.A] [26.A] [33.A].

Both have cons and pros: the one-way equation techniques are easier to implement, and less expensive computationally. Indeed, they do not require to extend the computational domain with a layer of particular dissipative medium. However, if some excellent absorption can be obtained at a given incident angle, optimization at several angles requires higher order conditions that become rapidly complex to implement and eventually instable. In addition, the one-way approaches do not apply to evanescent waves. As a result, such ABC's have to located were propagating waves only prevail.

On the other hand, stretched coordinate techniques such as PML are more difficult to implement, and more expensive in terms of memory and running time. However, they have much better performances as they theoretically do not provoke any reflections at any incidence and frequency, and are valid for evanescent modes. In his paper [19.A], Bérenger was the first to propose the use of spilt-field technique. Maxwell's equations were solved in an artificial medium (non-Maxwellian medium) surrounding the computational domain (as shown in figure 11.A). The main feature of that medium is that it is lossy magnetically and electrically to attenuate transmitted fields. The splitting of field components and proper ratio of magnetic and electric conductivities allows one to provoke negligible reflections at the boundary of the computational domain for arbitrary incidence and frequency. However, it should be noted that fields must be computed in the entire extended PML domain, which requires the manipulation and storage of many more field components. In his work Bérenger implemented this method for the FDTD algorithm [20.A].

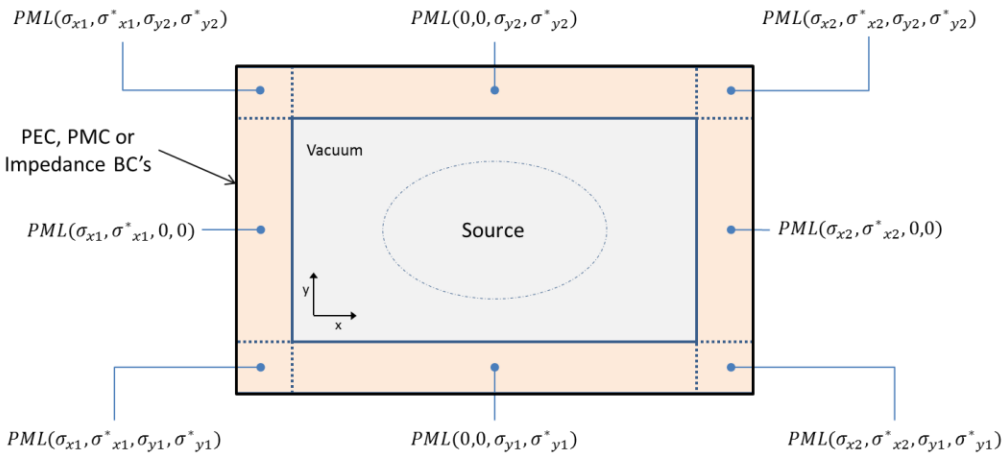

Figure 11.A, 2D TLM computational domain truncated by PML layer [26.A]

Several implementations of PML medium in TLM algorithm are presented in the literature. For instance, Pena and Ney used a coupling between TLM nodes in the computational domain and FDTD nodes that simulated the PML layer medium [33.A]. A full-3D PML-TLM node was later developed, but 30 voltages were required to completely simulate the PML medium [25.A]. Dubard and Pompei presented a modification to the TLM-PML algorithm that uses a reduced number of voltages, hence some better performance in terms of memory and running time [23.A] [24.A].

Later Le Maguer and Ney [34.A] developed a new TLM based algorithm for PML that accounts for the evanescent waves. Indeed, these waves were not sufficiently attenuated in the PML layer which required extending the PML layer thickness or locating the boundary at larger distance from scatterer. It is this algorithm that is presented next, since it provides an optimal performance for the 3D TLM SCN-based cells. Also, it is the PML-TLM node which is implemented in the general TLM solver of our Laboratory.

The mathematical formulation of PML SCN-based TLM

The basic idea of PML layer is to elaborate an artificial material which produces zero reflection at its interface, from impinging waves of any kind coming from real media and at any frequency. The penetrating fields in the PML continuous media should also be attenuated so that the layer can be limited within a short distance. Thus, PML is also a lossy medium [19.A]. However, the discrete version of the theoretical PML medium is not perfect and small reflections

can occur from the interface with the computational domain. The magnetic and electric conductivity profiles can be optimized, yielding minimum level of reflection with a minimum layer thickness. The PML discretized medium can be limited by some impedance boundary conditions instead of PEC or PMC [19.A] [33.A], to further minimize the layer thickness. This is easily implemented as TLM allows arbitrary loading by just computing the reflection coefficient in the node arms. It should be kept in mind that fields must be computed for all times in the PML medium and, since field components are split, up to twice as many unknowns must be manipulated. Consequently, the PML layer thickness must be minimized to avoid substantial additional computer expenditure.

In the PML layer that surrounds the computational domain the electromagnetic field components are split into two sub-components, i.e:

$$E_i = E_{ij} + E_{ik} \tag{26.Aa}$$

$$H_i = H_{ij} + H_{ik} \tag{26.Ab}$$

where the 3-tuple indices are defined as $(i, j, k) \in \{(x, y, z), (y, z, x), (z, x, y)\}$. The fields in the PML medium are governed by the following equations

$$\varepsilon_i \varepsilon_o \frac{\partial E_{ij}}{\partial t} + \sigma_{ej} E_{ij} = \frac{1}{\alpha_j} \frac{\partial H_k}{\partial j} \tag{27.Aa}$$

$$\varepsilon_i \varepsilon_o \frac{\partial E_{ik}}{\partial t} + \sigma_{ek} E_{ik} = -\frac{1}{\alpha_k} \frac{\partial H_j}{\partial k} \tag{27.Ab}$$

$$\mu_i \varepsilon_o \frac{\partial H_{ij}}{\partial t} + \sigma_{mj} H_{ij} = -\frac{1}{\alpha_j} \frac{\partial E_k}{\partial j} \tag{27.Ac}$$

$$\mu_i \varepsilon_o \frac{\partial H_{ik}}{\partial t} + \sigma_{mk} H_{ik} = \frac{1}{\alpha_k} \frac{\partial E_j}{\partial k} \tag{27.Ad}$$

where σ_{ej} is the electrical conductivity in the j-*th* axis direction for propagating modes absorption, the factor α_j, which is greater than unity, damps the evanescent modes in the same direction, μ_i and ε_i are the medium relative permeability and permittivity respectively in the i-*th* axis direction.

The matching condition for full absorption of a PML layer in the i-*th* axis direction is achieved by fulfilling the following relation [19.A] [34.A] [35.A]:

$$\frac{\sigma_{ei}}{\varepsilon_i \varepsilon_o} = \frac{\sigma_{mi}}{\mu_i \mu_o} \tag{28.II}$$

After discretizing the modified Maxwell's curls equations for the PML cells, and applying similar procedures like in normal Maxwellian cells [11.A], one obtains:

$$\Delta i E_{ij}^{(n)} = Ae_{ij}\bar{C}_{ij}\left(a_{jni} + a_{jpi} + \hat{Y}_{sij}a_{eij} - 2a_{eik}\right) \tag{29.Aa}$$

$$\Delta i E_{ik}^{(n)} = Ae_{ik}\bar{C}_{ik}\left(a_{kni} + a_{kpi} + \hat{Y}_{sik}a_{eik} - 2a_{eij}\right) \tag{29.Ab}$$

$$Z_o \Delta i H_{ij}^{(n)} = Am_{ij}\bar{D}_{ij}\left(a_{jnk} - a_{jpk} + \hat{Z}_{sij}a_{mij} - 2a_{mik}\right) \tag{29.Ac}$$

$$Z_o \Delta i H_{ik}^{(n)} = Am_{ik}\bar{D}_{ik}\left(-a_{knj} + a_{kpj} + \hat{Z}_{sik}a_{mik} - 2a_{mij}\right) \tag{29.Ad}$$

where the triple $(i,j,k) \in \{(x,y,z),(y,z,x),(z,x,y)\}$, and the different parameters used in previous equations are defined in table 4.A.

Table 6.A, update equation parameters in TLM algorithm for PML cells

$\bar{C}_{ij} = \dfrac{s\Delta i}{2\varepsilon_i \alpha_j \Delta j \Delta k}$	$\bar{D}_{ij} = \dfrac{s\Delta i}{2\mu_i \alpha_j \Delta j \Delta k}$
$\hat{Y}_{sij} = 4\left(\dfrac{\varepsilon_i \alpha_j \Delta j \Delta k}{s\Delta i} - \dfrac{1}{2}\right)$	$\hat{Z}_{sij} = 4\left(\dfrac{\mu_i \alpha_j \Delta j \Delta k}{s\Delta i} - \dfrac{1}{2}\right)$
$Ae_{ij} = \dfrac{4}{4 + G_{ij}}$	$Am_{ij} = \dfrac{4}{4 + R_{ij}}$
$G_{ij} = Z_o \dfrac{\sigma_{ej} s}{\varepsilon_i}$	$R_{ij} = Z_o \dfrac{\sigma_{mj} s}{\varepsilon_i}$

where $s = 2c_o \Delta t$. Now, by applying (27.A) and (29.A) we obtain

$$\begin{pmatrix} \Delta xE_x \\ \Delta yE_y \\ \Delta zE_z \\ Z_o\Delta xH_x \\ Z_o\Delta yH_y \\ Z_o\Delta zH_z \end{pmatrix}_n = \begin{pmatrix} \Delta xE_{xy} + \Delta xE_{xz} \\ \Delta xE_{yx} + \Delta xE_{yz} \\ \Delta xE_{zx} + \Delta xE_{zy} \\ Z_o\Delta xH_{xy} + Z_o\Delta xH_{xz} \\ Z_o\Delta xH_{yx} + Z_o\Delta xH_{yz} \\ Z_o\Delta xH_{zx} + Z_o\Delta xH_{zy} \end{pmatrix}_n + \begin{pmatrix} \Delta xE_x \\ \Delta yE_y \\ \Delta zE_z \\ Z_o\Delta xH_x \\ Z_o\Delta yH_y \\ Z_o\Delta zH_z \end{pmatrix}_{n-1} \tag{30.A}$$

At this point, (i.e., after calculating fields inside the PML cells), the algorithm continues as in normal TLM cells. This is one of the very attracting features of TLM algorithm, either from programming perspectives or for code reusablity.

After calculating fields inside the PML cells, reflected voltages are calculated from incident ones and fields at the center, similar to the standard SCN:

$$\begin{pmatrix} V_{\mathrm{ref},1} \\ V_{\mathrm{ref},2} \\ V_{\mathrm{ref},3} \\ V_{\mathrm{ref},4} \\ V_{\mathrm{ref},5} \\ V_{\mathrm{ref},6} \\ V_{\mathrm{ref},7} \\ V_{\mathrm{ref},8} \\ V_{\mathrm{ref},9} \\ V_{\mathrm{ref},10} \\ V_{\mathrm{ref},11} \\ V_{\mathrm{ref},12} \\ V_{\mathrm{ref},13} \\ V_{\mathrm{ref},14} \\ V_{\mathrm{ref},15} \\ V_{\mathrm{ref},16} \\ V_{\mathrm{ref},17} \\ V_{\mathrm{ref},18} \\ V_{\mathrm{ref},19} \\ V_{\mathrm{ref},20} \\ V_{\mathrm{ref},21} \\ V_{\mathrm{ref},22} \\ V_{\mathrm{ref},23} \\ V_{\mathrm{ref},24} \end{pmatrix}_n = \begin{pmatrix} \Delta xE_x + Z_o\Delta zH_z - V_{in,12} \\ \Delta xE_x - Z_o\Delta yH_y - V_{in,9} \\ \Delta yE_y - Z_o\Delta zH_z - V_{in,11} \\ \Delta yE_y + Z_o\Delta xH_x - V_{in,8} \\ \Delta zE_z - Z_o\Delta xH_x - V_{in,7} \\ \Delta zE_z + Z_o\Delta yH_y - V_{in,10} \\ \Delta zE_z + Z_o\Delta xH_x - V_{in,5} \\ \Delta yE_y - Z_o\Delta xH_x - V_{in,4} \\ \Delta xE_x + Z_o\Delta yH_y - V_{in,2} \\ \Delta zE_z - Z_o\Delta yH_y - V_{in,6} \\ \Delta yE_y + Z_o\Delta zH_z - V_{in,3} \\ \Delta xE_x - Z_o\Delta zH_z - V_{in,1} \\ \Delta xE_{1,x} - V_{in,13} \\ \Delta yE_{1,y} - V_{in,14} \\ \Delta zE_{1,z} - V_{in,15} \\ \Delta xH_{1,x} - V_{in,16} \\ \Delta yH_{1,y} - V_{in,17} \\ \Delta zH_{1,z} - V_{in,18} \\ \Delta xE_{2,x} - V_{in,19} \\ \Delta yE_{2,y} - V_{in,20} \\ \Delta zE_{2,z} - V_{in,21} \\ \Delta xH_{2,x} - V_{in,22} \\ \Delta yH_{2,y} - V_{in,23} \\ \Delta zH_{2,z} - V_{in,24} \end{pmatrix}_n \tag{31.A a}$$

where each field component is split into two subcomponents, as in (26.A a) and (26.Ab)):

$$\begin{pmatrix} E_x \\ E_y \\ E_z \\ H_x \\ H_y \\ H_z \end{pmatrix}_n = \begin{pmatrix} E_{1,x} + E_{2,x} \\ E_{1,y} + E_{2,y} \\ E_{1,z} + E_{2,z} \\ H_{1,x} + H_{2,x} \\ H_{1,y} + H_{2,y} \\ H_{1,z} + H_{2,z} \end{pmatrix}_n \tag{31.A b}$$

As in standard TLM cells, the next process is the connection process, in which we calculate incident voltages for each cell represented by the vector equation:

$$\begin{pmatrix} V_{in,1}(k,l,m) \\ V_{in,2}(k,l,m) \\ V_{in,3}(k,l,m) \\ V_{in,4}(k,l,m) \\ V_{in,5}(k,l,m) \\ V_{in,6}(k,l,m) \\ V_{in,7}(k,l,m) \\ V_{in,8}(k,l,m) \\ V_{in,9}(k,l,m) \\ V_{in,10}(k,l,m) \\ V_{in,11}(k,l,m) \\ V_{in,12}(k,l,m) \\ V_{in,13}(k,l,m) \\ V_{in,14}(k,l,m) \\ V_{in,15}(k,l,m) \\ V_{in,16}(k,l,m) \\ V_{in,17}(k,l,m) \\ V_{in,18}(k,l,m) \\ V_{in,19}(k,l,m) \\ V_{in,20}(k,l,m) \\ V_{in,21}(k,l,m) \\ V_{in,22}(k,l,m) \\ V_{in,23}(k,l,m) \\ V_{in,24}(k,l,m) \end{pmatrix}_{n+1} = \begin{pmatrix} V_{\mathrm{ref},12}(k,l-1,m) \\ V_{\mathrm{ref},9}(k,l,m-1) \\ V_{\mathrm{ref},11}(k-1,\mathrm{l},m) \\ V_{\mathrm{ref},8}(k,l,m-1) \\ V_{\mathrm{ref},7}(k,l-1,m) \\ V_{\mathrm{ref},10}(k-1,l,m) \\ V_{\mathrm{ref},5}(k,l+1,m) \\ V_{\mathrm{ref},4}(k,l,m+1) \\ V_{\mathrm{ref},2}(k,l,m+1) \\ V_{\mathrm{ref},6}(k+1,l,m) \\ V_{\mathrm{ref},3}(k+1,l,m) \\ V_{\mathrm{ref},1}(k,l+1,m) \\ V_{\mathrm{ref},13}(k,l,m) \\ V_{\mathrm{ref},14}(k,l,m) \\ V_{\mathrm{ref},15}(k,l,m) \\ V_{\mathrm{ref},16}(k,l,m) \\ V_{\mathrm{ref},17}(k,l,m) \\ V_{\mathrm{ref},18}(k,l,m) \\ V_{\mathrm{ref},19}(k,l,m) \\ V_{\mathrm{ref},20}(k,l,m) \\ V_{\mathrm{ref},21}(k,l,m) \\ V_{\mathrm{ref},22}(k,l,m) \\ V_{\mathrm{ref},23}(k,l,m) \\ V_{\mathrm{ref},24}(k,l,m) \end{pmatrix}_n \tag{32.A}$$

An interesting fact about the PML TLM node is that the first 12 ports are reserved for voltages exchanges. However, the remaining 12 ports, are reserved for stubs, to allow the cell to represent the PML non Maxwellian medium and only for internal usage.

5- Matched impedance boundary conditions

Single frequency waveguide matching is easily implemented with TLM as it is done by terminating the waveguide section limiting the computational domain by the mode wave-impedance which is real for propagating modes. Note that this can be done only for single mode operation and at one frequency [36.A]. On the other hand, wideband matching can be achieved with PML. Layers are located at the guide section planes surrounding the discontinuity. They can be located very close to discontinuities as PML also absorbs evanescent modes.

A.7 TLM meshes

Basic TLM algorithms have been developed for Cartesian grids just like FDTD Yee-algorithm. However, one major drawback of this meshing scheme is that Cartesian cells don't match curved boundaries at the interface between two different media in the computational domain. This means that staircase approximation can only be used. Another issue is that fine-details need to be meshed using small cells far beyond the negligible dispersion limit (which is usually around ten cells per wavelength). As a result, we are obliged to use very fine mesh, which is very costly in terms of memory and computational time [26.A].

In order to tackle the above issues, algorithms for parallelepipedic (hexahedral) cells were initially developed. Then, irregular (or non-homogeneous) meshing were proposed [38.A] [26.A]. However, the meshing is structured, which means that any cell shares any face with one adjacent cell only. No interpolation is necessary in this case. Concurrently, different TLM algorithms were derived for different curvilinear coordinate systems such as cylindrical or spherical. These are useful in cases of highly spherical or cylindrical symmetries in the computational domain.

To better approximate curved boundaries, structured tetrahedral meshing, as used in finite integration technique (FIT) was developed [39.A][40.A]. Taking advantage from the advancement in meshing technologies, other meshing techniques were developed such as non-structured block meshing [41.A]. It allows one to better approximate fine details with small meshes and homogeneous zones with larger meshes. However, some instability was reported when local time steps were used to reduce the computational time [41.A] [42.A]. In this thesis

one shall consider parallelepipedic structured meshes, with nonhomogeneous cells sizes (irregular meshing) [38.A] [26.A].

An important point to mention, knowing that the TLM algorithm that we have worked on in this thesis, is valid for any types of linear media, one could use it to do a simulation for a computational domain, meshed by a very irregular non-structured mesh (with some restrictions) [37.A]. This can be done by using the transformation techniques presented by Ward and Pendry' paper [37.A], without any loss of information, by transforming the cells geometrical variations into the material properties matrices.

References

[1.A] C. Christopoulos, The Transmission-Line Modeling (TLM) Method in Electromagnetics, Arizona: Morgan & Claypool, 2006.

[2.A] P. B.Johns, "A Symmetrical Condensed Node for the TLM Method," *IEEE Transactions on Microwave Theory and Techniques,* Vols. MTT-35, no. 4, pp. 370-377, 1987.

[3.A] S. Akhtarzad and P. Johns, "Generalised elements for t.l.m method of numerical analysis," *PROC.IEE,* vol. 122, no. 12, 1975.

[4.A] P. B. Johns and R. L. Beurle, "Numerical solution of 2-dimensional scattering problems using a transmission-line matrix," *Proc.IEE,* vol. 118, no. 9, September 1971.

[5.A] W. J. R. Hoefer, "The Transmission-Line Matrix Method-Theory and Applications," *IEEE Transactions on Microwave Theory and Techniques,* Vols. MTT-33, no. 10, pp. 882-893, 1985.

[6.A] S. Akhtarzad and P. Johns, "Solutions of Maxwell's equations in three space dimensions and time by the t.l.m method of numerical analysis," *PROC. IEE,* vol. 122, no. 12, 1975.

[7.A] M. N. Sadiku, Numerical Techniques in Electromagnetics, CRC Press, July, 2000.

[8.A] W. J. R. Hoefer, P. Tusser and U. Siart, Time Domain Methods in Electrodynamics, Berlin:

Springer, 2008.

[9.A] S. Akhtarzad and P. B. Johns, "Three-Dimensional Transmission-Line Matrix Computer Analysis of Microstrip Resonators," *IEEE Transactions on Microwave Theory and Techniques,* Vols. MTT-23, no. 12, pp. 990-997, 1975.

[10.A] P. Saguet and E. Pic, "Utilisation d'un nouveau type de neoud dans la méthode TLM en 3 dimensions," *Electronics Letters,* vol. 18, no. 11, pp. 479-480, mai 1982.

[11.A] S. L. Maguer, "Développements de nouvelles procédures numériques pour la modélisation TLM: Application à la caractérisation de circuits plaqués de structures à symétrie de révolution en bande millimétrique," These, L'Université de Bretagne Occidentale, 1998.

[12.A] Q. Zhang and W. J. R. Hoefer, "Characteristics of New 3D Distributed Node TLM Meth with Cells of Arbitrary Aspect Ratio," in *IEEE MTT-S Digest,* 1994.

[13.A] A. J. Wlodarkzyk, V. Trenkic, R. A. Scaramuzza and C. Christopoulos, "A Fully Integraged Multiconductor Model for TLM," *IEEE TRANSACTIONS ON MICROWAVE THEORY AND TECHNIQUES,* vol. 46, no. 12, pp. 2431-2437, 1998.

[14.A] V. Trenkic, C. Christopoulos and T. M. Benson, "Theory of the Symmetrical Super-Condensed Node for the TLM," *IEEE Transactions on Microwave Theory and Techniques,* vol. 43, no. 6, pp. 1342-1348, 1995.

[15.A] R. F. Harrington, Time-Harmonic Electromagnetic Fields, John Wiley & Sons, INC., 2001.

[16.A] S. M. Rao, D. R. Wilton and A. W. Glisson, "Electromagnetic Scattering by Surfaces of Arbitrary Shape," *IEEE Transactions on Antennas and Propagation,* Vols. AP-30, no. 3, pp. 409-418, 1982.

[17.A] Z. Shao, W. Hong and H. Wu, "A Z-Transform-Based Absorbing Boundary Condtions for 3-D TLM-SCN Method," *IEEE Transactions on Microwave Theory and Techniques,* vol. 50, no. 1, pp. 222-225, 2002.

[18.A] D. Pasalic, J. Bornemann and R. Vahldieck, "Absorbing Boundary Conditions in the Frequency-Domain TLM Method and Their Application to Planar Circuits," *IEEE Transactinos on Microwave Theory and Techniques,* vol. 49, no. 8, pp. 1469-1476, 2001.

[19.A] J. P. Berenger, "A perfectly matched layer for the absorption of electromagnetic waves," *J. Comput. Phys.,* vol. 114, no. 2, pp. 110-117, 1994.

[20.A] J.-P. Bérenger, Perfectly Matched Layer (PML) for Computational Electromagnetics, Arizona: Morgan & Claypool, 2007.

[21.A] J. A. Casiblanco, D. Seetharamdoo, M. Berineau, M. Ney and F. Gallee, "Surface Boundary conditions for lossy dielectrics to model electromagnetics wave propagation in tunnels," in

EUCAP, 2009.

[22.A] Z. Chen, "The Transmission Line Matrix (TLM) Method and its Boundary Treatments," Thesis,University of Ottawa, 1992.

[23.A] J.-L. Dubard and D. Pompei, "Optimization of the PML Efficiency in 3-D TLM Method," *IEEE Transactions on Micrwave Theory and Techniques*, vol. 48, no. 7, pp. 1081-1088, 2000.

[24.A] J. Dubard and D. Pompei, "Simulation of Berenger's perfectly matched layer with a modified TLM node," *IEE Proc.-Microw. Antennas Propag*, vol. 144, no. 3, pp. 205-207, 1997.

[25.A] N. M. P. Traslavina, "Contrtibution Au Développement De Conditions Aux Limites Absorbantes Pour La Méthode TLM Avec Applications à L'Analyse De Circuits Hyperfréquences," Thése; L'Université De Rennes 1, 1997.

[26.A] A. Taflove and S. C. H. , Computational Electrodaynamics, The Finite-Difference Time-Domain Method, Norwood: Artch House, INC., 2005.

[27.A] A. J. Ward and J. B. Pendry, "Refraction and geometry in Maxwell's equaions," *Journal of Modern Optics*, vol. 43, no. 4, pp. 773-793, 1996.

[28.A] J. Paul et al, "Time-Domain Simulation of Thin Material Boundaries and Thin Panels Using Digital Filters in TLM," *Turk J Elec Engin*, vol. 10, no. 2, pp. 185-198, 2002.

[29.A] J. Lanoe, S. L. Maguer and M. M. Ney, "A Fractional Derivative Operator for Surface Impedance TLM Modeling," *IEEE Microwave and Wireless Components Letters*, vol. 17, no. 9, pp. 625-627, 2007.

[30.A] M. M. Ney, "Modeling of highly conducting boundaries with TLM," *Electromagnetics*, vol. 16, no. 5, pp. 521-536, 1996.

[31.A] J. A. Morente, J. A. Porti and M. Khalladi, "Absorbing Boundary Conditions for the TLM Method," *IEEE Transactions on Microwave Theory and Techniques*, vol. 40, no. 11, pp. 2095-2099, 1992.

[32.A] J. G. Balschak, "A comparative study of absorbing boundary conditions," *Journal of Computational Physics*, vol. 77, pp. 109-139, 1988.

[33.A] N. Pena and M. M. Ney, "Absorbing-boundary conditions using perfectly matched layer(PML) technique for three-dimensional TLM simulations," *IEEE Transactions on Microwave Theory and Techniques*, vol. 45, pp. 1749-1755, 1997.

[34.A] S. L. Maguer and M. M. Ney, "Extended PML-TLM node: an efficient approach for full-wave analysis of open structures," *Int. J. Numer. Model*, vol. 14, pp. 129-144, 2001.

[35.A] J. Fang and Z. Wu, "Generalized Perfectly Matched Layer for the Absorption of Propagation and Evanescent Waves in Lossless and Lossy Media," *IEEE Transactions on Microwave Theory and Techniques,* vol. 44, no. 12, pp. 2216-2222, 1996.

[36.A] N. R. S. SIMONS and E. BRIDGES, "Method for Modelling Free Space Boundaries in TLM Situations," *ELECTRONICS LETTERS,* vol. 26, no. 7, pp. 453-455, 1990.

[37.A] A. J. Ward and J. B. Pendry, "Refraction and geometry in Maxwell's equaions," Journal of Modern Optics, vol. 43, no. 4, pp. 773-793, 1996.

[38.A] D. Al-Mukhtar and J. Sitch, "Transmission-line matrix method with irregularly graded space," *IEE PROC,* vol. 128, no. 6, 1981.

[39.A] P. Swell, *et al*, "Transmission-Line Modeling (TLM) Based Upon Unstructured Tetrahedral Meshes," *IEEE Transactions on Microwave Theory and Techniques,* vol. 53, no. 6, pp. 1919-1928, 2005.

[40.A] P. Sewell, *et al*, "Transmission-Line Modeling Using Unstructured Triangular Meshes," *IEEE Transactions on Microwave Theory and Techniques,* vol. 52, no. 5, pp. 1490-1497, 2004.

[41.A] Z. Li, S. L. Maguer and M. Ney, "On the dispersion of a non-orthogonal TLM cell," *International Journal of Numerical Modelling: Electronic Networks, Devices and Fields,* vol. 21, no. 3, pp. 205-219, 2008.

[42.A] Z. Li, "Contributions aux techniques de maillages irréguliers dans la méthode TLM:Applicqtions au calcul électromagnetique de structures à détails fins et interface non-cartésienns," These, L'Université de Bretagne Occidentale, 2005.

[43.A] N. Peña, M. M. Ney, "A General Formulation of a Three-dimensional TLM Condensed Node with the Modeling of Electric and Magnetic Losses and Current Sources," *12th Annual Review of Progress in APPlied Computational Electromagnetics,* pp. 262-269, 18-22 March 1996.

Etudes d'un modèle temporel efficace pour la simulation d'objets communicants contenant des milieux complexes

Résumé

Au cours de ce projet de thèse, nous avons travaillé sur les techniques numériques dans le domaine temporel en électromagnétisme pour les structures comprenant des matériaux complexes. Nous avons utilisé la méthode "Transmission-Line Matrix" (TLM) comme une méthode de calcul pour mettre en œuvre un simulateur électromagnétique général. Ensuite, nous l'avons validé par plusieurs comparaisons avec des solutions analytiques et des mesures. Pour faciliter les simulations de structures à géométrie complexe, nous avons développé une interface utilisateur graphique (GUI) pour le simulateur. Nous avons développé une analyse théorique complète des phénomènes de dispersion numériques et des conditions de stabilité du modèle TLM lorsque des milieux complexes sont impliqués. Cela permet d'optimiser les ressources de l'ordinateur en fonction du niveau de précision requis. L'autre problème que nous avons abordé est le problème basse fréquence dans les techniques du domaine temporel. En effet, le pas temporel requis devient en général très petit et fait exploser le temps de calcul. Pour ce problème classique, nous avons proposé des solutions nouvelles en appliquant des techniques de cartographie. Ces solutions sont proposées sur la base de la modification du tenseur métrique de l'espace et du temps et la transformation du problème en un problème bien posé. Enfin, dans la dernière partie du projet nous avons effectué la comparaison entre les méthodes FDTD et TD-TLM en simulant des structures avec des milieux très contrastés en termes de paramètres constitutifs. Cette étude confirme que la TLM possède une convergence plus rapide que la FDTD. On peut l'expliquer par la nature locale de l'algorithme TD-TLM. Cette différence de convergence a été aussi nettement observée en présence de maillages irréguliers (structurés), lorsque le rapport des tailles de maille augmente.

1. Chapitre I : Introduction Générale

Dans ce chapitre, nous présentons une brève discussion sur les méthodes numériques en général et les différentes formes des équations de Maxwell. Nous discutons aussi de la portée et les limites de ce travail. De plus, nous discutons et justifions l'utilisation de la méthode TLM pour atteindre l'objectif qui est de mettre en œuvre un solveur électromagnétique pour les milieux linéaires généraux avec des géométries arbitraires.

La méthode TLM "Transmission line matrix" est une méthode de calcul des champs basée sur la superposition d'ondes locales canalisées par des lignes de transmission interconnectées [1]. On l'assimile à un modèle de propagation numérique spatio-temporel de Huygens. Les principales caractéristiques de cette méthode de calcul sont:

- Précision : génère une dispersion (erreur de vitesse) plus faible que la méthode des différences-finies temporelles (FDTD). Le caractère condensé de la cellule (SCN) la rend plus précise que la FDTD lorsque les contrastes entre milieux et/ou les rapports de maillages irréguliers augmentent.
- Calcul des champs : toutes les composantes sont calculées au centre de la cellule au même pas temporel.
- Interface : les composantes tangentielles des champs sur les faces de la cellule sont aussi calculées simultanément ce qui aligne tout type de paroi et rend l'interface avec d'autres méthodes plus facile.
- Coût de calcul : demande plus d'opérations que la FDTD mais fonctionne toujours au pas temporel maximum (minimum de dispersion).
- Coût de mémoire : L'information supplémentaire sur les champs et la meilleure précision se paie par un stockage d'un plus grand nombre de variables (18 tensions de bras au maximum).
- Types de solutions : Appartenant à la classe des méthodes volumiques temporelles dites rigoureuses [2] [2], elle peut traiter une géométrie arbitraire avec des milieux non linéaires, anisotropes et des structures très hétérogènes.

2. Chapitre II : La physique des milieux complexes

Dans ce chapitre, nous discutons brièvement la physique des milieux complexes et de montrer leur comportement lorsqu'ils sont soumis à un champ électromagnétique. D'une manière générale, l'action d'un champ électromagnétique sur un milieu induit une polarisation qui est une réaction de la structure interne de la matière. De la même manière, des densités de courant qui peuvent y être induites provoquent en général des phénomènes de dissipation. Les interactions décrites ci-dessus sont caractérisées par des paramètres constitutifs qui lient les champs $\vec{E}$ et $\vec{H}$, respectivement aux champs d'induction $\vec{D}$ et $\vec{B}$ ainsi que les densités de courant associées. La nature de ces relations appelées "constitutives" indique la nature plus ou moins complexe du milieu. Par exemple, un milieu simple homogène est défini par trois paramètres constitutifs, la permittivité ε, la perméabilité μ et la conductivité σ. Dans ce cas, tous sont des scalaires positifs et constants, c'est à dire, indépendants du temps, de la fréquence du signal et [3]. Les relations constitutives sont donc de simples expressions de proportionnalité entre les champs cités plus haut :

$$\vec{D} = \varepsilon\vec{E} \quad (1.a)$$

$$\vec{B} = \mu\vec{H} \quad (1.b)$$

$$\vec{J} = \sigma\vec{E} \quad (1.c)$$

Si un des paramètres constitutifs ne remplit plus les hypothèses simples émises ci-dessus, alors le milieu est dit "complexe". Ce milieu tombe alors dans les différentes catégories citées ci-dessous, dépendent du paramètre ou des paramètres impliqués [3] :

- Hétérogène : Un des paramètres dépend des coordonnées spatiales.
- Dispersif : Un des paramètres est fonction de la fréquence.
- Anisotrope : Un des paramètres dépend de la direction du champ et doit s'exprimer sous la forme d'un tenseur.
- Chiral : Les phénomènes électriques et magnétiques sont couplés et les relations constitutives font apparaître des paramètres de chiralité liant le champ électrique et magnétique.
- Non linéaire : Un des paramètres dépend de l'amplitude des champs.
- Non stationnaire : Un des paramètres dépend du temps.

Un milieu peut appartenir à plusieurs des catégories mentionnées ci-dessus, augmentant encore plus sa complexité. D'une façon générale, un milieu est complexe mais il est souvent possible d'effectuer une simplification, par exemple sur une bande de fréquences ou pour de petites amplitudes, de façon à faire l'hypothèse d'un milieu simple. Cependant, pour des applications bien spécifiques, la nature complexe du milieu est justement utilisée ou pour des fréquences élevées ou de grandes amplitudes, celle-ci ne peut plus être négligée. Par conséquent, un modèle mathématique des paramètres constitutifs plus élaborés doit être mis en œuvre, basé sur le comportement physique du milieu. Dans un deuxième temps, ce modèle devra être inséré dans les équations de Maxwell pour déterminer la configuration des champs et la densité de courant correspondante, prenant ainsi en compte la complexité du milieu.

Dans ce chapitre, nous avons présenté plusieurs types de milieux complexes tels que :

- **Milieu dispersive**

Un milieu est considérée dispersif si une ou plusieurs de ses paramètres constitutifs $\varepsilon(\omega), \mu(\omega), \sigma(\omega)$est ε dépendante de la fréquence. Un exemple est un milieu de Debye où la permittivité est définie par [4]:

$$\bar{\bar{\varepsilon}}_r = (\varepsilon_\infty + \frac{\varepsilon_s - \varepsilon_\infty}{1 + j\omega\tau_o})\bar{\bar{I}}_3 \quad (2)$$

où ε_∞ , ε_s sont respectivement les permittivités à très haute fréquence et en DC, τ_o est le temps de relaxation du milieu.

- **Milieu anisotrope**

Un milieu est considéré comme anisotrope si ses paramètres constitutifs sont dépendants de la direction. Dans ce cas les paramètres constitutifs deviennent des tenseurs. Par exemple, un milieu anisotrope diélectrique est caractérisé de manière général par [3] :

$$\bar{\bar{\varepsilon}}_r = \begin{pmatrix} \varepsilon_{xx} & \varepsilon_{xy} & \varepsilon_{xz} \\ \varepsilon_{yx} & \varepsilon_{yy} & \varepsilon_{yz} \\ \varepsilon_{zx} & \varepsilon_{zy} & \varepsilon_{zz} \end{pmatrix} \quad (3)$$

où $\bar{\bar{\varepsilon}}_r$ est une matrice hermitienne.

- **Milieu chiral**

Dans le domaine fréquentiel les relations constitutives du milieu chiral sont exprimées de la façon suivante [5]:

$$\bar{D}(\omega) = \varepsilon(\omega)\bar{E}(\omega) - \frac{j\kappa(\omega)}{c_o}\bar{H}(\omega) \quad (4.a)$$

$$\bar{B}(\omega) = \mu(\omega)\bar{H}(\omega) + \frac{j\kappa(\omega)}{c_o}\bar{E}(\omega) \quad (4.b)$$

où ε, μ sont respectivement la permittivité et la perméabilité, c_o est la vitesse de la lumière dans le vide et κ est le paramètre de chiralité. Dans cet exemple, les paramètres , ε, μ, κ dépendent de la fréquence selon les relations :

$$\kappa(\omega) = \frac{\omega_o \omega}{\omega_o^2 - \omega^2 + j2\omega_o\xi\omega} \quad (5.a)$$

$$\varepsilon(\omega) = \varepsilon_o\varepsilon_\infty + \frac{(\varepsilon_s - \varepsilon_\infty)\varepsilon_o\omega_{oe}^2}{\omega_{oe}^2 - \omega^2 + j2\xi_e\omega} \quad (5.b)$$

$$\mu(\omega) = \mu_o\mu_\infty + \frac{(\mu_s - \mu_\infty)\mu_o\omega_{om}^2}{\omega_{om}^2 - \omega^2 + j2\xi_m\omega} \quad (5.c)$$

où ω_o représente la fréquence de résonnance caractéristique du milieu chiral, ξ est le facteur d'atténuation. Les pulsations ω_{oe} et ω_{om} sont respectivement les fréquences de résonnances des modèles diélectriques et magnétiques, ξ_e, ξ_m leur facteur d'atténuation correspondant. Les constantes ε_s, μ_s sont respectivement les valeurs statiques de permittivité et perméabilité et ε_∞, μ_∞ leur valeur asymptotique correspondante vers les hautes fréquences.

- **Milieu ferrimagnétique**

Dans un milieu ferrimagnétique le tenseur de perméabilité dépend du champ magnétique statique externe appliqué et l'état d'aimantation intérieur de l'échantillon de ferrite suit l'équation de Landau-Lifshitz-Gilbert [6] :

$$\frac{d\vec{M}}{dt} = -\gamma \vec{M} \times \vec{H}_{eff} + \frac{a}{M_s} \vec{M} \times \frac{d\vec{M}}{dt} \quad (6)$$

Lorsque le champ externe appliquée atteint une certaine amplitude, le support magnétique est saturé. Pour un petit champ électromagnétique perturbant, on peut caractériser le milieu saturé par le modèle du tenseur Polder [3] :

$$\mu = \begin{pmatrix} \mu_{xx} & \mu_{xy} & 0 \\ \mu_{yx} & \mu_{yy} & 0 \\ 0 & 0 & \mu_{zz} \end{pmatrix} \quad (7.a)$$

D'autre part, si le champ magnétisant appliqué ne n'impose pas la saturation de l'échantillon ferrite, on doit utiliser des modèles plus sophistiqués comme celui de Gelin et al [3] qui prend en compte l'existance des domaines qui subsistent hors saturation. Ceci conduit à un modèle de tenseur complet :

$$\mu = \begin{pmatrix} \mu_{xx} & \mu_{xy} & \mu_{xz} \\ \mu_{yx} & \mu_{yy} & \mu_{yz} \\ \mu_{zx} & \mu_{zy} & \mu_{zz} \end{pmatrix} \quad (7.b)$$

Pour résumer, l'échantillon ferrite a des propriétés qui sont fonction de l'amplitude du champ de magnétisation appliquée. Lorsque le champ magnétique continu appliqué est au-delà d'une certaine valeur, l'échantillon de ferrite atteint l'état de saturation. Dans ce cas, il devient homogène et les tenseurs de perméabilité peut être décrit par le modèle de Polder (7.a). Toutefois, si le champ magnétisant diminue, des domaines ayant des propriétés magnétiques différentes apparaissent et le milieu n'est plus homogène. Dans un tel scénario, le tenseur de perméabilité suit généralement le modèle plus général (7.b) développés par Gelin et al. [5] [6]. Le calcul des composantes du tenseur à l'intérieur de l'échantillon non saturé nécessite la résolution de l'équation GLL (6). Cette équation est une équation différentielle partielle non linéaire et généralement très difficile à résoudre en particulier pour les géométries non-canoniques. En résolvant (6), on peut calculer l'état d'aimantation à l'intérieur de chaque domaine. Habituellement, le processus de calcul des tenseurs de perméabilité, en particulier pour la ferrite non-saturé, est un processus en plusieurs étapes qui doit être mené avec soin pour déboucher sur des résultats fiables. Dans un premier temps, il est nécessaire d'avoir des données expérimentales sur ses propriétés (telles que la température de Curie, ses dimensions, son état de magnétisation initiale ... etc.). Ces données ont généralement une certaine incertitude en raison d'erreurs expérimentales. Cette incertitude peut affecter la solution des équations GLL et, par conséquent, fausser l'état d'aimantation des domaines. La résolution des problèmes impliquant des ferrites non saturées constitue une contribution majeure de ce travail et des applications sont détaillées dans le chapitre V, dans le cadre de la validation du simulateur TLM.

.

3. Chapitre III : La méthode "Transmission Line Matrix" (TLM), état de l'art

Dans ce chapitre, nous présentons l'état de l'art de l'algorithme TLM pour les milieux linéaires complexes, avec la description complète de l'algorithme pour les nœuds SCN-TLM. Toutefois, l'annexe A est consacrée à l'histoire de la TLM et les algorithmes SCN-TLM pour les milieux simples et les différents types de conditions aux limites :

Dans [7] et [8], les auteurs ont présenté une cellule condensée symétrique (SCN) pour les milieux anisotropes. Des études de dispersion du modèle pour ces milieux ont été effectuées. Dans l'approche TLM présentée ici, deux étapes sont proposées: Dans la première, une simple mise à jour des champs dans le vide est effectuée [8] [9]. Dans le processus standard, les tensions réfléchies du nœud TLM pour effectuer l'itération suivante sont calculées par les valeurs des composantes des champs au centre et les tensions incidentes à l'itération précédente [9].

La présence d'un milieu doit être prise en compte. Il est normalement d'usage d'ajouter des bras réactifs (stubs) soit au maximum 6 tensions supplémentaires pour le nœud SCN-TLM [9]. Dans l'approche présentée ici, cette présence de milieux est plutôt prise en charge par un filtrage de la séquence temporelle des champs au centre de la cellule avant le calcul des tensions réfléchies pour l'itération suivante. Il s'agit en fait d'une formulation générale commune à toute sorte de milieux tels que les milieux anisotropes dispersifs par exemple pour lesquels l'utilisation de bras réactifs n'est pas possible. Par exemple, dans le cas d'utilisation de cellules cubiques on économise ainsi la manipulation et le stockage de 6 tensions mais au prix d'un filtrage qui remplace le produit de convolution théoriquement nécessaire dans le cas général. Il doit être noté cependant que dans le cas de milieux simples, les produits de convolutions deviennent triviaux.

- ***Modèle théorique***

Les équations rotationnelles de Maxwell, peuvent s'écrire dans le domaine temporel et pour un milieu général sous la forme compacte [3] [9] :

$$\begin{bmatrix} \nabla \times H \\ -\nabla \times E \end{bmatrix} - \begin{bmatrix} J_{ef} \\ J_{mf} \end{bmatrix} = \frac{\partial}{\partial t}\begin{bmatrix} \varepsilon_o E \\ \mu_o H \end{bmatrix} + \begin{bmatrix} \bar{\bar{\sigma}}_e * E \\ \bar{\bar{\sigma}}_m * H \end{bmatrix} + \frac{\partial}{\partial t}\begin{bmatrix} \varepsilon_o \bar{\bar{\chi}}_e & \frac{\bar{\bar{\xi}}}{c_o} \\ \frac{\bar{\bar{\zeta}}}{c_o} & \mu_o \bar{\bar{\chi}}_m \end{bmatrix} * \begin{bmatrix} E \\ H \end{bmatrix} \tag{8}$$

où $\bar{\bar{\chi}}_e, \bar{\bar{\chi}}_m$ sont respectivement les tenseurs de susceptibilité électrique et magnétique, $\bar{\bar{\sigma}}_e, \bar{\bar{\sigma}}_m$ les tenseurs de conductivité électrique et magnétique, et $\bar{\bar{\xi}}$, $\bar{\bar{\zeta}}$ les tenseurs de chiralité [9]. Et * indique la convolution temporelle. Nous pouvons observer dans (8) plusieurs termes :

1- Les opérateurs spatiaux et temporel ($\nabla \times, \nabla ., \partial/\partial t$)
2- Les tenseurs caractérisant les milieux $\bar{\bar{\chi}}_e, \bar{\bar{\chi}}_m, \bar{\bar{\sigma}}_e, \bar{\bar{\sigma}}_m, \bar{\bar{\xi}}, \bar{\bar{\zeta}}$

Ceci illustre les deux étapes de l'algorithme proposé : la propagation des ondes et leurs interactions avec les milieux.

L'application de l'algorithme TLM dont les détails peuvent être trouvés dans [9] [8] [10] [11], conduit aux équations de mise à jour des tensions et des champs suivantes :

- Diffusion des tensions aux nœuds TLM :

$$V_{n+1}^{inc} = \bar{\bar{S}} V_{n+1}^{ref} \tag{9}$$

- Evaluation des champs au centre d'un nœud dans l'espace libre :

$$\begin{bmatrix} E_o \\ H_o \end{bmatrix}_{n+1} = \bar{\bar{\Lambda}} \left(\begin{bmatrix} E_c \\ H_c \end{bmatrix}_n + \bar{\bar{Z}}\, V_{n+1}^{inc} \right) \tag{10}$$

- Correction des champs au centre d'un nœud due à la présence de la matière :

$$\begin{bmatrix} E_c \\ H_c \end{bmatrix}_{n+1} = \left(\begin{bmatrix} E_o \\ H_o \end{bmatrix}_{n+1} ; \begin{bmatrix} E_c \\ H_c \end{bmatrix}_{n-M+1:n} \right) * \bar{\bar{\Gamma}} \tag{11}$$

où $\bar{\bar{\Gamma}}$ est une matrice 6x6xM représentant un filtre d'ordre M dans le domaine temporel (figure 1) dont les éléments sont donnés par :

$$\bar{\bar{\Gamma}}_{ij}(z) = \frac{\sum_{k=0}^{M} b_{ijk} z^{-k}}{1+\sum_{k=1}^{M} a_{ijk} z^{-k}} = b'_o + \frac{\sum_{k=1}^{M} b'_{ijk}\, z^{-k}}{1+\sum_{k=1}^{M} a_{ijk} z^{-k}} \tag{12}$$

On notera que la procédure de correction des champs s'applique en présence d'un milieu. Cependant, si nous sommes dans le cas limite où le milieu est l'espace libre la matrice de correction est diagonale dont les éléments sont des fonctions de Dirac. Ces dernières rendent les produits de convolution triviaux.

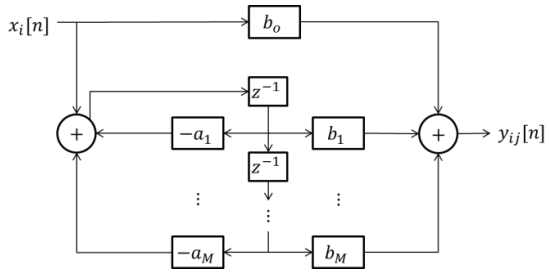

Figure 1, Schéma bloc du filtre $\bar{\bar{\Gamma}}_{ij}(z)$

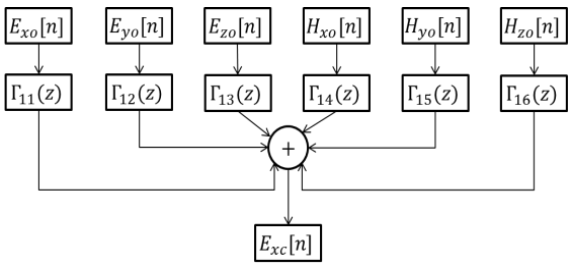

Figure 2, Procédure de filtrage global pour la composante du champ électrique E_{xc} dans la direction x.

- Connexion effectuant le transfert des tensions entre les nœuds :

$$V_{n+2}^{ref} = \bar{\bar{A}} \begin{bmatrix} E_c \\ H_c \end{bmatrix}_{n+1} + \bar{\bar{B}} V_{n+1}^{inc} \tag{13}$$

Dans cette étape, les tensions réfléchies sont calculées à tous les accès du nœud SCN. Elles seront utilisées comme tensions incidentes aux nœuds voisins pour l'itération suivante.

Les matrices $\bar{\bar{S}}, \bar{\bar{\Lambda}}, \bar{\bar{Z}}, \bar{\bar{A}}, \bar{\bar{B}}$ sont des matrices à éléments constants et peuvent être trouvées dans [9]. La matrice de filtrage $\bar{\bar{\Gamma}}$ contient 36 filtres à réponse impulsionnelle infinie (RII). Pour chacun, le numérateur et dénominateur ont un degré M. Pour un milieu dispersif ayant son modèle physique établi (Debye, Lorentz pour $\bar{\bar{\varepsilon}}(\omega)$ [4], Polder ou Gelin [6]pour $\bar{\bar{\mu}}(\omega)$), des logiciels mathématiques sont utilisés pour extraire les coefficients des filtres. Dans le cas général d'un milieu dispersif dont les paramètres constitutifs sont donnés dans le domaine fréquentiel (données expérimentales incluses), des méthodes de traitement de signal comme celle de Prony ou LSM (moindres carrés) peuvent être utilisées [12]. Il s'agit d'extraire les pôles et résidus des données pour une approximation de Padé et ensuite appliquer une transformée bilinéaire pour trouver les coefficients des filtres [12].

4. Chapitre IV : Analyse de la stabilité et de la dispersion analyse d'une de l'approche unifiée de la TLM pour les milieux complexes linéaires généraux

Dans ce chapitre, nous présentons une méthode systématique pour l'étude et l'analyse des caractéristiques de dispersion et de stabilité de la méthode dans les milieux linéaires complexes. Plus particulièrement, on montrera la pertinence de l'étude qui permet de déterminer la taille de maille et le pas temporel associé pour un niveau d'erreur due à la dispersion acceptable. Cela permet de réduire au minimum l'effort de calcul requis**.**

En milieux continus, on entend par dispersion la modification de la vitesse de phase soit en raison de la variation de la fréquence de fonctionnement ou en raison de la variation du nombre d'ondes en cas de milieux anisotropes (appelée l'anisotropie de vitesse) [4] [3]. Etant donné que la vitesse de phase est une fonction du nombre d'onde, on peut dire que la dispersion est un phénomène qui relie la fréquence du signal et le vecteur d'onde. Dans les milieux échantillonnés spatialement il existe une erreur de vitesse additionnelle liée à la taille de l'échantillonnage relativement à la longueur d'onde du signal. Cette dépend aussi de la direction de propagation de l'onde (anisotropie). Il existe cependant, des directions où cette erreur est nulle, c'est à dire que la vitesse de l'onde simulée est égale à la vitesse physique quelle que soit la fréquence. Mais il existe toujours dans un cas général un phénomène d'erreur de vitesse de propagation apportée par le modèle numérique et qui dépend du processus d'échantillonnage spatio-temporel [13] [4] [14] [15]. Cette erreur devient négligeable lorsque la taille électrique des mailles devient petite par rapport à la longueur d'onde considérée [13] [14]. Elle dépend aussi du

pas temporel utilisé, bien qu'en TLM on opère toujours au pas temporel maximum qui assure la stabilité.

Dans ce contexte, une question importante se pose: comment choisir le maillage de façon optimale ? En d'autres termes, comment faire le meilleur compromis entre la taille des mailles (des exigences de calcul) et le niveau tolérable de dispersion numérique ? Une première réponse serait de faire une simulation initiale avec des mailles relativement grande (environ $\lambda_{min}/10$, puis de raffiner le maillage progressivement jusqu'à ce que les résultats convergent. Cependant, quand on a affaire à des problèmes hétérogènes, en particulier ceux avec des milieux complexes, le remaillage successif du domaine et répétant chaque fois le calcul n'est pas une option acceptable. En outre, pour un maillage donné il est important d'avoir un procédé systématique pour calculer le pas temporel maximal dans le but de minimiser le temps de simulation.

En ce qui concerne les modèles temporels, leur domaine de validité en termes de dispersion et leur stabilité n'ont pas été complètement étudiés en présence des milieux complexes et en particulier pour la méthode TLM. Dans cette thèse, ces deux sujets sont étudiés dans le cadre de la TLM en milieux complexes formulée selon la procédure générale pour la cellule SCN développée dans ce travail.

Dans la plupart des publications, soit pour la FDTD ou la TLM [4] [13], les auteurs utilisent l'inégalité suivante en règle générale, pour calculer la taille maximale de cellule qui maintient un certain niveau acceptable de dispersion :

$$\{\Delta x, \Delta y, \Delta z\} \leq Min\left[\frac{\lambda_o}{10\sqrt{\varepsilon_r \mu_r}}\right] \tag{14}$$

où λ_o est la longueur d'onde en espace libre, ε_r et μ_r sont respectivement la permittivité et la perméabilité du milieu. Chaque fois que le domaine de calcul est constitué de milieux non homogènes (ce qui est généralement le cas), il faut utiliser la dimension de cellule minimum, de sorte que la dispersion globale reste négligeable partout. Ce point est la raison de l'opérateur "min" dans (7). En fait, cette relation (qui est en accord avec l'approche présentée plus tôt) est valable pour les milieux sans pertes, non dispersifs et isotropes. Toutefois, lorsque des milieux complexes sont impliqués et où il est nécessaire de ne pas dépasser une certaine limite de dispersion, un test de convergence de maille doit être appliqué. Cela implique que des simulations successives avec un maillage plus fin, au moins à certains endroits, doivent être effectuées.

L'alternative à un test de convergence mentionné plus haut est de connaître le niveau de dispersion maximum a priori. Par conséquent, on peut utiliser une taille maximale de cellule dans toutes les régions qui ne nécessitent pas la résolution spatiale fine (requis seulement par l'approximation géométrique fine de détails).

- **Equations de dispersion dans les milieux continus**

Dans un milieu continu general, la propagation d'une onde plane dans une direction arbitraire $\vec{k}$ débouche sur une solution non triviale dans le domaine spectral, si la condition suivante est remplie :

$$\det\left(\omega\bar{\bar{I}}_6 + \omega\bar{\bar{M}}(\omega) - j\bar{\bar{\sigma}}(\omega) + \bar{\bar{\Lambda}}\right) = 0 \tag{15.a}$$

où ωest la pulsation, $\bar{\bar{M}}$ et $\bar{\bar{\sigma}}$ les tenseurs de milieux, et $\bar{\bar{\Lambda}}$ les opérateurs de rotation dans le domaine spectral :

$$\bar{\bar{\Lambda}} = \begin{pmatrix} 0 & 0 & 0 & 0 & +k_z & -k_y \\ 0 & 0 & 0 & -k_z & 0 & +k_x \\ 0 & 0 & 0 & +k_y & -k_x & 0 \\ 0 & -k_z & +k_y & 0 & 0 & 0 \\ +k_z & 0 & -k_x & 0 & 0 & 0 \\ -k_y & +k_x & 0 & 0 & 0 & 0 \end{pmatrix} \tag{15.b}$$

- **Equations de dispersion dans les milieux discrétisés**

$$\det\left(\bar{\bar{T}} - \bar{\bar{\Psi}}\left(\bar{\bar{\Lambda}}\bar{\bar{\Gamma}}(z)\bar{\bar{Q}} - \bar{\bar{\Phi}}\right)\right) = 0 \tag{16}$$

où les matrices $\left\{\bar{\bar{T}}, \bar{\bar{\Psi}}, \bar{\bar{\Lambda}}, \bar{\bar{\Gamma}}(z), \bar{\bar{Q}}, \bar{\bar{\Phi}}\right\}$ sont bien définis dans le quatrième chapitre de la thèse.

4.a. Dispersion en milieu anisotrope

Dans une première expérience numérique illustrée à la figure 3, nous choisissons, un milieu sans perte anisotrope non magnétique. La fréquence de fonctionnement est $f = 500MHz$, et Δt_{max} a été utilisé.

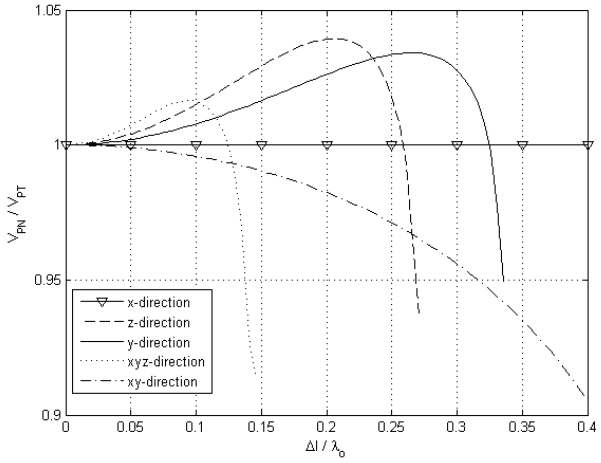

Figure 3, courbes de dispersion dans un milieu anisotrope non magnétique à différentes directions de propagation, où $\bar{\bar{\varepsilon}}_r = diag\{1,2,3\}$

Comme nous pouvons le voir dans la figure 3, l'onde propagée dans des directions différentes ont des caractéristiques de dispersion différentes. Par exemple, dans la direction x il n'y a aucune dispersion, alors qu'elle est maximale dans la direction de la diagonale principale du cube (1,1,1).

Si l'on choisit une formule empirique tel que (14), le pas spatial maximal sera $\lambda_o/10\sqrt{\varepsilon_{r,Max}} = 0.057\ \lambda_o$, pour une erreur de dispersion négligeable. Cette taille de maille selon la figure 4, correspond à une erreur de vitesse maximum d'environ 1,0%..

4.b. Milieu de Debye

La permittivité d'un milieu dispersif de Debye non magnétique est donnée par (2). Dans la figure 4, différentes courbes de dispersion pour différents matériaux de Debye dans la direction axiale sont illustrées pour $f = 79.6\,MHz$. V_{PN} est la vitesse de phase numérique, V_{PT} est la vitesse de phase théorique calculée pour le milieu continu (8.a) [9]. Chaque courbe de dispersion est étalonnée par rapport à sa vitesse de phase théorique. Pour le choix du pas temporel, nous avons utilisé une valeur légèrement plus petite que Δt_{max} pour accélérer les calculs effectués par Mathematica pour la solution de l'équation de dispersion. Comme prévu, la figure 5 montre que dispersion augmente avec ε_s, puisque la taille électrique de la maille augmente das ce cas.

Si nous choisissons la formule empirique (14), le pas spatial maximal est $\lambda_o/10\sqrt{\|\varepsilon_r(f)\|}$. Le tableau 1 montre la différence entre le choix de taille de maille après l'étude de dispersion formelle proposée pour 1,0% d'erreur de dispersion et celui par rapport à la formule simple (14).

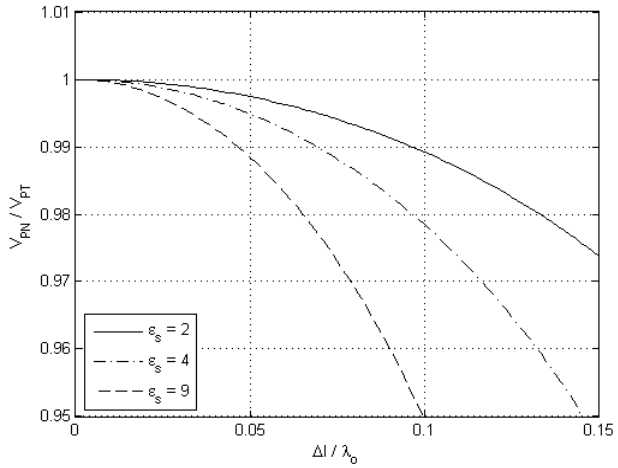

Figure 4, courbes de dispersion en milieu Debye dans la direction diagonale des cellules (1,1,1) avec $\varepsilon_s = \{2,4,9\}$, $\varepsilon_\infty = 1$ et $\tau_o = 100ps$

Tableau 1, comparaison entre l'approche proposée rigoureuse et la règle (14) pour la taille maximale de la cellule en termes de besoins en mémoire pour le milieu de Debye du cas de figure 4

ε_s	$\Delta l/\lambda_o$ critère (14)	$\Delta l/\lambda_o$ 1.0% erreur	Gain en mémoire %
2.0	0.071	0.095	239.5%
4.0	0.050	0.068	251.6 %
9.0	0.033	0.045	253.6 %

Dans le milieu dispersif continu, il est bien connu que la vitesse de phase de l'onde dépend de la fréquence. Ainsi, le comportement d'un modèle discret doit converger vers le modèle continu lorsque $\Delta l/\lambda_o \to 0$. La figure 5 montre les courbes de dispersion d'un milieu de Debye pour une propagation dans le plan xOy en comparaison du modèle échantillonné pour différentes valeurs de Δl. En résolvant les équations de Maxwell dans le domaine spectral pour le milieu continu de Debye, la solution analytique de l'équation de dispersion est :

$$k_x^2 + k_y^2 = k_o^2 \tag{17.a}$$

où k_o^2 est le module au carré du vecteur de nombre d'onde et donnée par :

$$k_o^2 = \left\| \frac{\omega_o^2}{c_o^2} \left(\frac{j\varepsilon_\infty - \tau_o \omega_o \varepsilon_s}{\tau_o \omega_o - j} \right) \right\| \tag{17.b}$$

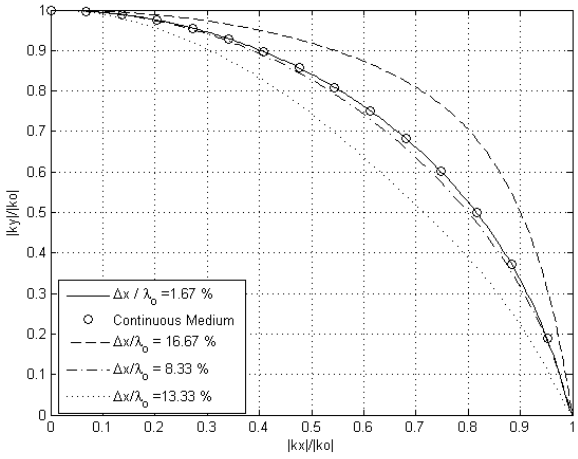

Figure 5, composantes du vecteur d'onde $k_x - k_y$ pour différentes valeurs de Δx dans un milieu échantillonné de Debye, avec $\varepsilon_\infty = 1, \varepsilon_s = 2, \tau_o = 1.667n,\ \omega_o = \pi 10^9 rad/sec$

On peut observer sur la figure 5 la convergence du modèle échantilloné de la solution analytique (17.a) et (17.b) lorsque le pas spatial Δx diminue.

5. Chapitre V : Résultats, Applications et Discussions

Dans ce chapitre, le simulateur électromagnétique est brièvement décrit. Par rapport au simulateur TLM existant au laboratoire, ce travail a contribué à son extension aux milieux complexes et l'ajout d'une interface avec un mailleur pouvant appréhender des formes géométriques arbitraires de façon conviviale. Des tests de validité à la fois des modèles de milieux intégrés et de l'interface sont aussi présentés.

5.a. Simulateur TLM

- Il permet de simuler des structures tridimensionnelles avec une géométrie générale et en présence de milieux complexes.
- Le solveur est écrit pour les équations de Maxwell dans le système de coordonnées cartésiennes.
- Il utilise un maillage hexaédrique irrégulier structuré (approximation par escalier des frontières courbes).
- Il peut gérer n'importe quel média linéaire (paramètre indépendants des valeurs des champs), dispersif, non homogène, anisotrope et chiral défini jusqu'au niveau de la cellule.
- Le domaine de calcul peut être tronqué en utilisant différents types de conditions aux limites telles que la couche parfaitement adaptée (PML), conducteurs électriques parfaits (PEC) et parois magnétiques (PMC). Il peut aussi imposer des conditions d'impédance (par exemple une condition de rayonnement ou d'impédance de mode dans un guide).
- Il est possible d'utiliser un PMC et/ou un PEC en tant que plans de symétrie (ou asymétrie) afin de réduire l'effort de calcul.
- Le solveur est équipé de fonctions pour afficher les grandeurs électromagnétiques (champs, densités de courant) sur une zone ou des points n'importe où à l'intérieur du domaine de calcul à la fois dans le temps et dans le domaine fréquentiel (par FFT ou DFT).
- Bien que plusieurs cellules TLM aient été développées, le solveur utilise la cellule condensée (SCN) qui est le meilleur choix pour les milieux complexes puisque, contrairement au nœud symétrique condensé hybride (HSCN) et au nœud symétrique super condensé (SSCN), les impédances des lignes sont toujours celle de l'espace libre et ne nécessite donc aucun traitement aux interfaces entre milieux.
- Le solveur peut calculer les champs lointains en dehors du domaine de calcul en utilisant l'équivalence par l'intégration des sources fictives sur la surface de Kirchhoff entourant toutes les sources (rayonnement d'antennes et calcul de surface équivalente radar (SER)).
- Permet plusieurs types d'excitation, comme le port localisée, zones d'excitation (gabarit de modes) et par surface de Huygens.

- Le solveur est écrit en langage FORTRAN90, dans lequel nous avons importé plusieurs fonctions de la bibliothèque de calcul NAG. Le solveur peut travailler à la fois sous Windows ou Linux.
- On remarquera que le code peut être parallélisé pour effectuer les calculs sur les machines de traitement parallèle. Ceci sera effectué dans le cadre d'un projet DGA (MEDUSES 2), en collaboration avec l'Université de Nice (LEAT) et le CINES (Centre Informatique National de l'Enseignement Supérieur) à Montpellier.

5.b. Interface graphique par le logiciel GiD

Nous avons également terminé de tester le solveur avec l'interface GiD [9] pour différents exemples sur des antennes, des cavités, des guides d'ondes, par exemple.

Les possibilités offertes par cette interface sont multiples :

I. Création de la géométrie, en dessinant toutes les régions du domaine de calcul.
II. Définir et attribuer les propriétés des matériaux à différentes régions jusqu'au niveau de la cellule.
III. Définir les conditions aux limites et les plans de symétries au cas échéant.
IV. Définir les sources et les points ou zones de lecture.
V. Définir la surface Kirchhoff pour la transformation en champ proche-champ lointain.

Cette interface graphique facilite l'entrée de géométries complexes (les figures 6 et 7); il nous permet également de voir et vérifier la structure avant de faire les simulations. Cette interface graphique facilite l'entrée de géométries complexes (les figures 6 et 7); il nous permet également de voir et vérifier la structure avant de faire les simulations. Les différentes couleurs représentent différentes zones (surface de Kirchhoff ou milieux) du domaine de calcul

.

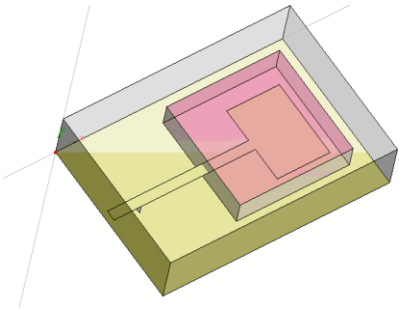

Figure 6, Antenne Patch créés à l'aide GiD [16]

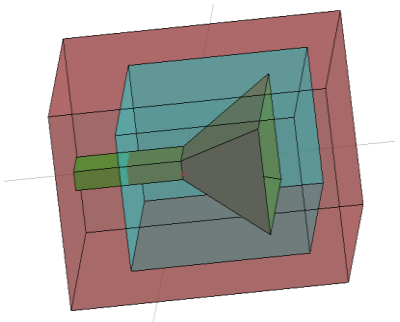

Figure 7, Antenne conique créé en utilisant GiD [16]

5.c. Exemples d'application

I. Cavité cubique remplie d'un matériau isotrope à pertes

Dans un premier exemple de validation du modèle TLM général, le Tableau 2 montre la comparaison des fréquences de résonance d'une cavité remplie d'un milieu anisotrope. Le Tableau 3 montre le facteur de qualité d'une cavité cubique remplie d'un matériau isotrope à pertes (dispersif), en fonction de la fréquence.

Tableau 2, cavité résonante rectangulaire 30x30x60 cm, rempli d'un matériel anisotrope εxx = 8, εyy =2 εzz =2, μ xx=8, μ yy=2 μ zz=2, μ ij, εij = 0 si i ≠ j.

modes	Simulation	Théorie
$\mathbf{f_{110}}$	176.8 MHz	176.78 MHz
$\mathbf{f_{111}}$	216.6 MHz	216.51 MHZ
$\mathbf{f_{102}}$	280.1 MHz	279.51 MHz
$\mathbf{f_{112}}$	306.7 MHz	306.19 MHz

Tableau 3, facteur de qualité d'une cavité cubique de=30 cm, remplie d'un matériau isotrope à pertes et dispersif εr =4.0, μr=1.0, $tan(\delta) = \sigma/(\omega_o \varepsilon_r \varepsilon_o)$, $\omega_o$la première fréquence de résonance.

$\boldsymbol{Q = f_o/\Delta f}$ **(Simulation)**	$\boldsymbol{Q = 1/\tan(\delta)}$ **(Théorie)**
18.6	19.1
25.97	25.42
38.52	38.12
76.18	76.25

On peut remarquer la bonne concordance entre la simulation TLM et la théorie [3].

II. Diffraction d'une sphère en matériau chiral par une onde plane

Le deuxième exemple concerne la diffraction d'une sphère remplie d'un milieu chiral dispersif (5.a) (5.b) (5.c)par une onde plane. Une comparaison avec une solution donnée par la série de Mie est utilisée comme référence [17] [18].

Les résultats sont présentés à la figure 8. Les équations de dispersion sont choisies de telle façon qu'à la fréquence de 0.5 GHz les paramètres du milieu soient $\varepsilon_r = 4.0, \mu_r = 2.0, \kappa = 0.0314$.

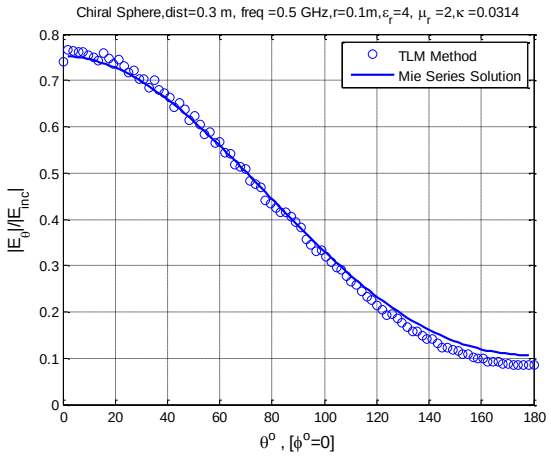

Figure 8, diffraction par une onde plane d'une sphère en matériau chiral de rayon 10 cm. Comparaison avec la série de Mie utilisée comme référence [18].

Les résultats sont présentés à la figure 8. On remarque une excellente adéquation du modèle TLM du simulateur et la solution analytique de la série de Mie. Aucun problème de stabilité n'a été observé pour les exemples présentés (2000 itérations).

III. Coefficient de réflexion d'une lame chirale dispersive dans un guide à plaques parallèles

Un autre exemple de validation concerne le calcul du coefficient de réflexion d'une lame chirale dispersive dans un guide à plaques parallèles illustré à la figure 9.

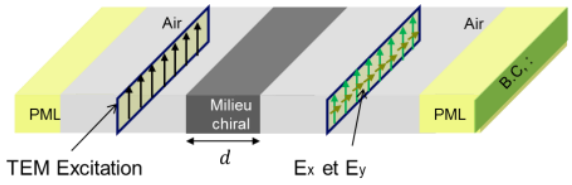

Figure 9. Guide d'ondes à plaques parallèles chargé par un échantillon chiral

La simulation a été effectuée à large bande par excitation temporelle à l'aide d'une impulsion gaussienne couvrant la bande de 1 à 3 GHz. Les paramètres du milieu chiral sont donnés par les relations (5.a), (5.b) et (5.c) dont les paramètres de l'échantillon sont montrés dans le tableau 4.

Tableau 4, Paramètres de l'échantillon chiral de la figure 10.

ε_∞	$4{,}0\ \varepsilon_o$	ω_h	$2\pi * 3{,}5\ 10^9$ rad/sec
ε_s	$4{,}4\ \varepsilon_o$	δ_h	$0{,}12\ \omega_h$
ω_e	$2\pi * 3{,}5\ 10^9$ rad/sec	τ_k	$0\ ps;\ 10{,}0\ ps$
δ_e	$0{,}14\ \omega_e$	ω_k	$2\pi * 3{,}5\ 10^9$ rad/sec
μ_∞	μ_o	δ_k	$0{,}1\ \omega_e$
μ_s	$1{,}1\mu_o$	d	$5{,}0\ mm$

Le coefficient de réflexion est illustré à la figure 10 et montre une bonne concordance avec la solution analytique. On notera que le cas $\tau_k = 0$ correspond au cas limite d'un milieu de Lorentz pur.

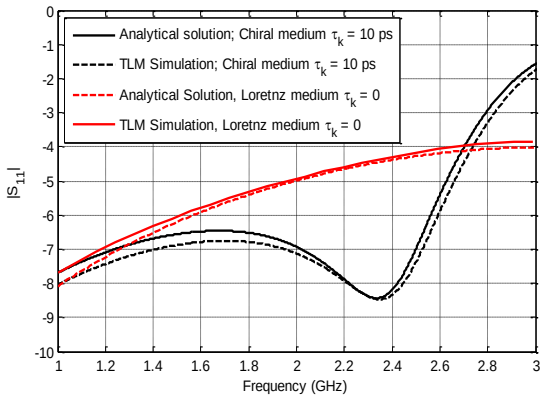

Figure 10. S_{11} d'un guide chargé par une lame chirale pour validation du simulateur TLM (cellules cubiques $\Delta l = 0{,}5\ mm$, 10^5 itérations).

IV. Paramètres S d'un guide d'ondes chargé par un échantillon de ferrite

Une fois le modèle validé, on l'a appliqué pour la caractérisation à large bande d'un guide d'onde métallique chargé par un échantillon de ferrite non saturé, cas pour lequel il n'existe pas de solution analytique. A noter aussi, que les logiciels commerciaux pour la plupart ne peuvent traiter ce type de milieu à cause de la difficulté de représenter la magnétisation jusqu'au niveau de la cellule pour obtenir une bonne précision.

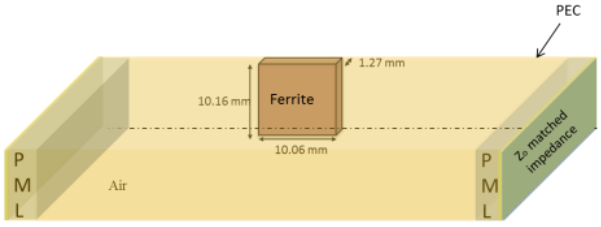

Figure 11. WR90 guide d'ondes de dimensions rectangulaire 10,16 cm x 22,86 mm chargé par échantillon de ferrite non saturé.

Comme le montre dans la figure 11, nous avons utilisé des couches PML avec 10 cellules d'épaisseur comme conditions aux limites absorbantes. La couche PML est terminée par l'impédance de l'espace libre pour améliorer l'absorption.

L'échantillon de ferrite a été caractérisé par un tenseur adéquat [6] qui prend en compte les domaines magnétiques du milieu ferrite non saturé. Une carte magnétostatique a été aussi insérée dans le simulateur TLM pour affiner la magnétisation de l'échantillon et tenir compte du champ démagnétisant qui dépend de la forme de l'échantillon. La figure 12 montre une comparaison avec CST [19] et la mesure pour un échantillon magnétisé de façon moyenne homogène (approximation).

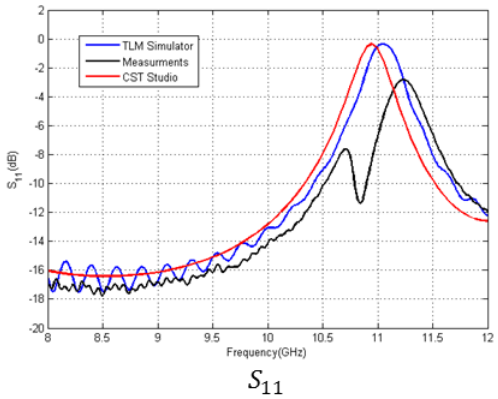

Figure 12. Coefficient de réflexion d'un guide chargé par un échantillon de ferrite non saturé magnétisé de façon homogène.

Les deux modèles numériques concordent assez bien avec la mesure avec un léger avantage pour la TLM. Cependant, ils ne reproduisent pas la première résonance et il y a un décalage en fréquence pour la 2^{e} résonance.

L'introduction de domaines avec des tenseurs locaux augmente considérablement le temps de calcul. Nous avons pu cependant faire une approximation de l'état de magnétisation en divisant l'échantillon en 9 sous-domaines (figure 13) à tenseur uniforme et comparer avec COMSOL [20] qui n'est pas un logiciel basé sur une approche temporelle et qui n'utilise pas un maillage hexaédrique.

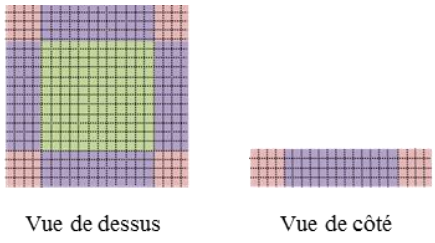

Figure 13. Approximation du ferrite par neuf sous-domaines magnétisés de façon homogène

La figure 14 montre des comparaisons entre les mesures (effectuées par le groupe de recherche sur les matériaux du Lab-STICC à l'Université de Brest [21]) et des solutions

numériques obtenues par le solveur TLM. Cette fois, on peut observer dans toutes les figures que les résultats produits par le simulateur TLM et COMSOL sont plus proche de la mesure que dans l'expérience précédente. En particulier, la résonance secondaire apparaît autour de 10,6 GHz et révèle qu'elle n'est pas due à un couplage parasite produit pendant la mesure. Les différences entre la mesure et les solutions numériques peuvent s'expliquer comme suit : tout d'abord, la décomposition en neuf sous-domaines homogènes pour approcher la magnétisation de l'échantillon n'est peut-être suffisante. Deuxièmement, le modèle physique pour établir le tenseur du milieu ferrite n'est pas parfait et peut introduire des erreurs. Cependant, des études doivent être encore faites pour les évaluer. Enfin, les mesures sont entachées d'erreurs également difficiles à quantifier.

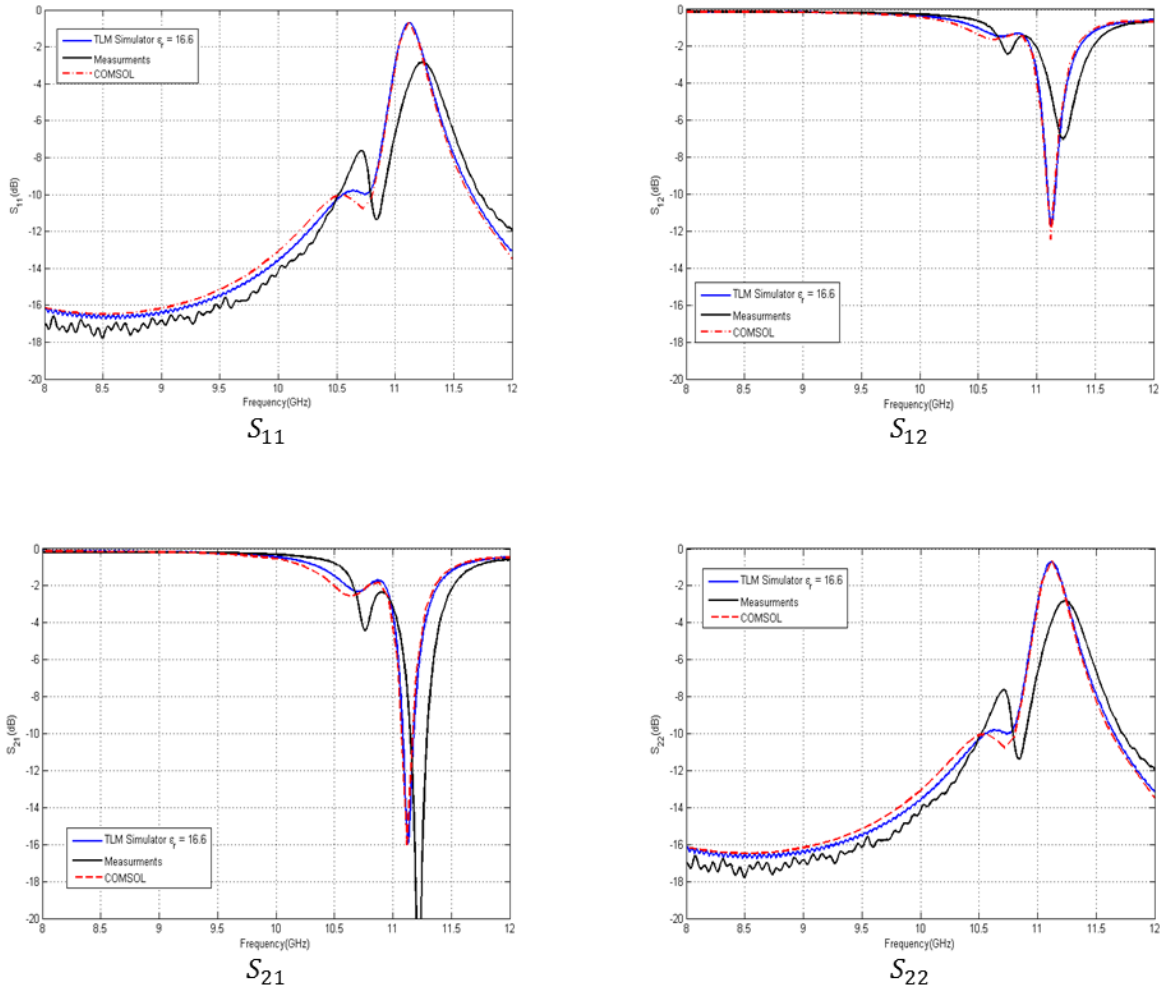

Figure 14. Paramètres S d'un guide chargé par un échantillon de ferrite non saturé avec l'approximation de la magnétisation par 9 sous-domaines homogènes (figure 13).

On peut aussi observer que les résultats de simulation obtenus par COMSOL sont très proches de ceux du simulateur TLM, même si COMSOL est un solveur dans le domaine de la fréquence et basé sur les éléments-finis (FEM) dont l'échantillonnage spatial est tétraédrique. Ceci peut

aussi indiquer que les mesures sont entachées d'une erreur plus élevée qui peut expliquer les différences.

Pour s'assurer d'une convergence du modèle TLM, la magnétisation DC de l'échantillon a été décrite au niveau de la cellule. La figure 15, montre la comparaison avec les mesures [21]en termes de paramètres S du guide d'onde chargé par l'échantillon de ferrite non homogène illustré à la figure 11. Comme nous pouvons le voir, le tenseur de perméabilité local dans chaque cellule donne une meilleure concordance avec la mesure. La première résonance est maintenant bien marquée. Toutefois, contrairement à la deuxième résonnance, son niveau et sa position montrent une différence relativement marquée.

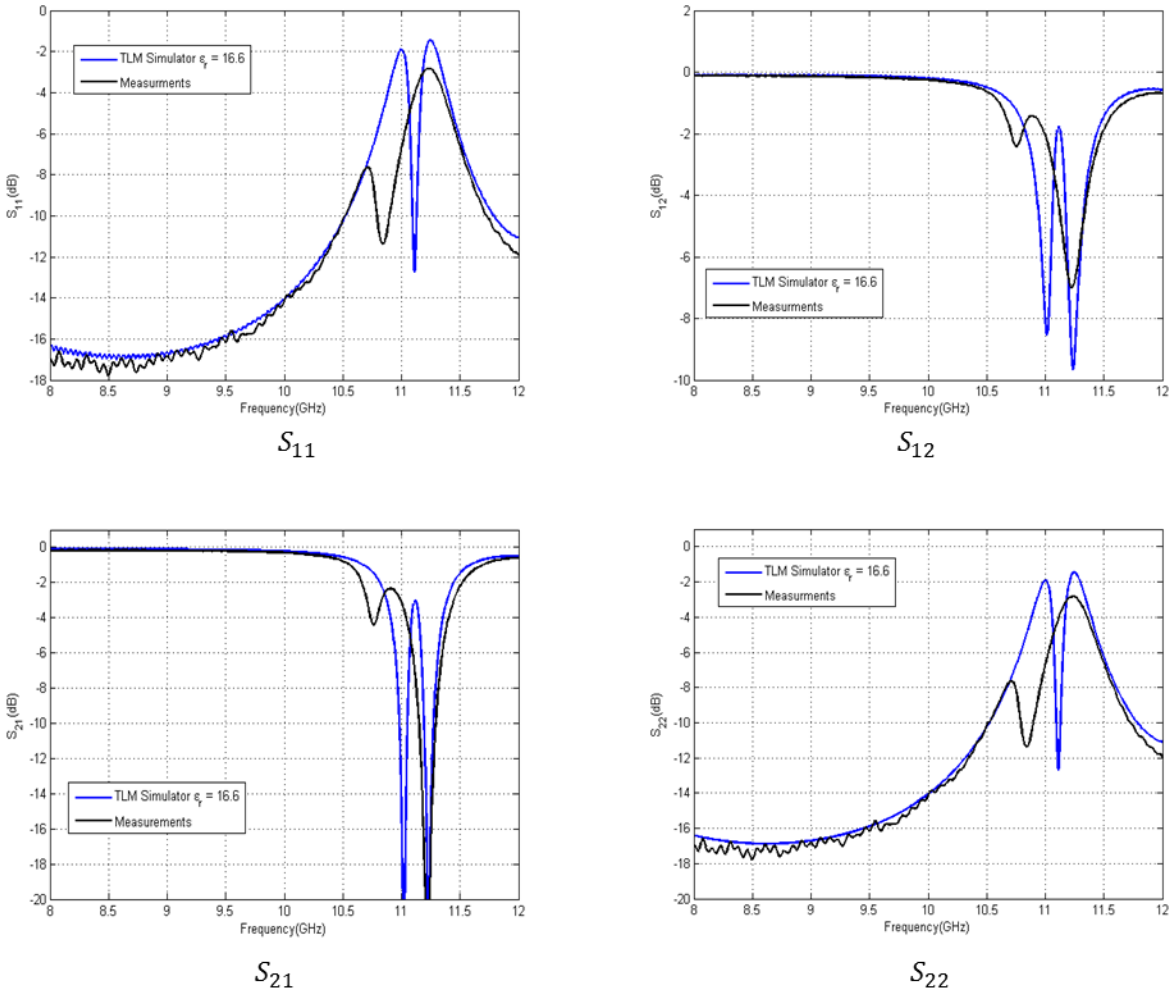

S_{11} S_{12} S_{21} S_{22}

Figure 15. Paramètres S d'un du guide chargé (figure 11) par un échantillon de ferrite échantillonnée au niveau de la cellule TLM.

Les raisons des différences observées ont déjà été mentionnées plus haut. On notera cependant que des mesures expérimentales répétées ont montré une petite différence en raison de la sensibilité du processus d'aimantation et le placement de l'échantillon à l'intérieur du guide

d'ondes. Il est intéressant de noter que l'utilisation du logiciel commercial COMSOL était presque impossible du fait que la procédure automatique de maillage débouchait sur un nombre de cellules exhaustif, empêchant ainsi tout résultat dans un temps de calcul raisonnable. La description du tenseur au niveau de la cellule n'a pas été possible avec les autres logiciels commerciaux. Enfin, on a noté qu'après 10^5 itérations en TLM, aucune instabilité n'a été observée pour toutes les simulations. Ceci tend à montrer que l'algorithme TLM modifié pour les milieux complexes est stable. Une démonstration théorique serait nécessaire pour valider cette observation.

6. Chapitre VI : Cas limites de méthodes dans le domaine temporel : basse fréquence et haut contrastes des paramètres constitutifs

Dans ce chapitre, deux questions principales ont été discutées. Au début, nous avons présenté les problèmes multi-échelles et de basse fréquence dans les techniques du domaine temporel et leurs difficultés associées. Ensuite, nous avons proposé des solutions nouvelles en appliquant des techniques de cartographie. Ils sont basés sur la modification de la métrique des deux domaines de l'espace et du temps et de transformer le problème initial en un problème bien posé et facile à résoudre. Toutefois, d'autres études doivent être menées pour connaître le potentiel de ces approches de cartographie. Dans la deuxième partie de ce chapitre, nous avons abordé d'autres cas difficiles pour les méthodes dans le domaine temporel, à savoir leurs performances en présence d'interfaces entre milieux à contraste élevé ou zones à taille de maillage très différent lorsque des maillages irréguliers (mais structurés) sont utilisés. Plus particulièrement, la comparaison entre FDTD méthodes et TD-TLM ont été réalisées. Les résultats de simulations numériques confirment clairement que la TD-TLM produit une meilleure convergence que la FDTD pour les deux cas ci-dessus. Cela signifie que la méthode TD-TLM a besoin d'un moins grand nombre de mailles que la FDTD pour le même niveau de précision.

6.a. Le problème basse fréquence dans les techniques du domaine temporel

Certains cas difficiles qui ont plusieurs impacts sur les méthodes dans le domaine temporel ont été étudiés et des solutions proposées. Tout d'abord, le problème de basse fréquence qui conduit généralement à des difficultés multi-échelle a été examiné. Pour éviter toute erreur de grossièreté (résolution spatiale), il est démontré que le pas temporel devient très faible pour assurer la stabilité. En conséquence, le temps de simulation explose et le signal de la réponse est très largement échantillonné au-delà du critère de Nyquist. Pour ce problème classique, nous avons proposé une nouvelle solution basée sur l'espace ou l'espace-temps des techniques de cartographie. Dans ce genre de cartographie, l'objectif est de transférer le domaine de calcul original dans un nouveau dans lequel le problème de basse fréquence disparaît. Des exemples simples sont présentés avec des résultats prometteurs.

6.b. Comparaison entre les méthodes FDTD et TD-TLM en présence d'interfaces entre milieux très contrastés en termes de paramètres constitutifs

Enfin, dans la dernière partie du travail nous avons effectué la comparaison entre les méthodes FDTD et SCN-TLM en simulant des structures avec des milieux très contrastés en termes de paramètres constitutifs. Cette étude confirme que la TLM (SCN) possède une convergence plus rapide que la FDTD (ou la méthode d'intégrations finies FIT) en maillage hexaédrique. On peut l'expliquer par la nature locale de l'algorithme TLM. Cette différence de convergence a été aussi nettement observée en présence de maillages irréguliers (structurés), lorsque le rapport des tailles de maille augmente. Ceci est aussi expliqué par le caractère local de l'algorithme TLM.

- **Example : Fréquences de coupure d'un mode dans un guide d'onde rectangulaire partiellement rempli par un diélectrique**

Dans cette expérience, on calcule la fréquence de coupure du mode dominant d'un guide d'ondes rectangulaire, de section $a = b = 10\,cm$, partiellement rempli par une plaque diélectrique de permittivité ε_r (figure 16).

L'objectif de cette expérience est d'étudier l'effet de l'interface entre les deux diélectriques (l'air et la lame diélectrique) utilisant à la fois la TLM et la FDTD. La solution analytique est considérée comme référence pour la comparaison [22].

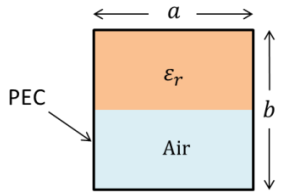

Figure 16, section transversale d'un guide d'onde partiellement rempli d'un diélectrique

Dans la figure 17, nous reportons l'erreur relative par rapport à la solution analytique pour différentes valeurs de permittivité et plusieurs discrétisations spatiales. Nous pouvons clairement observer la meilleure précision de la TLM. En outre, nous pouvons voir l'augmentation plus rapide de l'erreur relative de la FDTD avec la permittivité par rapport à la TLM. Par exemple, la TLM avec 10 cellules par longueur d'onde peut fournir une précision similaire à la FDTD avec 40 cellules par longueur d'onde pour un contraste élevé. Cependant, cet avantage diminue pour de faibles contrastes. On doit noter que pour être sûr que l'erreur soit due de façon prédominante à la mise à jour des champs à l'interface et non à la différence de dispersion (la FDTD est plus dispersive que la TLM), nous avons choisi la fréquence limite supérieure avec $\varepsilon_r = 40$ pour le calcul de λ_d. Par conséquent, nous pouvions négliger les effets de dispersion numériques sur toute la bande de fréquence.

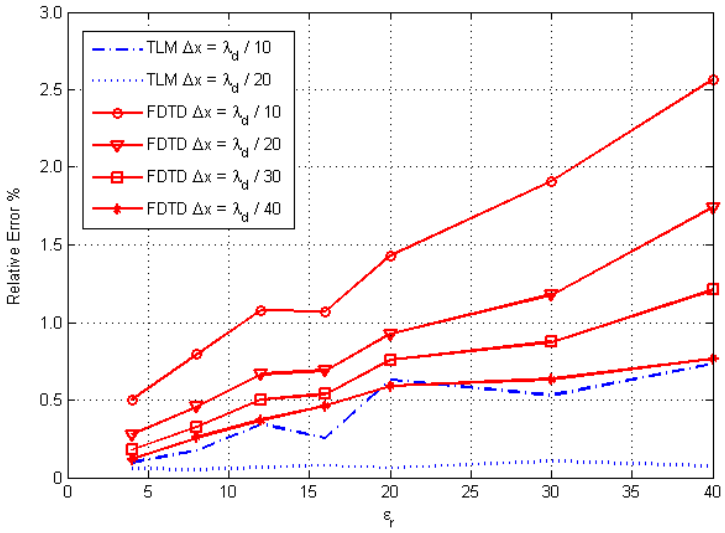

Figure 17, erreur relative de la fréquence de coupure du mode dominant du guide de la figure 16 en comparaison avec solution analytique [22]

Dans cette expérience, nous avons utilisé des cellules cubiques, et nous avons effectué 100 000 itérations pour les deux méthodes. Par contre, si le pas temporel maximal a été utilisé pour la TLM un pas temporel deux fois inférieur a été utilisé pour la FDTD pour assurer la stabilité. Enfin, d'autres simulations confirment les mêmes tendances pour les cas de maillages irréguliers (structurés) lorsque le rapport des tailles des mailles entre deux zones augmente.

7. Conclusion Générale

Dans ce travail de thèse, nous nous sommes concentrés principalement sur des techniques numériques dans le domaine temporel pour l'électrodynamique, y compris en présence de milieux complexes. En particulier, nous avons étudié la méthode "Transmission-Line Matrix" (TLM) comme la méthode de calcul choisie pour sa mise en œuvre dans un simulateur électromagnétique. Le modèle doit pouvoir traiter des géométries et des supports tridimensionnels généraux possédant des paramètres constitutifs arbitraires mais linéaires. Dans le chapitre II, nous avons présenté différents milieux complexes linéaires et discuté comment les champs électromagnétiques interagissent avec eux. Dans le chapitre III, nous avons révisé brièvement la théorie de la TLM depuis ses débuts jusqu'à un algorithme avancé qui peut traiter les médias complexes de façon générale. Ensuite, le simulateur TLM du laboratoire a été amélioré par l'ajout d'une interface avec le moteur de calcul TLM permettant une entrée simplifiée et conviviale de structures à géométrie complexe. Cette interface graphique (GUI) rend le simulateur convivial. En outre, le cœur de calcul TLM a été complété avec des fonctionnalités supplémentaires, y compris un environnement unifié qui permet de simuler des

matériaux non traditionnels tels que les médias chiraux, anisotropes et dispersifs. Enfin, nous avons effectué de nombreuses expériences pour valider à la fois le simulateur TLM et le module GUI par plusieurs comparaisons avec des solutions analytiques, des résultats générés par d'autres simulateurs commerciaux et les mesures.

Les solveurs EM commerciaux dans le domaine temporel que nous avons testés sont limités par rapport à notre simulateur TLM en termes de matériaux qu'ils peuvent appréhender. D'abord, quand il s'agit de milieux dispersifs, ils utilisent des méthodes dans le domaine fréquentiel uniquement (pour éviter l'utilisation de filtres dans le domaine temporel). D'autre part, ils sont limités lorsqu'il s'agit de milieux complexes fortement hétérogènes. Dans le cas des ferrites non saturées par exemple, on obtient des résultats validés uniquement lorsque chaque ce milieu est décrit avec un tenseur local défini au niveau de la cellule. Une telle définition n'a pu être entreprise qu'avec notre simulateur TLM, les logiciels commerciaux produisant des temps de calcul prohibitifs.

Dans le chapitre suivant, nous avons développé une analyse théorique complète des phénomènes de dispersion numériques et les conditions de stabilité pour le modèle TLM en présence de milieux complexes. Cette analyse était nécessaire car la simple règle, généralement utilisée et valable pour les milieux simples, n'a pas été prouvée valide en présence de milieux complexes. Par exemple, il a été montré que dans certains cas la taille maximale des mailles a été sous-estimée, ce qui augmente inutilement le coût de calcul. Par conséquent, il est recommandé qu'en présence de milieux complexes (dispersifs, anisotropes), une évaluation de la dispersion et de la stabilité soit effectuée au préalable. Des exemples montrent un gain de temps substantiel en faisant cette analyse.

En cinquième chapitre, nous avons présenté, le simulateur TLM et son interface graphique, puis nous avons présenté plusieurs expériences numériques pour validation, comme les antennes, guides d'ondes. L'utilisation de la transformation optique pour construire des cas complexes dont la solution analytique est connue a aussi été validée. Enfin, nous avons effectué une expérience d'un guide chargé par un échantillon de ferrite. Nous avons trouvé une très bonne concordance avec les mesures et d'autres logiciels comme CST et COMSOL.

Dans le chapitre VI, nous avons étudié le problème basse fréquence dans les techniques du domaine temporel. En effet, le pas temporel requis devient en général très petit et fait exploser le temps de calcul. Pour ce problème classique, nous avons proposé des solutions nouvelles en appliquant des techniques de cartographie. Ces solutions sont proposées sur la base de la modification du tenseur métrique de l'espace et du temps et la transformation du problème en un problème bien posé. Enfin, dans la dernière partie du projet nous avons effectué la comparaison entre les méthodes FDTD et TD-TLM en simulant des structures avec des milieux très contrastés en termes de paramètres constitutifs. Cette étude confirme que la TLM possède une convergence plus rapide que la FDTD. On peut l'expliquer par la nature locale de l'algorithme TD-TLM. Cette différence de convergence a été aussi nettement observée en présence de maillages irréguliers (structurés), lorsque le rapport des tailles de maille entre deux zones augmente.

Références

[1] P. B. Johns et R. L. Beurle, «Numerical solution of 2-dimensional scattering problems using a transmission-line matrix,» *Proc.IEE,* vol. 118, n° 19, September 1971.

[2] M. Krumpholz et P. Russer, «A field theoretical derivation of TLM,» *IEEE Transactions on Microwave Theory and Techniques,* vol. 42, n° 19, pp. 1660-1668, 1994.

[3] L. Landau et E. M. Lifshitz, Electrodynamcis of Continuous Media, Pergamon Press, 1984.

[4] A. Taflove and S. C. H. , Computational Electrodaynamics, The Finite-Difference Time-Domain Method, Norwood: Artch House, INC., 2005.

[5] M. I. Yaich, M. Khalladi et M. Essaadi, «Efficient Modeling of Chiral Media Using SCN-TLM Method,» *Serbian Journal of Electrical Engineering,* vol. 1, n° 12, pp. 249-254, 2004.

[6] P. Gelin et K. Berthou, «New consistent model for ferrite permeability tensor with arbitrary magnetization state,» *IEEE Transactions on Microwave Theory and Techniques,* vol. 45, n° 18, pp. 1185-1192, 1997.

[7] P. B.Johns, «A Symmetrical Condensed Node for the TLM Method,» *IEEE Transactions on Microwave Theory and Techniques,* Vols. MTT-35, n° 14, pp. 370-377, 1987.

[8] J. Paul, C. Christopoulos et D. W. P. Thomas, «Generalized Material Models in TLM- Part 2: Materials with Anisotropic Properties,» *IEEE Transactions on Antennas and Propagation,* vol. 47, n° 110, pp. 1535-1542, 1999.

[9] A. L. Farhat, S. L. Maguer, P. Quéffélec et M. Ney, «TLM Extension to Electromagnetic Field Analysis of Anisotropic and Dispersive Media: A Unified Field Equation,» *IEEE Transactions on Microwave Theory and Techniques,* vol. 60, n° 18, pp. 2339-2351, 2012.

[10] J. Paul, C. Christopoulos et D. W. P. Thomas, «Generalized Material Models in TLM- Part I: Materials with Frequency-Dependent Properties,» *IEEE Transactions on Antennas and Propagation,* vol. 47, n° 110, pp. 1528-1534, 1999.

[11] M. M.Ney et N. Pena, «A General Formulation of a Three-dimensional TLM Condensed Node with the Modeling of Electric and Magnetic Losses and Current Sources,» *12th Annual Review of Progress in Applied Computational Electromagnetics,* pp. 262-269, 18-22 March 1996.

[12] L. L. Scharf, Statistical Signal Processing, Detection, Estimation, and Time Series Analysis, ADDISON-WESLEY PUPLISHING COMPANY, 1991.

[13] C. Huber, M. Krumpholz et P. Russer, «Dispersion in aniotropic media modeled by three-dimensional TLM,» *IEEE Transactions on Microwave Theory and Techniques,* vol. 43, n° 18, pp.

1923-1934, 1995.

[14] M. Krumpholz et P. Russer, «A generalized method for the calculation of TLM dispersion relations,» chez *23rd European Microwave Conference*, 1993.

[15] P. Russer et M. Krumpholz, «The Hilbert Space Fromulation of the TLM Method,» *Interantional Journal of Numerical Modelling: Electronic Networks, Devices and Fields*, vol. 6, pp. 29-45, 1993.

[16] http://www.gidhome.com/.

[17] S. J. Adams, ELECTROMAGNETIC THEORY, McGRAW-HILL BOOK COMPANY, INC., 1941.

[18] V. Demir, A. Elsherbeni, D. Worasawate et E. Arvas, «A Graphical User Interface (GUI) for Plane-Wave Scattering from a Conducting, Dielectric, or Chiral Sphere,» *IEEE Antennas and Propagation Magazine*, vol. 46, n° 16, pp. 94-99, October 2004.

[19] https://www.cst.com/.

[20] http://www.comsol.com/.

[21] Armel Le_Goullec, G. Verissimom, P. Queffelecm, V. Laurm, I. Albert et T. Girard, «Ferrite-based phase shifters design: the modeling problem of nonsaturated anisotropic ferrites,» chez *Microwave Symposium Digest (IMS), 2013 IEEE MTT-S International*, Seattle.

[22] T. G. Mihran, «Microwave Oven Mode Tuning by Slab Dielectric Loads,» *IEEE Transactions on Microwave Theory and Techniques*, Vols. MTT-26, n° 16, pp. 381-387, 1978.

[23] L. D. Landau et E. M. Lifshitz, The Classical Theory of Fields, PERGAMON PRESS, 1962.

[24] Z. Cai et J. Bornemann, «Generalized spectral-domain analysis for multilayered complex media and high-Tc superconductor applications,» *IEEE Transactions on Microwave Theory and Techniques*, vol. 40, n° 112, pp. 2251 -2257, 1992 .

Résumé

Au cours de ce projet de thèse, nous avons travaillé sur les techniques numériques dans le domaine temporel en électromagnétisme pour les structures comprenant des matériaux complexes. Nous avons utilisé la méthode «Transmission-Line Matrix» (TLM) comme une méthode de calcul pour mettre en œuvre un simulateur électromagnétique général. Ensuite, nous l'avons validé par plusieurs comparaisons avec des solutions analytiques et des mesures. Pour faciliter les simulations de structures géométriques complexes, nous avons développé une interface utilisateur graphique (GUI) pour le simulateur. Nous avons développé une analyse théorique complète des phénomènes de dispersion numériques et les conditions de stabilité du modèle TLM lorsque des milieux complexes sont impliqués. Cela permet d'optimiser les ressources de l'ordinateur en fonction du niveau de précision requis. L'autre problème que nous avons abordé est celui en basse fréquence dans les techniques du domaine temporel. En effet, le pas temporel requis devient en général très petit et fait exploser le temps de calcul. Pour ce problème classique, nous avons proposé des solutions nouvelles en appliquant des techniques de cartographie. Ces solutions sont proposées sur la base de la modification du tenseur métrique de l'espace et du temps et la transformation du problème en un problème bien posé. Enfin, dans la dernière partie du projet nous avons effectué la comparaison entre les méthodes FDTD et TD-TLM en simulant des structures avec des milieux très contrastés en termes de paramètres constitutifs. Cette étude confirme que la TLM possède une convergence plus rapide que la FDTD. On peut l'expliquer par la nature locale de l'algorithme TD-TLM. Cette différence de convergence a été aussi nettement observée en présence de maillages irréguliers (structurés), lorsque le rapport des tailles de maille augmente.

Mots-clés : TLM, FDTD, Calcul électromagnétique, Milieux complexes

Abstract

During this PhD project, we worked on time-domain numerical techniques in electromagnetism for analysing structures that include complex media. We used transmission-line matrix method (TLM) as a computational method to implement a general electromagnetic simulator. Then, it was validated by several comparisons with analytical solutions and measurements. To facilitate the simulations of complex geometry, we developed a graphical user interface (GUI). After that, we developed a complete theoretical analysis for numerical dispersion phenomena and stability conditions for the TLM model, when dealing with complex media. This provides the possibility to optimize the computer resources according to the required level of accuracy. The next problem we tackled was the low-frequency problem in time-domain techniques for which the time step becomes very small; as a result, the simulation time becomes exhaustive. We proposed some novel solutions by applying mapping techniques. These are based on modifying the metric tensor of the space and time frame and transforming the problem into a well-posed one. Finally, in the last part of the thesis, we performed comparison between FDTD and TD-TLM methods in simulating structures with highly contrasted media in terms of constitutive parameters. This study confirms that the TLM method has a significantly better convergence than FDTD. This is explained by the local character of the TLM algorithm. This difference in convergence was also observed for irregular (structured) meshing, when adjacent mesh size ratio increases.

Keywords : Time-domain methods, Transmission-line matrix method, Complex linear media, Low frequency, problem, Transformation, optics, High contrast media, Finite difference time-domain method, Dispersion and stability analysis

TELECOM Bretagne

n° d'ordre : 2015telb0334

Télécom Bretagne

Technopôle Brest-Iroise - CS 83818 - 29238 Brest Cedex 3

Tél : + 33(0) 29 00 11 11 - Fax : + 33(0) 29 00 10 00